Experimental Studies of the Unusual and Fragile Ferromagnetism of $LaCrGe_3$ and $LaCrSb_3$

By

RAHIM R. ULLAH
DISSERTATION

Submitted in partial satisfaction of the requirements for the degree of

DOCTOR OF PHILOSOPHY

in

Physics

in the

OFFICE OF GRADUATE STUDIES

of the

UNIVERSITY OF CALIFORNIA

DAVIS

Approved:

---

Valentin Taufour, Chair

---

Rajiv R.P. Singh

---

Inna M. Vishik

Committee in Charge

2024

# Contents

# List of Figures

# Abstract

This dissertation details my exploration of two compounds: $LaCrGe_3$ and $LaCrSb_3$. While their names differ by only two letters, and therefore their compositions by only one element, they are quite different. The relevant question to ask about these two ferromagnetic systems is: "what happens when their ferromagnetism is suppressed?" Although the magnetic phase diagram of $LaCrGe_3$ under pressure has previously been charted, there are aspects of its rich temperature-pressure-magnetic field phase space that are contested. In particular, through a meticulous study of its magnetic domain behavior, I provide evidence in favor of the existence of multiple ferromagnetic states in $LaCrGe_3$. We find that investigating domain behavior can lead to a more accurate way of characterizing new materials and perhaps a method of probing crossovers between ferromagnetic states. On the other hand, the ferromagnetism of $LaCrSb_3$ is relatively robust to pressure. Therefore, I use Fe substitution to suppress its Curie temperature and discover the first reported magnetic phase diagram of its kind—one with an avoided quantum tricritical point. The $LaCr_{1-x}Fe_xSb_3$ system has a temperature-chemical substitution-magnetic field phase diagram that is ripe with magnetic features for closer examination. Further study of both materials will likely lead to additional discoveries in the world of magnetism.

# Acknowledgements

It is difficult for me to imagine that a PhD can be completed without help from a village. Here is a special acknowledgement to those who have generously supported me throughout this six year endeavour.

First, I would like to thank my advisor, Valentin Taufour, for his patience. Although we did not always see eye-to-eye, it is because of his guidance, genuine excitement towards my magnetization measurements, and his push to actually understand those measurements, that I developed into the scientist I am today.

To Peter Klavins. It is difficult to say where condensed matter labs in Davis would be without Peter's encyclopedic knowledge of everything, ability to stay nearly calm when 'you can't make this stuff up' complications arise, and willingness to help transfer helium for the $n^{th}$ time, even if it was 4 o'clock on a Friday. I will fondly remember uncrating new machines off the loading dock, moving sensitive instruments from room to room with a pallet jack, and 'having to jig something up' with spare parts from the room of requirement. While it is difficult for an outside observer to see how these tasks were directly related to the PhD, they certainly were necessary, and definitely the most fun.

To Xiangdong Zhu, for imaging the magnetic domain phenomena that I obsessed over for a majority of my PhD, reminding me to not to spend too much time doing what the theorists are supposed to do, and for setting an example for how quickly papers can be written.

To the members of my committee. I would like to thank Professor Inna Vishik for knowing how to re-frame questions in a way that I can understand them, and for consistently bringing inspirational speakers to condensed matter seminar. I also acknowledge Professor Rajiv Singh for reminding me that there is always more to learn and investigate when it comes to the distinction between first and second order phase transitions, and for letting me TA electronics lab whenever I needed to.

Speaking of electronics lab, Eric Prebys was instrumental for always having a spot for me to TA Physics 116. It was during this class that I actually learned the things I thought I knew about electronics, although I am also grateful that Eric never forgot to give me the answer key to the Verilog FPGA code. Cheers to keeping alive the idea that a practical knowledge of analog electronics is a vital component of experimental physics.

To the members of the Taufour Lab, past and present, although our projects were separate on paper, I am grateful that they were intertwined in practice. No one can compete with Edward Cardenas' wide range of experiences and insights. I will miss our early-morning therapy sessions, mid-day quests for bits and bobs, and evening exchanges of recommended TV shows and films to relentlessly quote the following day. I am thankful that I had Jackson Badger as the senior student to look up to. He was a great role model and exemplified a 'keep your head down and do you science' attitude that I should have embraced earlier. I am also thankful for Jeff Harvey's genuine kindness, for showing me the ropes early on, and for setting me up with a solid foundation in self-flux synthesis. I have had countless wonderful scientific discussions with Hanshang Jin, Zihao Shen, and Yunshu Shi. With their expertise and technical know-how, I know the lab is in good hands.

I have appreciated the support of members of condensed matter labs across the hall: Igor Vinograd, Cameron Chaffey, Rashad Kadado, Phurba Sherpa, Journey Byland and others. You have all been helpful beyond borrowing tools, juggling nitrogen dewars, and transferring helium.

I am also indebted to members of the Moler Group for putting the possibility of doing a PhD in physics on the map. So thank you to Kam, John Kirtley, Zheng Cui, Aaron Rosenberg, Christopher Watson, Hilary Noad, and Sean Hart for putting up with the bright-eyed undergrad who wondered why anyone would want to do anything besides experimental physics.

There are many friends who have helped me through the most difficult times of my PhD. Highlights include Sam Girvin for reliably hosting the gold standard of Friendsgiving parties, and for proving that you can get a well-paying job just by knowing how to use opamps. Jason Chen for adventures involving slabs of wood and bicycle parts. Ian Bennett for knowing that sometimes, you just have to have a day. Varun Tolani, for being the 'let's just pick up where we left of' kind of friend.

Of course my parents. For making sure there was always food on the table, a roof over my head, and a home to come back to.

Most importantly, I recognize the uncountably infinite amount of support from Iliana Bray and her love and encouragement through thick and thin.

# List of Publications

Chapters 2 and 3 of this thesis contain material from the following publications or preprints:

1. **R.R. Ullah**, P. Klavins, X.D. Zhu, and V. Taufour. Magnetic domain depinning as possible evidence for two ferromagnetic phases in $LaCrGe_3$. *Physical Review B*, **107**, 184431 (2023)

2. **R.R. Ullah**, J.S. Harvey, Y. Wu, H.B. Cao, J.R. Badger, P. Klavins, and V. Taufour. Avoided quantum tricritical point and emergence of a canted magnetic phase in $LaCr_{1-x}Fe_xSb_3$. *Submitted to Physical Review Letters* (2024)

In addition, I contributed samples, measurements, or calculations to the following publications:

1. K. Rana, H. Kotegawa, **R.R. Ullah**, J.S. Harvey, S.L. Bud'ko, P.C. Canfield, H. Tou, V. Taufour, and Y. Furukawa. Magnetic Fluctuations in the itinerant ferromagnet $LaCrGe_3$ studied by $^{139}La$ NMR. *Physical Review B*, **99**, 214417 (2019)

2. Z.E. Brubaker, J.S. Harvey, J.R. Badger, **R.R. Ullah**, D.J. Campbell, Y. Xiao, P. Chow, C. Kenney-Benson, J.S. Smith, C. Reynolds, J. Paglione, R.J. Zieve, J.R. Jeffries, and V. Taufour. Pressure-induced suppresiion of ferromagnetism in the itinerant ferromagnet $LaCrSb_3$. *Physical Review B*, **101**, 214408 (2020)

3. XD Zhu, **R. Ullah**, and V. Taufour. Oblique-incidence Sagnac interferometric scanning microscope for studying magneto-optic effects of materials at low temperatures. *Review of Scientific Instruments*, **92**, 043706 (2021)

4. K. Rana, H. Kotegawa, **R.R. Ullah**, E, Gati, S.L. Bud'ko, P.C. Canfield, H. Tou, V. Taufour, and Y. Furukawa. Magnetic properties of the itinerant ferromagnet $LaCrGe_3$ under pressure studied by $^{139}La$ NMR. *Physical Review B*, **103**, 174426 (2021)

5. A.L. Gross, L. Falling, M.C. Staab, M.I. Montero, **R.R. Ullah**, D.M. Nisson, P. Klavins, K.J. Koski, N.J. Curro, V. Taufour, S. Nemsak, and I.M. Vishik. Copper migration and surface oxidation of $Cu_xBi_2Se_3$ in ambient pressure environments. *Journal of Physics: Materials*, **5**, 044005 (2022)

6. Z. Shen, X.D. Zhu, **R.R. Ullah**, P. Klavins, and V. Taufour. Anomalous depinning of magnetic domain walls within the ferromagnetic phase of the Weyl semimetal $Co_3Sn_2S_2$. *Journal of Physics: Condensed Matter*, **35**, 045802 (2022)

# Chapter 1

# Introduction

"So what do you do?" My wedding party pitch[1] about my work in the Taufour Lab goes as follows: the question to ask is 'why are we still studying magnetism?' Although we have used magnets for thousands of years, there is no unifying underlying theory of magnetism, and there are still new magnetic phenomena out there just waiting to be discovered.

Beginning as early as the discovery that rocks with magnetic impurities point North, there has been no question of magnetism's utility and role in our day-to-day lives. Our electrified world is made possible by permanent magnets, compounds that inherently sustain magnetic fields. A vast majority of the electricity we use is produced by spinning turbines connected to generators which contain strong permanent magnets and operate using Faraday's law: a changing magnetic flux yields electricity. It does not matter whether the turbines are spun by steam created from burning fossil fuels or from controlled nuclear fission. It does not matter if the turbine is driven by the wind that blows through the air or by water rushing through a hydroelectric dam. In each of these cases, the generator is the same. Electric motors are just generators in reverse and they are seemingly everywhere,[2] not just in the electric vehicles occupying prime parking real estate—even your car's gasoline engine relies on an electric motor to get started.

Permanent magnets have applications in computing as well, since ferromagnetic materials can form magnetic domains that are able to represent the 1's and 0's on which classical computing is entirely based. Traditional spinning platter hard drives made of ferromagnetic materials form the backbone of the internet. Your credit card number is encoded on the black stripe with ferromagnetic domains, so in a way, magnetism enables our capitalist society to exist, for better or for worse.

[1] A wedding party pitch is like an elevator pitch, but instead of being able to simply alight at a different floor than the person who posed the question, you are stuck at the dinner table and have to keep the conversation going throughout a three course meal.

[2] Most electric motors use permanent magnets. They are found in cordless and corded tools, and small household appliances such as your coffee grinder, hairdryers, fans, electric toothbrushes, etc.

Since permanent magnets do not require any external power to function, they have a way of working in the background of our everyday lives. In some cases, it is frustrating when things are or become non-magnetic.[3] The advent of stainless steel refrigerator doors means fridge magnets no longer work to hold up pictures. Demagnetized screwdriver bits are maddening to use. A hotel access card always seems to demagnetize at the worst possible time.

Now that you are aware of the utility and ubiquity of permanent magnets, your next question is inevitably along the lines of "so your research is about making better magnets?" Well, no. While a chemist or engineer might try to make a better magnet, one with favorable properties such as a large magnetic moment (a measure of its strength) or a high Curie temperature, a physicist makes a magnet with the goal of understanding something new about magnetism. Take the Curie temperature, $T_{\mathrm{C}}$, as an example for comparison. The $T_{\mathrm{C}}$ of magnetic materials is the temperature below which the material becomes ferromagnetic, and above which no longer produces a magnetic field. So far, the permanent magnets I have mentioned (which are very likely to be $Nd_2Fe_{14}B$, $T_{\mathrm{C}} \approx 600\,\mathrm{K}$) have a $T_{\mathrm{C}}$ well above room temperature, so we do not even consider the possibility that they will lose their magnetism.[4] The magnets that I create and study, however, do not even become magnetic until reaching low temperatures, temperatures at least below 100 K. These magnets are not going to replace the ones in your earbuds. In fact, the interesting physics seems to appear when we make magnets worse by driving $T_{\mathrm{C}}$ to even lower temperatures and decreasing their magnetic moment with non-thermal tuning parameters such as pressure or chemical substitution. So, as a physicist, I am not researching magnets for potential utility; rather, I am investigating novel magnetic phenomena with the goal of hoping to understand a little bit more about how magnetism works.

"Low temperatures...do you mean superconductivity? Did you work on LK-99?" Superconductivity is indeed the first quantum phenomenon people think about when they consider physics that only reveals itself at low temperatures. Specifically, it is possibility of *room temperature* superconductivity that attracts news media and excites the general public. This sentiment is surprising since resistance to electrical current is not really something that gets in the way of our day-to-day lives.[5] Still, claims of the discovery of a room temperature superconductor are widely reported throughout news outlets, regardless of how unsubstanti-

[3] In some cases, the opposite is true. For example, a magnetized mainspring in a mechanical wristwatch can wreak havoc on its timekeeping ability. In response, Rolex introduced the Milgauss in 1954, a watch designed to withstand magnetic fields up to 1000 gauss, for the scientific researcher who works near fields.

[4] There is one exception where you probably have experienced, albeit unknowingly, reaching $T_{\mathrm{C}}$—a rice cooker. Inexpensive, simple, one-switch rice cookers utilize a magnetic switch with a $T_{\mathrm{C}}$ just above the boiling point of water. The rice is cooked once all of the water has been absorbed or boiled away, and hence the temperature rises above $T_{\mathrm{C}}$, the magnetic switch becomes non-magnetic and cuts off the power to the heating element.

[5] Unless you happen to be personally responsible for transmitting electricity across our power grid. Or, like me, are in charge of refilling dewars with liquid helium so the superconducting magnets they contain remain cold so they do not quench and possibly explode.

ated they are[6] or vanilla their proposed potential applications.[7] Perhaps it is because room temperature superconductivity is so elusive that people find it so alluring. The idea that superconductivity can possibly occur at room temperature is at odds with the belief that low temperatures are required because only at low temperatures are the quantum interactions responsible for superconductivity not disrupted by the thermal fluctuations caused by temperature. But what if I told you we already had access to a purely quantum phenomenon that works at room temperature? What if I told you it has its own collection of elusive properties that scientists do not yet fully understand?

In its simplest description, a permanent magnet originates from unpaired electrons that each have a spin, $S$. Spin is a type of angular momentum that is unique to quantum mechanics, so by definition, permanent magnets are an inherently quantum phenomena. With that in mind, it is actually an amazing fact that magnets work at room temperature at all. Imagine for a moment that the long-range alignment of spins required for ferromagnetism, that is, a permanent magnet, was catastrophically interrupted by temperature. Sure with Ampere's Law you could still get magnetic fields from running current through a loop of wire. Since generators rely on permanent magnets, however, electrical current could only be produced by the chemistry that takes place inside of batteries. Think of all of the aforementioned uses of magnets that would now be encumbered by batteries. Needless to say, our world would be quite different from what it is today. So while scientists search for a room temperature superconductor, let us be thankful that magnetism, the other quantum phenomenon, works at room temperature and beyond.

Inevitably during the wedding party pitch, there will be some question about theoretical physics versus experimental physics.[8] Personally, I stumbled into experimental physics because it allowed me to tinker and problem-solve in a real-world context. A major goal in magnetism research is to find new magnetic compounds. It is difficult to theoretically predict whether a compound will exist at all, let alone whether it will be magnetic, and if so, estimate its Curie temperature, or the size of its magnetic moment [1]. This difficulty comes from the fact that solving the Schrodinger equation[9] is computationally impossible to do for the Avogadro's number of particles in a sample. Mixing together a few elements, heating them up and slowly cooling them down to see if crystals form, and if they do, placing them in various machines that determine the crystal's properties is comparatively easy. The work I present in this thesis is based on experimental data taken on magnetic compounds that I grew. The theory will have to come later.

[6] LK-99 was the most memorable during my PhD. My main takeaway from that fiasco is that perhaps we should reconsider the value we ascribe to density functional theory (DFT) calculations.

[7] The lossless transfer of power is a popular one, or simply the fact that existing technologies that rely on superconductivity, such as medical imaging via MRI or magnetic sensing via SQUID, would no longer need to be cooled down. What inventions would actually precipitate if a room temperature superconductor were to be discovered is up to your imagination.

[8] This is probably due to the advent of the TV show *The Big Bang Theory*.

[9] Since magnetism is a quantum phenomenon.

This thesis is dedicated to magnetic moment, $m$, and its brother, $M$, the magnetization,[10] both of which originate from the spin, $S$, the quantum mechanical angular momentum that makes magnetism possible. Specifically, the majority of this thesis is based on my measurements of $M$ of two different ferromagnetic compounds, $LaCrGe_3$ and $LaCrSb_3$, which were both grown in-house, by me, starting from raw elements. From my analysis of my magnetization measurements, I propose two new ideas that should aid the discovery of even more unusual magnetic phenomena. First, I propose that analyzing magnetic domain behavior can be used as a tool to discern crossovers between multiple ferromagnetic states. Second, I propose that novel magnetic phases appear in the vicinity of a quantum tricritical point. This thesis will detail how I arrived at these two conclusions and what they mean.

[10] $M = m/V$ where $V$ is the volume of the sample

## 1.1 Overview

First, I will discuss $LaCrGe_3$ and how I was able to pair careful measurements with a 20 year old magnetometer and textbook domain wall theory to solve a mystery. While certain probes of $LaCrGe_3$ suggest that two ferromagnetic states (FM1 and FM2) exist, evidence for the two states had not yet been recognized in magnetization data. Furthermore, the unusual magnetization curve of $LaCrGe_3$ had been previously observed, but not well understood. By studying the domain behavior of $LaCrGe_3$ we were able to explain its unusual magnetization curve and provide supporting evidence for its two ferromagnetic states. This project exemplifies the idea that just because a material has been heavily studied, does not mean that there is not more we can learn about it.[11]

Next, I will discuss $LaCrSb_3$, which is the realization of the idea that interesting physics appears when we tune a magnet to make it worse, i.e., lower its magnetic moment and Curie temperature. In this case, I substitute increasing amounts of Fe in place of Cr to make single crystals of $LaCr_{1-x}Fe_xSb_3$ and study how its magnetic state develops. As expected, the magnetic moment and Curie temperature initially decrease. As more Fe is added, however, the previously ferromagnetic compound becomes antiferromagnetic. While we are aware of the utility of ferromagnets, an antiferromagnet's utility is not readily seen in the day to day. Still, research has shown that antiferromagnetism may be a key player in next generation technology [2]. Tuning a ferromagnet into an antiferromagnet, however, is not an unusual occurrence, and the novelty of this project only becomes apparent when we apply magnetic field. By applying magnetic field to the antiferromagnetic samples of $LaCr_{1-x}Fe_xSb_3$, we are able to approach the rare quantum tricritical point (QTCP). At a QTCP, the competing interactions of ferromagnetism and antiferromagnetism are expected to diverge. For the first time, however, we show that the quantum tricritical point is ultimately avoided by the appearance of a new magnetic phase.

The physics ends with my discussion of the unusual ferromagnetism of $LaCrGe_3$ and $LaCrSb_3$. I have not just been a 'physicist' for the past decade, however, I have been an 'experimental physicist,' so I find it appropriate to conclude my thesis with a short chapter that focuses on the details of my experimental work. I hope the tips and tricks I provide will help expedite, ever so slightly, a future PhD student's discovery in the realm of magnetism.

[11] In fact, my advisor, Valentin Taufour, performed more complicated measurements on $LaCrGe_3$ to map its magnetic phase diagram and discover that ferromagnetic quantum criticality in this system is avoided by the appearance of a new magnetic phase. Still, towards the end of this project, he confessed that he was ready to close the chapter on $LaCrGe_3$.

# Chapter 2

# $LaCrGe_3$

## 2.1 A Short History of the Project

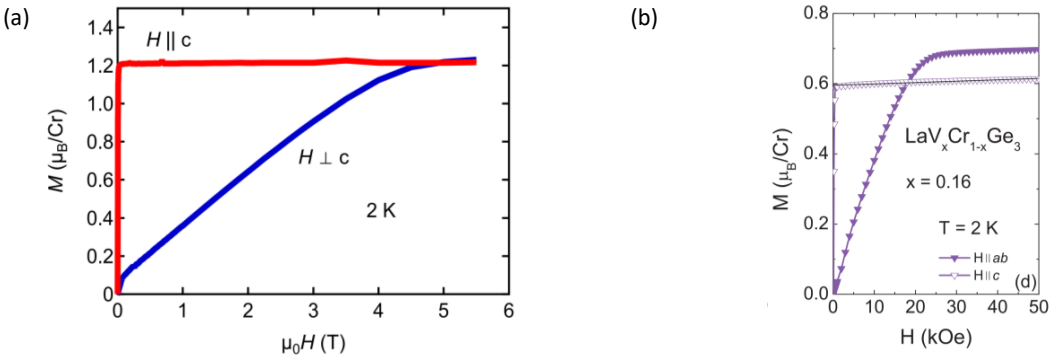


**Figure 2.1:** With the concept of hard axis ordering fresh in our minds [3], we noticed that $LaCrGe_3$, and even more so La(Cr,V)$Ge_3$, were potential candidates for the phenomenon. (a) Magnetization as a function of applied magnetic field ($M(H)$) for $LaCrGe_3$ [4] shows a small discrepancy in the saturation magnetization between the two crystallographic directions. (b) When V is substituted in for Cr, the published $M(H)$ curves [5] appear to show an even larger difference in the saturation magnetization along the two crystal axes. While we eventually determined that this discrepancy is a measurement artifact (discussed in detail in Section 4.1.1), these two figures caused us to take a closer look at the magnetization of $LaCrGe_3$ in the hopes of better understanding its unusual magnetization curves.

This project was initially prompted by the paper by Hafner *et al.* [3]. Their recognition of the prevalence of hard axis ordering in Kondo lattice ferromagnets made us wonder if the phenomena occurs in non-Kondo lattice compounds. Hard axis ordering describes the case where the ferromagnetic (FM) order points along the hard axis, that is, at zero field, the FM moments align along the axis which has a lower spontaneous magnetization ($M_s$) compared to the non-ordering axis. An anisotropic $M_s$ is surprising, as it breaks our rotating moment-based understanding of ferromagnetism. Valentin recalled two cases where he had seen the hard axis and the easy axis magnetizations saturate to different moments. First, in his own overview

of quantum criticality in $LaCrGe_3$ [4], a figure (reproduced in Fig. 2.1(a)) shows anisotropic magnetization as a function of applied field ($M(H)$) which hints at the hard axis overtaking the easy axis near their magnetometer's maximum 5 T field. Second, in a study of the effects of V substitution in $LaCrGe_3$, the authors present anisotropic $M(H)$ curves (reproduced in Fig. 2.1(b)) that show a significant difference in the spontaneous magnetization along each axis, so it is possible to interpret that V substitution induces hard axis ordering in $LaCrGe_3$ [5].

We eventually ruled out hard axis ordering in $LaCrGe_3$, V substituted or otherwise. The small discrepancy in the un-substituted sample, as well as the sizeable difference in the V substituted samples, were both due to poor sample alignment in the magnetometer. I will revisit hard axis ordering and the importance of sample alignment in Section 4.1.1. While this chapter is unrelated to hard axis ordering, it was during the search for hard axis ordering in $LaCrGe_3$ that we found something equally puzzling. Our investigation involved measuring $M(H)$ along each axis (i.e., $H||c$ and $H||ab$) at different temperatures to check for differences in $M_s$, a change in anisotropy, or an anomaly in the demagnetization factor. In particular, checking for anomalies in the demagnetization factor required a careful look at the low-field region of the $M(H)$ measurements, so we started to measure hysteresis loops as well. As expected, the hysteresis loops decreased in size as temperature was increased until they eventually disappeared. Rather unexpectedly, however, further increasing temperature caused the hysteresis loop to open up again before reaching $T_C$.

I first learned about the unusual magnetization curve in $LaCrGe_3$ when Zach Brubaker, a fellow grad student, caught me in the hallway and brought up the anomaly in the magnetization as a function of temperature ($M(T)$) curve in the samples I had grown for him. He drew the puzzling magnetization curve on the door-mounted whiteboard. The magnetization increases at the Curie temperature, but then suddenly drops and settles to a temperature independent value. While I would later describe the shape of the $M(T)$ curve as resembling a shark-fin, at the time, I did not know enough about magnetization measurements to say anything helpful. We left it at "something to ask Valentin about."[1]

$LaCrGe_3$ was the first compound I synthesized, but it was a system that Valentin had worked extensively on during his postdoc, performing careful resistivity measurements under pressure to map out its magnetic phase diagram. $LaCrGe_3$ was being studied as a system to investigate quantum criticality, i.e., research the question "what happens when the ferromagentic state is suppressed?" As such, an onslaught of difficult measurements were being performed by a group of talented scientists in Ames, IA to try to better under-

[1] While Zach's investigation of $LaCrGe_3$ did not result in a complete project (he already had an abundance of material for his PhD, *High Pressure Studies of Quantum Materials* [6]), I also contributed to his project on $LaCrSb_3$, a compound I will talk extensively about later in Chapter 3. I am listed as a co-author of his paper for precisely two reasons: 1) I was able to ship him new samples when he realized he brought powdered sample to a neutron diffraction experiment that required single crystals; 2) I reconfigured our PPMS breakout box so he could run his custom pressure experiment while the Lawrence Livermore National Labs PPMS was down.

stand the compound's rich magnetic phase diagram. These measurements—thermal expansion, resistivity, specific heat, x-ray diffraction, neutron diffraction, $\mu$SR measurements, all with the added complication of being under pressure—resulted in an alternative interpretation of the $LaCrGe_3$ magnetic phase diagram [7]. Furthermore, there was still no explanation of the perplexing $M(T)$ curve that had been observed in all previous studies of the compound [5, 8]. Perhaps there was something missed in the un-substituted, ambient pressure sample.

What I enjoy most about this project is that I was able to explain a puzzling feature with magnetization measurements in a commercially available machine and a textbook-level understanding of magnetic domain theory. Furthermore, the measurement techniques and the accompanying domain pinning theory has already shown its usefulness explaining anomalous phenomena in low-field $M(T)$ curves of other materials [9]. I am excited to see what other systems will benefit from our analysis.

*The following sections are based on the article that was published in Physical Review B [10]*

## 2.2 Synthesis

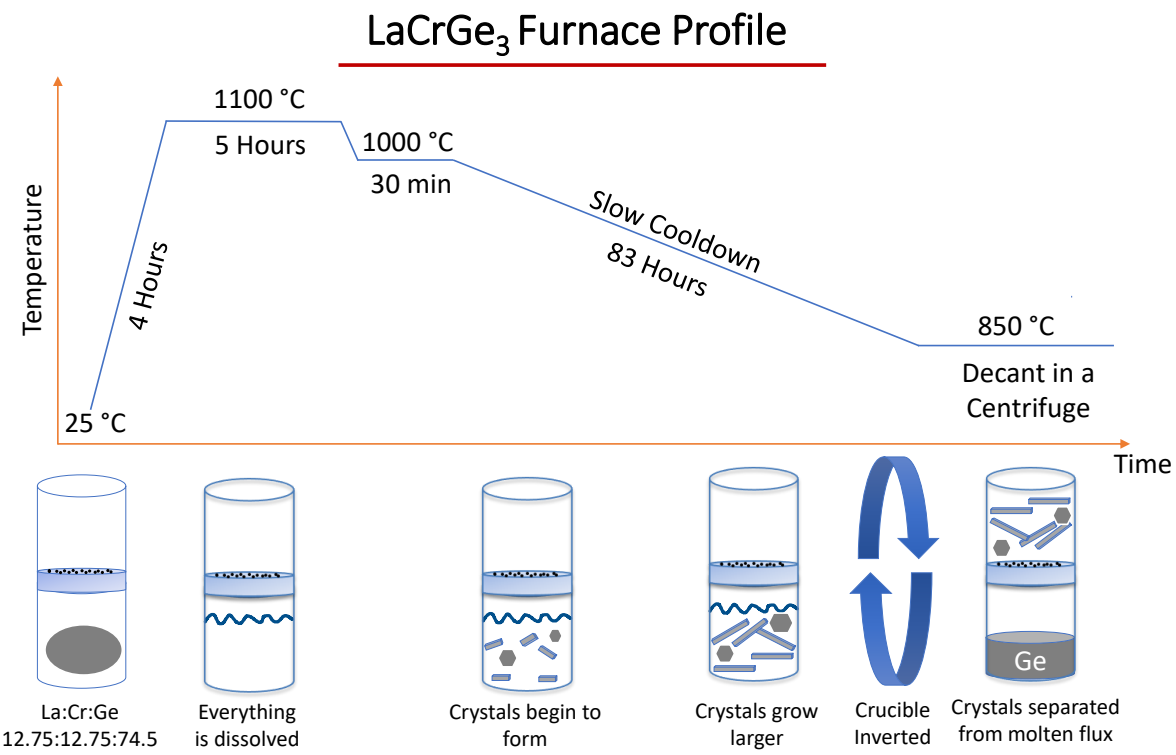


**Figure 2.2:** The temperature profile we used to grow single crystals of $LaCrGe_3$ is a modified version of the one developed by Lin *et al.*[11]. The cooldown time from 1100°C to 1000°C was reduced to 1 hour since it is unlikely that crystal growth takes place at these temperatures. The slow cooldown from 1000°C to 850°C (this spin temperature was increased from 825°C) was lengthened from 65 hours to 83 hours. Extending the cooldown time up to 120 hours did not result in larger crystals. Below the temperature profile is a schematic diagram of the inside of the crucible during the different steps of crystal growth.

As a synthesis lab, we specialize in growing our single crystal samples in-house. Unlike labs which focus on a particular method of measurement (ARPES, STM, scanning SQUID, scanning MOKE, neutron diffraction etc.), we do not have the luxury of getting samples in the mail. So it is appropriate to begin with how I made the $LaCrGe_3$ for this project.

Typically, new compounds are first synthesized in chemistry labs, perhaps by arc melting elements together on stoichiometry resulting in polycrystalline samples. If characterization determines, or even hints, that the compound is worth studying further, a different lab that specializes in single crystal synthesis may begin to develop a method for growing single crystals of the compound.[2] $LaCrGe_3$ follows this prescribed sequence of events. The first polycrystalline synthesis of $LaCrGe_3$ was performed by Bie *et al.* [8] and the

[2]This can be a complicated process involving numerous trials adjusting an abundance of parameters including the ratio of elements and temperature profile. Jackson Badger and Valentin performed such trials to create single crystals of the superconductor $LaNiGa_2$ [12] which had previously only been synthesized in polycrystalline form. Armed with single crystals, they were able to determine that the initially proposed crystal structure was incorrect.

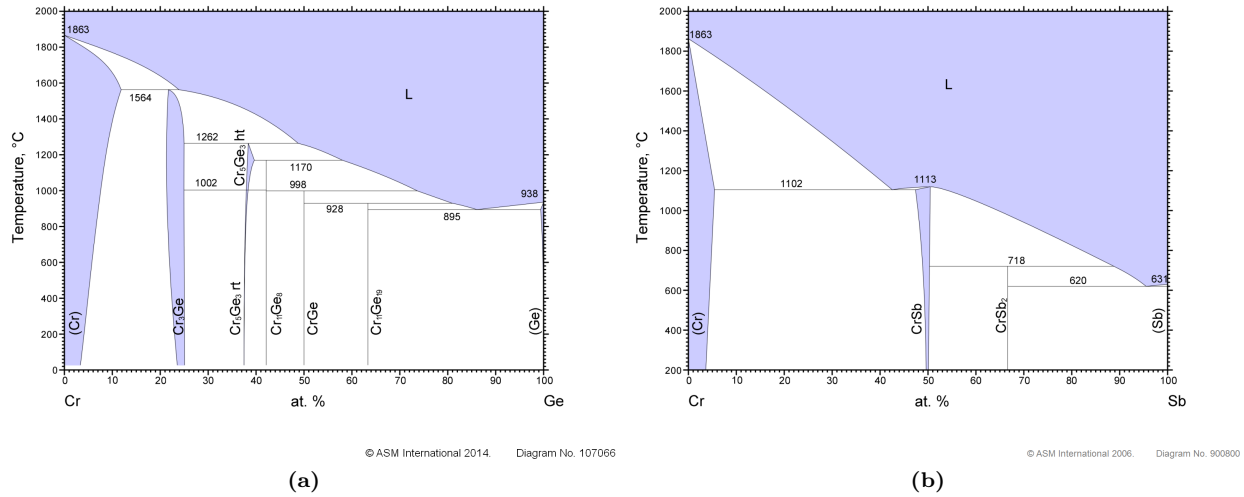


**(a)** **(b)**

**Figure 2.3:** (a) The CrGe binary phase diagram [13] and (b) the CrSb binary phase diagram [14]. Both of these diagrams show that Ge and Sb are suitable fluxes, *i.e.*, they lower the melting point of Cr. Comparing these diagrams, we see that Sb is a better flux than Ge, which is one of the reasons why $LaCrSb_3$ does not need to be arc melted while $LaCrGe_3$ does.

first single crystals were synthesized by Lin *et al.* [5] in Paul Canfield's lab, where Valentin was a postdoc and research scientist. I was fortunate that the recipe for making $LaCrGe_3$ had already been well-established by the time it was my turn to work on the compound.

Single crystals of $LaCrGe_3$ were synthesized with a self-flux solution growth technique [11] following the temperature profile in Fig. 2.2 and beginning with a non-stoichiometric ratio of 12.75 : 12.75 : 74.5 of Ames Laboratory La pieces, 4N Aesar Cr crystallites, and 6N Alfa Aesar Puratronic Ge pieces. The La pieces should be silver in color, and the dull gray or white color that emerges on the surface is due to oxidation and should be removed with a stainless steel brush reserved for use on La. La pieces from Ames lab are noticeably softer than the 4N REacton La used in my initial batches and can be cut with a good pair of side cutters as opposed to benchtop mounted bolt cutters. The 4N Cr pieces are impractical to cut, so the amount of the La and Ge should be calculated from a starting Cr mass.

The constituent elements were arc melted together in an Ar environment in a custom-built apparatus[3]. Figure 2.3 compares the binary phase diagrams of Cr-Ge and Cr-Sb and shows that while Sb drives the melting temperature of Cr to well below the 1200°C maximum temperature for quartz ampoules, Ge does not. Therefore, $LaCrGe_3$ needs to be arc melted whereas $LaCrSb_3$ does not. When the arc touches the Ge, the Ge tends to explode and disperse elements throughout the chamber. To prevent this catastrophe, the La

[3]Commercial arc furnaces are also an option. With some machining and a knowledge of vacuum and water plumbing, however, it is possible to build your own. An arc furnace uses an electrical arc powered by a TIG welder (Tungsten Intert Gas, although the suits have renamed it Gas Tungsten Arc Welding or GTAW) to locally heat whatever is touching the arc to temperatures around five times higher than the 1200°C to 1500°C of our box furnaces. The heating takes place in a vacuum chamber that can be pumped down and back-filled with Ar. The elements are placed in a divot in a copper hearth, which is water-cooled to prevent it from melting

should be placed on top, and the arc should touch it first. When heated by the arc, the La will liquefy and engulf everything below it. The mass of the arc-melted ingot should be measured and compared to the mass of the constituent elements. Small losses can be expected (in the range of $1-2\%$). A gain, however, could be the result of oxidation and would warrant checking the arc furnace for leaks and starting the synthesis process over again.

The arc melted ingot is then placed into a Canfield Crucible Set [15]. The crucible set is sealed in a quartz tube in a 160 mmHg partial pressure of Ar. The sealed ampoule is heated from room temperature to 1100°C over a 4 hour period and held at that temperature for 5 hours to ensure complete dissolution. The reaction is cooled to 1000°C in 2 hours before being slowly cooled to 850°C over an 83 hour period. At 850°C, the ampoule is quickly removed from the furnace and placed into a centrifuge where the liquid flux is separated from the solidified crystals. This step of the synthesis is diagrammed in Fig. 2.2. $LaCrGe_3$ single crystals form hexagonal prisms, where the $a$ and $b$ axes form the hexagonal faces that grow along the $c$ axis.[4]

I discovered that reaction placement within the furnace had a large effect; reactions placed closer to the door of the furnace yielded large single crystals while those placed deeper into the furnace resulted in delicate needles. This observation leads us to believe that a thermal gradient is beneficial to this particular synthesis. Perhaps the thermal gradient makes convection currents inside the crucible that either keep the liquid well-mixed or help break up unfavorable nucleation sites, or both. The realization that the placement in the furnace is important is the result of running two batches at the same time and keeping track of where each batch was inside the furnace.[5] The batches were initially staggered in order to make retrieval with tongs from the furnace easier, however, once we figured out that the batches further away from the door consistently resulted in needle-like samples, batches were both placed close to the door.

Figure 2.4(a) shows an example of large $LaCrGe_3$ crystals that, in addition to my experiments, were able to be used for nuclear magnetic resonance (NMR) measurements [16, 17] as well as inelastic neutron diffraction measurements (Kelly Neubauer and Pencheng Dai, unpublished). A selection of crystals were crushed into a fine powder, and powder x-ray diffraction data was collected with a Rigaku MiniFlex diffractometer. A resulting XRD pattern is shown in Figure 2.4(b), and we confirmed that these crystals were of the correct phase by comparing the measured pattern to previous reports [8].

[4] You might find that in contrast to thin films made using molecular beam epitaxy, the flux-growth of synthesis of single crystals is comparatively medieval, but that does not make it any less valuable.

[5] This is a testament to how keeping careful records is integral to doing good science.

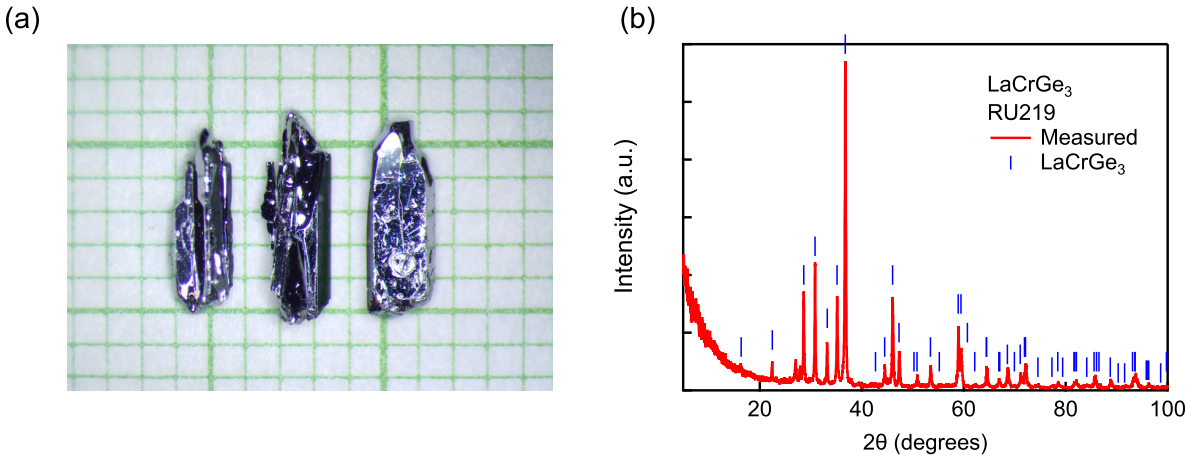


**Figure 2.4:** (a) An example of the larger $LaCrGe_3$ single crystals that can be grown. We found that placing the reactions closer to the door of the furnace resulted in samples like the ones pictured, whereas reactions placed further from the door resulted in small, needle-like samples. (b) An example of a powder x-ray diffraction (PXRD) pattern. The red line is the measured spectra. The blue tick marks are the peak locations associated with $LaCrGe_3$ previously reported by Ref. [8]. As demonstrated, when faceted single crystals are powdered, no obvious extraneous peaks appear in the measured data.

## 2.3 Studying Magnetic Domain Behavior and its Relationship to FM1 and FM2

The ferromagnetic compound $LaCrGe_3$ ($T_C = 85\,K$, $BaNiO_3$-type crystal structure) is a proven playground for studying the suppression of ferromagnetism under pressure. Many multiprobe experiments have mapped its temperature-pressure-magnetic field phase diagram [18, 19, 4, 17, 7]. These experiments exploring ferromagnetic quantum criticality in $LaCrGe_3$ take place in extreme conditions and consequently leave unsolved mysteries. For example, one such mystery is the magnetic phase that appears in place of a quantum critical point. This magnetic phase was initially proposed to be an $AFM_Q$ phase [18, 4] in agreement with the theoretical proposals of avoided ferromagnetic quantum critical points [20, 21, 22, 23, 24, 25, 26, 27], but the Q-vector has proven difficult to determine, and recently, a short-ranged FM order phase has been suggested as an alternative [7]. The mystery relevant to our study, however, is the one surrounding the existence of two ferromagnetic states, FM1 and FM2, within the FM region of $LaCrGe_3$.

The possibility of two ferromagnetic phases existing in $LaCrGe_3$ was first recognized based on a broad maximum in the temperature derivative of resistivity, $d\rho_{ab}/dT$ [19], that resembled that in $UGe_2$, in which two ferromagnetic phases are well established [30, 31, 32, 33]. In $UGe_2$, the phases have distinct moments and the magnetic ground state evolves from FM2 ($M_0 \approx 1.5\,\mu_B$/U) to FM1 ($M_0 \approx 0.9\,\mu_B$/U) at pressure $p_x \approx 1.2\,GPa$, before becoming paramagnetic above $p_c \approx 1.5\,GPa$. In $LaCrGe_3$, however, applying pressure

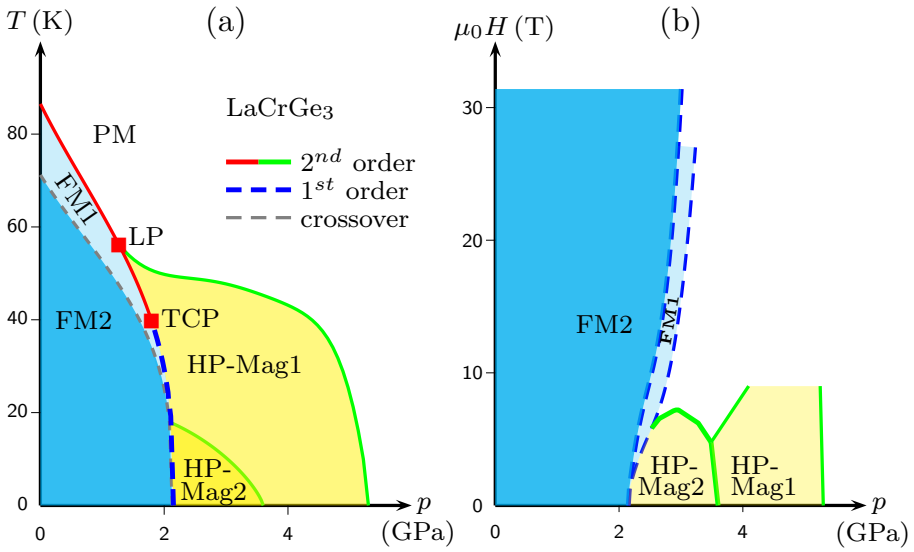


**Figure 2.5:** (a) Temperature-pressure and (b) magnetic field-pressure phase diagrams of $LaCrGe_3$ deduced from resistivity, magnetization, and $\mu$SR measurements [18, 19, 4]. The paramagnetic (PM), high-pressure magnetic phases (HP-Mag1 and HP-Mag2) and the two ferromagnetic phases (FM1 and FM2) are indicated. The Lifshitz point (LP) and tricritical point (TCP) are also shown. (a) At zero field, a broad maximum in the temperature derivative of resistivity has been interpreted as a crossover between two ferromagnetic phases FM1 and FM2. Under pressure, the crossover line merges with the first-order transition line between FM and HP-Mag2. (b) Under applied field at low temperature there are successive field-induced first-order transitions into the FM1 and FM2 states.

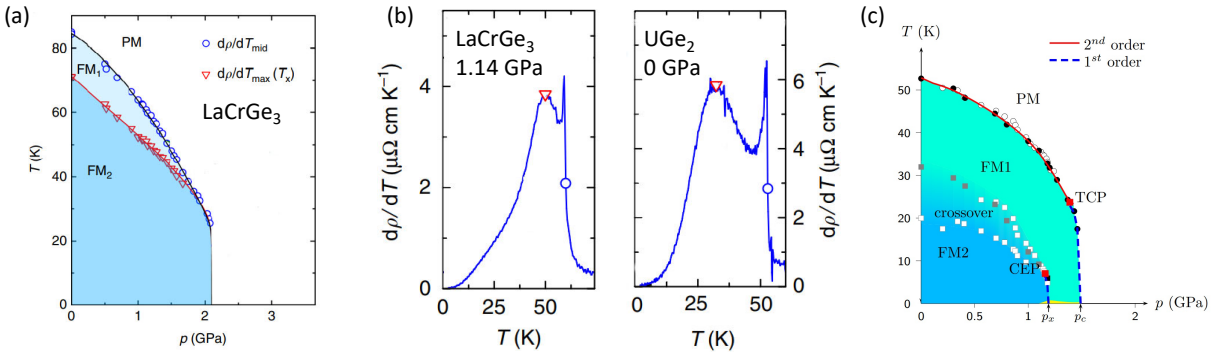


**Figure 2.6:** (a) The $T$ v. $p$ phase diagram for $LaCrGe_3$ shows the presence of two ferromagnetic states, FM1 and FM2 (Fig. 1(d) in Ref. [28], $AFM_Q$ phases omitted for clarity). The two phases merge such that FM1 does not exist at low temperature. (b) The criteria in $d\rho/dT$ used to determine that there is a crossover to a distinct FM2 state (red triangle) below the PM-FM1 transition (open blue circle) (Fig. 2(a) and Fig. 2(b) in Ref. [28]). The $d\rho/dT$ curves for $LaCrGe_3$ and $UGe_2$ are remarkably similar. (c) The $T$ v. $p$ phase diagram for $UGe_2$ (Fig. 1 in Ref. [29]). Unlike FM1 in $LaCrGe_3$, the FM1 state in $UGe_2$ exists at low temperatures.

causes the crossover boundary between FM1 and FM2 to merge with the quantum phase transition line (i.e. $p_x = p_c$), and FM1 is not accessible at zero temperature, as shown in Fig. 2.5a. Nevertheless, applying magnetic field separates the phases again (see Fig. 2.5b), and features of a phase transition are readily observed and form two planes of first order transitions, called wings, ending at quantum wing critical points [19]. At ambient pressure, however, there is no genuine phase transition between FM1 and FM2. Instead, there is a crossover regime which is allowed if FM1 and FM2 have the same symmetry, as is the case in $UGe_2$ where the only difference between the two phases is the size of the magnetic moment. Under ambient pressure, evidence for a crossover at $T_x \approx 70\,\mathrm{K}$ in $LaCrGe_3$ has been observed in many physical properties, such as $d\rho_{ab}/dT$ [19], $d\rho_c/dT$ [7], specific heat [11], and thermoelectric power [34], but features of FM1 and FM2 have yet to be recognized in magnetization, $M$.

Here, we present magnetization data on $LaCrGe_3$ that supports the existence of FM1 and FM2. Our spatially-resolved images of magnetic domains reveal a significant change in the domain structure on either side of the expected FM1-FM2 crossover. We find that the temperature dependence of the coercive field, $H_c$, shows the rare case in which $H_c$ increases with temperature and reaches a local maximum at 72.5 K, near $T_x \approx 70\,\mathrm{K}$ where the crossover between FM1 and FM2 is reported to occur. Furthermore, we observe the unusual situation where the virgin magnetization curve is limited by domain wall pinning at high temperatures ($T \gtrsim 60\,\mathrm{K}$), but subsequently shows no domain wall pinning at low temperatures ($T \lesssim 60\,\mathrm{K}$). We are able to incorporate this change between domain-wall immobility and mobility into a simple model that beautifully recreates the previously unexplained features observed in the magnetization curves of $LaCrGe_3$ under low applied magnetic fields. Finally, we show that the difference in domain wall mobility is likely caused by a change in the ferromagnetic exchange constant and magnetic moment, thus consistent with a crossover between two ferromagnetic states.

There is evidence that two ferromagnetic states are not uncommon in fragile FM systems. In the case of $LaCrGe_3$, we recognized that the FM1-FM2 crossover can be detected in magnetization by way of spatially resolved images as well as bulk DC magnetization measurements. Other measurements also show anomalies in similar temperature regions that may stem from the crossover. For example, our domain-wall pinning and depinning analysis is directly supported by AC susceptibility measurements (reproduced in Fig. 2.7) which indicate domain pinning in the similar temperature region of increased coercivity [35, 36]. Interestingly, the AC susceptibility data shows two peaks, which also appear in two other compounds with ferromagnetic quantum phase transitions, UCoAl [38] and $Sr_3Ru_2O_7$ [39]. A sharp peak below $T_C$ and near $T_x$ was also observed in recent AC susceptibility measurements (reproduced in Fig. 2.7(d)) with the field applied perpendicular to the $c$ axis [37]. Additional evidence for the FM1-FM2 crossover can be found in thermoelectric power measurements (reproduced in Fig. 2.8) where the local minimum attributed to the crossover in $UGe_2$ [40]

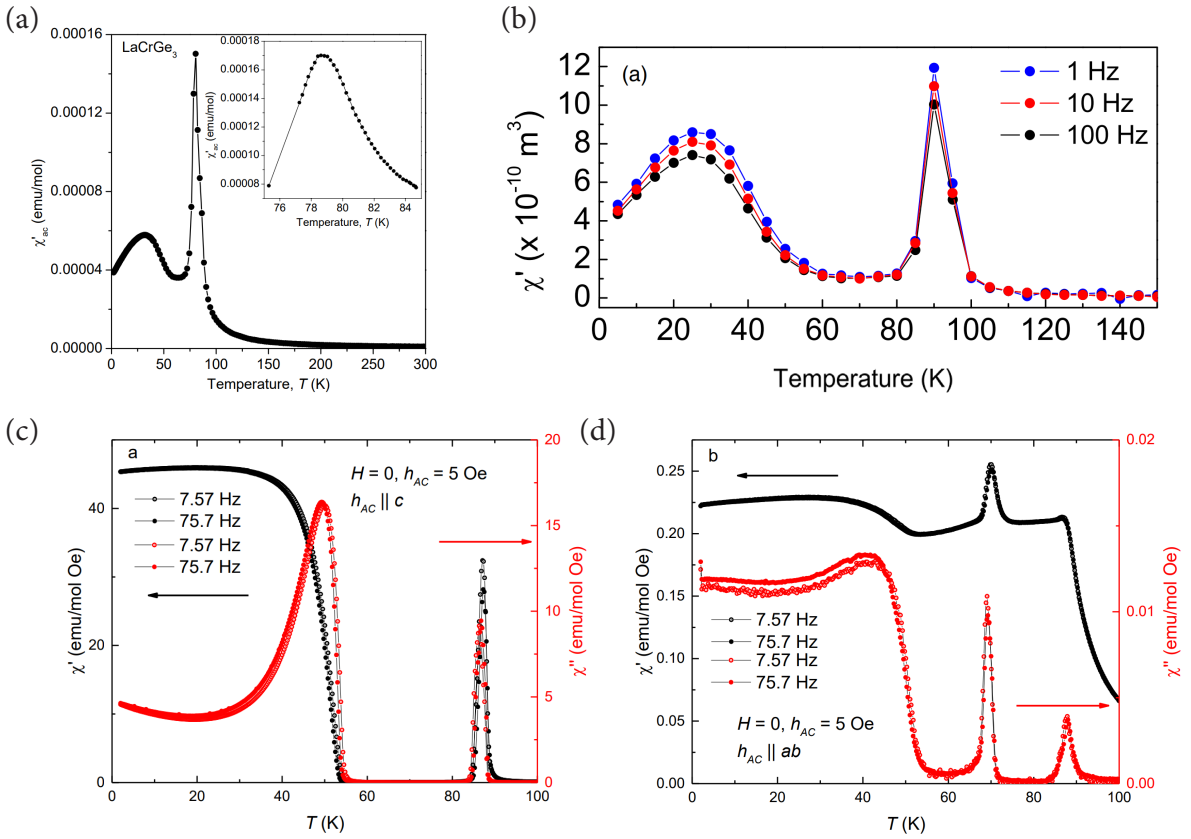


**Figure 2.7:** AC magnetic susceptibility is another tool that can probe the ferromagnetic domain and FM state behavior in $LaCrGe_3$. (a) The first AC susceptibility measurements of $LaCrGe_3$ were performed on polycrystalline samples in 2009 (Fig. A1-2(a) in Haiying Bie's PhD thesis, Ref. [35]). (b) In 2021, Bosch-Santos *et al.* (Fig. 4 in Ref. [36]) also measured AC susceptibility and made the connection to the domain behavior: the diminished response in the 60 K-80 K range below $T_C$ could be a consequence of pinned domains. With single crystal samples, Xu *et al.* (Fig. 6 in Ref. [37]) were able to investigate AC susceptibility with the perturbing magnetic field ($h_{AC}$) along the (c) easy axis ($c$ axis) and the (d) hard axis ($ab$ plane). (c) The easy axis measurement is consistent with the aforementioned polycrystalline studies: there is a sharp feature at $T_C$ followed by a broad increase in signal below 50 K. It makes sense that the easy axis measurement mirrors the polycrystalline measurement since the response along the hard axis is two orders of magnitude smaller than that of the easy axis. (d) The hard axis measurement reveals an astounding feature at $T_x \approx 70$ K; a sharp peak that occurs in both $\chi'$ and $\chi''$. Furthermore, along this hard axis, it appears that the peak at $T_x$ is even larger than the one at $T_C$. This may be the clearest feature of a crossover between FM1 and FM2 in magnetization.

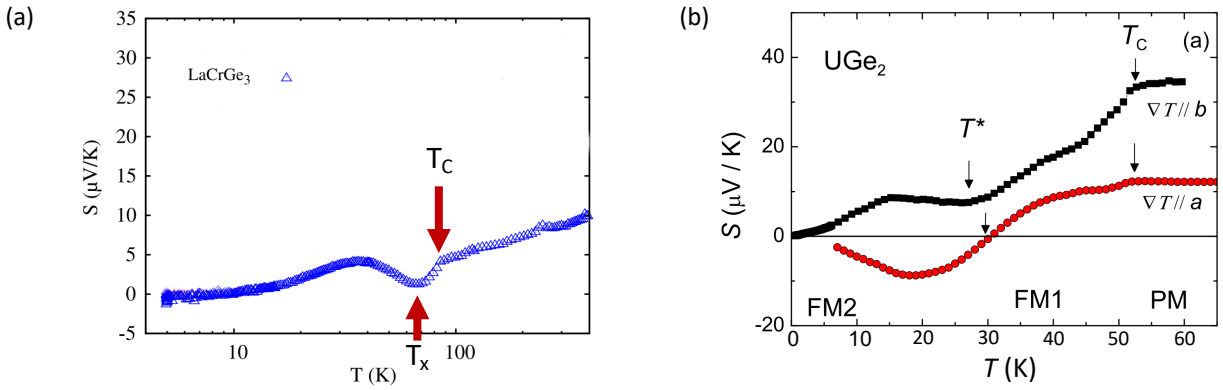


**Figure 2.8:** Thermoelectric power ($S$) measured in (a) $LaCrGe_3$ (Fig. 7 in Ref. [34]) and (b) $UGe_2$ (Fig. 1 in Ref. [40]). (b) In $UGe_2$, $T_C$ (PM-FM1 transition) and $T^*$ (FM1-FM2 crossover, analogous to $T_x$) were identified as a shoulder and a minimum in the thermoelectric power, respectively. (a) Following the criteria established by $UGe_2$, we add red arrows to highlight the shoulder ($T_C$) and the minimum ($T_x$, FM1-FM2 crossover) of the thermoelectric power in $LaCrGe_3$.

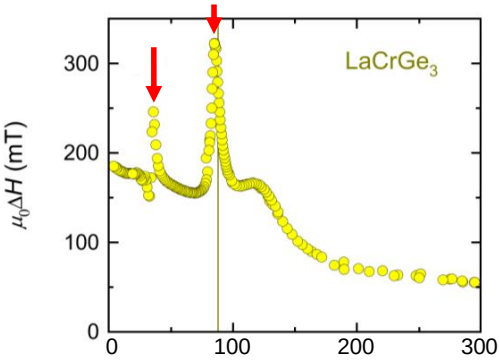


**Figure 2.9:** The electron spin resonance (ESR) linewidth (Fig. 5 in Ref. [41]). We add red arrows to point out the two distinct peaks. The peak on the right corresponds to $T_C$. Although the peak on the left occurs well below $T_x \approx 70\,\mathrm{K}$, a similar peak is observed in the AC susceptibility (see Fig. 2.7).

also appears in $LaCrGe_3$ [34] at the same temperature where the crossover is reported to occur at ambient pressure. There are also two peaks in the ESR spectra [41] (reproduced in Fig. 2.9) which can be found in other compounds with two FM states such as $La_{1-x}Te_xMnO_3$ [42]. Due to these similarities in features to other FM compounds with rich magnetic phase diagrams, along with our fresh look at features in magnetization, both of which can be explained by the existence of multiple ferromagnetic states, it is unlikely that the FM phase in $LaCrGe_3$ is a simple one.

### 2.3.1 Magnetic Domain Imaging

*Magnetic domain imaging reveals the change in magnetic domain structure on either side of the crossover.*

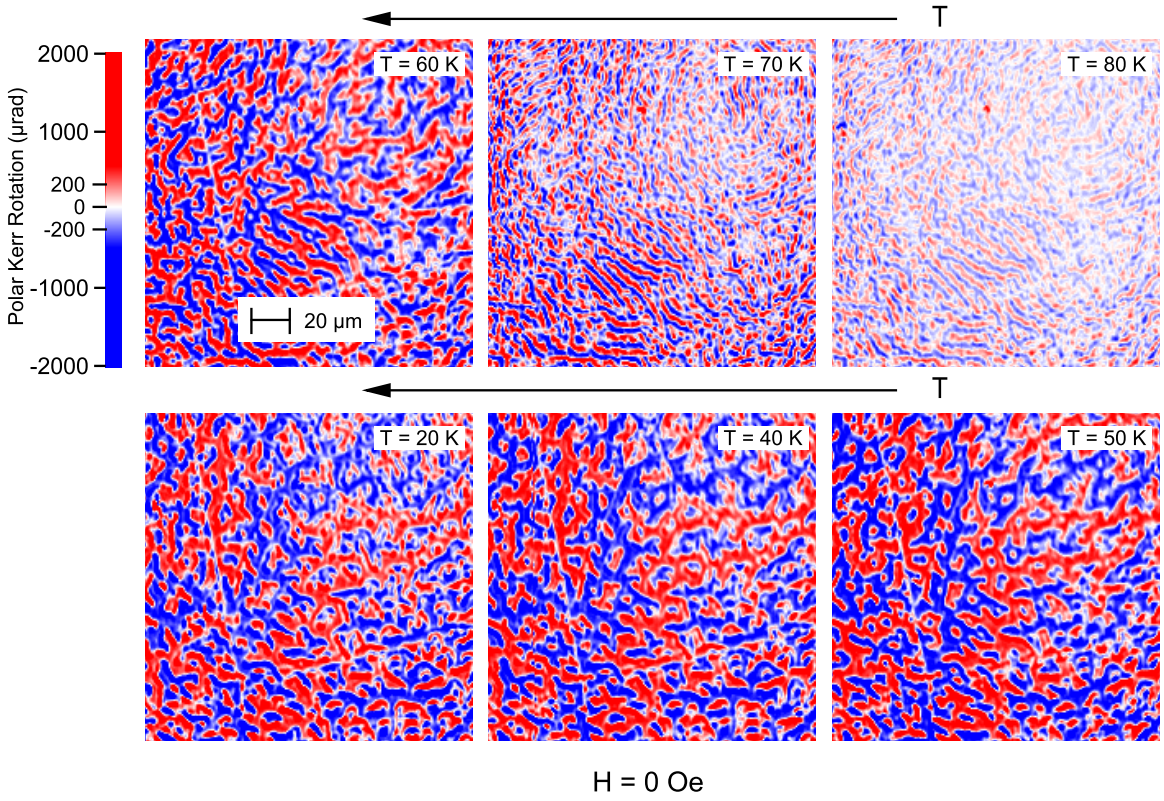


**Figure 2.10:** Polar Kerr rotation images of a polished *ab* face of $LaCrGe_3$ acquired while cooling in zero applied field (ZFC) from 80 K down to 20 K. The scan area shown is 170 $\mu$m x 170 $\mu$m. Positive values of Kerr rotation are shown in red and indicate a region of magnetization pointing out of the page, while negative values are shown in blue and depict a region of $M$ pointing into the page. The striking similarity of the domain structure between 80 K and 70 K is evidence for domain wall pinning in that range of temperature. In contrast, we observe a drastic change in the size and shape of the domains when the sample is cooled from 70 K to 60 K. The depinning of domain walls upon cooling is unusual, and may be due to the crossover between FM1 and FM2.

Polar magneto-optical Kerr effect (MOKE) images of the *ab* face of a $LaCrGe_3$ single crystal are acquired using a normal-incidence Sagnac interferometric scanning microscope [43, 44, 45]. The microscope has a spatial resolution of 0.85 $\mu$m and a sensitivity of 0.4 $\mu$rad. The sample is placed in an optically accessible flow cryostat, and its temperature can be varied from 470 K to 9.5 K. Longitudinal MOKE images of the *ac* face of a $LaCrGe_3$ single crystal are acquired with an oblique-incidence Sagnac interferometric scanning microscope [46] with a spatial resolution of 25 $\mu$m.

Since the $LaCrGe_3$ single crystal naturally grows along its $c$ axis, the *ab* face is obtained by polishing with fine 0.1 $\mu$m particle size $Al_2O_2$ polishing papers. Bulk magnetization was measured before and after polishing, and no magnetic impurities potentially picked up from polishing were observed.

MOKE images of magnetic domains on an *ac* face of an as-grown $LaCrGe_3$ single crystal were reported in an earlier study using an oblique-incidence Sagnac interferometric scanning microscope down to 77.4 K [46]. This earlier study was limited to liquid nitrogen temperatures and thus, domain structures on both sides of the FM1-FM2 crossover were not investigated. Here, we are able to take these measurements of the *ac* face down to 20 K. Still, because the easy magnetization axis (i.e., the *c* axis) lies in the *ac* plane, an oblique-incidence microscope had to be used in order to image magnetic domains using longitudinal and transverse Kerr rotation effects. In our present study, we image the *ab* face of the sample with the polar MOKE using a normal-incidence microscope which has a much better spatial resolution (0.85 $\mu$m compared to 25 $\mu$m) and two orders of magnitude better sensitivity compared to an oblique-incidence microscope.

We examine magnetic domains on the *ab* face down to 20 K. The images shown in the top row of Fig. 2.10 were taken at 80 K, 70 K, and 60 K while cooling down in zero applied field. Between 80 K and 70 K, the domain structure remains unchanged, and only the contrast increases at lower temperature in response to the increasing spontaneous magnetization, $M_s$. Between 70 K and 60 K, however, there is a dramatic change in domain structure. When comparing the domains at 60 K to those at 70 K and 80 K, both the shape and the size of the domains change substantially. In contrast, there is a relatively small change in the images between 60 K and 20 K.

The lack of change in domain structure between 80 K and 70 K indicates that the domain walls are pinned in this temperature region which roughly encompasses the FM1 state. The subsequent and sudden change in domain structure upon cooling further marks the depinning of domain walls between 70 K and 60 K. Furthermore, the change in domain size suggests that the energy cost of the domain wall has changed between these two temperatures. In fact, it coincides with the crossover from FM1 to FM2 reported to occur in this temperature region.

It is unusual for domain wall depinning to occur upon cooling an FM material. This is because the thermal energy available to overcome the energy barrier to wall movement is reduced at lower temperature. Similar MOKE imaging studies were performed on the magnetic domains in single crystals of the Weyl semimetal $Co_3Sn_2S_2$ [9]. Those studies support the notion that the domain walls become depinned over a narrow range of temperature while cooling down, therefore explaining an anomalous downturn in magnetization feature that had garnered considerable attention [47, 48, 49, 50, 51, 52, 53, 54, 55, 56, 57]. A different MOKE study reported by Lee *et al.* suggest that the underlying cause of the change in domain wall mobility in $Co_3Sn_2S_2$ is a domain wall transition from linear walls to Bloch walls, afforded by the unusually large dimensionless anisotropy factor, $K$ [56]. In the case of $LaCrGe_3$, $K$ is one order of magnitude smaller than that of $Co_3Sn_2S_2$ and therefore a domain wall transition is unlikely. A spin-polarized low energy electron microscopy (SPLEEM) [58] may confirm whether such a transition within the domain walls has occurred

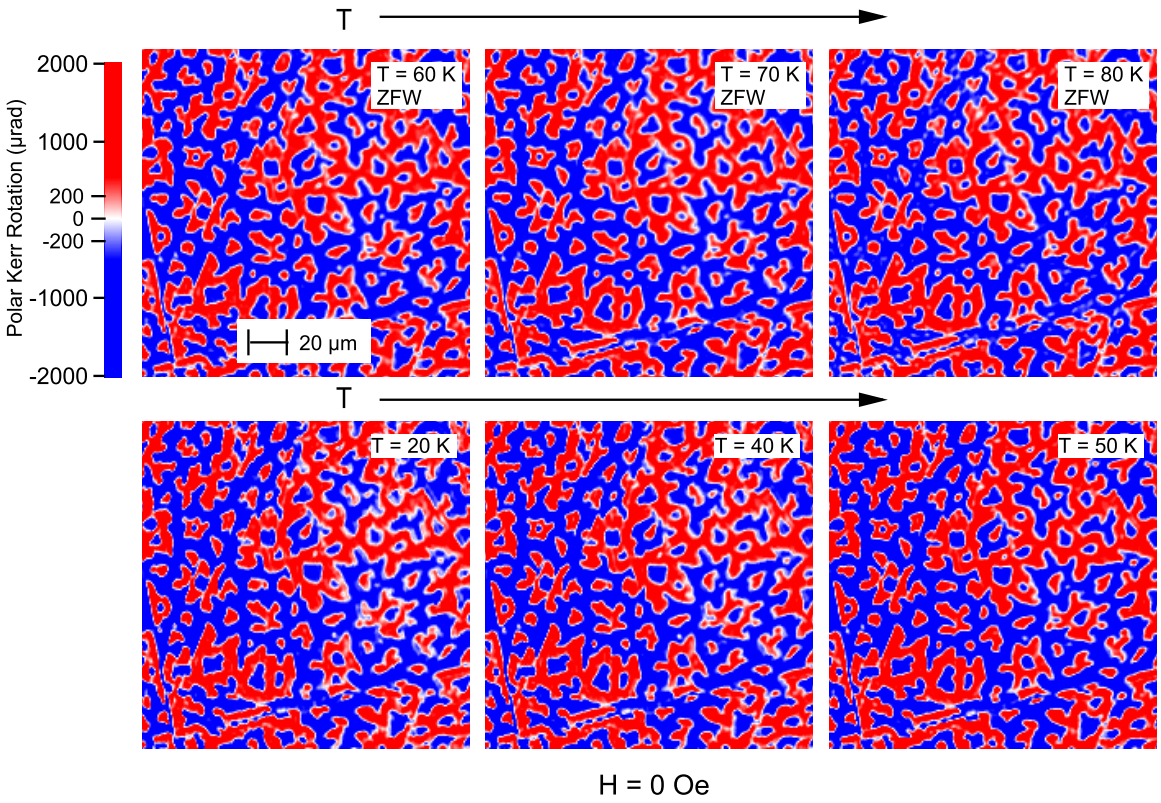


**Figure 2.11:** Polar Kerr rotation images of the same polished *ab* face in a similar area as Fig. 2.10. These images were taken while warming in zero field from 11.5 K after initially cooling in an applied field of $H = 3000$ Oe. Since the domain walls move freely at low temperatures, once the field is turned off at 11.5 K, there is no detectable remanent magnetization. Unlike the ZFC case shown in Fig. 2.10, there is no change in the domain structure when warming from FM2 to FM1 (ZFW, zero field warming). This lack of change, however, is consistent with a domain wall pinning region in FM1.

or otherwise. Even without the knowledge of the spin alignment inside domain walls, the distinct domain structures observed above and below 70 K are convincing evidence for the existence of two ferromagnetic states.

While the MOKE images shown in Fig. 2.10 clearly demonstrate a change in domain structure on either side of the FM1-FM2 crossover, in this section, we provide additional MOKE studies supporting our observation of domain pinning in FM1 and depinning in FM2.

Figure 2.11 shows images taken while warming in zero field (ZFW) from 11.5 K from a similar area as Fig. 2.10. While the sample was cooled to 11.5 K in $H_{\text{applied}} = 3000$ Oe, removing the field at low temperatures resulted in a net zero magnetization, which matches demagnetization theory and is consistent with the lack of domain wall pinning at low temperatures. Upon warming in zero field, the images taken throughout the temperature range below $T_C$ are indistinguishable to the eye. Unlike the ZFC images shown in Fig. 2.10, these ZFW images do not show a considerable change in the domain structure between FM1

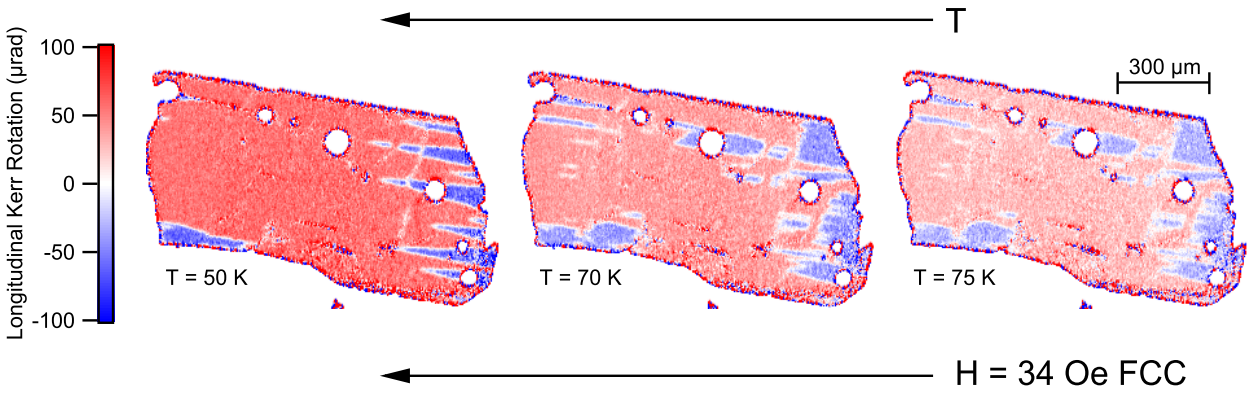


**Figure 2.12:** Longitudinal Kerr rotation images of an as-grown *ac* face of $LaCrGe_3$ acquired while field-cooling in $H = 34$ Oe applied to the left as indicated by the arrow. Positive values of Kerr rotation are shown in red and represent regions where $M$ is aligned with the applied field. Negative values are shown in blue and indicate regions where $M$ is anti-aligned with the field. We observe similar domain behavior to that of the *ab* plane discussed in Fig. 2.10. There is little change in the domain structure between 75 K and 70 K, which we attribute to domain pinning in the FM1 state. Below 60 K, there is a significant change in the domain structure, as shown by the image taken at 50 K, which we attribute to the depinning of domain walls in the FM2 state. Images at additional temperatures are shown in Fig. 2.13.

and FM2. This result is consistent with domain wall pinning at high temperatures and is not in conflict with the existence of the FM1 state.

We also revisited the same *ac* plane studied in [46], this time using liquid helium to obtain images below 77.4 K. These images, shown in Fig. 2.12, were taken while cooling in an applied field of $H_{\text{applied}} = 34$ Oe in the direction indicated by the arrow in the figure. The images taken at 75 K and 70 K are representative of those in the FM1 state showing little change in domain structure. Below 60 K, the domain structure changes significantly as shown by the 50 K image. Additional MOKE images of the *ac* plane are shown in Fig. 2.13.

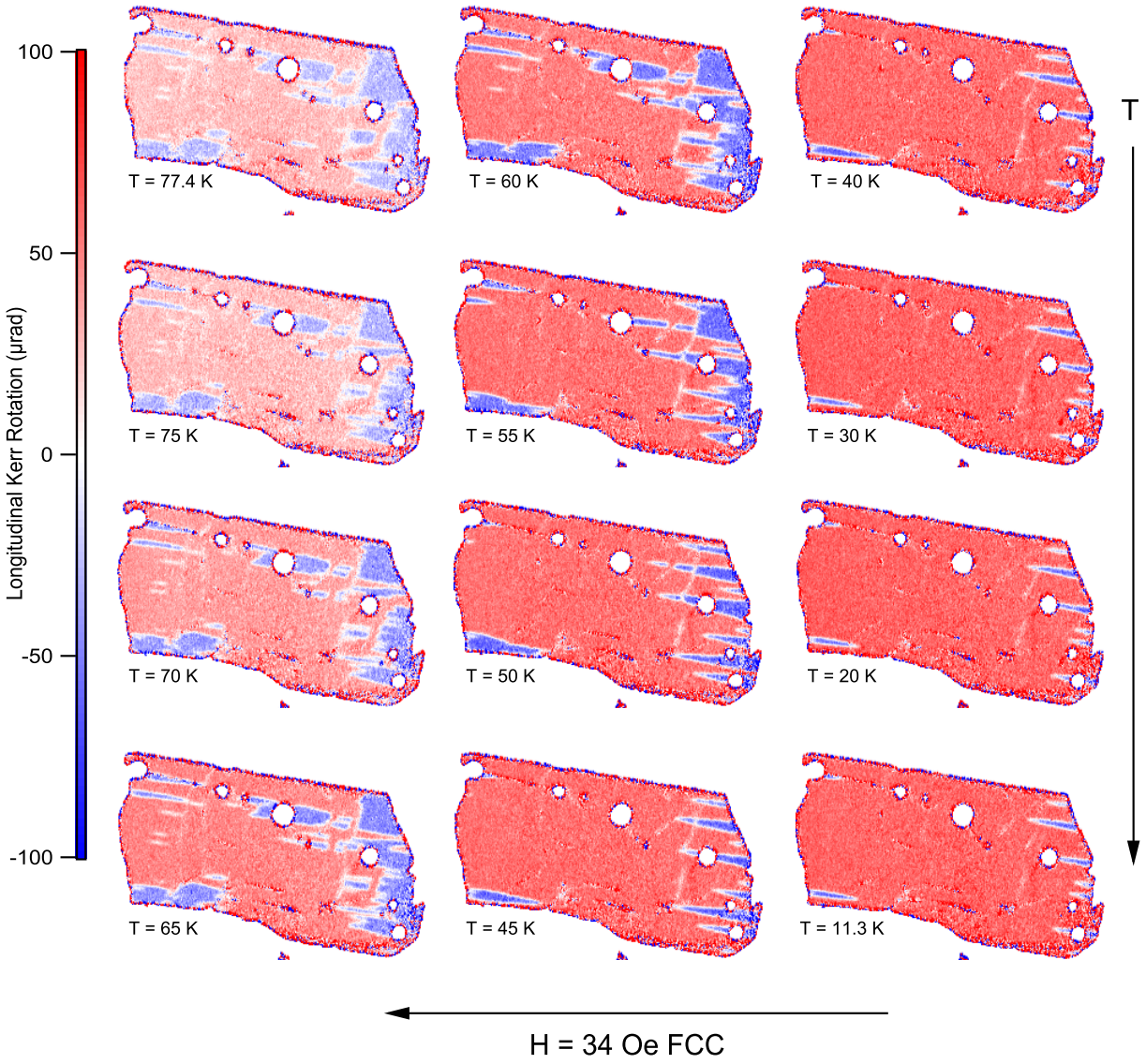


**Figure 2.13:** Additional MOKE images of the *ac* plane. The field is applied in the direction shown and the red regions correspond to field-aligned magnetization.

### 2.3.2 Bulk Magnetization Experimental Details

We use a Quantum Design Magnetic Property Measurement System (MPMS) to measure the magnetization of the sample with the applied magnetic field oriented parallel to the $c$ axis. Magnetization as a function of temperature ($M(T)$) was measured in various constant applied fields and by the following methods: field-cooled-cooling (FCC), field-cooled-warming (FCW), and zero-field-cooling (ZFC). For FCC, the field is applied at $T = 300\,\mathrm{K}$ and the magnetization of the sample is measured while temperature is lowered to base temperature, $T = 2\,\mathrm{K}$. With the field still on, the magnetization is measured while increasing temperature up to $T = 300\,\mathrm{K}$ for the FCW measurement. For ZFC, the sample is cooled from above $T_\mathrm{C}$ to base temperature in zero applied field. Then the field is applied and the magnetization is measured while the sample is warmed.

Isothermal magnetization as a function of applied field ($M(H)$) was measured at a selection of temperatures below $T_\mathrm{C}$. Hysteresis loops were measured starting in a zero-field-cooled state to observe the virgin magnetization curve before sweeping field up to $\pm 7\,\mathrm{T}$. Before each measurement, the sample temperature was raised above $T_\mathrm{C}$ to $110\,\mathrm{K}$ in order to clear the magnetic history of the sample before the subsequent measurement. Furthermore, the field was systematically oscillated to zero to minimize the remanent field in the magnet and the sample chamber. Our calibration with a paramagnetic standard shows that the remanent field of the magnet after this procedure is roughly $8\,\mathrm{Oe}$. These steps are important because we are specifically interested in the coercive field and the virgin curve which are relatively low-field phenomena.

### 2.3.3 Reappearing Hysteresis Loops and Domain Pinning Virgin Curves

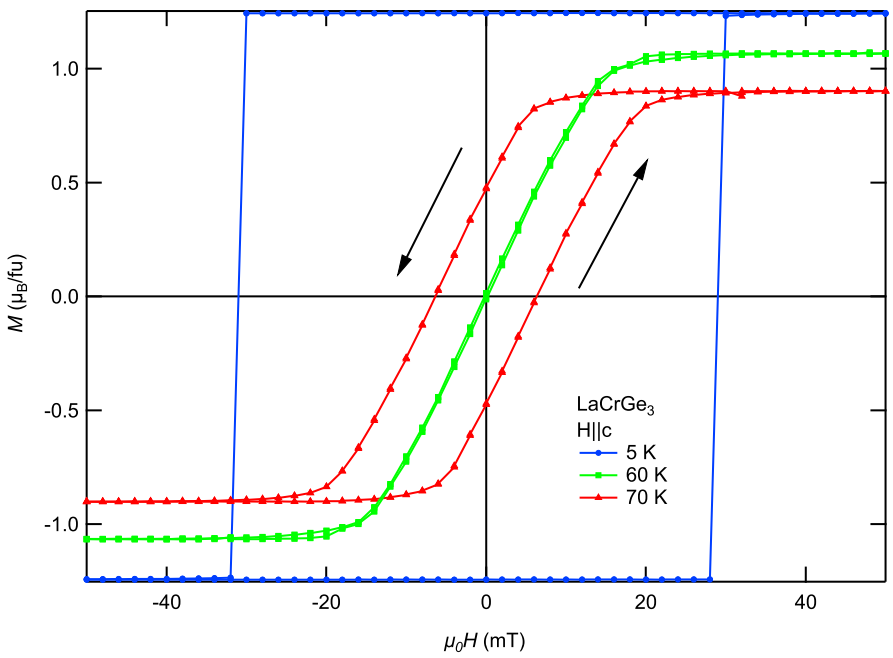


**Figure 2.14:** Magnetic hysteresis loops measured at different temperatures below the Curie temperature ($T_C = 85\,\mathrm{K}$). Starting at 2 K, the hysteresis loops are rectangular and shrink in size as $T$ increases until they close completely near 40 K. Surprisingly, the hysteresis loop opens up again before reaching $T_C$.

By measuring hysteresis loops at different temperatures, we find changes in loop shape, coercivity, and virgin magnetization curve that are consistent with domain wall pinning in the high temperature FM1 state, followed by depinning in the low temperature FM2 state. At low temperatures, the loops are rectangular, characterized by a remanent magnetization that is nearly equal to $M_s$ and a sudden reversal of the sample magnetization ($M$) at the coercive field ($H_c$). Similar rectangular loops were recently reported [37]. As expected, the hysteresis loops shrink in width with increasing temperature until they fully close. Surprisingly, $LaCrGe_3$ is a rare case in which further increasing the temperature causes the hysteresis loop to reappear, albeit with a much more gradual change in $M$ compared to the low $T$ loops. An example of these three kinds of hysteresis loops can be found in Fig. 2.14.

By plotting $H_c$ as a function of temperature, as shown in Fig. 2.15(a), we can see the low $T$ ($T < 40\,\mathrm{K}$ for this particular sample) and high $T$ ($62.5\,\mathrm{K} < T < T_C$ for all samples measured) regions of coercivity, separated by a region where the coercivity is minimal ($40\,\mathrm{K} < T < 60\,\mathrm{K}$). Our results are consistent with a recent report [37]. In the low $T$ region, the magnitude of $H_c$, as well as the temperature at which $H_c$ disappears, is sample-dependent, which leads us to believe it is related to sample quality and defects (as discussed further in Section 2.4.2). The coercivity at high $T$, however, is evident in all samples measured,

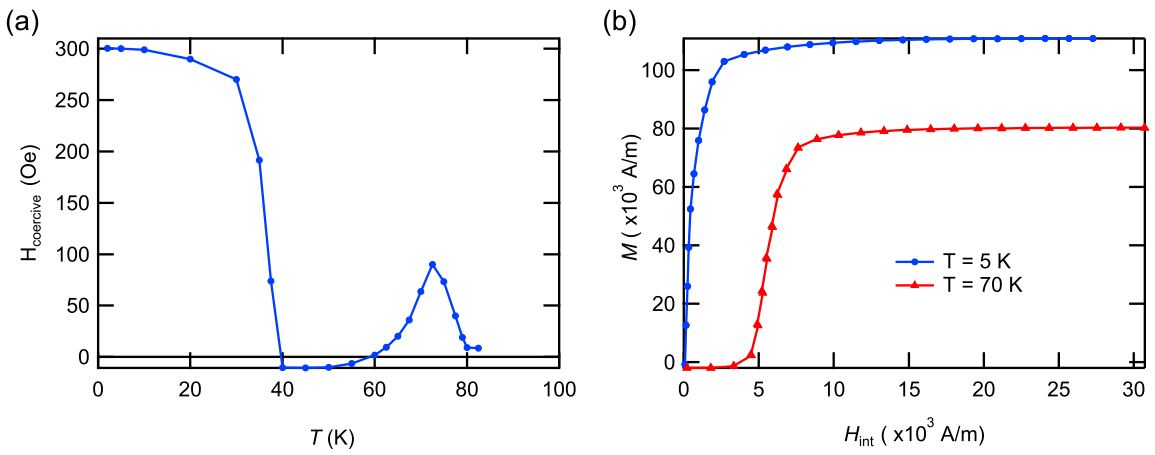


**Figure 2.15:** (a) The coercive field, $H_c$, as a function of temperature shows the low $T$ and high $T$ regions of coercivity are separated by a region where $H_c \approx 0$. The increase of coercive field with temperature in the 67 K to 72.5 K region is unusual and may be due to a crossover between FM1 and FM2. (b) The virgin magnetization curves reveal an atypical change in domain wall mobility. In the low temperature FM2 state, the virgin magnetization curve follows demagnetization theory, which means the domain walls are not pinned. In the higher temperature FM1 state, the hesitance for the virgin curve to increase with field suggests domain wall pinning.

and occurs at the same temperatures with similar magnitudes, which suggests it is related to an intrinsic property of the compound. This repeatability between samples is consistent with the scenario that the high $T$ coercivity originates from the FM1-FM2 crossover.

A careful analysis of the virgin magnetization curves and their relationship to the shape of the hysteresis loops confirms our domain pinning hypothesis. Examples of the low $T$ and high $T$ curves are shown as the blue dots and red triangles, respectively, in Fig. 2.15(b). At low $T$, the virgin curve increases linearly with a slope of $1/N_c$, where $N_c$ is the demagnetization constant along the $c$ axis (see Section 2.4.1 for details), and $M$ saturates to $M_s$ at an applied field much lower than $H_c$. This behavior can only occur if the domain walls are able to move freely. On the other hand, in the high $T$ region of coercivity, the virgin curve barely increases in response to $H_{\text{applied}}$ until $H_{\text{applied}} = H_c$. This behavior suggests that domain wall pinning is present in this range of temperatures [59, 60].

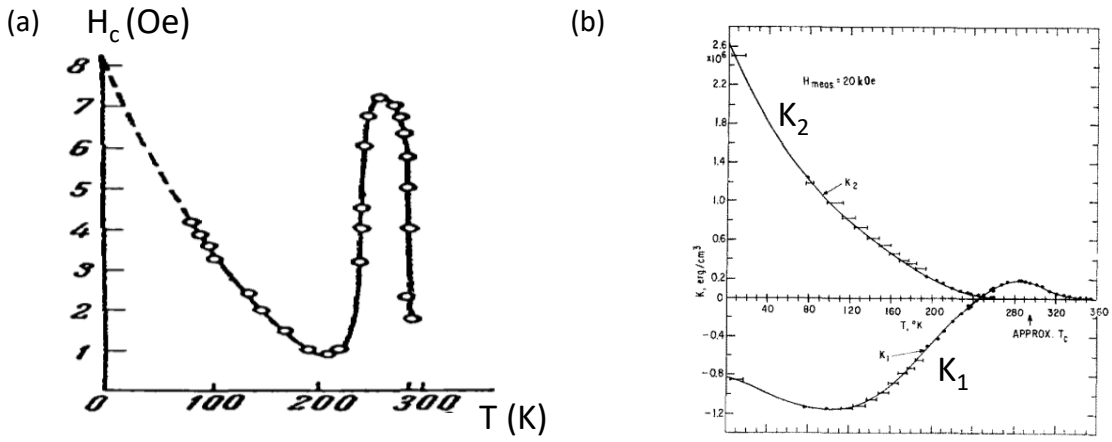


**Figure 2.16:** (a) The temperature dependence of the coercive field ($H_c$) in gadolinium (Fig. 8 in Ref. [61]) shows a similar shape to that of $LaCrGe_3$. It has a local maximum just below its $T_C = 290\,K$, followed by a local minimum near 200 K. (b) The unusual temperature dependence of the coercive field can be explained by an unusual temperature dependence of the anisotropy constants, $K_1$ and $K_2$ (Fig. 1 in Ref. [62]). In Gd, $K_1$ and $K_2$ are of comparable magnitude, and $K_1$ changes sign. On the other hand, $LaCrGe_3$ exhibits a more standard anisotropy as shown in Fig. 2.29(a), so anisotropy is not responsible for its coercivity.

$LaCrGe_3$ is not the first sample to display an $H_c$ that re-emerges with increasing temperature. For example, in Gd, the coercivity is also split between two regions by a minimum $H_c$ below its $T_C = 289\,K$ [61, 63], as shown in Fig. 2.16(a). This similarly shaped coercivity plot in Gd, however, is due to a change of sign of the anisotropy constant $K_1$ and comparatively large values of $K_2$ [64, 62], as shown in Fig. 2.16(b). In contrast, no anomaly is observed in the temperature dependence of the anisotropy constants in $LaCrGe_3$ (see Fig. 2.29 in Section 2.4.3).

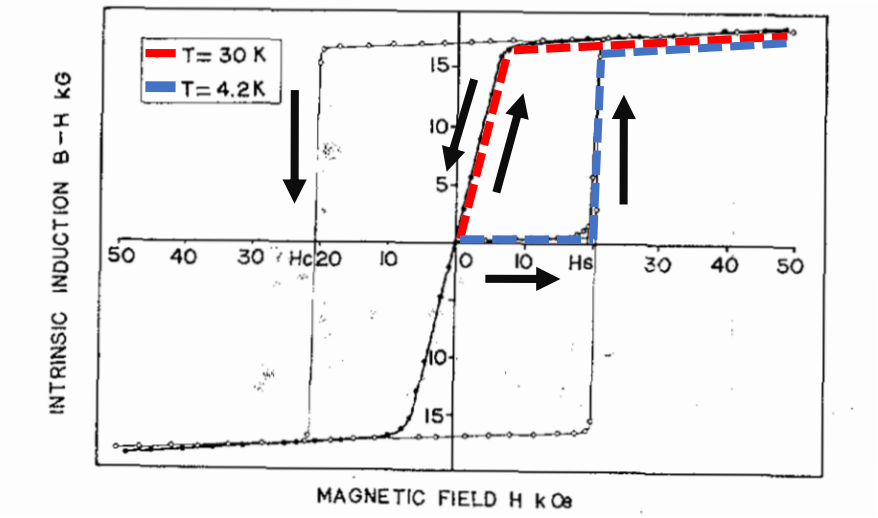


**Figure 2.17:** $Dy_3Al_2$ ($T_C = 94\,K$ [65]) shows a more typical temperature dependence of a ferromagnetic hysteresis loop (Fig. 1 in Ref. [66]). At 30 K, the virgin magnetization curve increases linearly with applied field (presumably following demagnetization theory). At 4.2 K, the virgin curve does not increase until nearly 2 T is applied. This is evidence for strong domain pinning at low temperatures (on its own, this curve might be interpreted as a spin-flip transition (AFM-FM), however, there is no evidence for an AFM phase in $Dy_3Al_2$ [65]). It is more common for domain walls to be pinned at low temperatures [60]. We highlight the high temperature and low temperature virgin magnetization curves in red and blue, respectively, to match the colors used in Fig. 2.15(b).

Typically, anisotropy increases as temperature is lowered, causing domain walls to narrow and pin [60, 67, 68]. The compound $Dy_3Al_2$ is one such example of this typical change in domain wall mobility due to anisotropy. As seen by a change in shape of the virgin curve (Fig. 2.17), the domain walls in $Dy_3Al_2$ move freely at high $T$ while domain wall pinning occurs at low $T$ [60, 69, 70]. In contrast, the opposite is true in $LaCrGe_3$, which means a mechanism other than anisotropy is responsible for the domain wall behavior we observe.

We believe it is no coincidence that the local maximum of coercivity in the domain pinning region occurs at 72.5 K, which is near the reported temperature of the crossover between FM1 and FM2. We will show that a change in the ferromagnetic state could be responsible for the domain wall pinning behavior in $LaCrGe_3$ in Section 2.3.6.

### 2.3.4 Deconstructing the $M(T)$ Anomaly

*In this section, we demonstrate the relevance of the atypical domain wall behavior by showing how it can explain the previously observed, but not well understood, $M(T)$ curves.*

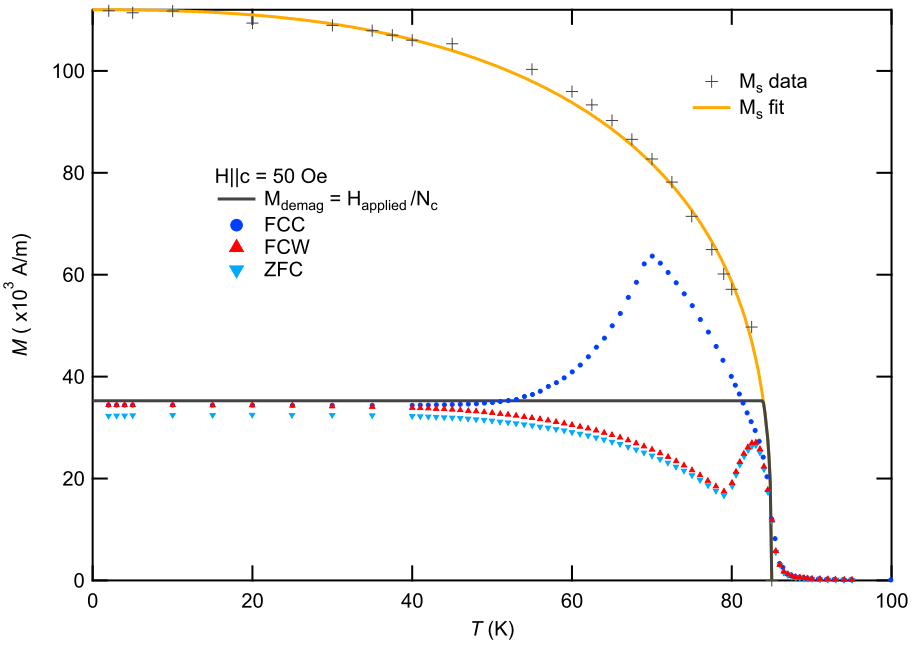


**Figure 2.18:** $LaCrGe_3$ has non-standard field-cooled-cooling (FCC, shown as blue dots) and field-cooled-warming (FCW, shown as red triangle) magnetization curves. These curves deviate from $M$ determined by demagnetization theory (black curve), and $M_s$, the spontaneous magnetization (data shown as black crosses, fit by Kuz'min theory [71] in yellow). The zero-field-cooled (ZFC, light blue triangles) data is remarkably similar to the FCW data.

The anomalous magnetization curve measured at low fields in $LaCrGe_3$ has previously been observed in studies of single crystals [11, 37] as well as polycrystals [36]. While the anomalous features in the curve were correctly attributed to changes in the magnetic domains and demagnetization effects [11], in this section we will explain exactly how these features are caused by non-traditional domain behavior resulting from the crossover from FM1 to FM2.

To understand the unusual magnetization curve in $LaCrGe_3$, we first need to understand what we expect the magnetization curves to look like without domain wall pinning and depinning. In the absence of ferromagnetic domain formation, the magnetization should follow the spontaneous magnetization ($M_s$) represented by the yellow curve in Fig. 2.18(a). $M_s$ can indeed be measured if a sufficiently high field is applied ($H > NM_s$, where $N$ is the demagnetization factor which is determined by the shape of the particular sample measured, see Section 2.4.1) to overcome domain formation, or equivalently, demagnetization effects. At lower applied fields, however, domains form and demagnetization theory can be used to determine the

expected magnetization. When $H_{\text{applied}} < NM_s$, the expected magnetization is $M_{\text{demag}} = \frac{H_{\text{applied}}}{N}$. $M_{\text{demag}}$ is temperature independent and is depicted by the black line in Fig. 2.18(a) for $H = 50\,\text{Oe}$.

It is evident that the low field (below $NM_s$) FCC, FCW and ZFC data, shown respectively as dark blue dots, red triangles, and light blue triangles in Fig. 2.18(a), deviate significantly from $M_s$ and $M_{\text{demag}}$ in the temperature region between 55 K and 82 K. In the FCC case, $M$ rises above $M_{\text{demag}}$ and reaches a distinct peak before decreasing and settling to a lower, temperature independent value matching $M_{\text{demag}}$. In ferromagnets, a decrease in the FCC magnetization along the easy axis is not trivial to explain. A spin-reorientation or an antiferromagnetic transition come to mind as possibilities, but neutron diffraction measurements have not found evidence for either [72, 7].

The FCW curve is also anomalous as it follows $M_{\text{demag}}$ at temperatures below 40 K, but then decreases below $M_{\text{demag}}$ before suddenly increasing to rejoin the FCC curve just below $T_{\text{C}}$. It is unusual to have discrepancies between FCW and FCC magnetizations. Hysteresis between warming and cooling is unexpected, and is often seen when there is a first order phase transition between two magnetic states. In this case, however, there is no evidence for a phase transition between two different magnetic states in other probes [18, 19, 7].

The ZFC curve is remarkably similar to the FCW curve, differing only by a small decrease in magnitude. ZFC curves often have a much smaller low $T$ magnetization than the FCC and FCW curves, since ferromagnetic domains often have some degree of pinning at low temperatures, and the field ($H = 50\,\text{Oe}$ in this case) is only applied after cooling the sample to $T = 2\,\text{K}$ allowing domains to form. In $LaCrGe_3$, however, the domain walls at low temperatures move freely, and therefore the ZFC curve nearly matches $M_{\text{demag}}$ at low temperatures.

### 2.3.5 Modeling the $M(T)$ Curve

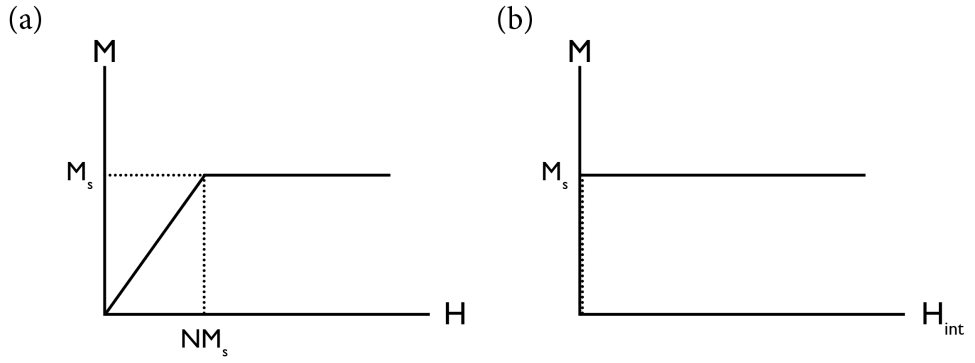


**Figure 2.19:** (a) When measuring the $M(H)$ from a zero-field-cooled state along the easy axis of a ferromagnet of finite size, $M$ initially increases linearly with field (as long as the domains are not pinned). This linear increase is due to the formation of ferromagnetic domains which can be mathematically described by demagnetization theory. According to this theory, $M$ in the linearly increasing region is $M = \frac{1}{N}H_{\text{applied}}$, and the internal field $H_{\text{int}} = H_{\text{applied}} - NM$ is equal to zero. The demagnetization factor, $N$, is a factor determined by the geometry of the sample. For example, a sphere has $N = 1/3$, $N$ along an infinitely long rod is 0, and $N$ for rectangular prism of comparable dimensions is given by a formula by Aharoni [73]. (b) By plotting $M(H_{\text{int}})$, we see that the magnetization saturates as soon as $H_{\text{int}}$ is nonzero, as expected for a ferromagnet below $T_{\text{C}}$.

In this section, I will develop the simple model that shows how the strange FCC and FCW magnetization curves are the result of the pinning and depinning of domain walls discussed in the previous sections. In the absence of domain pinning, there are two magnetizations that we would expect to measure: the spontaneous magnetization ($M_s$) or the magnetization according to demagnetization theory ($M_{\text{demag}}$). The measured FCC magnetization sits between these two values, and here I will show how this is possible.

$M_s(T)$ is theoretically the maximum magnetization one could measure while measuring $M(T)$. Experimentally, $M_s$ is a fingerprint for a ferromagnetic compound. $M_s$ is found from $M(H)$ measurements along the easy-axis by taking the y-intercept of the line fit to the saturated region at high fields. This procedure can be performed at various temperatures up to $T_{\text{C}}$ (where $M_s = 0$) to construct $M_s(T)$. As seen in Fig. 2.18(a), we do not observe any unusual behavior in $M_s(T)$ (black '+' symbols), and it fits well according to the theory by Kuz'min [71].

Figure 2.19(a) is a schematic diagram of an $M(H)$ curve for a ferromagnet with an easy magnetization direction and no domain wall pinning, measured from a zero-field-cooled state (where $M \approx 0$ when $H = 0$). Notice that the initial magnetization increases linearly with applied field; it does not saturate to $M_s$ immediately. Demagnetization theory can mathematically describe why the $M$ is not immediately saturated at zero applied field. The reasoning is based on the demagnetization field: $H_d$. In any finite sample with a magnetization $M$, there is a demagnetization field $H_d = -NM$, where $N$ is a demagnetization factor determined by the sample dimensions (discussed further in Section 2.4.1). As a result, the H-field inside the

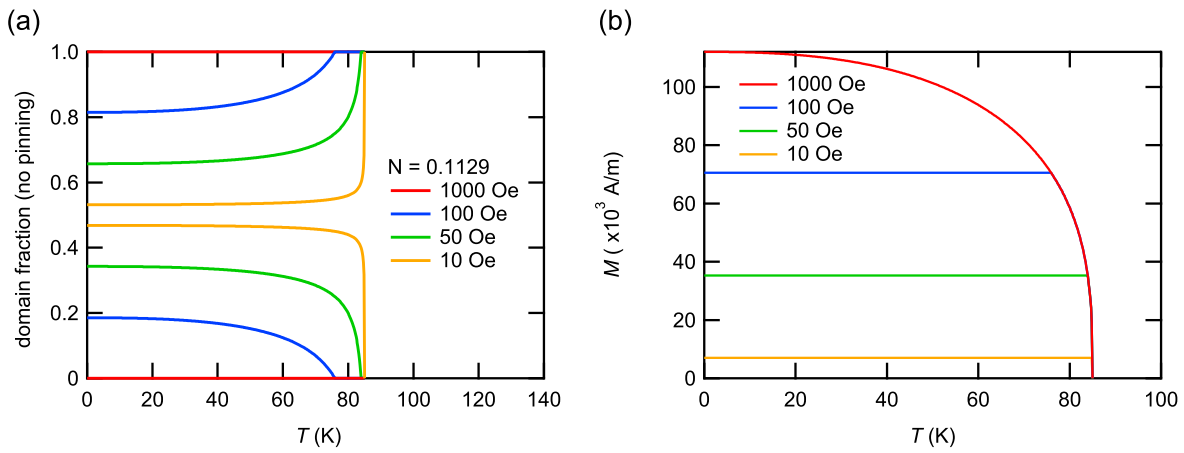


**Figure 2.20:** Theoretical plots of the (a) domain fraction and (b) the magnetization as a function of temperature at various applied fields with no pinning. (a) The temperature dependence of the domain fraction as dictated by demagnetization theory, *i.e.*, $M = H_{\text{applied}}/N$ for different applied fields. The lines above 0.5 show $n_{\text{up}}$ while the lines below 0.5 represent $n_{\text{down}}$. (b) The magnetization that results from the domain fractions as determined by Eq. 2.6. The unusual features of the experimental $M(T)$ curve for $LaCrGe_3$ are not reproduced. If we instead hold the domain fraction, $n_{\text{up}}$, constant for a range of temperature, we recover the unusual features observed in the experimental $M(T)$ curve for both FCC and FCW measuring methods (see Fig. 2.18 and Fig. 2.22).

sample, $H_{\text{int}} = H_{\text{applied}} + H_d$, is less than the applied field. In fact, as shown by the diagram (Fig. 2.19(a)) the initial slope of the magnetization is $1/N$.[6] Therefore in the demagnetization limited region,

$$M_{\text{demag}} = \frac{1}{N} H_{\text{applied}}, \tag{2.1}$$

and $H_{\text{int}} = 0$ in this linearly increasing region of $M$. It makes sense that we do not immediately measure $M_s$, as there is no field to align the single rotating moment along our axis of measurement. Also notice that unlike $M_s$, which is a property of the particular compound being measured, $M_{\text{demag}} = \frac{1}{N} H_{\text{applied}}$ only depends on the shape of the sample being measured via $N$ and the applied field (controlled by the magnetometer), and it is temperature independent. As a testament to the validity of demagnetization theory, $M_{\text{demag}}$ is plotted as the black line in Fig. 2.18(a), which faithfully reproduces the magnetization below 40 K at 50 Oe. $H_d$ takes a maximum value when the sample magnetization has saturated, so we can define the maximum demagnetization field $H_{d,max} = NM_s$. It is only when $H_{\text{applied}} > |H_{d,max}|$ (*i.e.*, when $H_{\text{int}} > 0$) that $M_s$ is measured. This is shown schematically in Fig. 2.19(b) and with experimental data in Fig. 2.15(b).

An alternative and *equivalent* approach to using demagnetization theory is to consider the formation of ferromagnetic domains and the motion of the domain walls between them. From the domain point of view, the linearly increasing region of $M(H)$ is due to the applied field moving ferromagnetic domains walls and adjusting the fraction of aligned and anti-aligned domains in the sample. In a material with strong uniaxial

[6] Slope is rise over run. If $M$ starts at the origin and rises to $M_s$ at field $NM_s$, then the slope is simply $1/N$.

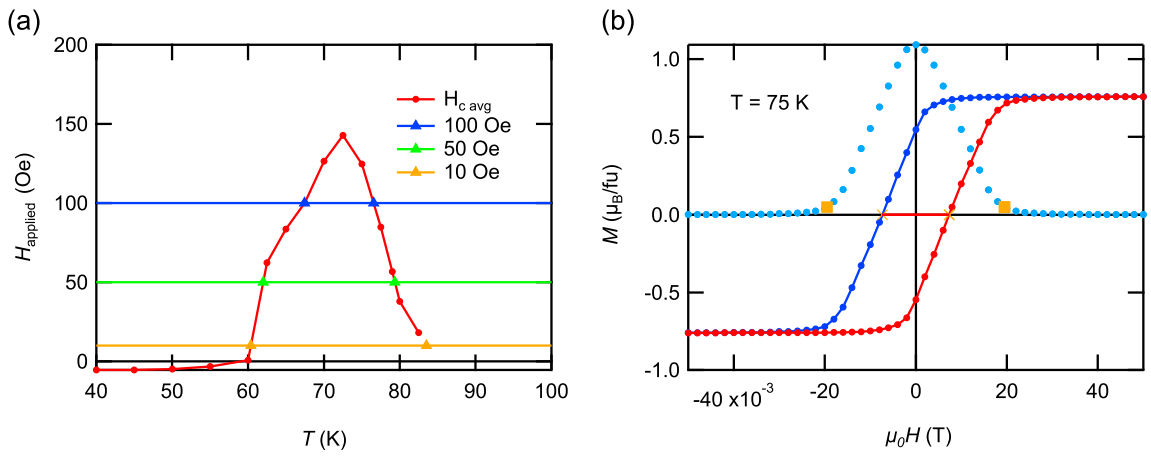


**Figure 2.21:** (a) By finding the intersection between $H_{c\ \mathrm{avg}}$ and a particular applied field, we find the temperatures at which the domains pin and de-pin for each field. $H_{c\ \mathrm{avg}} = (H_c + H_{\mathrm{shoulder}})/2$ takes into account the wide range of field in which the domain walls move in the high $T$ hysteresis loops. $H_c$ is the coercive field, the field required to make $M = 0$ after it was previously saturated to $M = M_s$. We define $H_{\mathrm{shoulder}}$, as the field at which the magnetization just begins to change from its fully polarized value. (b) The red line on the $x$ axis is the hysteresis width, and the gold crosses at its endpoints signify $H_c$. The light blue dots is the subtraction $M(-H) - M(+H)$, and the gold squares show $H_{\mathrm{shoulder}}$.

anisotropy, such as $LaCrGe_3$, we only need to take into account the fraction of domains aligned with the field, $n_{\mathrm{up}}$, and those anti-aligned with the field, $n_{\mathrm{down}}$. A schematic of such a domain configuration is depicted in Fig. 2.25(b-d). Since the maximum magnetization of the sample is $M_s$, the relationship between the measured magnetization and the number of up and down domains is

$$M = n_{\mathrm{up}} M_s - n_{\mathrm{down}} M_s \tag{2.2}$$

Since $n_{\mathrm{up}} + n_{\mathrm{down}} = 1$ we can simplify the preceding equation to

$$M = (2n_{\mathrm{up}} - 1)M_s \tag{2.3}$$

Ferromagnetic domains and demagnetization theory are equivalent ways to describe why $M_s$ is not experimentally measured in low applied fields. Since they are equivalent pictures for describing the magnetization when $H_{\mathrm{applied}} < |H_{d,max}|$, we can equate Eq. 2.1 and Eq. 2.3:[7]

$$(2n_{\mathrm{up}} - 1)M_s = \frac{1}{N} H_{applied} \tag{2.4}$$

[7]This breakthrough of equating the domain and demagnetization pictures occurred while having lunch with Valentin at the picnic tables outside of the math building. Why not outside the physics building? Was it to avoid eavesdropping passersby potentially scooping our epiphany? The truth is simple. There are no picnic tables outside of the physics building. Imagine if there were.

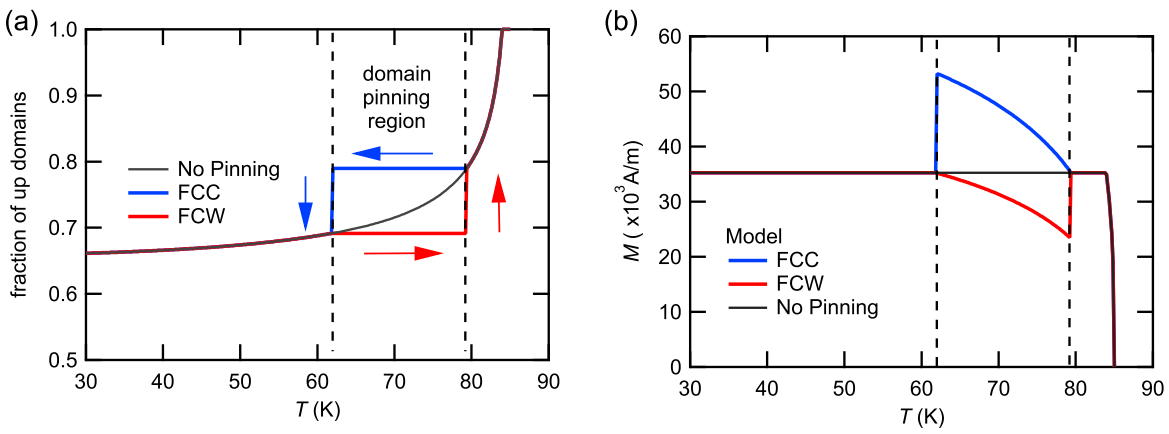


**Figure 2.22:** (a) Without domain wall pinning, the domain fraction traces the black curve to satisfy demagnetization. The pinning region causes the domain fraction to trace different paths while cooling (blue curve) and warming (red curve). (b) By plotting the magnetization that results from these two different paths, we find that the previously unexplained features in both the FCC and FCW curves are faithfully reproduced. A direct comparison of the model and experimental data at $H = 50\,\mathrm{Oe}$ and at other applied fields is shown in Fig. 2.23(b).

This expression matches that found in the textbook by Tremolet [60]. This equation can be rearranged to solve for the temperature dependence of $n_{\mathrm{up}}$.

$$n_{\mathrm{up}} = \frac{1}{2M_s(T)} \min\left\{ M_{\mathrm{demag}} = \frac{1}{N} H_{\mathrm{applied}}, M_s \right\} + \frac{1}{2} \tag{2.5}$$

where the minimum function is used to correctly model $M$ just below $T_{\mathrm{C}}$ and avoid the unphysical result where the measured magnetization is greater than $M_s$. Equation 2.5 yields the black line in Fig. 2.22(a) that shows the fraction of field-aligned magnetic domains as a function of temperature. Interestingly, the fraction of field-aligned domains decreases as temperature decreases, which happens in order to maintain the temperature independent $M_{\mathrm{demag}}$ while $M_s$ increases as $T$ lowers. This result is counterintuitive when we think of the typical magnetization curve which does not consider demagnetization effects and therefore does not exhibit the decrease in the fraction of field-aligned domains.

Now we can finally talk about domain pinning and depinning. From the virgin curves of the hysteresis loops, we determined that the domains are pinned at high temperatures ($60\,\mathrm{K} < T < T_{\mathrm{C}}$) and are free to move at low temperatures ($T < 60\,\mathrm{K}$). The particular temperature at which the domain walls pin and de-pin is dependent on the applied field, the criteria for which is described in Fig. 2.21(a). When the domains are pinned, the domain fraction is held constant. When the domains depin, the domain fraction returns to the value determined by demagnetization theory. The domain fraction is held constant when the domains pin, while depinning returns the fraction to the demagnetization value. As a result of the domain pinning, the domain fraction takes different paths when cooling and warming, seen as the blue and red lines in

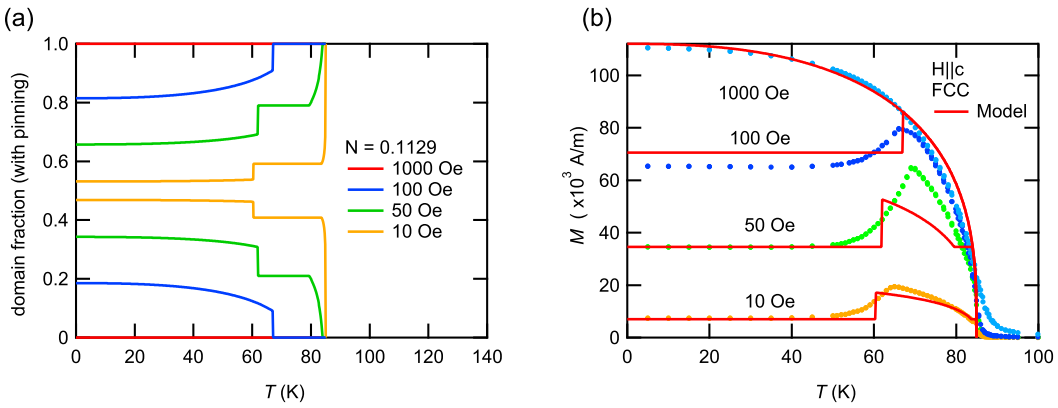


**Figure 2.23:** (a) The temperature dependence of the domain fraction during field-cooling as dictated by our domain pinning criteria. When the domains are pinned, the domain fraction is held constant. $n_{\rm up}$ is described by the curves above a 0.5 domain fraction, while $n_{\rm down}$ is described by the curves below 0.5. (b) The magnetization derived from the domain fraction curves in (b) using Eq. 2.6, are in good agreement with the data, particularly at lower applied fields.

Fig. 2.22(a), respectively. We can calculate the magnetization that results from these model FCC and FCW domain fraction paths with the following equation

$$M = (2n_{\rm up} - 1)M_s(T) \tag{2.6}$$

The resulting magnetization curves are presented in Fig. 2.22(b). During field-cooled-cooling, there is no pinning immediately below $T_{\rm C}$, so $M$ takes the expected shape according to demagnetization theory. When the temperature is lowered into the pinning region, the domain fraction is held constant, so $M$ increases proportionally to $M_s$. The downturn near 60 K is due to the domain walls depinning and the magnetization returning to $M_{\rm demag}$. In the field-cooled-warming case, the deviation of $M$ from $M_{\rm demag}$ begins around 60 K, where $M$ begins to decease with increasing $T$. This decrease is due to the domain fraction being held constant by pinning, so $M$ follows the shape of $M_s$. $M$ continues to decrease until around 80 K, when the domain walls de-pin, and consequently $M$ rapidly increases to rejoin the FCC curve. These model magnetization curves faithfully reproduce the characteristic features of the anomaly seen in the data (Fig. 2.18). As expected, these features are smoothed out in the experimental data, where, unlike in our model, the pinning and depinning are partial and progressive. We find the match between the two, however, to be compelling evidence that the abnormal $M(T)$ curve is due to domain wall pinning and depinning.

In conclusion, we recognize that a textbook equation relating demagnetization effects and magnetic domains can be used to model low-field ferromagnetic magnetization curves. With Eq. 2.5 in an experimentalist's toolbox, it is possible to check whether anomalous features in $M(T)$ are due to demagnetization or the unusual behavior of magnetic domains before more exotic possibilities are suggested or explored.

### 2.3.6 Domain Wall Theory and Multiple Ferromagnetic States

At this point, I have presented the measurements I performed (with the exception of the MOKE images which were taken by Professor Zhu), the data I analyzed and the 'simulation' I wrote as evidence that $LaCrGe_3$ has a peculiar temperature dependence of domain pinning. Specifically, that the ferromagnetic domains in the system are pinned at high temperatures, but depin and are free to move at low temperatures. I have also correlated this change in domain behavior to the crossover between FM1 and FM2 by way of their occurrence in the same range of temperature. In this section, I attempt to use theory to escalate the correlation to causation to show that the FM1/FM2 crossover actually causes the change in domain behavior. As a result, we see that carefully considering domain effects may be a way to probe crossovers between ferromagnetic states which can otherwise be difficult to observe.

A wise man once said, "six months in the lab with save you an hour in the library,"[8] and this sentiment very much applies to the following analysis. We begin with the theory that describes how readily domain walls move in response to an externally applied magnetic field. Theory shows that, in the absence of sample defects, an applied magnetic field must overcome an energy barrier $\Delta\gamma$ to move a domain wall. It has been shown that $\Delta\gamma \propto e^{\frac{-\delta}{a}}$ [60, 67, 68], where $\delta$ is the width of the domain wall and $a$ is the lattice spacing between local magnetic moments.

In $LaCrGe_3$, the nearest neighbor Cr atoms lie along the $c$ axis and although XRD, neutron diffraction, and thermal expansion measurements [7] show that the $c$ lattice parameter unusually increases during cooling, the change is small and would increase pinning at low temperatures. As a result, whether domain walls are easy or difficult to move depends on how wide or how narrow they are, respectively. In a mean field, local moment model, the width of the domain wall $\delta$, is proportional to the spin of the magnetic ion $S$, the distance between magnetic moments $a$, the exchange constant $J_{ex}$ and the anisotropy constant $K$, as follows [75, 60, 76, 67]

$$\delta = \pi S \sqrt{\frac{2J_{ex}}{aK}} \tag{2.7}$$

The temperature dependence of $K$ that we measure agrees with theory (Section 2.4.3) and usually causes

[8] **An Homage to John Kirtley and the Kirtley Rules:** There was a bulletin board in the basement lab I worked in as an undergraduate. While that bulletin board had all sorts of notes, sketches, and musings posted to it, the most prominent was a 8.5"x11" sheet of paper thumb-tacked to the top which read "Kirtley's Rules." On paper, John Kirtley was our visiting research scientist, one of the founding father's of scanning SQUID microscopy, his tool of choice for probing new physics for which he won a Buckley prize. To me, John was the one who showed me that there was a place in physics for students who knew how to solder, tinker with instrumentation, and lift heavy equipment even though they achieved a triple-threat of nearly failing their 1st year classical mechanics, E&M, and modern physics classes. John was always a patient mentor, taking the time to train me on the various instruments in lab and was even supportive of my craziest ideas such as adding sample illumination capability to his workhorse scanning SQUID microscope. Anyway, **Rule No. 7** clearly states "6 months in the lab will save you an hour in the library," which is exactly the sentiment of this section. Despite becoming the Taufour lab's MPMS expert after years of magnetization measurements and analysis, if I had to guess how much magnetic theory I learned in that time spent in the lab, I would say about an afternoon's worth of reading Blundell [74].

the domain walls to narrow and become pinned at lower temperatures. In contrast, we observe that domains walls in $LaCrGe_3$ become pinned at higher temperatures. Ruling out unusual anisotropy, we can consider the existence of two different exchange constants, $J_{ex1}$ and $J_{ex2}$, which lead to the two distinct anomalies at $T_C$ and $T_x$ that indicate the two different ferromagnetic states. This is an appropriate consideration since having two different interactions is the basis for a 'two-channel Stoner' model which was proposed to describe an itinerant d-electron ferromagnet such as $LaCrGe_3$, and predicts FM1 and FM2, as well as the appearance of an AFM phase under pressure [27]. In addition, this 'two-channel Stoner' model is compatible with $UGe_2$ [32] and $ZrZn_2$ [77] where the existence of FM1 and FM2 are well established.

We can now take the ratio of the domain wall widths in the two FM states and cancelling out the $a$ and $K$ terms which do not appear to be affected by the change of FM state.

$$\frac{\delta_{FM1}}{\delta_{FM2}} = \frac{S_1\sqrt{J_{ex1}}}{S_2\sqrt{J_{ex2}}} \tag{2.8}$$

While we do not have an instrument that can measure the exchange constant directly, in a mean field, local moment picture, the exchange constant can be related to the Curie temperature. According to Blundell ([76] Pg. 91 Eq. 5.17)

$$T_C = \frac{2zJ_{ex}J(J+1)}{3k_B} \tag{2.9}$$

Where $z$ is the number of nearest neighbors and $J$ is the total angular momentum of the magnetic ion. For 3d ions (such as chromium), the orbital angular moment $L$ is quenched so $L = 0$ and $J = S$, leading to

$$T_C = \frac{2zJ_{ex}S(S+1)}{3k_B}. \tag{2.10}$$

This relationship makes sense as a stronger ferromagnetic interaction should lead to a higher $T_C$. In practice, we can rearrange this equation to solve for $J_{ex}$ in term of $T_C$ which is measurable with a number of probes such as resistivity or magnetization.

$$J_{ex} = \frac{T_C}{S(S+1)}\frac{3k_B}{2z} \tag{2.11}$$

Substituting this expression in for our domain width ratio, we have

$$\frac{\delta_{FM1}}{\delta_{FM2}} = \sqrt{\frac{T_C}{T_x}}\frac{\sqrt{\frac{S_1^2}{S_1(S_1+1)}}}{\sqrt{\frac{S_2^2}{S_2(S_2+1)}}} \tag{2.12}$$

Where $T_x$ is the crossover temperature. At zero field, $T_x \approx 70\,\mathrm{K}$ was identified in resistivity [19]. While our

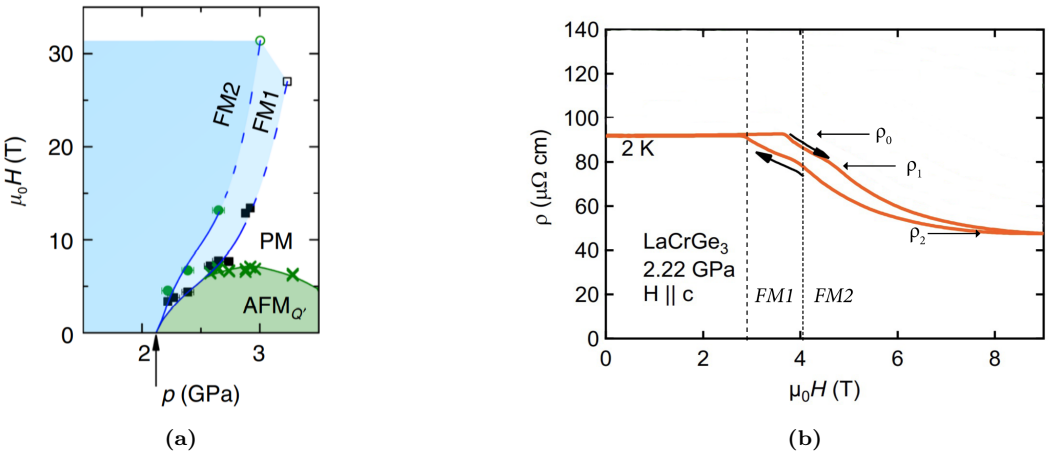


**Figure 2.24:** (a) $H$ v. $p$ phase diagram at $T = 2\,\mathrm{K}$ from Kaluarachchi *et al.* (Fig. 4(d) in Ref. [19]). At 2.22 GPa it is possible to access the non-ferromagnetic state, FM1, and FM2 by increasing the applied field. (b) $\rho(H)$ at 2.22 GPa from Taufour *et al.* (Fig. 5 in Ref. [4]). By measuring resistivity as $LaCrGe_3$ is tuned through its ferromagnetic phases, we can compare the spin of FM1 and FM2 using Eq. 2.15.

temperature dependence of the coercive field shows a local maximum near $T_x$, AC susceptibility measurements along the *ab* plane show an incredibly large and sharp peak at $T_x = 70\,\mathrm{K}$ [37].

Handling the spin terms, $S_1$ and $S_2$ appears to be tricky at first since we cannot directly measure $M_s(T = 0)$ in FM1. As a workaround, we can estimate the change in spin between FM1 and FM2 by the loss of magnetic scattering between the two phases as reported previously [4]. In Fig. 2.24(a) we can see at 2.22 GPa both FM1 and FM2 can be accessed by applying field. In Fig. 2.24(b) $\rho(H)$ was measured at 2.22 GPa, and there is a clear drop in the resistivity as the state changes from the non-ferromagnetic state (short range order clusters [7], $AFM_Q$[18]) to FM1 and then to FM2. The missing piece of the puzzle is an equation that relates $\rho$ to $S$.

Peski-Tinbergen and Dekker describe the resistivity of a ferromagnetic metal (Ref. [78] Pg. 935 Eq. 5-4)

$$\rho = \frac{m^2 k_F N}{\pi n e^2 \hbar^3} J^2 [S(S+1) - \sigma^2 - \sigma \tanh(\frac{3T_C\sigma}{2TS(S+1)})] \tag{2.13}$$

where $m$ is the effective mass, $k_F$ is the Fermi wavevector, $N$ is the number of ions per unit volume, and $n$ is the electron density. $J$ in this equation is the exchange interaction between the conduction electron and the ion and $S$ is the spin of the magnetic ion. The $\sigma$ factor is called the 'average orientation' or the 'average spin' and is just the total spin or total moment summed with a thermal factor from statistical mechanics (the magnetization at temperature $T$). When $T = 0$, $\sigma = S$ and when $T > T_C$, $\sigma = 0$.

Peski-Tinbergen and Dekker emphasize that their model is 'not satisfactory' for the low temperature region ($T \lesssim \frac{1}{2}T_C$, in which case $\sigma \approx S$). Their model neglects spin-waves, which they argue should be

considered for the low temperature region. This stipulation is initially concerning since $T_C = 85\,K$ and $T_x = 70\,K$ and the data that we are using is at $T = 2\,\mathrm{K}$. At 2.22 GPa, however, $T_C$ and $T_x$ are suppressed to low temperatures, so $T = 2\,K$ is in the range between $T_C$ and $\frac{1}{2}T_C$. Since our ultimate goal here is to merely estimate whether having two ferromagnetic phases has the potential to change the domain wall width in a direction consistent with our experimental observations, we decide to use and even make approximations on their theory.

Above $T_C$, there is no magnetic order so $\sigma$ is zero [79]. A ratio that Peski-Tinbergen and Dekker comment on is $\rho(\sigma)/\rho(0)$ which originated from De Gennes and Freidel [80]. They claim that for temperatures "not too far below $T_C$, the collisions between the conduction electrons and the spin-lattice can be considered elastic. In this approximation, they [De Gennes and Freidel] find for the dependence of $\rho$ on the average spin $\sigma$ the following formula" (Ref. [78] Eq. 5-5., Ref. [80] Eq. 4.3)

$$\frac{\rho(\sigma)}{\rho(0)} = 1 - \frac{\sigma^2}{S(S+1)} \tag{2.14}$$

Where $\rho(\sigma)$ describes the resistivity below $T_C$ and $\rho(0)$ describes the resistivity above $T_C$. This equation can be derived from Eq. 2.13 if the tanh term is omitted. The $-\sigma$ tanh term was Peski-Tinbergen and Dekker's improvement over Kasuya's model [79] which only has a $-\sigma$ term, leading to an infinite $d\rho/dt$ just below $T_C$. If we take the liberty to make the approximation that $\sigma = S$ (which occurs at zero temperature), we recover the exact ratio we need to analyze the $\rho(H)$ data from Fig. 2.24 in the context of our equation for the width of a domain wall (Eq. 2.12)

$$\frac{S^2}{S(S+1)} = 1 - \frac{\rho(\sigma)}{\rho(0)} \tag{2.15}$$

In this equation we take $\rho(\sigma)$ as the resistivity in an FM state, and $\rho(0)$ as the resistivity in the non-ferromagnetic state. Using these quantities extracted from Fig. 2.24(b), we get our final result:

$$\frac{\delta_{FM1}}{\delta_{FM2}} \approx 0.56 \tag{2.16}$$

Our rough theoretical approximation shows that the domain walls in the high temperature FM1 state are expected to be shorter, and therefore more difficult to move, than the domain walls in the lower temperature FM2 state. This result from allowing for two ferromagnetic states is consistent with our experimental observation that the magnetic domains are pinned at high temperatures near 70 K and subsequently de-pin as the temperature is lowered, resulting in an unusual magnetization curve and temperature dependence of coercivity.

Applying a similar approximation to the expression for the energy cost per unit area of a Bloch domain wall [76],

$$\sigma_{BW} = \pi S \sqrt{\frac{2J_{ex}K}{a}} \tag{2.17}$$

yields the same ratio as Eq. 2.16, which implies that the cost of a domain wall is larger in the FM2 state. This result means that we expect to see fewer domain walls in the FM2 phase compared to the FM1 phase, which is consistent with our MOKE images presented in Fig. 2.10 that show the domains are larger in the FM2 phase than in the FM1 phase. A schematic diagram intended to clarify the relationship between the size of domains and the energy cost of a domain wall is presented in Fig. 2.25.

### 2.3.7 Conclusion

So far, I have presented three experimental measurements as evidence for domain pinning in $LaCrGe_3$ when $T_x < T < T_C$. While I began with the MOKE images, as we believed they are the most effective at convincing the reader of the significant domain-related change at $T_x$, they were the last measurements performed chronologically. In chronological order, the hysteresis loops and the unusual temperature dependence of the coercivity were measured first. Although that result was intriguing, we did not think it would make for a strong publication on its own. We had an idea that the hysteresis loops were related to the mysterious magnetization curve since the anomalous features—the reappearance of hysteresis and the downturn in the field-cooled magnetization—occurred at the same temperature. Developing the simple domain pinning model that could explain the $M(T)$ curve with pinning temperatures determined from the coercivity data gave the project serious momentum. On a parallel timeline, Professor Zhu had finished building his MOKE microscope and his images of my samples made it possible to confirm the domain pinning region with our own two eyes. The assertion that these experimental features were due to the FM1/FM2 crossover and the rough theoretical work supporting that notion came last. In conclusion, our bulk and spatially-resolved magnetization measurements independently show the unusual case where the domains are pinned at high temperatures and depin at low temperatures. We then find that a crossover between FM1 and FM2 could cause the change of domain wall mobility we observe. Our discovery joins a number of other probes that show anomalies in a similar temperature region and support the existence of FM1 and FM2 in $LaCrGe_3$.

Enough history. What's the "so what?" When I presented this work at March Meeting 2023 in Las Vegas, I chose the title 'The unusual ferromagnetism of $LaCrGe_3$ through the lens of magnetic domain depinning.' Naturally, the "so what?" depends on what lens you want to look through.

From an engineering standpoint, we can wonder if there are applications for free moving domain walls at low temperatures and pinned domain walls at high temperatures. We have seen that the more usual case

(where domains are pinned at low temperatures and free-moving at high temperatures) can be exploited to increase the data density of magnetic storage with Heat Assisted Magnetic Recording (HAMR) technology developed by Seagate [81],[9] so it is not an impossible thought that our magnet may have useful applications. One might view the low temperature hysteresis loops as useful for memory applications. A contemporary reference on $LaCrGe_3$ from the Canfield group [37] with many of the same measurements, but an alternative interpretation, focuses on these remarkably square hysteresis loops. They note that they have the following two features that are common in single-domain nano-magnets, but are atypical in bulk ferromagnetic samples. First, the remanent magnetization is equal to the saturation magnetization[10] and second, the flip from $+M_s$ to $-M_s$ is incredibly sharp. While these are both desirable features for memory, my investigation of the hysteresis loops at low temperature (see Section 2.4.2) revealed a large variance in the coercivity—some samples had no coercivity and no remanent field at low temperature. It is likely that with further investigation, one may discover the source of these low temperature hysteresis loops (sample defects, surface characteristics etc.) and possibly be able to tune the coercive field. Until then, we consider the domain pinning region of $LaCrGe_3$ to be intrinsic, and therefore a target for potential applications.

From the viewpoint of an experimental physicist exploring magnetism, this research is a wake-up call that domain behavior should be respected. In the case of $LaCrGe_3$, we demonstrate the possibility that the domain behavior is a reflection of a crossover between FM states, which has otherwise proven difficult to detect. With this revelation in mind, there are most likely other systems where magnetic anomalies were overlooked or simply dismissed as "domain effects." It is important to study low-field phenomena instead of applying high fields to avoid domain effects altogether as the magnetic characterization of new or newly single crystal compounds typically goes. For completeness, the initial characterization should include field-cooled-cooling, field-cooled-warming and zero-field-cooled $M(T)$ measurements. If there is hysteresis present in $M(H)$, then its temperature dependence should be measured, even beyond the temperature at which the coercivity disappears. If magnetic anomalies during these measurements occur, the domain pinning and depinning analysis from this work is an available tool to use before exploring or suggest more exotic possibilities such as the coexistence of ferromagnetism and antiferromagnetism. A theme of this thesis is that although magnetism plays an important role in our every day lives, it is still very much a mystery. I think respecting magnetic domains is an important part to solving that mystery.

[9] With HAMR, a laser mounted ahead of the read/write head locally warms up the magnetic material such that the target domains can be flipped with a comparatively small magnetic field, therefore not affecting nearby domains.

[10] In the general ferromagnetic hysteresis loop found in textbooks the remanent magnetization is usually smaller than the saturation magnetization.

## 2.4 Appendices

The following sections are longer-form versions of the appendix that appeared in the *Physical Review B* article. They intend to provide technical details of the analysis abbreviated in the main text.

### 2.4.1 Demagnetization Factors

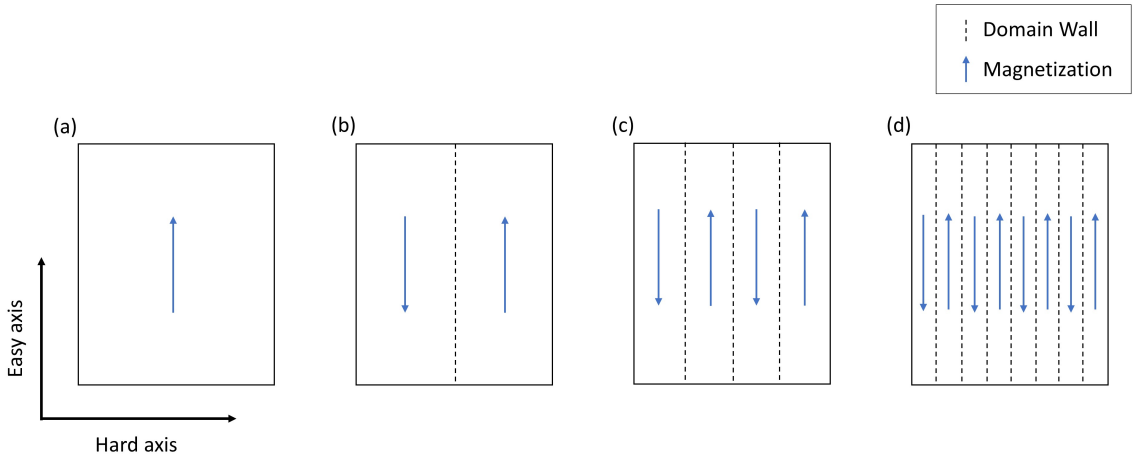


**Figure 2.25:** A schematic of the different domain configurations for a ferromagnetic with an easy axis. Panel (a) is single-domain and therefore has a net magnetization and a maximal energy due to the resulting external field. Panels (b-d) each have an equal number of up and down domains, therefore an overall net zero magnetization, however, they differ in the size of the domains, the number of domain walls and the resulting external field. If there is a large energy cost of a domain wall, then fewer domain walls and therefore domains will form. If the energy cost of a domain wall is small, then it is favorable for more domains to form like it (d) which will have significantly less external field than (b).

Since our study involves magnetic domain behavior, the demagnetizing field, $H_d = -NM$, plays an important role in our analysis. While the measured magnetization ($M$) is a property of the compound in the particular temperature and field environment, the demagnetization factor ($N$) is unique to the size and shape of the sample. In this section, we will explain how we determined $N$ for the primary sample we measured for this project.

Pictures of the sample used for all of the measurements which include $N$ in the analysis presented so far are shown in Fig. 2.26. We measured the dimensions of the sample from these photographs taken against mm-grid paper. We then used the mean length and mean width to approximate the half-hexagonal rod as a rectangular prism, so we could use the formula given by Aharoni [73] to estimate the demagnetization factors along each axis. With this method, we found $N_a = 0.341$, $N_b = 0.492$, and $N_c = 0.166$.

$N_c$ can also be determined from $M(H)$ measurements in temperature ranges where there is no domain wall pinning and the easy axis virgin magnetization forms a straight line with slope $1/N_c$ through the origin.

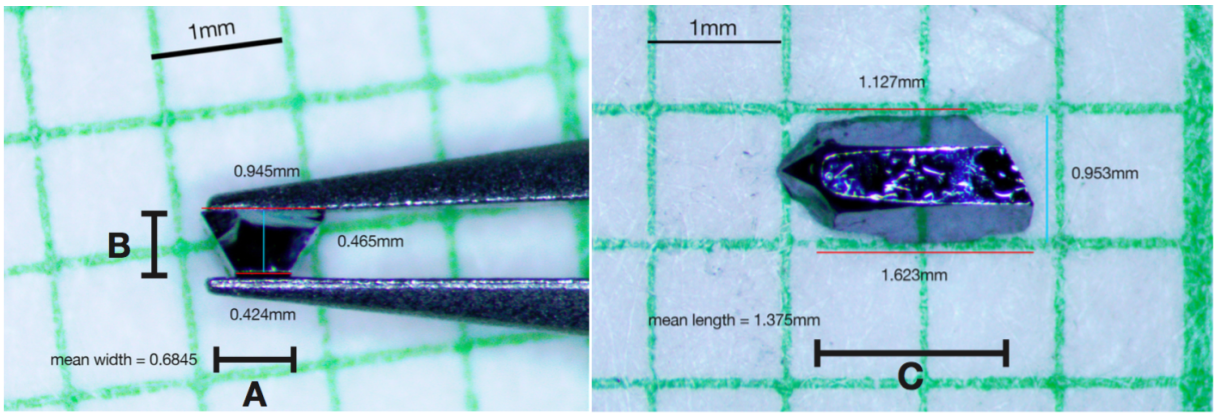


**(a)** **(b)**

**Figure 2.26:** Most of the magnetic measurements were done on the $LaCrGe_3$ crystal pictured. One side was lightly polished flat and parallel to the opposite face. We determined the size from pictures of the sample on mm grid paper. From these measurements we were able to estimate the demagnetization factors $N_a$, $N_b$ and $N_c$.

In $LaCrGe_3$, this condition is met for temperatures $\sim 50\,\mathrm{K}$ and below. For temperatures around $60\,\mathrm{K}$ and above, however, the virgin curves do not initially follow demagnetization theory due to the presence of domain wall pinning. Experimentally, there is a small variation of the extracted $N$ across virgin magnetization curves measured at different temperatures, so in practice, the smallest value found is chosen to avoid the unphysical consequence that $H_{\mathrm{int}}$ is negative. From our magnetization measurements, we found $N_c = 0.1129$. A difference of $\sim 0.05$ for $N_c$ is within reason according to Lamichhane *et al.* [82] where a similar method for finding $N$ from sample size followed by correcting $N$ from magnetization measurements was used.

This value of $N_c$ is reasonable for two reasons. First, we see that $M = \frac{H_{\mathrm{applied}}}{N_c}$ closely matches the measured $M$ in the temperature independent region of the $M(T)$ curve shown in Fig. 2.18 that we argue is simply the demagnetization value. Second, as shown in Fig. 2.15(b), using $N_c$ to compute $H_{\mathrm{int}}$ makes the virgin curve increase nearly vertically to saturation, as expected for an easy axis ferromagnet.

With a working value of $N_c$, $N_a = 0.3631$ and $N_b = 0.524$ are found from ratios determined from the sample dimensions. For $H||ab$ measurements, the field is applied along the $A$ dimension labelled in Fig. 2.26(a), so $N_a$ is used to calculate $H_{\mathrm{int}}$, which is necessary for calculating anisotropy constants.

This same method of determining the demagnetization factor was used for the additional samples measured to study sample variation of the coercivity. As seen in Fig. 2.27, the demagnetization factors accounts for the low temperature magnetization in $M(T)$ and the slope of the virgin curve in $M(H)$ in these additional samples.

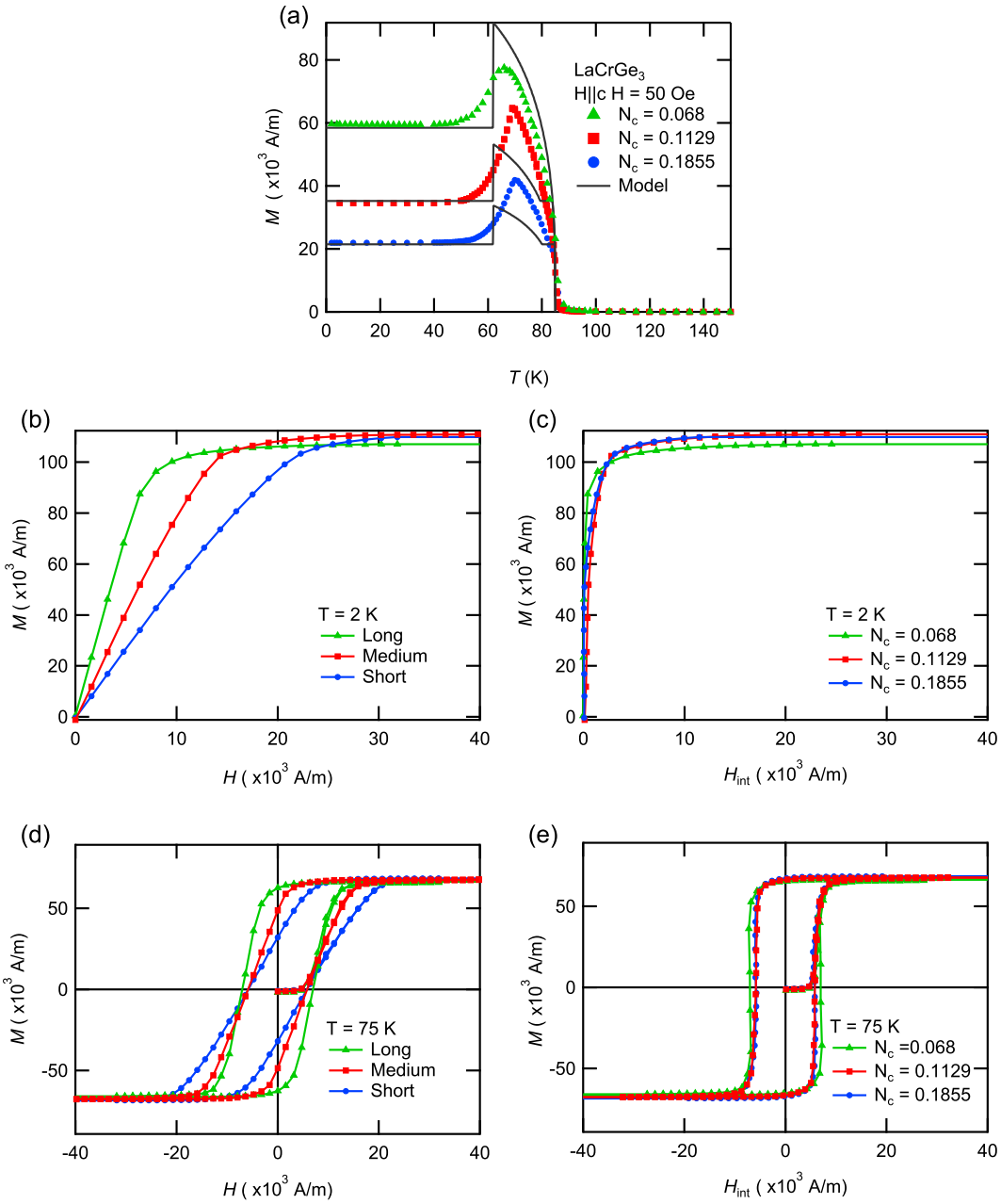


**Figure 2.27:** (a) A comparison of the magnetization as a function of temperature curves at $H = 50\,\text{Oe}$ for three different samples. When $T < 50\,\text{K}$, $M = H_{\text{applied}}/N_c$ as dictated by demagnetization theory. The demagnetization factor, $N_c$ is sample dependent and as a result, longer samples with smaller $N_c$ have larger $M$ for a given applied field in this low temperature region. (b) The initial magnetization curves, or virgin curves were measured for three different samples starting from a zero-field-cooled state. These curves follow demagnetization theory that says the slope of the virgin curve should be $1/N$, where $N$ is the demagnetization factor. As expected, longer samples have steeper slopes, and shorter samples have shallower slopes. (c) By finding $N_c$ for each sample measured, we can correct for demagnetization by plotting $M(H_{\text{int}})$ and we find that $M$ reaches $M_s$ when $H_{\text{int}} > 0$, as expected for a ferromagnet being measured with the field applied along its easy-axis. (d) Hysteresis loops measured at $T = 75\,\text{K}$ in our three different samples. Since this is in the domain wall pinning region, $M$ initially hesitates to increase. During the initial increase in $M$, as well as during the magnetization reversals, $M$ changes with a different slope depending on the sample. These different slopes, however, are simply a result of the differently-sized samples having different $N_c$. Although the slopes are different, the loops have the same coercive field ($H_c$ is the field at which $M = 0$ after $M$ was previously $M_s$). (e) We correct for demagnetization effects by plotting $M(H_{\text{int}})$, and find that the hysteresis loops are nearly identical across all three samples.

### 2.4.2 Sample Dependent Features

Any discussion of magnetic domains or hysteresis requires us to consider variations from sample to sample. In this section, we repeat many of the magnetic measurements we performed in the main section on two additional single crystal samples with different shapes and sizes in order to help explain which magnetic features are intrinsic to $LaCrGe_3$ and which features are sample dependent. Among the characteristics that are sample dependent, we are able to determine which ones are due to differences in the size and shape of the sample via demagnetization factors, and which properties may instead be due to defects in the sample.

In $LaCrGe_3$ measured along the easy $c$ axis, the effects of $N_c$ are apparent in both $M(T)$ and $M(H)$ measurements. The unusual $M(T)$ curve is only measured at low fields, specifically when $H_{\text{applied}} < N_c M_s$. According to this relationship, we expect short samples with large $N_c$ to show the anomaly up to higher fields than longer samples with smaller $N_c$. We also note that the temperature-independent magnetization observed when $T < 50\,\text{K}$ is exactly dictated by demagnetization theory, $M = H_{\text{applied}}/N_c$. As a result, for a given applied field, a longer sample will settle to a higher magnetization compared to a shorter sample. This can be seen in Fig. 2.27(a), where we plot $M(T)$ at $H = 50\,\text{Oe}$ for three samples, along with our model which accounts for the different values of $N_c$.

In $M(H)$ along the $c$ axis, the demagnetization factor most obviously appears in the virgin curve when $T \lesssim 60\,\text{K}$. In this temperature region, we found that the domain walls in $LaCrGe_3$ are depinned, or free to move according to demagnetization theory, and therefore, the slope of the virgin curve in this linearly increasing region is simply $1/N_c$. From this equation, we expect the virgin curves of different samples to have different slopes: long samples will have steeper virgin curve slopes than shorter samples do. This relationship can be seen in Fig. 2.27(b) which plots the virgin magnetization curves for our three samples. These different slopes are simply due to the demagnetization factor, $N_c$, which we can correct for by plotting $M$ against internal field, $H_{\text{int}}$, instead as shown in Fig. 2.27(c).

We also recognize that the high temperature ($T \gtrsim 60\,\text{K}$) hysteresis loops have a sample-dependent component that is also explained by $N_c$. Although $M$ in these loops does not initially increase following demagnetization theory due to domain wall pinning, we find that when $M$ does start to increase, it does so with a slope equal to $1/N_c$. We can see this phenomenon in Fig. 2.27(d) where, like in Fig. 2.27(b), the longer samples have steeper slopes. Furthermore, we find that this is the same slope as the magnetization reversal curves, which indicates that the initial increase in $M$ up to saturation and the magnetization reversal share the same underlying mechanism [60]. These different slopes across different samples are simply explained by the variety of demagnetization factors. Since our samples have a similar $H_c$ in this range of temperatures, as shown in Fig. 2.28(a), when we factor in $N_c$ to plot $M(H_{\text{int}})$ (Fig. 2.27(e)), we find that the hysteresis

loops in this high temperature region are nearly identical across our three samples.

The hysteresis loops at low temperature, however, are not identical across all samples. In Fig. 2.28(b), we plot $M(H_{\text{int}})$ for all three samples at $T = 2\,\text{K}$ to show the drastic variation between samples. The original sample has the rectangular-shaped hysteresis loops also observed in a recent study [37]. While the longest sample also has a rectangular loop at $T = 2\,\text{K}$, it has a significantly smaller $H_c$. Finally, the shortest sample is unique because it does not have a remanent magnetization, and does not have a rectangular shape. Instead, this short sample has a double-triangular shape with the saturated moment returning to the demagnetization theory curve before $H_{\text{int}} = 0$. Furthermore, Fig. 2.28(a) shows that at low temperatures, $H_c$, as well as the temperature at which $H_c$ disappears, are sample-dependent. The shortest sample measured ($N_c = 0.1855$) has a negligible $H_c$, while the longest sample ($N_c = 0.068$) has less than one third the $H_c$ as the sample measured in the main text ($N_c = 0.1129$), and this coercivity disappears at a relatively low temperature.

It is clear that the low-temperature hysteresis loops are wildly variable, with no obvious trend based on sample size. Naively, we might expect longer samples to have larger $H_c$ due to the increased energy cost of forming the longer domain wall necessary to nucleate a reversed domain. This hypothesis, however, does not match the $H_c$ v. $T$ data across the three samples presented here, along with the additional two from Xu *et al.* [37]. Therefore, unlike the magnetic features discussed previously, where the sample-dependence was determined by the size of the sample via the demagnetization factor, we are unable to draw conclusions regarding the relationship between $N_c$ and $H_c$ at low temperatures. Exploring the role of sample defects may help explain the sample-dependence of these low temperature hysteresis loops.

Defects, however, are difficult to quantify, and it is difficult to predict how defects will affect the magnetization measurements. One way to quantify a sample's quality, or lack of defects, is by measuring its residual resistivity ratio, or "triple R" (RRR), which is the ratio between the resistivity at high temperature and the resistivity at low temperature, i.e., $\rho(300\,K)/\rho(2\,K)$. Exploring RRR and its effect on the low temperature hysteresis loops in $LaCrGe_3$ may be the next step to determining the role defects play in the sample dependence of these magnetic features.

In conclusion, by measuring three different samples with different demagnetization factors, we are able to show which magnetic features are sample-dependent and can be explained by demagnetization effects, and which features are sample-dependent but in a way that is currently not understood. Since the extreme variation of the low temperature hysteresis loops does not affect domain wall pinning, our domain wall pinning/depinning model still reproduces the qualitative features of the unusual $M(T)$ curve for samples with different demagnetization factors. Still, more work needs to be done to solve the mystery of which parameters affect the low temperature hysteresis loops.

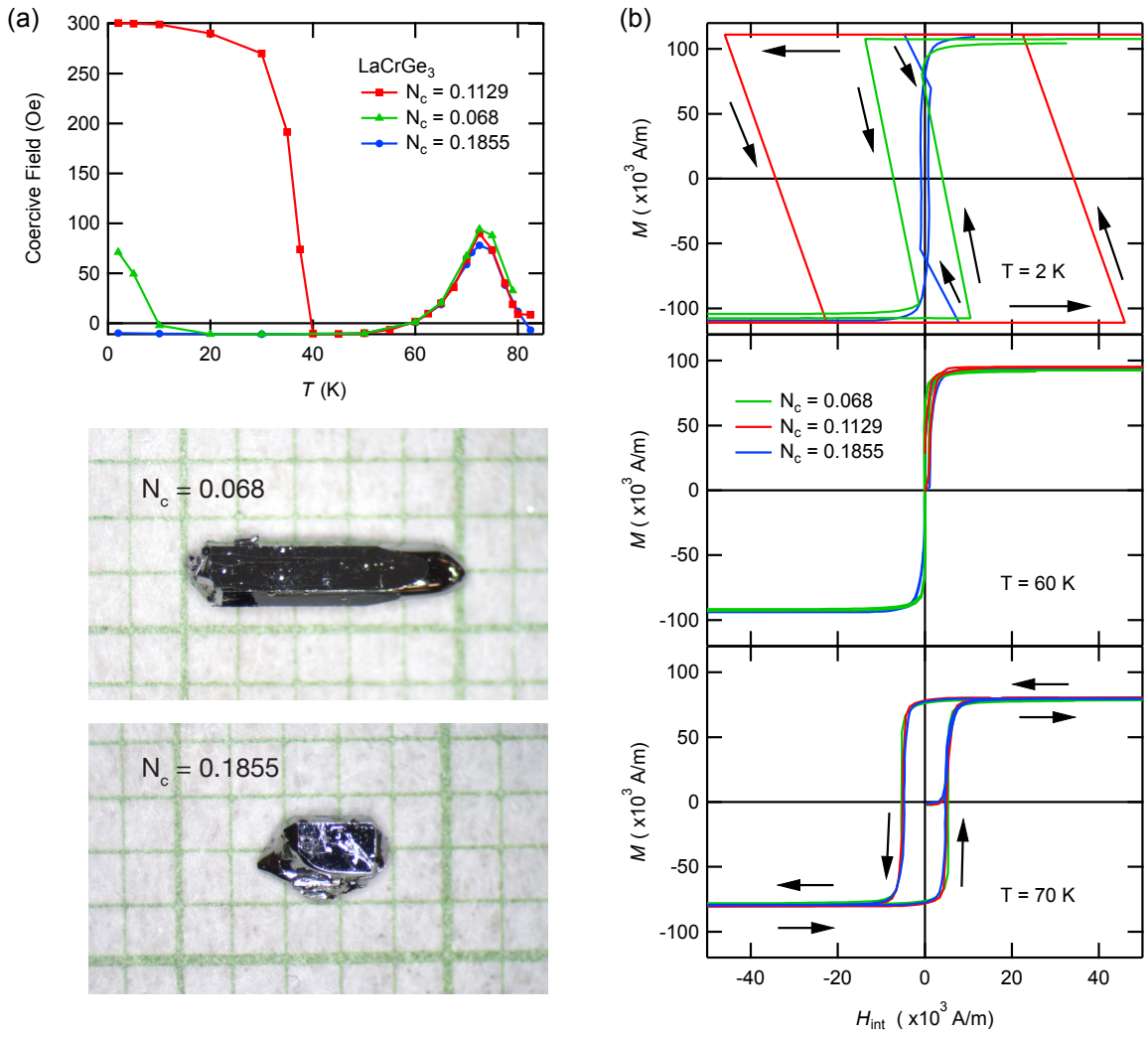


**Figure 2.28:** (a) A comparison of the temperature dependence of the coercive field, $H_c$, across three different samples. Below 40 K, the hysteresis loops vary significantly across the three samples. In one sample, no coercivity was observed. Furthermore, there is no trend based on sample size; longer samples do not necessarily have higher coercive fields, as shown by comparing the green curve for the $N_c = 0.068$ sample to the red curve for the shorter $N_c = 0.1129$ sample. This suggests that the low temperature hysteresis is due to defects, but more research needs to be done to confirm. On the other hand, the coercive field is nearly identical across all three samples when it appears again at high temperatures (60 K$< T < T_C$). We take this as evidence that the hysteresis in this range of temperatures is due to an intrinsic property of $LaCrGe_3$. (b) A comparison of the hysteresis loops measured across three different samples at $T = 2$ K. The loops vary significantly across samples and in a way not obviously explained by differences in $N_c$.

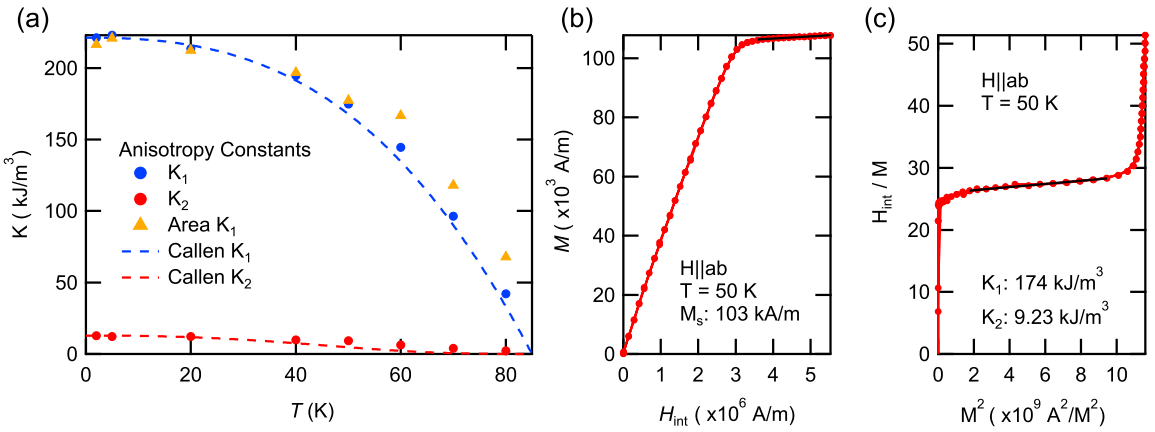


**Figure 2.29:** (a) The anisotropy constants as a function of temperature. There do not appear to be any anomalies in $K_1$ or $K_2$, which may initially be surprising given the strange behavior in $M(T)$. (b) $M(H_{\text{int}})$ measured along the hard axis. The linear region at high field is fit to a line to extract the spontaneous magnetization $M_s$. (c) By plotting $H_{\text{int}}$ v. $M^2$ and fitting the linear portion to Eq. 2.27, we can extract the anisotropy constants $K_1$ and $K_2$.

### 2.4.3 Regarding Anisotropy

The original reason for revisiting $LaCrGe_3$ was to check for hard axis ordering, perhaps by an unusual temperature dependence of the anisotropy constants. Measuring the anisotropy involves measuring $M(H)$ along the hard axis and the easy axis at different temperatures, and it is during these measurements that I observed the anomalous temperature dependence of coercivity that warranted even further investigation.

An unusual temperature dependence of the anisotropy constants $K_1$ and $K_2$ can cause strange magnetic phenomena. The coercivity as a function of field curve in Gd has a remarkably similar shape to the initial one I measured in $LaCrGe_3$, it is also split between two regions by a minimum $H_c$ below its $T_C = 289\,\text{K}$ [61, 63]. This similarly shaped coercivity plot in Gd, however, is due to a change of sign of the anisotropy constant $K_1$ and comparatively large values of $K_2$ [64, 62]. The results of our anisotropy analysis on $LaCrGe_3$ are summarized in Fig. 2.29(a), and we find that $K_1$ and $K_2$ in $LaCrGe_3$ follow a standard temperature dependence. So unlike in the case of Gd, anisotropy alone cannot explain the unusual temperature dependence of $H_c$ in $LaCrGe_3$.

In this section, I aim to derive in detail the three different ways to calculate the anisotropy constants, $K_1$ and $K_2$, for a hexagonal ferromagnet with a hard and easy axis, such as $LaCrGe_3$. An abbreviated version of these derivations appeared in my paper, but in this thesis I present this slightly longer version of the derivation. I hope this section helps future experimentalists wrap their heads around magnetocrystalline anisotropy.

The first way to measure the anisotropy constants is a method first detailed by Sucksmith [83]. The Sucksmith method involves measuring $M$ as a function of $H_{\text{applied}}$ along the hard axis of the ferromagnet,

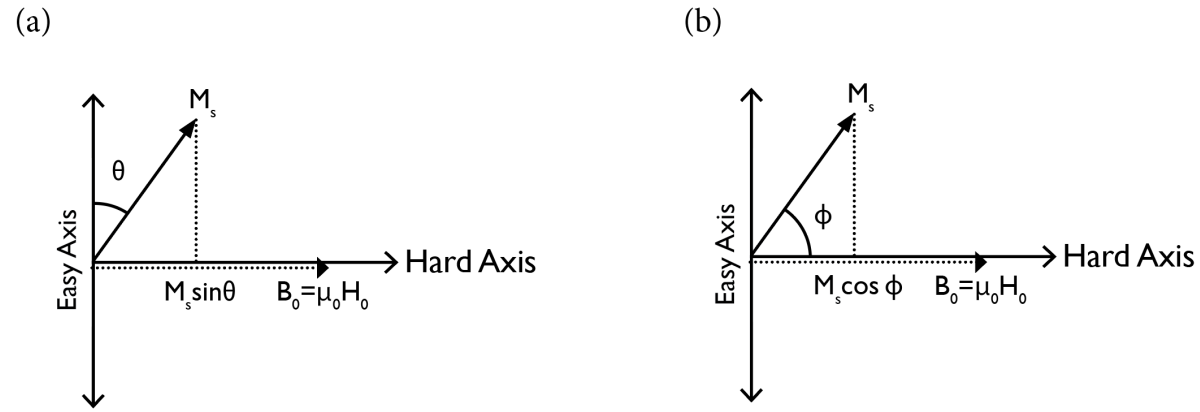


**Figure 2.30:** (a) $\theta$ is defined as the angle between the magnetic moment (with a magnitude equal to the spontaneous magnetization, $M_s$) and the easy axis or easy magnetic direction. (b) $\phi$ is defined as the angle between the magnetic moment and the applied magnetic field.

and relating that measurement to an expression for the minimum of an energy density. The energy density we consider is a sum of the anisotropy energy density and the Zeeman energy.

$$\epsilon = \epsilon_{\text{anisotropy}} + \epsilon_{\text{Zeeman}} \tag{2.18}$$

The anisotropy energy density for a hexagonal system is given by

$$\epsilon = K_1 \sin^2\theta + K_2 \sin^4\theta \tag{2.19}$$

where $K_1$ and $K_2$ are the anisotropy constants and $\theta$ is the angle between magnetic moment, $M$, and the easy magnetic axis direction (the $c$ axis for $LaCrGe_3$) as shown schematically in Fig. 2.30(a).

The Zeeman energy, which describes the interaction between the moment and the applied magnetic field, is given by

$$\epsilon_{\text{Zeeman}} = -\vec{M} \cdot \vec{B} = -M\mu_0 H \cos\phi \tag{2.20}$$

where $\phi$ is the angle between the moment and the applied magnetic field $H$, as shown schematically in Fig. 2.30(b). This energy would not be entirely correct if we ignored the demagnetization field. To take the demagnetization field into account, we should instead explicitly use $H_{\text{int}}$

$$H_{\text{int}} = H_{\text{applied}} + H_{\text{demag}} = H_{\text{applied}} - NM_{\text{measured}} \tag{2.21}$$

where $M_{\text{measured}}$ is the measured sample magnetization.

When measuring the magnetization along the hard axis, the measured magnetization is $M_{\text{measured}} =$

$M_s \sin\theta$ in which $M_s$ is the spontaneous magnetization. $M_s$ is given by the y-intercept of the line fit to the saturated magnetization at high field as depicted in Fig. 2.29(b). As a result, the theta-dependent energy density is

$$\epsilon = K_1 \sin^2\theta + K_2 \sin^4\theta - \mu_0 M_s H_{\text{int}} \sin\theta \tag{2.22}$$

Nature tells us that a system will settle into the lowest possible energy state. So to figure out what angle $\theta$ the magnetic moment will take, we need to minimize this energy density with respect to $\theta$. Taking the derivative and setting it equal to zero gives us

$$\frac{\delta\epsilon}{\delta\theta} = 2K_1 \sin\theta\cos\theta + 4K_2 \sin^3\theta\cos\theta - \mu_0 M_s H_{\text{int}} \cos\theta = 0 \tag{2.23}$$

In this equation, $\cos\theta = 0$ or $\theta = \pi$ is simply the trivial solution in which the magnetization is all along the hard axis. So we are left with

$$2K_1 \sin\theta + 4K_2 \sin^3\theta - \mu_0 M_s H_{\text{int}} = 0 \tag{2.24}$$

Remembering that $M_{\text{measured}} = M_s \sin\theta$, we can rewrite the $\sin\theta$ as $\frac{M}{M_s}$.

$$\mu_0 M_s H_{\text{int}} = 2K_1 \frac{M}{M_s} + 4K_2 \Big(\frac{M}{M_s}\Big)^3 \tag{2.25}$$

By re-arranging this equation, we can solve for the anisotropy constants $K_1$ and $K_2$.

$$\mu_0 H_{\text{int}} = 2K_1 \frac{M}{M_s^2} + 4K_2 \frac{M^3}{M_s^4} \tag{2.26}$$

$$\frac{\mu_0 H_{\text{int}}}{M} = 2K_1 \frac{1}{M_s^2} + 4K_2 \frac{1}{M_s^4} M^2 \tag{2.27}$$

Finally, by plotting $\frac{\mu_0 H_{\text{int}}}{M}$ v. $M^2$ we find $K_2$ from the slope which is $\frac{4}{M_s^4} K_2$ and $K_1$ from the intercept, $\frac{2}{M_s^2} K_1$, as seen in Fig. 2.29(c). To get the temperature dependence of $K_1$ and $K_2$, the Sucksmith method is performed on hard axis $M(H)$ measurements at various temperatures below $T_{\text{C}}$. Our results for $K_1$ and $K_2$ are shown, respectively, as the blue and red dots in Fig. 2.29(a).

We can compare our measured anisotropy to its theoretical temperature dependence given by the Callen-and-Callen law [84, 85]. Given $K_1^0$ and $K_2^0$, the anisotropy constants at zero temperature, and $M_s(T)$, the temperature dependence of the spontaneous magnetization, the anisotropy constants at temperature $T$ are given by

$$K_1(T) = \Big(K_1^0 + \frac{7}{8}K_2^0\Big)\Big(\frac{M_s(T)}{M_s(0)}\Big)^3 - \frac{7}{8}K_2^0\Big(\frac{M_s(T)}{M_s(0)}\Big)^{10} \tag{2.28}$$

$$K_2(T) = K_2^0\Big(\frac{M_s(T)}{M_s(0)}\Big)^{10} \tag{2.29}$$

For this Callen-and-Callen analysis, we used the $T = 2\,\mathrm{K}$ values from the Sucksmith method as $K_1^0$ and $K_2^0$. For $M_s(0)$, we use the $T = 2\,\mathrm{K}$ value of the spontaneous magnetization which is calculated from the y-intercept of the line fit to the saturated portion of an $M(H)$ measurement with $H||c$. $M_s(T)$ is calculated from $M_s(0)$ using theory from Kuz'min [71]. The theoretical $K_1(T)$ and $K_2(T)$ from this Callen-and-Callen analysis are shown, respectively, as the dashed blue and red lines in Fig. 2.29(a). Our measured values derived from the Sucksmith analysis are in agreement with the Callen-and-Callen law throughout the temperature range.

The final method we used to extract anisotropy from magnetization data involves computing the area between the easy and hard axis magnetization curves in $M(H)$ [86]. With this area method, $K_1$ is given by

$$K_1 = \epsilon_{001} - \epsilon_{100} \tag{2.30}$$

where $\epsilon_{001}$ and $\epsilon_{100}$ are the magnetic energies along the easy axis ($c$ axis) and the hard plane ($ab$ plane) respectively. The energy densities are calculated by the integral

$$\epsilon = \mu_0 \int_0^{H_{sat}} M dH = \mu_0 \int_0^{M_{sat}} H dM \tag{2.31}$$

The results of using the area method are shown as the golden triangles in Fig. 2.29(a). The values for $K_1$ agree at temperatures below 50 K, however, they appear to systematically deviate at higher temperatures. We can understand this deviation by looking at the $M(H)$ data at these temperatures which show a discrepancy in the saturation magnetization between the two axes. We found that when measuring along the hard axis of a ferromagnetic sample, small sample displacements from the radial center of the sample chamber can cause large deviations in the measured $M$ at high fields (refer to Section 4.1.1 for more details). In spite of our best efforts to radially center the sample in the MPMS, we found small discrepancies between easy axis and hard axis saturation magnetizations. Since the area analysis involves both easy and hard axis data, it is sensitive to these small mis-alignments unlike the Sucksmith method which only involves hard axis data.

In conclusion, our anisotropy analysis of $LaCrGe_3$ does not reveal any anomalies that would cause the re-opening of hysteresis loops or the shark-fin shape of the $M(T)$ curves.

# Chapter 3

# $LaCrSb_3$

## 3.1 A Short History of the Project

Investigating the effects of Fe substitution in single crystals of $LaCrSb_3$ was originally Jeff Harvey's project. Jeff Harvey was one year my senior in the PhD program, but ten years senior in age, and as a testament to his character, he invited me to his birthday party at Froggy's only a week after I had met him. In the lab, he taught me how to use the glass bench and let me shadow him while he prepared the synthesis of the $x = 0.4$, 0.5, 0.6 samples. For the record, that synthesis ended in disaster as a broken thermometer wire sent the furnace into thermal runaway and reached the 1500°C maximum temperature causing the sealed ampoules to explode. I hope that was a pure coincidence. Jeff made me feel welcome in the lab, and when he left the group after completing his Master's thesis, he even let me borrow his lab notebook as a reference.

My initial job was to turn Jeff's Master's thesis into something publishable. Valentin suggested that it should go quickly because all of the data was already taken, so what was left was simply editing down the thesis into a few pages in two-column format. After further investigating the magnetic properties of the system as part of my training on the MPMS,[1] however, we found $LaCr_{1-x}Fe_xSb_3$ to be more interesting than we initially believed. As a result, it ballooned into a much larger project, the one I presented for my qualifying exam in March 2021, and the one that is being submitted to journals as I am writing this very thesis in 2023.

Those further magnetization measurements suggested that $LaCr_{1-x}Fe_xSb_3$ contains a quantum tricritical point (QTCP). A QTCP is a point in the magnetic phase diagram where FM and AFM interactions are expected to diverge, a feature only seen in two previous systems ($CeTiGe_3$ [87] and $NbFe_2$ [88]). After

[1] Quantum Design Magnetic Property Measurement System. Specifically the XL model which can apply 7 T fields. The non-XL version is limited to 5 T.

additional substitutions were grown and even more measurements were performed, we instead found a novel magnetic phase diagram where the approached quantum tricritical point is ultimately avoided. This *avoided* quantum tricritical point is yet another example of the curious phenomena that are revealed when ferromagnetism is suppressed.

The first experimental observation of a QTCP reported in the $NbFe_2$ [88] system was published in *Nature Physics*, and the fact that the QTCP in $CeTiGe_3$ was announced in *Physical Review B* was likely a matter of unfortunate timing. The novel magnetic phase diagram of $LaCr_{1-x}Fe_xSb_3$, one containing the first observation of a QTCP avoided by the appearance of a new magnetic phase, is surely as important a discovery, especially since we realized the possibility that a QTCP was in fact avoided in the $NbFe_2$ and $CeTiGe_3$ systems as well. As such, for this project, we targeted higher impact journals. To fit the strict length and citation limit imposed by these higher impact journals, my original introduction was re-worked by Valentin (the expert on the avoidance of quantum criticality). In this thesis, however, I am able to bring back some of my own words and re-instate the citations that we deemed relevant, but were sacrificed for potential prestige.

### 3.1.1 Historical Background of $LaCrSb_3$

$LaCrSb_3$ was first synthesized in polycrystalline form by annealing cold-pressed pellets of a stoichiometric $(1:1:3)$ ratio of powders by Bylak and Jeitschko in 1995 [89]. A follow-up study of the magnetic properties by the same group on the same polycrystalline samples reported that $LaCrSb_3$ is ferromagnetic with a $T_C = 125 \pm 5\,K$ although they do not show the $M(T)$ curve [90]. They also measure $M(H)$ revealing a remanent magnetization and plot $1/\chi$ for dubious Curie-Weiss fitting. Ferguson *et al.* determined the crystal structure to be *Pbcm* (No. 57) in 1997 [91] using X-ray diffraction on polycrystalline samples formed by arc melting on-stoichiometry, as well as on rudimentary single crystals grown by heating a $1:2:3$ mixture of elements to $1000^\circ$ C and slowly cooling over 24 hours.

Investigation of the compound's magnetic and physical properties continued primarily on polycrystalline samples following a similar synthesis procedure to the aforementioned references. In 1998, Raju *et al.* [92] measured magnetization and neutron diffraction on polycrystalline samples made by annealing the elements in a $1:1:3$ ratio at $1000^\circ$ C for 3 days followed by cooling to room temperature over 2-4 days. They were able to measure resistivity on single crystals up to 1 mm in length grown by simply lengthening the slow cooldown from $1000^\circ$ C to room temperature to 8 days. Resistivity revealed a transition near $T = 125\,K$. Magnetization measurements suggested a ferromagnetic transition at the same temperature, and exhibited a difference between field-cooled-cooling and zero-field-cooled magnetization which can indicate

the presence of ferromagnetic domains. While their neutron diffraction results were able to confirm the ferromagnetic transition and that the spontaneous moment points along the $b$ direction, they did not reveal the forbidden peaks indicating $LaCrSb_3$'s unconventional magnetic structure core to the compound's intrigue. A following investigation of the magnetic properties of $LaCrSb_3$ using arc-melted polycrystalline samples was performed by Leonard *et al.* [93], and used thermal expansion measurements to confirm the zero-field transition temperature and the second order nature of the phase transition.

Less experienced single crystal synthesis students have a tendency to take an elitist stance when it comes to polycrystalline samples and results.[2] While polycrystalline samples inherently obscure anisotropy and muddy the quality of certain measurements, they lay necessary foundation for single crystal studies and more involved measurements. For example, the polycrystalline study by Dubenko *et al.* [94] that investigated the effects of substituting V, Mn, Fe, Cu, and Al on the Cr site by induction melting on stoichiometry[3] led us to study Fe substitution in single crystals. Furthermore, there are situations in which single crystals are impractical. For example, the signal from $\mu$SR measurements is proportional to the amount of sample, and while a mosaic of single crystals is ideal, it is often tedious. As a result, although single crystals of $LaCrSb_3$ were first synthesized as early as 2001, $\mu$SR[4] measurements on polycrystalline sample (3g, arc melted on stoichiometry and then annealed for 7 days) were performed much later in 2006 [95] and concluded that the spin reorientation did not involve a transition in the ordered moment.

$LaCrSb_3$'s unusual magnetic structure was not discovered until larger single crystals could be grown. Single crystals were first synthesized by Jackson *et al.* in 2001 [96]. A $4:3:13$ ratio was used, and the constituent elements were placed in alumina crucibles and heated according to the following temperature profile: heated to 1180°C and then cooled at a rate of 10°C/hr to 750°C. They also synthesized $LaVSb_3$ as a non-magnetic counterpart for comparison. Armed with single crystals, they were able to report the first measurements and analysis of $LaCrSb_3$'s anisotropic magnetic properties, revealing $b$ as the easy magnetic direction, and what appeared to be a second magnetic transition below $T_C$ at $T^* \leq 98\,K$ (strongly field dependent). They were also able to measure anisotropic resistivity and confirmed the transition at $T_C$, but found no corresponding anomaly at $T^*$.

Immediately following Jackson *et al.*'s preliminary characterization measurements, the same single crystals were used in a neutron diffraction study [97]. The neutron results confirmed that the feature at $T^* \leq 98\,K$ was indeed a spin-reorientation, and they also revealed that the magnetic moments tilt away from the $b$ axis towards $c$. This canting results in FM and AFM sublattices which hint that both kinds of magnetic interactions exist in the system. For a physicist interested in exploring quantum criticality, the next question is:

[2] a stance that is heavily reinforced by journal referees, according to UC Santa Cruz Professor Art Ramirez.
[3] with a slight deficit of Sb
[4] muon spin rotation

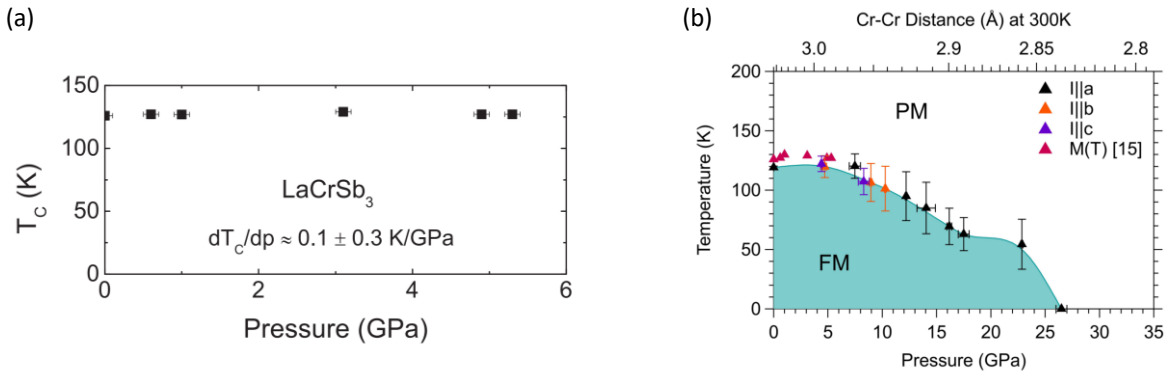


**Figure 3.1:** (a) Lin *et al.* discovered that $T_C$ in $LaCrSb_3$ is barely affected by pressure (Fig. 7(c) in Ref. [11]). (b) Brubaker *et al.* were able to measure features in resistivity up to much higher pressures (Fig. 4 in Ref. [98]). Beyond 6 GPa, $T_C$ is suppressed linearly with pressure. It takes up to 26.5 GPa to fully suppress the FM state. Further investigation of the magnetic state at these high pressures is difficult, so we turned to chemical substitution as a tuning parameter.

how can we suppress the FM interactions while enhancing the AFM interactions?

Pressure and chemical substitution are the tuning parameters available to alter a compound's magnetic state. Although substitutions studies came first chronologically, let me briefly mention pressure. Pressure was first used in an attempt to suppress $LaCrSb_3$'s ferromagnetic state by Lin *et al.* [11]. They used single crystals made with the $8:8-x:x:84$ ratio that would serve as the blueprint for the $LaCr_{1-x}Fe_xSb_3$ project. They were able to apply up to 5.3 GPa, and discovered a surprisingly robust ferromagnetic state with $T_C$ decreasing by less than 0.1 K per GPa. My former colleague, Zach Brubaker, later found that it took up to 26.5 GPa [98] to completely suppress the ferromagnetic state. Figures from these two studies which show the effect of pressure on $T_C$ are reproduced in Fig. 3.1. These incredible pressures make further investigation the region surrounding the suppressed FM state difficult, which is why we chose chemical substitution as our tuning parameter.

Unlike pressure, chemical substitution has reliably altered the magnetic behavior of $LaCrSb_3$. Following the polycrystalline substitution study by Dubenko *et al.* [94] (see Fig. 3.2) were a number of single crystal substitution studies. In 2006, Jackson *et al.* investigated substitution on the rare earth site with RE = Pr, Sm and Gd, in $La_{1-x}RE_xCrSb_3$[99] to study the interactions between 4f local moments and 3d itinerant moments. In each case, a 2nd magnetic transition due to the rare earth element was observed below the Cr ordering temperature. In 2013, Lin *et al.* studied V substitution in single crystal $LaCr_{1-x}V_xSb_3$ [11]. While vanadium and chromium are next to each other on the periodic table, vanadium is non-magnetic. Since Jackson *et al.* [96] proved that single crystals of both $LaCrSb_3$ and $LaVSb_3$ can be grown, at some substitution between the two, magnetism must disappear. With this in mind, V substitution for Cr would appear to be ideal for a scientist asking the question "what happens when ferromagnetism is suppressed?"

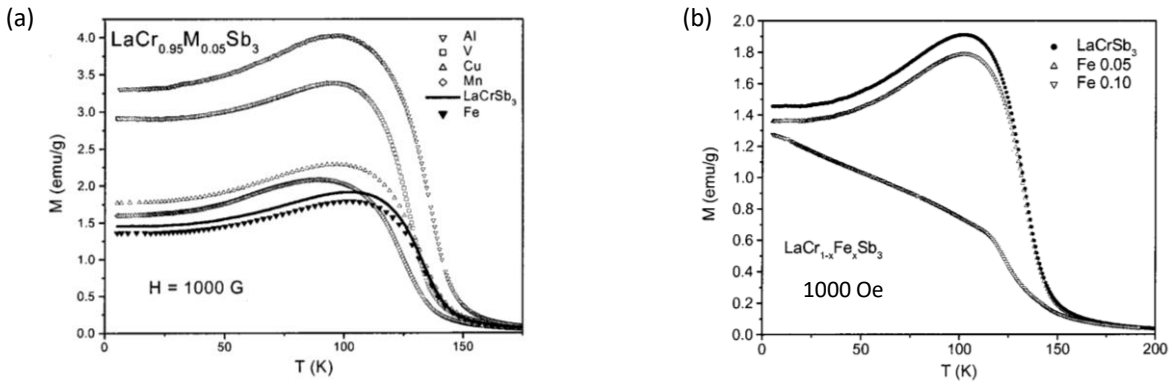


**Figure 3.2:** (a) The $M(T)$ curves for 5% substitutions of Al, V, Cu, Mn and Fe in $LaCrSb_3$ (Fig. 2 in Ref. [94]). Out of these elements, only Fe substitution (bottom curve) lowered the moment. (b) While the nominal 5% Fe substitution resulted in a small decrease in the magnetization, increasing the substitution to 10% dramatically changes the shape of the $M(T)$ curve (Fig. 4 in Ref. [94], field in figure corrected to reflect caption). This polycrystalline substitution study gave us the clue that Fe substitution may lead to a quantum critical point in $LaCrSb_3$.

$T_C$ was found to decrease with V substitution and they found transitions to a potentially 'complex magnetic state,' however, no features consistent with a ferromagnetic quantum critical point were observed. In 2016, Chen *et al.* revisited substitutions on the La site with Sr and Ca and found that both elements suppressed the AFM interactions, eliminating the spin canting and spin reorientation, and resulted in a simplified FM ground state [100].

In summary, over the past 28 years, the $LaCrSb_3$ system has been the subject of a number of investigations. What follows is my contribution to this unusual ferromagnet.

## 3.2 Synthesis

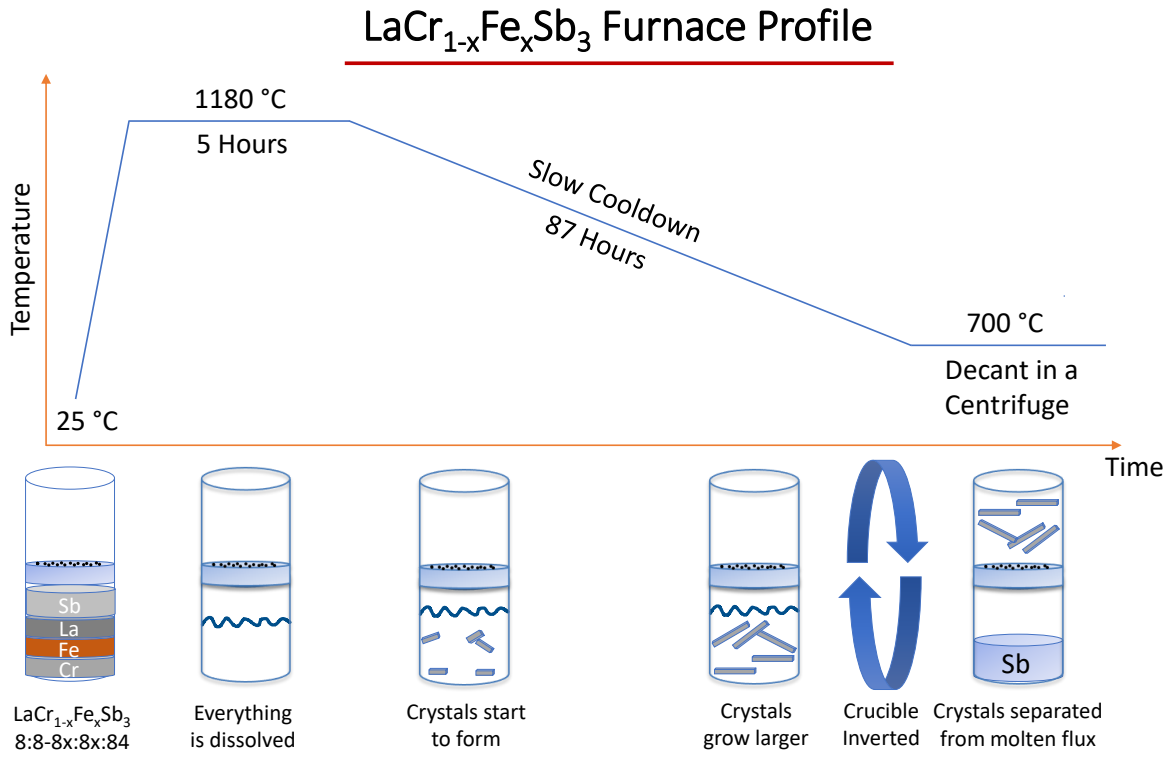


**Figure 3.3:** The temperature profile used to grow single crystals of $LaCr_{1-x}Fe_xSb_3$ based on the profile developed by Lin *et al.* [11]. The major change that we found is the decantation temperature could be lowered to 700°C from 750°C without the risk of the flux freezing. This extra range of temperature may be beneficial to crystal growth. Below the temperature profile, we show a schematic diagram of the different stages of crystal growth.

Single crystals of $LaCr_{1-x}Fe_xSb_3$ were synthesized via a self-flux solution growth technique resembling the one used in Lin *et al.* [11]. We used a non-stoichiometric ratio of $8 : 8-8x : 8x : 84$ of 4N REacton La pieces, 3N Alfa Products Cr plates[5] or 4N Aesar Cr crystallites[6], 4N Alfa Aesar -22 mesh Fe powder, and 5N Alfa Aesar Sb shot. The La pieces were brushed to remove any oxidation on the surface. The high purity elements were placed in a Canfield Crucible Set [15] with high melting temperature elements at the bottom (i.e. from bottom to top: Cr, Fe, La, Sb). The crucible set is sealed in a quartz tube in a 150 mmHg partial pressure of Ar. The sealed ampoule was then heated in a box furnace up to 1180°C, held at 1180°C for 5 hours to ensure complete dissolution, and slowly cooled to 700°C over 87 hours. At 700°C, the ampoule was pulled from the furnace and placed into a centrifuge to separate the excess molten material from the solid crystals. This procedure is diagrammed in Fig. 3.3.

[5] for syntheses $x = 0$, 0.05, 0.1, 0.2, 0.3, 0.4, 0.5, 0.6
[6] for syntheses $x = 0.15$, 0.25, 0.35, 0.45, 0.55

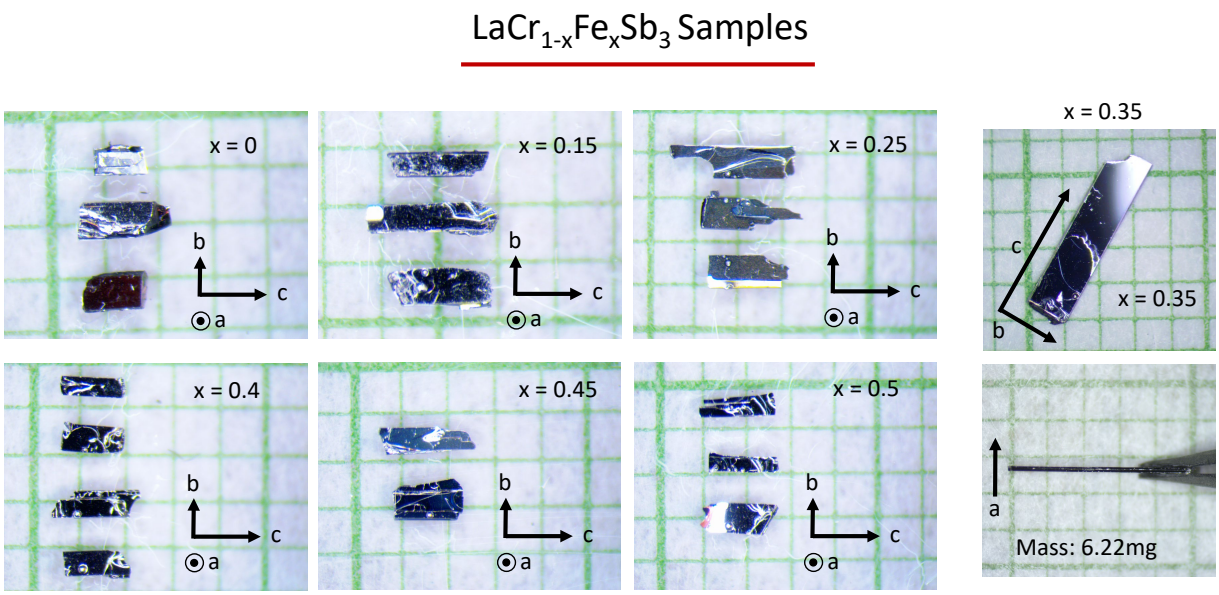


**Figure 3.4:** A selection of averaged sized samples for $x < 0.5$. The crystallographic axes are labelled. An outstandingly large and clean example of $x = 0.35$ is shown. As Fe substitution increases, crystals tend to form flat plates.

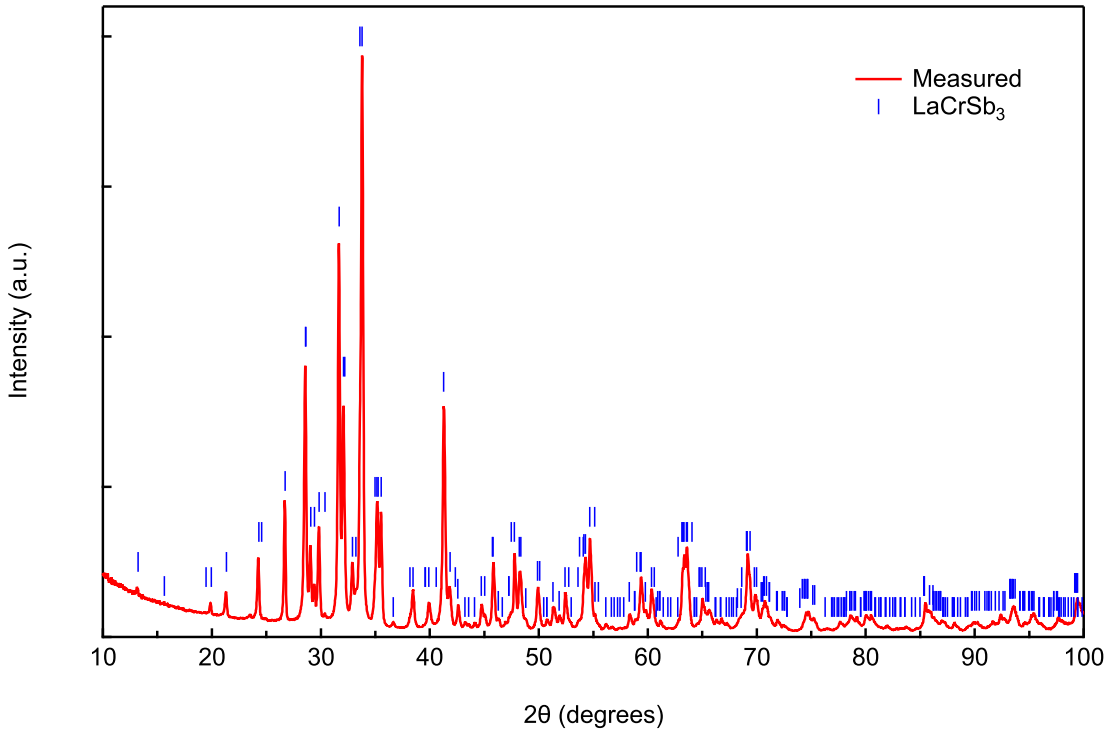


**Figure 3.5:** Powder x-ray diffraction (PXRD) of a selection of $LaCrSb_3$ samples. The red line is the measured data while the blue tick marks indicate the locations of previously reported $LaCrSb_3$ peaks [91].

We performed powder x-ray diffraction (PXRD) in a Rigaku MiniFlex 600 on faceted single crystals from each batch to confirm that the peak locations match those previously reported [91] (see Fig. 3.5). $LaCrSb_3$ crystals form thin rectangles with the long side parallel to the $c$ axis and the short side parallel to the $b$ axis. The thin rectangles stack along the $a$ axis [92]. A selection of crystals from substitutions up to $x = 0.5$ are shown in Fig. 3.4.

## 3.3 Another Case of the Avoidance of Quantum Criticality

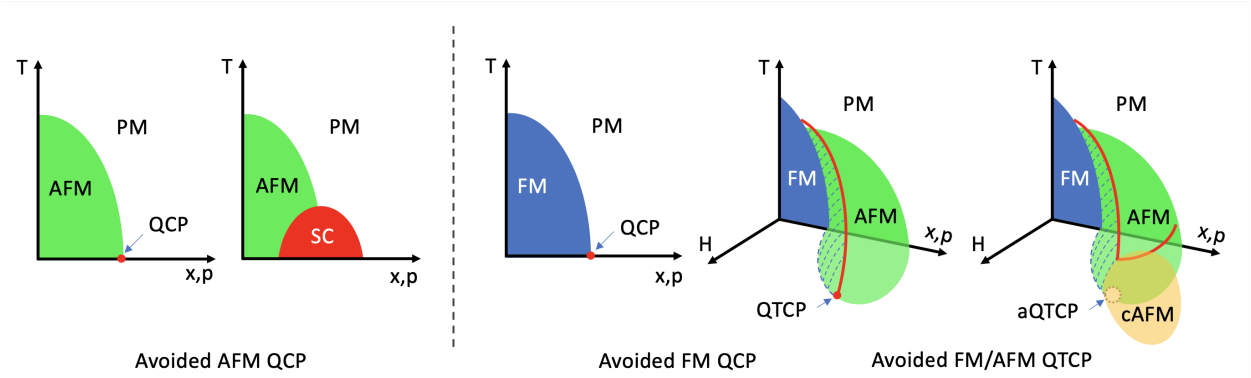


**Figure 3.6:** Antiferromagnetic (AFM) transitions can be suppressed by non-thermal parameters, such as substitution ($x$) or pressure ($p$), to zero temperature terminating at a point known as a quantum critical point (QCP). In many systems, the QCP is avoided by the appearance of new, sometimes superconducting, phases. It is rare, however, for ferromagnetic systems to suppress cleanly to a QCP. More often, the ferromagnetic transition becomes first order and a slew of modulated magnetic phases appear. These AFM phases can have tricritical points (TCP) which separate first and second order AFM to FM transitions. Through further tuning, these TCPs can be suppressed to zero temperature resulting in a quantum TCP (QTCP). In this study we report the avoidance of a QTCP by yet another phase, in this case a canted AFM phase. This discovery contributes an additional option to the seemingly endless possibilities of what can happen in suppressed magnetic systems.

Ferromagnets and antiferromagnets only become magnetic below the Curie temperature ($T_C$) or Néel temperature ($T_N$), respectively. These transition temperatures can be suppressed to lower temperatures by the application of tuning parameters such as magnetic field, chemical substitution, or pressure. With the right tuning parameter, it is sometimes possible to drive these magnetic phase transitions towards a quantum critical point (QCP), that is, a second order phase transition at zero kelvin. The approach of a QCP is often interrupted, however, and what occurs during the suppression of $T_C$ or $T_N$ towards zero temperature is relentlessly fascinating (as shown by the schematic phase diagrams in Fig. 3.6).

The antiferromagnetic (AFM) QCP, for example, is most famously avoided by the appearance of a superconducting dome in the cuprates, Fe-based, and heavy fermion superconductors [101, 102, 103, 104], resulting in the phase diagram sketched in Fig. 3.7(a). These unconventional superconductors have intrigued condensed matter researchers over the past few decades, and they are related by the fact that their superconductivity occurs in the near-QCP region of their phase diagrams.

This discussion is not limited to AFM systems as suppressing ferromagnetic (FM) transitions has also led to the discovery of unique magnetic phase diagrams filled with unexpected behavior and riddled with critical points. Like the AFM QCP, the FM QCP can also be avoided by a superconducting dome [105, 106, 107, 108], but other phenomena are also possible.

As observed in a number of different compounds under pressure ($UGe_2$ [33], $ZrZn_2$ [109], $CoS_2$ [110]),

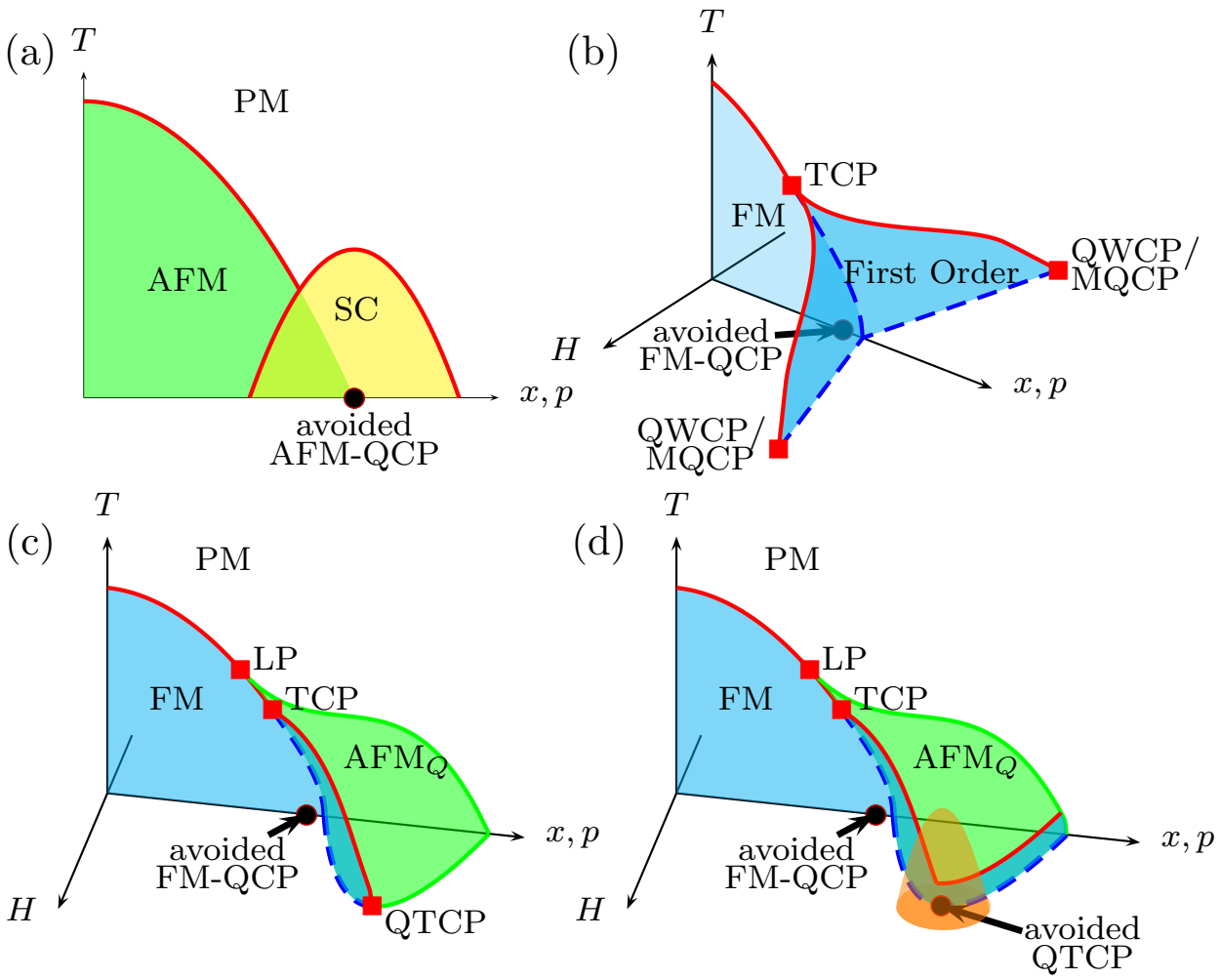


**Figure 3.7:** Schematic phase diagrams of avoided quantum critical points (QCP). (a) Antiferromagnetic (AFM) case with the emergence of superconductivity (SC). (b-d) Ferromagnetic (FM) cases with the emergence of (b) ferromagnetic wings under magnetic field $H$ and the possibility of a quantum wing critical point (QWCP) or a marginal quantum critical point (MQCP), (c) a modulated magnetic phase AFM$_Q$ and the possibility of a quantum tricritical point (QTCP). Panel (d) illustrates the case where the QTCP is avoided: the zero-temperature field-induced transition remains of the first order and a new phase emerges.

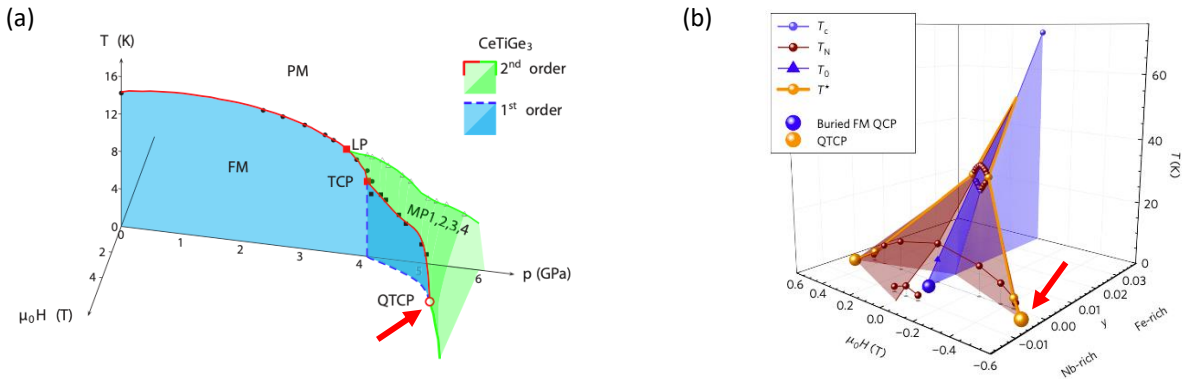


**Figure 3.8:** The red arrows indicate quantum tricritical points (QTCP) reported in (a) $CeTiGe_3$ (Fig. 10 in Ref. [87]) and (b) $Nb_{1-y}Fe_{2+y}$ (Fig. 5 in Ref. [88]). (a) The suppression of ferromagnetism in $CeTiGe_3$ is achieved by pressure, which complicates the further investigation of the new magnetic phases shown in green. (b) There is an extremely limited range of substitution in the $Nb_{1-y}Fe_{2+y}$ system. Only three samples were grown with small values of $y$: $Nb_{0.985}Fe_{2.015}$, $NbFe_2$, and $Nb_{1.01}Fe_{1.99}$. Furthermore, a second order phase transition at low temperatures was never observed. On the other hand, the FM state in $LaCrSb_3$ is suppressed by Fe-substitution enabling multiprobe studies of the compound unencumbered by the complications associated with high pressures. In addition, we show that a wide range of substitutions can be grown.

the PM-FM transition, typically the classic example of a second order phase transition, becomes first order at a tricritical point. In such a case, quantum criticality is not completely suppressed and can reappear under magnetic field. When magnetic field is applied along the easy axis of magnetization, tricritical wings emerge, as illustrated in Fig. 3.7(b) [111, 109, 33, 112]. The wings are bounded by second order lines that can terminate at zero kelvin at quantum wing critical points (QWCPs). In contrast to a QCP, no symmetry is broken at a QWCP. If the wing is accompanied by a Lifshitz transition, it will terminate at a marginal quantum critical point (MQCP) [113, 114].

The FM QCP can also be avoided by the appearance of an antiferromagnetic phase ($AFM_Q$) [111, 115, 116, 117, 118, 119, 18, 87, 120, 121, 122, 123, 124, 125]. The avoidance of the FM QCP by tricritical wings or by the appearance of an $AFM_Q$ phase is theoretically expected to be a generic result for metallic quantum ferromagnets [126, 21, 127, 22, 23, 128, 111, 27, 129], with the exception of systems that are noncentrosymmetric (theory [130], experiment with $CeRh_6Ge_4$ [131, 132, 133]) or have disorder (theory [134], experiment with (Mn,Fe)Si [135]).

Regarding the avoidance of the FM QCP by an $AFM_Q$ phase, yet another type of quantum criticality is possible: there could be a quantum tricritical point (QTCP) as depicted in Fig. 3.7(c) [88, 87, 136, 137, 138, 139, 140], where the zero-temperature transition from $AFM_Q$ to a field-polarized state changes from the first to the second order. At a QTCP, both FM and AFM fluctuations are expected to diverge simultaneously, so such systems would be ideal platforms for studying the interplay between these two spin correlations. In contrast to FM or AFM QCPs, few studies are aimed at approaching QTCPs. To date, only two systems have

been shown to have a QTCP: $NbFe_2$ by finely tuning the Nb-Fe ratio [88] and in $CeTiGe_3$ by applying high pressure [87] (the phase diagrams for these compounds are reproduced in Fig. 3.8). In both of these cases, however, further multiprobe investigation is limited by their experimentally restrictive tuning parameters, so the possibility remains that the QTCP is also avoided. That is, the zero-temperature field-induced transition remains of the first order and that new phases appear as illustrated in Fig. 3.7(d).

In this section of my thesis, I will report on a new system that is easily tunable towards a QTCP. We study the Fe-substituted $LaCrSb_3$ system, and demonstrate that a QTCP is approached, but ultimately avoided, continuing the trend of discovery of novel magnetic phase diagrams in suppressed FM systems. In addition, we were able to demonstrate the benefit of using chemical substitution instead of pressure for easier investigation of the magnetic order by using neutron diffraction to identify the canted AFM (cAFM) magnetic phase that appears above the putative QTCP. This experiment is the first example of an avoided QTCP, and provides further support for the idea that quantum criticality is ubiquitously avoided.

$LaCrSb_3$ is a ferromagnet ($T_C \sim 125\,K$ [141], orthorhombic crystal structure: *Pbcm* No. 57) with intricate magnetic properties. It does not obey the Curie-Weiss law above $T_C$ and has a smaller saturation moment than free ionic Cr suggesting some degree of itinerant magnetism [92, 93, 142, 96]. Giant anomalous Hall conductivity was recently reported and arises from Cr-d dominated nearly dispersionless bands in the vicinity of the Fermi level [143, 144]. Neutron diffraction revealed the spontaneous reorientation of moments from $c$ to $b$ at $T_{SR} = 95\,K$. We will refer to the ground state phase as $FM_b$, although there is a small AFM component resulting in a tilt (18°) of the moments towards the $c$-axis which subsists at least up to 7 T [97]. The complicated magnetic structure of $LaCrSb_3$, involving both FM and AFM interactions, makes it a natural candidate for achieving a QTCP.

While hydrostatic pressure is considered a 'clean' tuning parameter compared to chemical substitution, the ferromagnetism of $LaCrSb_3$ is particularly robust to pressure. Pressure had no effect on $T_C$ up to $p = 6\,GPa$ [11] and up to $p = 26.5\,GPa$ is required to fully suppress the FM state [98]. On the other hand, the magnetic order can be modified by various chemical substitutions [94, 99, 11, 100]. In particular, studies on polycrystalline samples of $LaCr_{1-x}R_xSb_3$ observed a reduction in saturation magnetization and $T_C$ in samples with $R$ = V, Mn, Fe, Cu [94]. Given that Fe often enhances FM interactions, it is somewhat counterintuitive that Fe substitution causes the most dramatic change in the magnetization and appears to strengthen AFM interactions in this system [94] ( Fig. 3.2). To build on these preliminary polycrystalline measurements, we decided to grow single crystals of $LaCr_{1-x}Fe_xSb_3$ to see what better samples and additional measurements could reveal about this unconventional magnet's journey towards quantum criticality.

Here, we report the synthesis of single crystal $LaCr_{1-x}Fe_xSb_3$ with nominal substitutions between $x = 0$ and $x = 0.6$ in steps of 0.05, perform a comprehensive study of their bulk magnetic properties, and map

the temperature-chemical substitution-magnetic field ($T-x-H$) phase diagram. Fe-substitution suppresses $T_{\mathrm{C}}$, however, an FM-QCP is avoided by the appearance of a tricritical point (TCP) at which the PM-FM transition becomes of the first order and by the appearance of an AFM phase. The TCP can be driven to lower temperatures upon increasing Fe content and magnetic field. A QTCP, however, is avoided by the transition remaining first order and the appearance of a new canted magnetic phase (cAFM). The phase diagram of $LaCr_{1-x}Fe_xSb_3$ is the first to showcase the possibility that a QTCP can be avoided, and also provides a roadmap for discovering magnetic canting in other materials due to the emergence of a cAFM phase near an avoided FM-AFM QTCP.

### 3.3.1 Phase Diagram

Figure 3.9(a) shows the $T-x$ phase diagram of $LaCr_{1-x}Fe_xSb_3$ determined from low-field (0.1 T) $M(T)$ measurements which are consistent with zero field $\rho(T)$ (Section 3.4.4, Fig. 3.27). When $x \leq 0.15$, the ground state is $FM_b$ (refer to Fig. 3.9(b)). As substitution is increased, the FM transition becomes of the first order (Section 3.4.3). When $x \geq 0.2$, the $M(T)$ curve exhibits a precipitous downturn in $M_b$ indicating the appearance of an $AFM_b$ state where the $b$ component of the moments are now antiferromagnetically aligned (see Fig. 3.9(c)). We determined the magnetic structure of the $AFM_b$ phase by neutron diffraction (Section 3.4.2). The easy moment direction changes to the $a$-axis for $x > 0.5$ ($AFM_a$) (see Fig. 3.9(d)).

The TCP at which the FM transition changes from second to first order exists at zero magnetic field, but is better revealed under applied field. Figure 3.10(a) shows $M(H)$ curves for $x = 0.2$. At low temperatures, the spin-flip transition between the $AFM_b$ and polarized $FM_b$ states exhibits hysteresis indicating the first order nature of the transition. This hysteresis is also observed in $\rho(H)$ (Fig. 3.28). Increasing the temperature causes the magnitude of the hysteresis to diminish. The hysteresis vanishes at 80 K, taken as the temperature of the TCP ($T_{TCP}$). The temperature dependence of the hysteresis for $0.2 \leq x \leq 0.5$ is shown in Fig. 3.10(b). With increasing $x$, the hysteresis is reduced and the temperature at which the hysteresis disappears shifts to lower temperature, indicating a decrease of $T_{TCP}$. Figure 3.10(c) shows $T_{TCP}$ as a function of $x$ and reveals an almost perfectly linear trend towards zero temperature where a QTCP is expected to occur. If a QTCP were to exist in the $LaCr_{1-x}Fe_xSb_3$ system, substitutions beyond the $x$ of the QTCP are expected to have a line of AFM-QCPs without hysteresis (see Fig. 3.7(c)). Instead, for $x > 0.4$, the hysteresis remains and $T_{TCP}$ slowly increases, indicating the persistence of a first order transition and therefore the avoidance of a QTCP.

Figure 3.10(c) also depicts the canted AFM (cAFM) phase surrounding the tricritical line. The orange region in Fig. 3.10(d) defines the cAFM phase, which is characterized by a region of linearly increasing

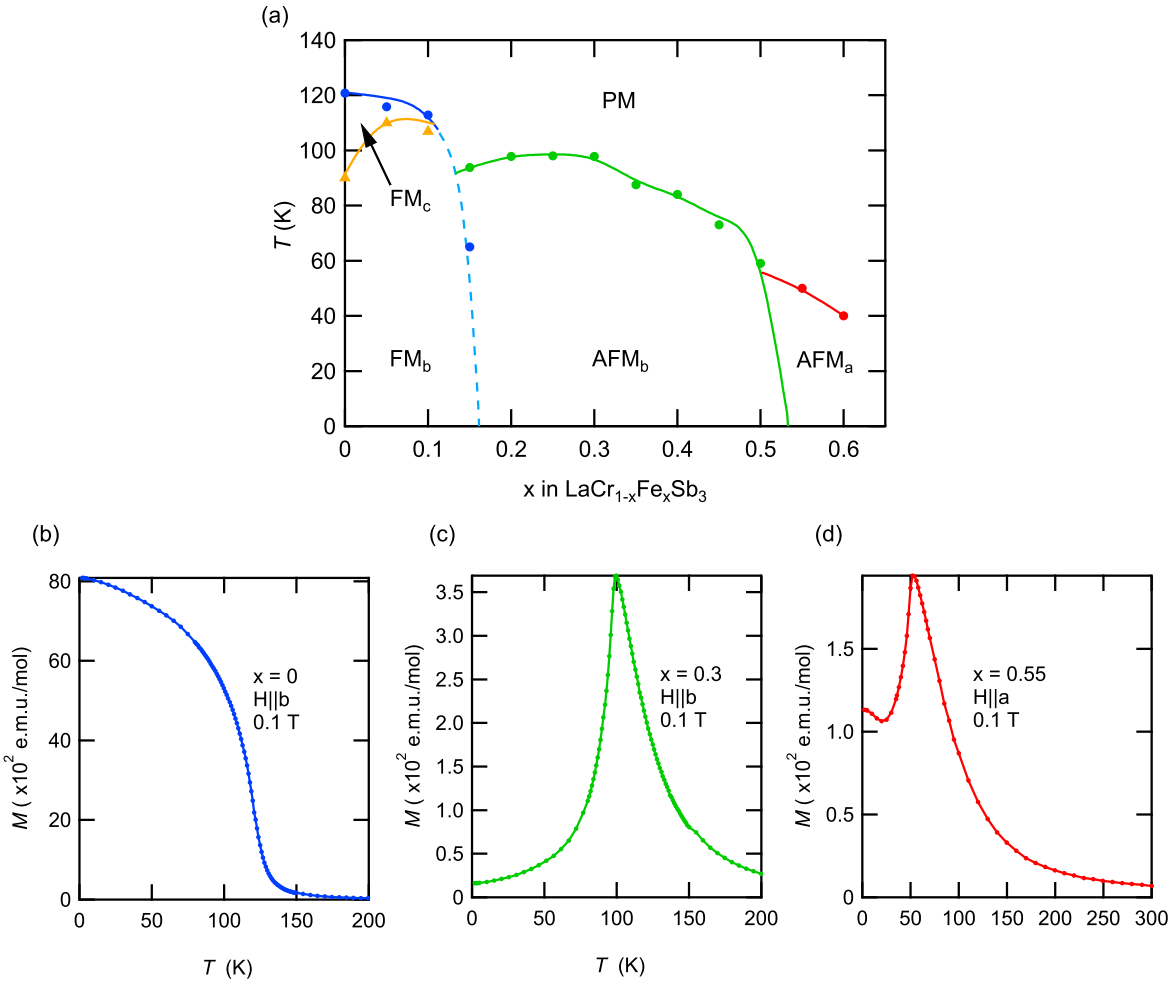


**Figure 3.9:** (a) The temperature vs Fe-substitution phase diagram. The lines are guides to the eye. (b) Representative $M(T)$ curves of the FM$_b$, AFM$_b$, and AFM$_a$ phases measured at $\mu_0 H = 0.1$ T. Up to $x = 0.1$, there is only a small decrease in $T_C$. As substitution is increased, the magnetism in the system changes dramatically. First, the PM-FM transition evolves from second order (solid blue line) to first order (dashed light blue line). (c) Starting around $x = 0.15$, an antiferromagnetic phase appears. This AFM$_b$ state continues through $x = 0.5$. (d) At substitutions higher than $x = 0.5$, yet another magnetic phase appears which preliminary measurements indicate is a modulated magnetic phase along $a$, AFM$_a$. Samples with substitution greater than $x = 0.6$ have yet to be grown.

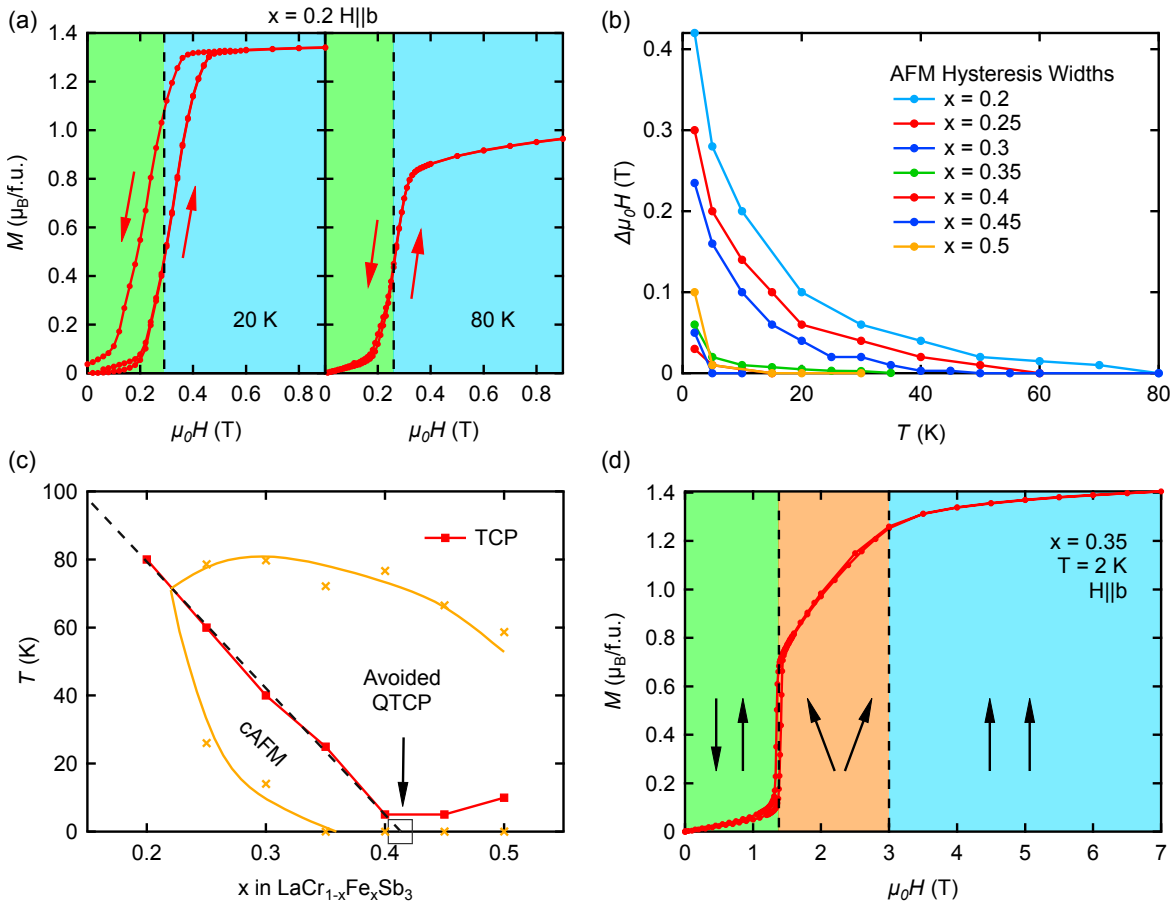


**Figure 3.10:** (a) Magnetization as a function of applied magnetic field, $M(H)$, at 20 K and 80 K for $x = 0.2$. Red arrows indicate increasing and decreasing field directions. Green and blue regions indicate the antiferromagnetic ($AFM_b$) and ferromagnetic ($FM_b$) phases, respectively. (b) The hysteresis widths extracted from similar $M(H)$ measurements as a function of temperature for different $x$ values. (c) Red squares indicate the $x$ dependence of the temperature of the tricritical point (TCP). The position of the avoided QTCP is marked by the black open square. Orange crosses represent the maximum and minimum temperature between which the cAFM phase is observed. Each point is observed at a different field. (d) $M(H)$ at 2 K for $x = 0.35$. The green, orange, and blue regions denote the $AFM_b$, cAFM, and $FM_b$ phases, respectively. Black arrows schematically represent the alignment of magnetic moments in each region.

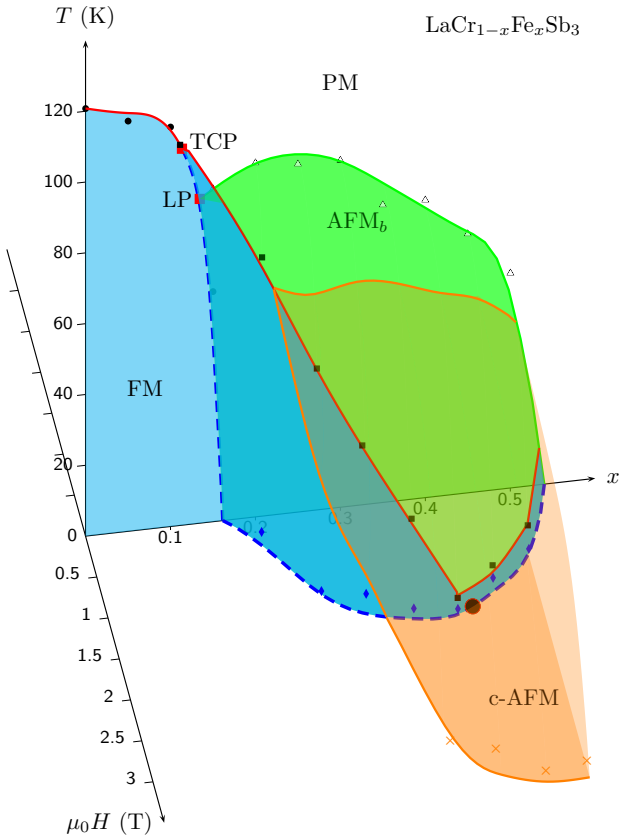


**Figure 3.11:** The temperature-chemical substitution-magnetic field ($T-x-H$) phase diagram for the $LaCr_{1-x}Fe_xSb_3$ system. The green and orange domes enclose the $AFM_b$ and cAFM phases, respectively. The dashed blue line indicates a first order transition. The black squares denote tricritical points (TCPs) which are joined by the red tricritical line. The large black dot is a placeholder for the putative position of the avoided QTCP.

$M(H)$ between the $AFM_b$ and $FM_b$ states. The cAFM state also appears as a broad bump in $\rho(H)$ (refer to Fig. 3.15(a)), as well as a kink in the $M(T)$ curve (refer to Fig. 3.15(b)). The alignment of the magnetic moments in these different phases was determined by neutron diffraction (Section 3.4.2) and is shown schematically by the black arrows. While the hysteresis and $T_{TCP}$ diminish with increasing $x$ up to $x = 0.4$, the cAFM phase expands and appears to bury the putative QTCP.

The resulting three-dimensional $T-x-H$ phase diagram of $LaCr_{1-x}Fe_xSb_3$ is shown in Fig. 3.11. The $T-H$ phase diagrams that were compiled to create this three-dimensional phase diagram are shown in Fig. 3.12 of Section 3.4. From these phase diagrams, as well as the $M(H)$ curves, we can see the increasing size of the cAFM dome as substitution is increased. Although a cAFM phase can be viewed as a combination of FM and AFM orders, it is interesting to note that the cAFM phase is not observed at low fields near the boundary between the FM and AFM regions. Instead, it only emerges near the tricritical line, when the TCP is driven towards lower temperatures. This observation suggests that the cAFM dome originates from the putative QTCP, even though the latter is ultimately avoided.

### 3.3.2 Discussion

The magnetic phase diagram of $LaCr_{1-x}Fe_xSb_3$ shows an FM QCP avoided by a first order FM transition and the subsequent appearance of a modulated magnetic phase. Both features have been observed experimentally in other compounds (CeRuPO [117], $LaCrGe_3$ [18]) and studied theoretically [127, 111, 129, 136]. While the avoidance of an FM QCP by these features is common, follow up investigation of these interesting regions of phase space in the $LaCr_{1-x}Fe_xSb_3$ system benefits from being tuned with chemical substitution rather than the application of pressure required by the aforementioned compounds. As an example, we were able to use neutron diffraction to determine the magnetic structure (Section 3.4.2) whereas there is an inherent difficulty in performing neutron diffraction under pressure. Furthermore, since $LaCr_{1-x}Fe_xSb_3$ yields relatively large single crystals in a wide range of $x$, it may be an ideal platform for a multi-probe investigation of 1st order FM phase transitions (Section 3.4.3) and of the region surrounding the avoided QTCP.

$LaCr_{1-x}Fe_xSb_3$ is the first example of an avoided QTCP. Previous experiments have suggested the existence of a QTCP in $Nb_{1-y}Fe_{2+y}$ [88] and $CeTiGe_3$ [87]. In the case of $CeTiGe_3$, the complication of pressure limited their study to tracking features exclusively in resistivity, obscuring the nature of the multiple magnetic phases observed near the reported QTCP. In $Nb_{1-y}Fe_{2+y}$, a second order transition at low temperatures was never actually observed, and the QTCP was extrapolated due to the restrictive range of substitution afforded by the binary. $LaCr_{1-x}Fe_xSb_3$ overcomes these limitations, and we introduce the new possibility that a QTCP is never actually realized. With this new possibility in mind, and with restrictive tuning parameters that make studies in the proximity of the QTCP difficult, it is possible that the QTCP is also avoided $Nb_{1-y}Fe_{2+y}$ and $CeTiGe_3$.

The scenario in which achieving quantum criticality was initially reported, but later found to be avoided, has occurred for both AFM and FM-QCPs. For a long time, $YbRh_2Si_2$ was believed to be a clear example of an AFM-QCP [145, 146]; then a superconducting phase was discovered in place of the QCP upon reaching temperatures below $T = 2\,\mathrm{mK}$ [147, 148]. $ZrZn_2$ was once believed to be a clear example of an FM-QCP [149], until tricritical wings were observed upon reaching lower temperatures in higher quality samples [109, 150, 112, 151]. If samples beyond $x = 0.4$ were not produced, or if the hysteresis in the AFM-FM transition did not appear above $T = 2\,\mathrm{K}$, or if magnetization and neutron measurements revealing the cAFM phase could not be performed easily, one would also have concluded the existence of a QTCP in $LaCr_{1-x}Fe_xSb_3$.

Given the prevalence of cases where QCPs in AFM and FM systems are avoided, one can wonder whether the avoidance of the QTCP reported here is a general feature of nature. The mechanism behind the emergence of superconductivity near quantum critical points remains unknown. In the case of the appearance of $AFM_Q$ phases instead of FM QCPs, the importance of quantum effects [126, 127, 21, 22, 23, 24], the influence of

magnetic anisotropy [23, 118], or specific band structure features have been proposed [152, 153, 27], but distinguishing between them is difficult [22]. The fact that some of these phases subsist up to relatively high temperatures is at odds with a purely quantum effect. However, we note that superconductivity in the cuprates and Fe-based superconductors is observed at significantly higher temperature than in organic or heavy fermion superconductors, indicating that quantum effects can dominate over a wide range of energies. In the case of the cAFM phase observed here, it is likely that multiple effects contribute simultaneously to the avoidance of quantum criticality. Further studies will tell whether a QTCP can be obtained under special crystalline symmetries or disorder, as proposed for FM-QCP [130, 131, 132, 134, 135].

All of this is not to say that the avoidance of a QTCP in La(Cr,Fe)$Sb_3$ and the possible avoidance of a QTCP in $Nb_{1-y}Fe_{2+y}$, $CeTiGe_3$ or future systems with approached QTCPs are any less interesting. As we have repeatedly observed, the behaviors (1st order FM, non-Fermi liquid) and phases (modulated magnetic, superconductivity) that surround the elusive FM QCP are captivating. Perhaps the same will apply to the QTCP. In the case of La(Cr,Fe)$Sb_3$, we observe the emergence of a cAFM phase. While this canted spin state has both FM and AFM components,[7] as mentioned previously, it does not appear at the boundary between the $FM_b$ and $AFM_b$ states ($x \approx 0.15$), rather, the cAFM state only appears around the tricritical line as it is suppressed to lower temperatures. This is evidence that the cAFM state is related to the avoidance of the QTCP, rather than competition between, for example, the Cr and Fe competing for magnetic order.

While not as exciting as superconductivity, magnetic canting has recently attracted attention as a way to tune the anomalous Hall effect (AHE). Unlike pure AFM and FM states, cAFM states have a spin structure that can be tuned continuously by an external magnetic field [154]. Therefore, cAFM states may exhibit control of the AHE due to the scaling relation of the AHE with magnetization [155, 156]. Canted spin states may also induce a chiral Hall effect and corresponding chiral magneto-optical effects [157]. Non-collinear antiferromagnets can display an intrinsic AHE from nonzero Berry curvature [158]. When the canting is small, the sign of the Hall effect can be switched easily, which could enable new spintronic applications [159]. The canted magnetization also gives rise to novel magneto-thermoelectric effects [160]. The phase diagram of La(Cr,Fe)$Sb_3$ where the emergence of a cAFM phase is observed in the vicinity of a FM-AFM QTCP provides a general guide to induce magnetic canting in other magnetic materials. In the past, the pursuit of AFM-QCP led to the discovery of unconventional superconductivity. Similarly, our results show that following the FM-AFM tricritical line can lead to the discovery of complex spin-textures.

[7] The canted spin state can be achieved by considering an AFM interaction at odds with magnetocrystalline anisotropy and Zeeman energy. This is discussed further in Section 3.4.5.

## 3.4 How to Build a Magnetic Phase Diagram

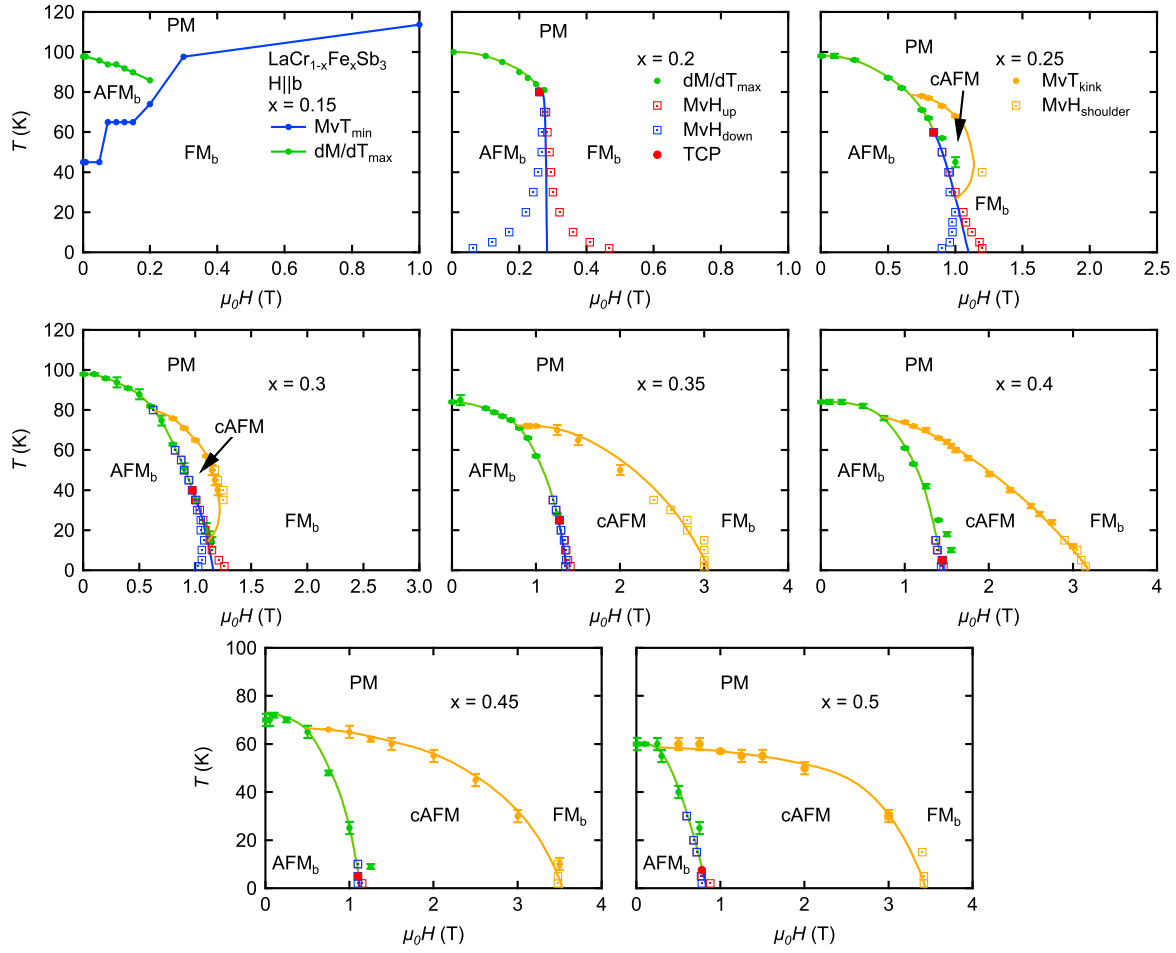


**Figure 3.12:** The temperature versus applied magnetic field phase diagram for $LaCr_{1-x}Fe_xSb_3$ $x = 0.15$ through $x = 0.5$ with $H||b$. The lines are guides to the eye. The green line indicates a second order phase transition, while the blue line indicates a first order phase transition. These two lines meet at the tricritical point, denoted by the red circle.

Constructing a magnetic phase diagram is simply about identifying features in measurements that reflect a change in state. The novel three-dimensional $T$–$x$–$H$ magnetic phase diagram $LaCr_{1-x}Fe_xSb_3$ presented in Fig. 3.11 was built by keeping track of specific features in magnetization measurements that correspond to a phase transition between magnetic states. In this section, I will deconstruct that phase diagram to reveal how exactly it was constructed.

We begin by holding the substitution ($x$) constant and looking at the magnetic behavior at different points in temperature-field $(T, H)$ space. The $T$ v. $H$ diagrams for substitutions $x \geq 0.15$ are presented in Fig. 3.12. These are the $T$ v. $H$ slices that were compiled to make the $T$–$x$–$H$ phase diagram in Fig. 3.11. These diagrams show at what temperature and field the AFM$_b$, cAFM, and FM$_b$ phases begin and end. They

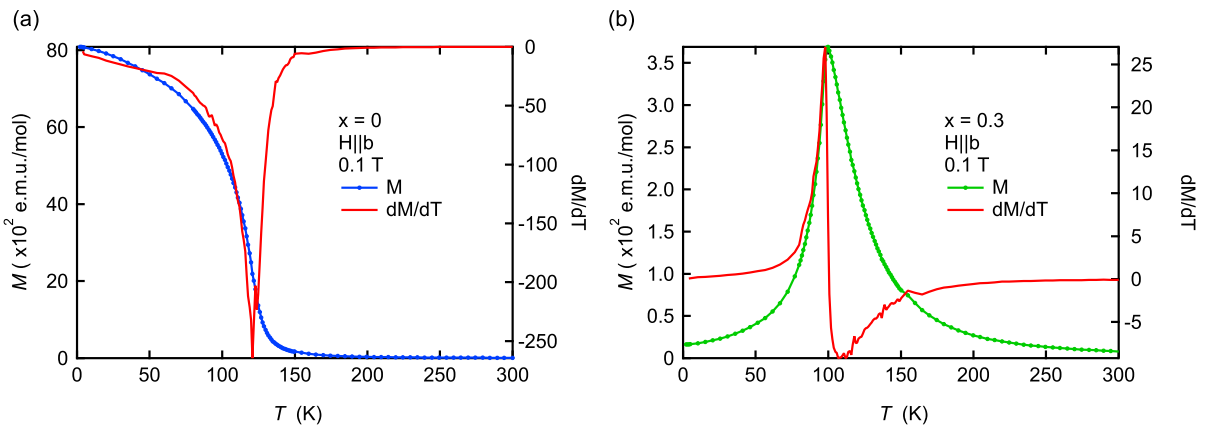


**Figure 3.13:** (a) For substitutions with an FM ground state ($x \leq 0.15$), the Curie temperature is determined by the $dM_b/dT$ minimum (red line) that signifies the steepest increase in $M_b$ (blue dots). (b) For substitutions with an AFM ground state ($x \geq 0.2$), the Néel temperature is determined by the $dM_b/dT$ maximum (red line) signifying the steepest decrease in $M_b$ (green dots).

also show the approach of a quantum tricritical point, as evident by the red dot which indicates the tricritical point appearing at lower temperatures as substitution is increased. In addition, these slices perhaps better show that the cAFM phase emerges from the tricritical point. The data points that make up these phase diagrams were determined as follows.

The blue dots indicate a phase transition to a ferromagnetic phase, i.e., a $T_C$. These points are determined by a minimum in the temperature derivative of the magnetization ($dM_b/dT$) which reflects the sharpest increase in $M$ at a given field during a field-cooled $M(T)$ measurement. This criterion is shown in Fig. 3.13(a), and was also shown to match a feature in resistivity (see Fig. 3.27). Only the $x = 0.15$ substitution has an FM ground state out of the substitutions shown in Fig. 3.12, and there, $T_C$ increases with field.

The green dots signify a phase transition to an antiferromagnetic phase, i.e., a $T_N$. These are determined by a maximum in the temperature derivative of the magnetization ($dM_b/dT$) which corresponds to the sharpest decrease in $M$ at a given field during a field-cooled $M(T)$ measurement.[8] This criterion is specifically shown in Fig. 3.13(b), and was also shown to match a feature in resistivity (see Fig. 3.27). $T_N$ decreases with increasing field and the antiferromagnetic transition is completely suppressed beyond a critical field (the $x$ intercept in Fig. 3.12).

The red and blue open squares signify the midpoints of the transitions between the AFM$_b$ to polarized FM$_b$ ($x < 0.35$) or AFM$_b$ to cAFM ($x \geq 0.35$) states upon increasing field and decreasing field, respectively. These points are determined from isothermal $M(H)$ measurements, and the particular criteria is shown

[8]That is not to say all steep drops in magnetization are due to an antiferromagnetic transition. Such drops in magnetization could be due to a spin reorientation, like that observed in $M_c$ in $LaCrSb_3$ or perhaps due to the sudden depinning of magnetic domains as I discussed extensively in Section 2.3. It is also misleading when researchers mention the possibility of an antiferromagnetic transition when referencing zero-field-cooled magnetization data. On its own, ZFC measurements should only be used to determine the existence of ferromagnetic domains.

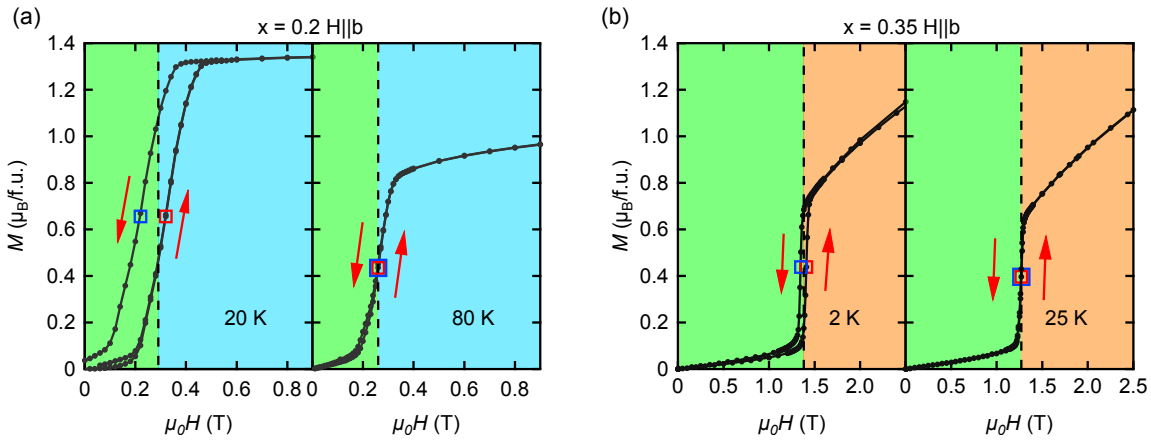


**Figure 3.14:** To measure the hysteresis of the (a) spin flip ($AFM_b$ to $FM_b$, $x = 0.2$ shown as an example) and (b) spin flop ($AFM_b$ to cAFM, $x = 0.35$ shown as an example) transitions, we find the midpoints in $M$ (i.e. $M_s/2$ for the spin flip case) of the transitions during increasing field (red open square) and decreasing field (blue open square). These symbols are the same ones used in the $T$ v. $H$ phase diagrams in Fig. 3.12. As shown in the right panel of each figure, increasing the temperature causes the hysteresis to diminish until it disappears completely, as shown by the overlap of of the red and blue squares. The dashed lines are used to separate the $AFM_b$ (green), $FM_b$ (light blue) and cAFM (orange) phases.

in Fig. 3.14. These are arguably the most important feature of the phase diagrams because they lay the foundation for the detection of tricritical points. The separation between the red and blue open squares is due to hysteresis indicative of a first order phase transition. By increasing temperature, the hysteresis decreases as seen by the merging of these points in Fig. 3.12 for $x \geq 0.2$. The overlap of these points indicates the disappearance of hysteresis and therefore the second order nature of the phase transition. We mark the lowest temperature at which these points merge with a red dot to signify the tricritical point (TCP) which indicates a transition between a first order phase transition and a second order phase transition.

Next, I will explain the criteria for the cAFM phase that emerges as the TCP is suppressed to lower temperatures. The golden dots originate from a distinct shoulder in the $M(T)$ curve as indicated by the black arrows in Fig. 3.15(b). This shoulder only starts to appear at fields above $1\,T$, and can be accompanied by a subsequent AFM transition for fields below 1.5 T. These golden dots form the high temperature region of the cAFM dome. At lower temperatures and higher fields, however, this criterion breaks down as it becomes difficult to distinguish a shoulder in the increasingly FM-like $M(T)$ curve. The lower temperature region is completed by the open gold squares which originate from the $M(H)$ measurement shown in Fig. 3.15(a). In $M(H)$, the cAFM state is characterized by a region of linearly increasing $M$, and the open gold square marks the change in slope when $M$ begins to saturate.

By now, there should be no mystery how the points on the phase diagram are either the result of an $M(T)$ measurement taken at a certain field, or an $M(H)$ measurement taken at a certain temperature. By keeping

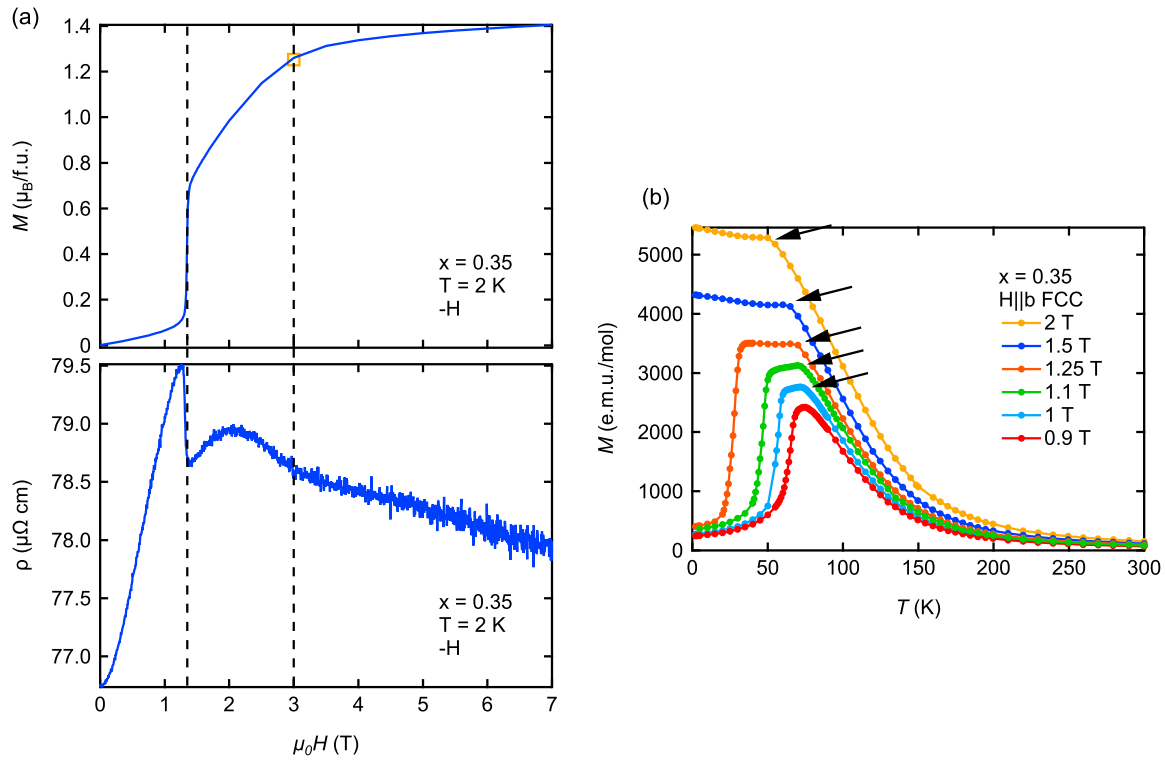


**Figure 3.15:** The open gold squares in the $T$ v. $H_b$ phase diagrams indicate the field induces transition between the cAFM and $FM_b$ states. (a) The cAFM phase is defined by a region of linearly increasing $M(H)$, and there is a change of slope when the cAFM-$FM_b$ transition occurs. In $\rho(H)$ the cAFM phase presents as a dome and there is also a change in slope when the cAFM-$FM_b$ transition occurs. (b) The golden dots in the $T$ v. $H_b$ phase diagrams come from a shoulder in the $M(T)$ curve as indicated by the black arrows. While the transition to the $AFM_b$ phase disappears at fields above $\approx 1.25\,\mathrm{T}$, the shoulder persists to much higher fields.

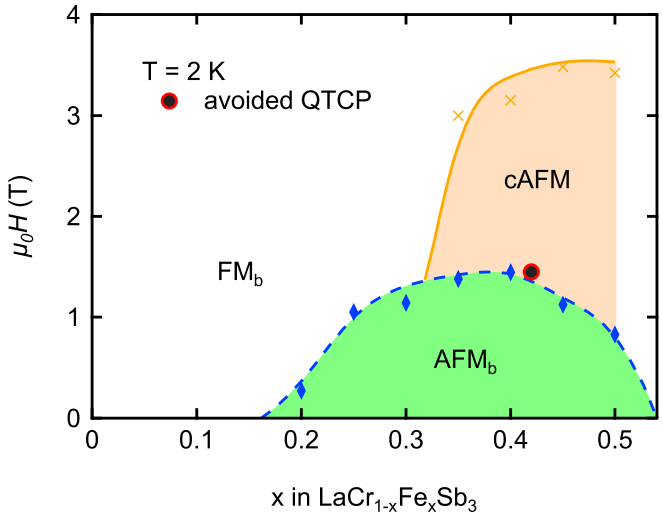


**Figure 3.16:** The applied magnetic field versus chemical substitution phase diagram at $T = 2\,\mathrm{K}$. The dashed blue line denotes a first order phase transition from the AFM$_b$ state to the FM$_b$ or cAFM states.

track of features like these, we can map where and how the transitions between magnetic states occur, and also attempt to solve what happens when ferromagnetism is suppressed. In the case of the La(Cr,Fe)Sb$_3$ system, we found the magnetic phase diagram is of a new type featuring an avoided quantum tricritical point. This phase diagram adds to the handful of prototypical magnetic phase diagrams illustrated in Fig. 3.7, and it will be exciting to see if more materials fit this mold, or what new magnetic phase diagrams will be revealed in the future. Next, I will show additional phase diagrams and magnetization data that are relevant to this system's magnetic behavior.

### 3.4.1 Additional Phase Diagrams and Magnetization Data

To help clarify the zero temperature $H-x$ plane of the $T-x-H$ phase diagram Fig. 3.11 we show the $H-x$ phase diagram in Fig. 3.16. The data points were taken from $M(H)$ measurements taken at 2 K. The golden crosses were determined by the same criteria as the open gold squares mentioned previously. Since the AFM$_b$ to FM$_b$ (or cAFM) transition exhibits hysteresis for all substitutions at 2 K, the blue diamonds represent the mean applied field of the transition, that is, the field marked by the black dashed line in Fig. 3.14.

Substitutions $x \leq 0.1$ were omitted from Fig. 3.12 since they have an FM$_b$ ground state, and therefore applying a field $H||b$ does not reveal any interesting features (there is no dome formed since the state is always FM$_b$). Substitutions through $x = 0.1$, however, preserve the spin reorientation feature seen in LaCrSb$_3$ in which spins aligned along the $c$ axis below $T_C$ reorient to align along $b$ at $T_{SR}$. In the $T$ v. $H$ diagrams with $H||c$ (Fig. 3.17), Fe substitution increases $T_{SR}$, as well as the $H||c$ necessary to break the FM$_b$ state.

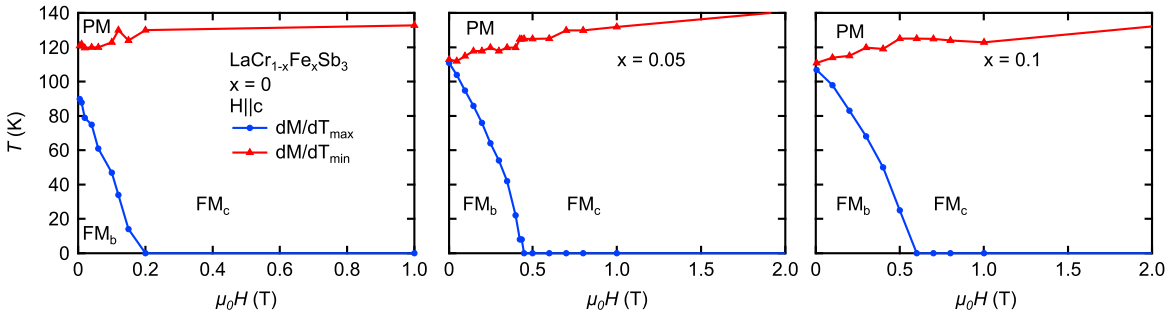


**Figure 3.17:** The temperature versus applied magnetic field phase diagram for $LaCr_{1-x}Fe_xSb_3$ through $x = 0.1$ with $H||c$. The blue dots that encompass the $FM_b$ state indicate the spin reorientation to or from $FM_c$.

In Fig. 3.18 we present $M(T)$ along each of the three crystal axes of $LaCr_{1-x}Fe_xSb_3$ for samples $x = 0$ through $x = 0.55$. The measurements were performed in an applied magnetic field of 0.1 T using a field-cooled-cooling procedure unless otherwise specified. For substitutions through $x = 0.1$, the spin reorientation is seen as a distinct drop in $M_c$ (see top row of Fig. 3.18).

At $x = 0.15$, the spin reorientation is no longer present and two features indicating an evolution of the magnetic state appear. The first is a sharp drop in $M_b$ near 96 K coupled with small decreases in $M_a$ and $M_c$. These features are consistent with an antiferromagnetic component along $b$ and suggest a strengthening of AFM interactions in the system. Following the downturn in $M_b$ is the first order FM transition discussed in Section 3.4.3.

From $x = 0.2$ to $x = 0.5$, $M_b$ exhibits a pronounced downturn to nearly its high temperature value while $M_a$ and $M_c$ also decrease at the same temperature. We confirmed that this feature is a true AFM transition with neutron diffraction. As substitution is increased, $T_N$ decreases. At $x = 0.55$, however, it appears that the primary AFM order axis changes to the $a$ axis.

In Fig. 3.19 we show $M(H)$ along each of the three crystal axes of $LaCr_{1-x}Fe_xSb_3$ for samples $x = 0$ through $x = 0.55$ at $T = 2$ K. For samples with an FM ground state ($x \leq 0.15$), the $b$ axis is the easy magnetic axis, while $a$ is the hard axis. The spin reorientation feature is evident by a kink in $M_c$. This kink occurs at higher fields in the $x = 0.05$ and $x = 0.1$ samples compared to the unsubstituted sample. Significant FM hysteresis along $b$ is observed in the $x = 0.15$ sample.

At low temperatures, the $x = 0.2$, 0.25, and 0.3 samples exhibit clear first order spin-flip transitions between the $AFM_b$ and polarized $FM_b$ states. More field is required to break the AFM ordering as substitution is increased. In this region of substitution, there is also a notable decrease in anisotropy between $a$ and $c$.

At $x = 0.35$, there is a spin-flop transition characterized by the significant region of linear $M(H)$ between the $AFM_b$ and $FM_b$ phases. This intermediate region is a result of the appearance of a new phase, a

canted-spin cAFM phase. This is the phase that buries the QTCP. The hysteresis in $M_b$ does not disappear, and the cAFM phase gets larger as substitution increases. At $x = 0.55$, the $a$ axis exhibits hysteresis, which, along with the downturn feature in $M(T)$, suggests a change in state to an $\mathrm{AFM}_a$ phase.

**Experimental Magnetization Details**

We use a Quantum Design Magnetic Property Measurement System XL (MPMS) to measure the magnetization of our samples as a function of temperature ($M(T)$) and applied magnetic field ($M(H)$). We measure $M(T)$ in constant applied magnetic fields up to 7 T, and we measure isothermal $M(H)$ in temperatures as low as 2 K. Magnetic measurements were performed with magnetic field applied separately along the $a$, $b$, and $c$ axis directions. Our MPMS only measures magnetization in the direction parallel to the applied field. For example, $M_b$ denotes the magnetization along the $b$ axis with the field applied along the $b$ axis. For all measurements, the crystals were mounted with Apiezon N grease to a strip of acetate placed in the radial center of plastic drinking straws. At higher substitutions, the crystals tend to be thin, brittle, and prone to breakage, so using a small amount of grease as a delicate method of affixing was necessary.

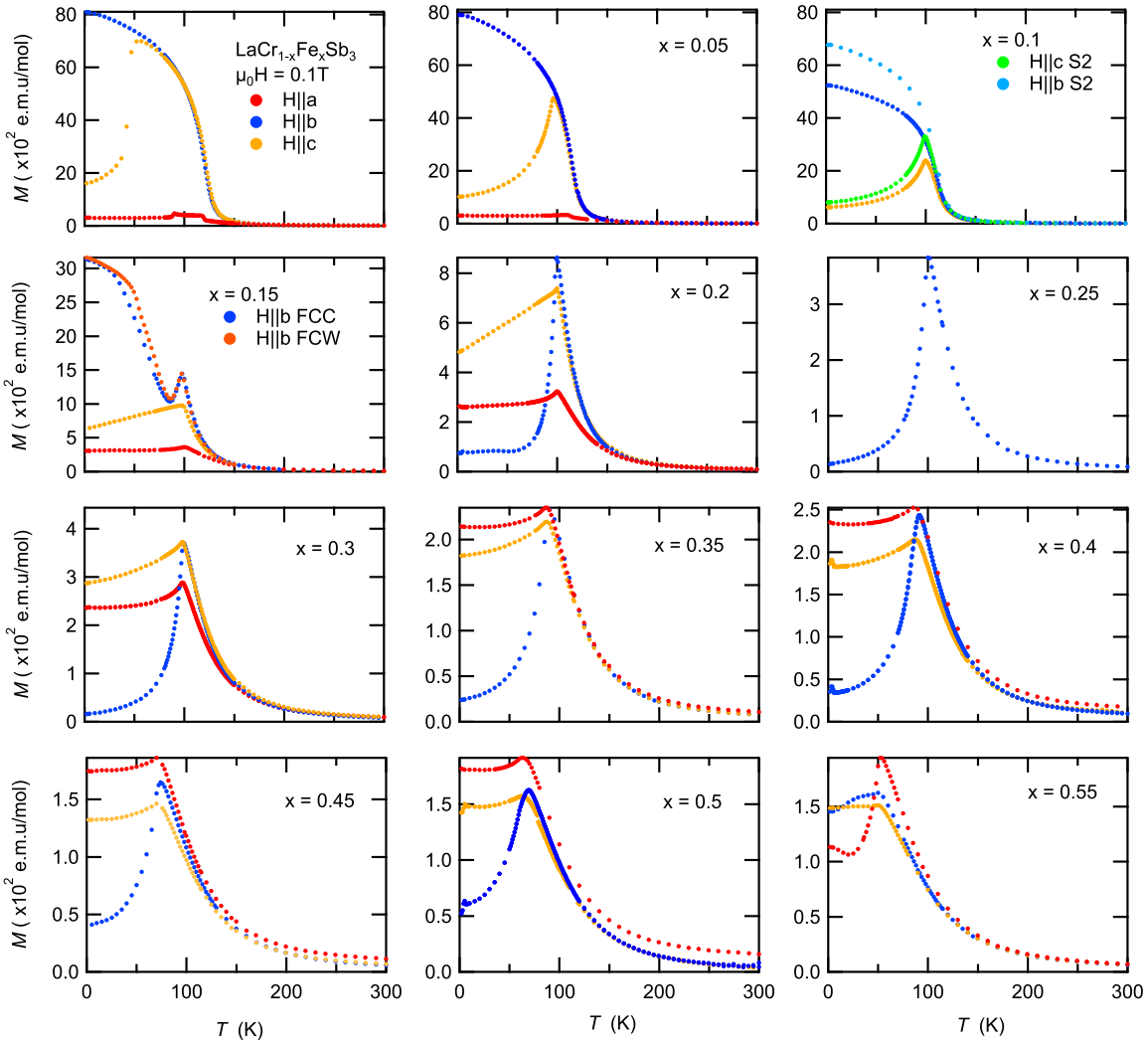


**Figure 3.18:** Magnetization as a function of temperature along each of the three crystal axes of $LaCr_{1-x}Fe_xSb_3$ in an $\mu_0 H = 0.1\,\mathrm{T}$ applied field.

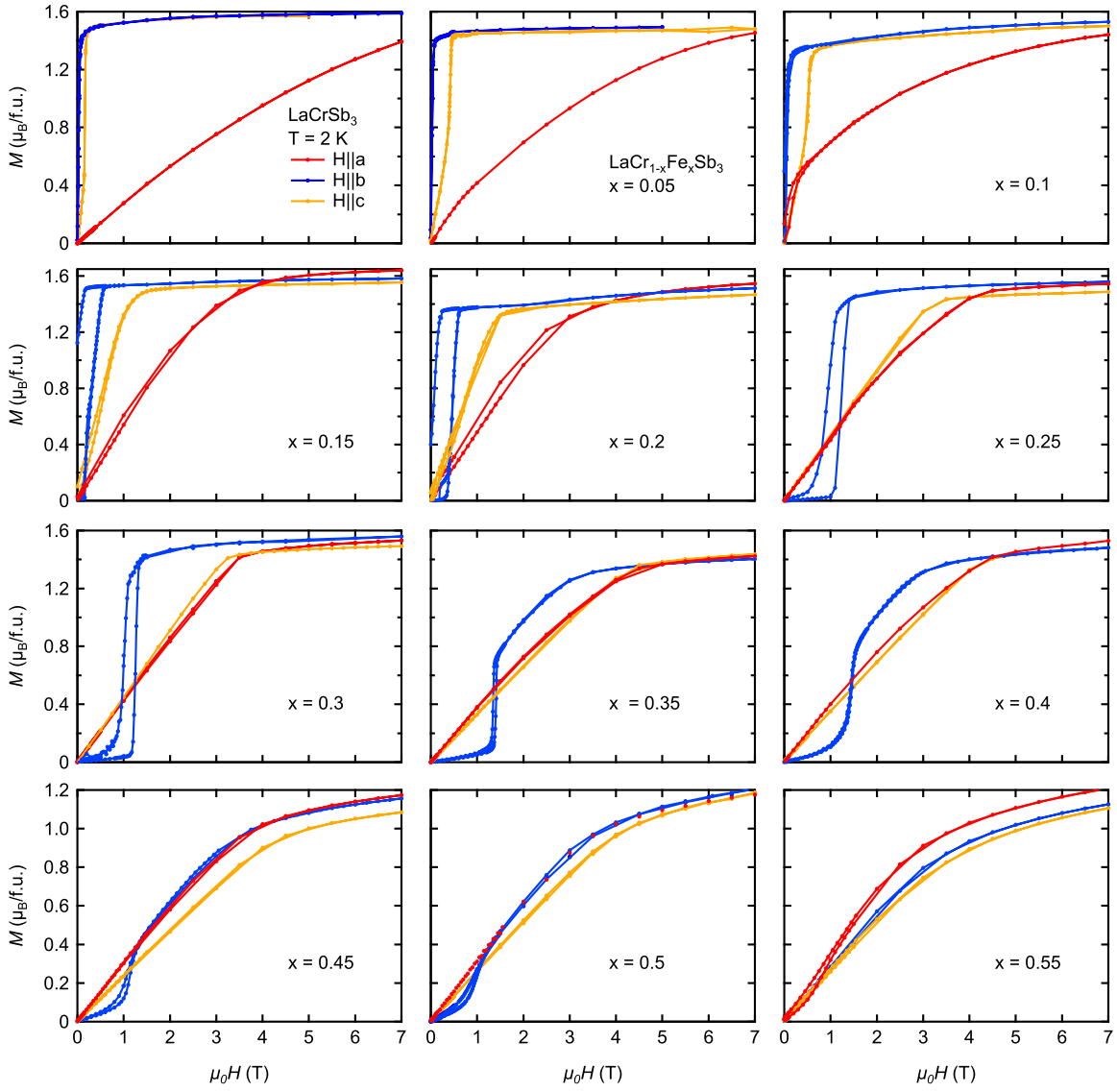


**Figure 3.19:** Magnetization as a function of applied field along each of the three crystal axes of $LaCr_{1-x}Fe_xSb_3$ at $T = 2\,\mathrm{K}$. Discrepancies in the spontaneous magnetization along each axis are most likely due to small displacements from the radial center in the MPMS (refer to Section 4.1.1 for more information).

### 3.4.2 Neutron Diffraction Results and Analysis

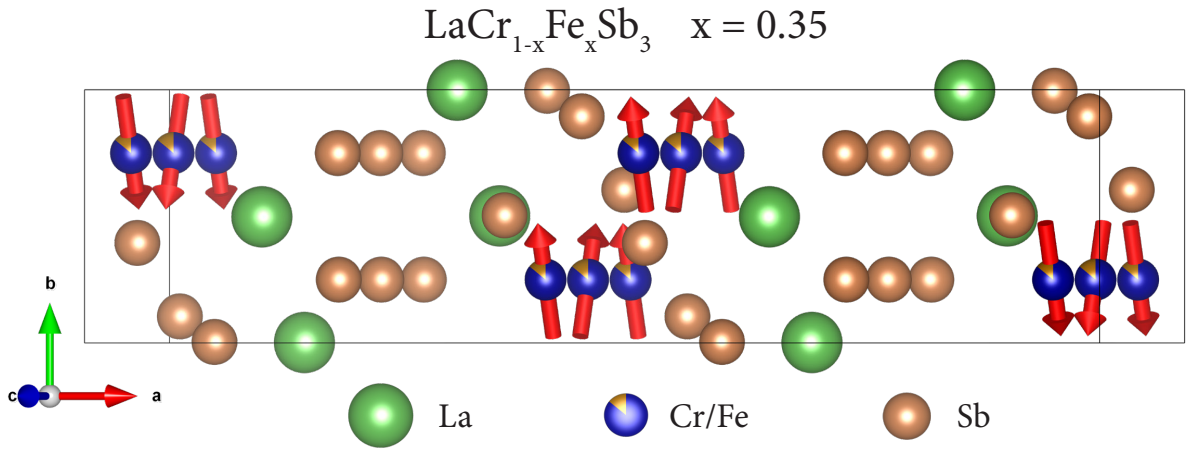


**Figure 3.20:** The magnetic structure of $LaCr_{1-x}Fe_xSb_3$ ($x = 0.35$) at zero field.

Granado *et al.* performed the first neutron diffraction measurements on $LaCrSb_3$ and studied its non-trivial magnetic structure [97]. Given the lack of pedagogical resources for analyzing neutron diffraction results, I have decided to spend some time explaining the $LaCrSb_3$ results with the hope that it will provide a glimpse of clarity to the explanation of our results on the substituted sample.

One of the many keys to understanding the relationship between magnetism and neutron diffraction peaks is the following sentence found in Granado *et al.*: "the magnetic intensity of a given reflection is sensitive only to the spin projection into the scattering plane." As an example, the (0 0 2) peak[9] is sensitive to magnetic moment in the *ab* plane, while the (0 2 0) peak is sensitive to moments in the *ac* plane. With this information in mind, we can understand how the temperature dependence of these peaks reveals a spin-reorientation.

The spin reorientation in $LaCrSb_3$ was first suggested by Jackson *et al.*[96][10] to make sense of their novel anisotropic magnetization measurements. The feature at $T^*$ would only become $T_{SR}$ after Granado *et al.* confirmed the spin reorientation with neutron diffraction. Specifically, they looked at the temperature dependence of the (0 0 2), (0 2 0) and (1 0 0) peaks. Below $T_C$ the (0 2 0) increases from baseline intensity, meaning the moment is the the *ac* plane. At $T_{SR}$, however, the (0 2 0) peak vanishes, indicating a loss of moment in the *ac* plane and at the same time, the (0 0 2) peak increases from baseline intensity and continues to increase as temperature is lowered. The (0 0 2) peak is sensitive to moment in the *ab* plane, however, we know that the moment does not point along *a* since if it did, the (0 2 0) would still have some

[9]Question: what is the difference between (001) and (002)? According to Bragg's Law, $n\lambda = 2d\sin(\theta)$, both peaks appear as a result of the same spacing $d$, however, the angle that they occur is different. Lower integer peaks occur at smaller angles that may not be observable by the constraints of the particular beamline. This is the same reason why for our measurements on the $x = 0.35$ sample, the AFM peak we observe is (1.5 0 0) rather than (0.5 0 0). (0.5 0 0) results in an angle that is not possible to measure with the experimental apparatus.

[10]The first group to grow single crystals of $LaCrSb_3$ and therefore, the first to be able to measure anisotropic magnetization.

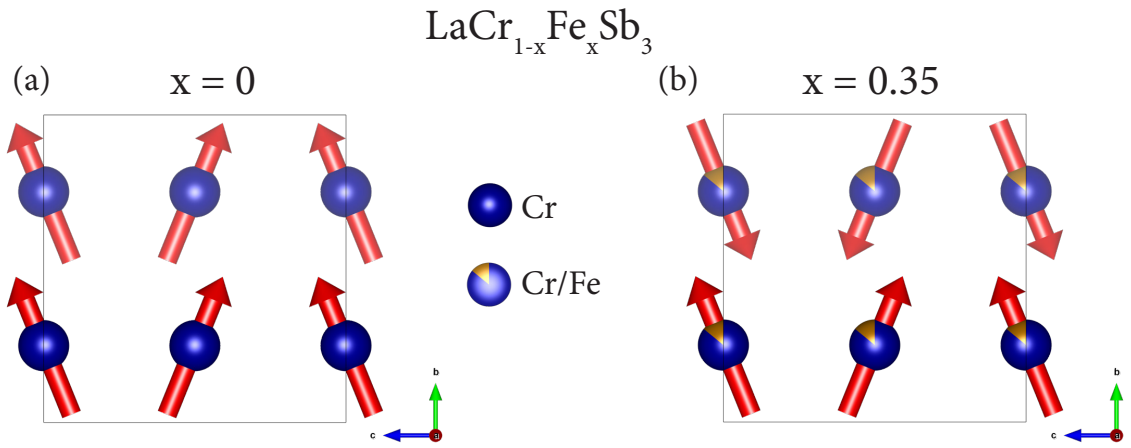


**Figure 3.21:** A comparison of the zero-field magnetic structures of (a) $LaCrSb_3$ [97] and (b) $LaCr_{1-x}Fe_xSb_3$ at low temperatures. (a) While the moments are ferromagnetically aligned along the $b$ axis, they cant towards $c$ at an 18° angle antiferromagnetically (Top row: left, right, left). (b) At $x = 0.35$ the moments antiferromagnetically aligned along $b$ (Leftmost column: down up), and antiferromagnetically aligned along $c$ (Top row: right, left, right).

contribution below $T_{SR}$. Furthermore, the (1 0 0) peak increases from baseline at $T_C$ and continues to increase as temperature is lowered, indicating the moment remains constrained to the $bc$ plane. The lack of moment along $a$ is also corroborated by bulk magnetization measurements which show that the $a$ is the hard magnetic direction. Therefore, neutron diffraction confirms that the moment reorients from $c$ to $b$ at $T_{SR}$.

In this simple example of a spin-reorientation, we have had to reason through the magnetic structure by analyzing the temperature dependence of a limited number of peaks and at the same time, make sure it is consistent with what is observed in bulk magnetization. Ideally, time and resources would allow for a full neutron spectra to be taken at each temperature and field so that the magnetic structure could be solved exactly for each point in $T - H$ phase space. Such a measurement, although illuminating, would be prohibitively costly and we are often left to discern magnetic features with only a handful of peaks, much like filling in a crossword puzzle with only half of the clues available. In a way, however, the neutron analysis of these three peaks merely confirmed the spin reorientation that Jackson *et al.* were able to correctly guess from their bulk $M$ measurements along each axis. The value of neutron diffraction is revealed when a full refinement of the spectra is performed, and features *not* suggested by bulk $M$ come to light.

At zero field, the refinement of the neutron spectra revealed that the moments are canted away from the $b$ axis towards $c$ at an 18° angle. This spin canting is depicted in Fig. 3.21(a), was found to be robust to applied fields of up to 7 T, and since the $c$ component is antiferromagnetically aligned, is undetectable by bulk measurements of $M$. While complex magnetic structures that do not contribute to the overall magnetization are difficult to observe in $M$, neutron diffraction is especially helpful for determining antiferromagnetic structures such as the AFM sublattice formed by this spin canting. Specifically, AFM alignments contribute

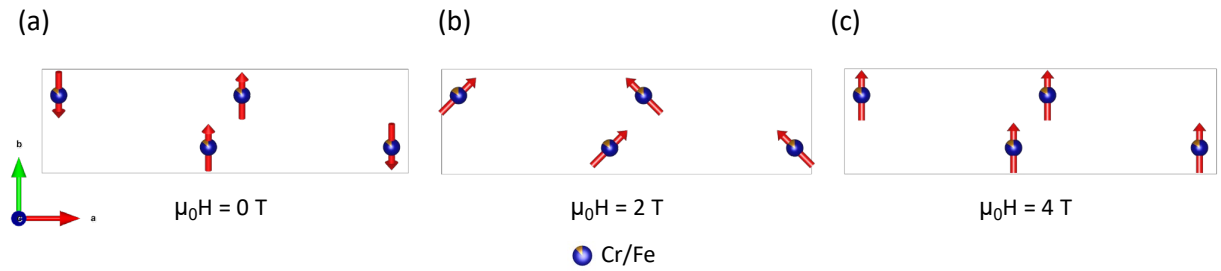


**Figure 3.22:** A schematic representation of the magnetic moments at (a) 0 T (b) 2 T and (c) 4 T applied along $b$ as inferred from the field dependence of the relevant peaks shown in Fig. 3.24 and Fig. 3.23(b). (a) At zero field ($AFM_b$), the moments primarily point along $b$ in a 'down-up-up-down' antiferromagnetic unit cell that is twice the size of the crystal unit cell along the $a$ direction. (b) When a 2 T field is applied, a spin flop transition takes places, and both spins cant away from $b$ towards $a$ at an angle that is controlled by the applied field. This represents the cAFM state. Spin flop transitions are discussed further in Section 3.4.5. (c) By 4 T, the polarized FM state is achieved and the moments fully point along $b$.

a new periodicity that results in diffraction peaks that would be forbidden by the crystal structure of the compound and only appear below a magnetic transition. In the case of $LaCrSb_3$, the evidence for this canting are the existence of $(h\ 0\ 2l+1)$ (e.g. (1 0 1))peaks forbidden by $LaCrSb_3$'s *Pbcm* space group [97].

The spin canting unveiled FM and AFM sublattices—ferromagnetic alignment along $b$ and antiferromagnetic alignment along $c$—which is an unusual magnetic structure to have. In fact, it is a clue that led us to believe $LaCrSb_3$ could lead to the realization of a quantum tricritical point (QTCP) where both FM and AFM flucuations are expected to diverge. The coexistence of AFM and FM interactions was puzzling enough for a follow up reference with the same title as Granado *et al.*, albeit in a different journal, which proposes a fully itinerant model as a solution [142]. Fully itinerant magnetism, however, would not result in the bulk magnetic properties observed: an easy axis that saturates and remains saturated up to 7 T. So the takeaway is that $LaCrSb_3$ has certain behaviors that can be explained by a local moment picture and some by an itinerant moment picture, i.e., it is a ferromagnet with some level of itinerancy.[11]

Just like Jackson *et al.* were able to suggest the existence of a spin reorientation in $LaCrSb_3$ and needed neutron diffraction measurements to confirm, we were able to guess the magnetic structure of the $AFM_b$, cAFM, and polarized $FM_b$ phases, but needed neutron diffraction to confirm. In summary, our neutron diffraction measurements were able to confirm a true $AFM_b$ state, and canting towards $c$ was also observed. They also revealed that the cAFM state is unexpectedly formed by moments pointing towards $a$. The very fact that the magnetic structures of these phases can be determined highlights an advantage of the substitution tuned $La(Cr,Fe)Sb_3$ system over those tuned by pressure. Since the neutron signal is

[11] It is worth mentioning that $LaCrGe_3$ is also often called an itinerant magnet although its bulk magnetic properties also behave like a single rotating local moment, and all of our text-book-level calculations based on a rotating local moment agree with our experimental data. The problem is that calling $LaCrSb_3$ and $LaCrGe_3$ itinerant magnets is not an accurate statement because it could imply that their magnetism originates from mobile electron spins. A more accurate way to talk about the magnetism is then, $LaCrSb_3$ and $LaCrGe_3$ are ferromagnets and their magnetism has some level of itinerancy.

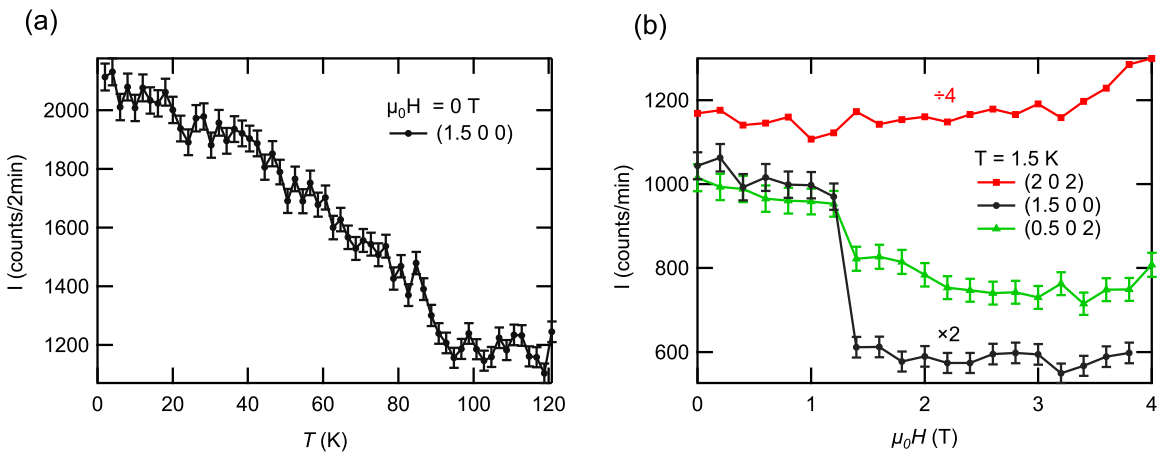


**Figure 3.23:** (a) The temperature dependence of the (1.5 0 0) peak at zero field yields a $T_N = 85\,K$ which corroborates our zero field resistivity and low field magnetization measurements. (b) The magnetic field dependence of the (1.5 0 0), (0.5 0 2), and (2 0 2) peak of $LaCr_{0.65}Fe_{0.35}Sb_3$ collected at $T = 1.5\,K$. There is a sharp drop of the intensity of the (1.5 0 0) peak near 1.3 T which is consistent with the field at which the spin-flip transition occurs in our bulk magnetization measurement. The (2 0 2) nuclear peak displays a small enhancement between 3 T and 4 T consistent with the transition from the cAFM phase to the polarized $FM_b$ phase.

proportional to the mass of the sample, but the sample must be small enough to fit into a pressure cell, there is an inherent difficulty in performing neutron diffraction measurements under pressure. As such, we are allowed to label the state $AFM_b$ rather than the lesser 'modulated magnetic phase' classification used in systems that lack neutron diffraction measurements.

**Experimental Method**

Neutron single crystal diffraction was performed to determine magnetic structure at the DEMAND instrument on the HB-3A beamline at the High Flux Isotope Reactor (HFIR) at Oak Ridge National Laboratory [161]. A neutron wavelength of 1.542 Å was used from a bent perfect Si-220 monochromator [161]. The magnetic and nuclear peaks were collected at 1.5 K at 0 T, 2 T, and 4 T within a 6 T Vertical Field Asymmetric Magnet with the magnetic field parallel to the lattice-$b$ direction. Possible magnetic structures were investigated by the magnetic space group approach, where the maximal magnetic space groups were obtained from the MAXMAGN program [162]. Magnetic structure refinements were carried out with the FullProf Suite program [163].

**Results**

The magnetic structures of the $AFM_b$, cAFM, and polarized $FM_b$ states were investigated with neutron diffraction on a $LaCr_{1-x}Fe_xSb_3$ $x = 0.35$ sample which exhibits the aforementioned phases at 0 T, 2 T, and 4 T, respectively.

The magnetic structure of the $AFM_b$ state determined from a full neutron diffraction refinement in zero

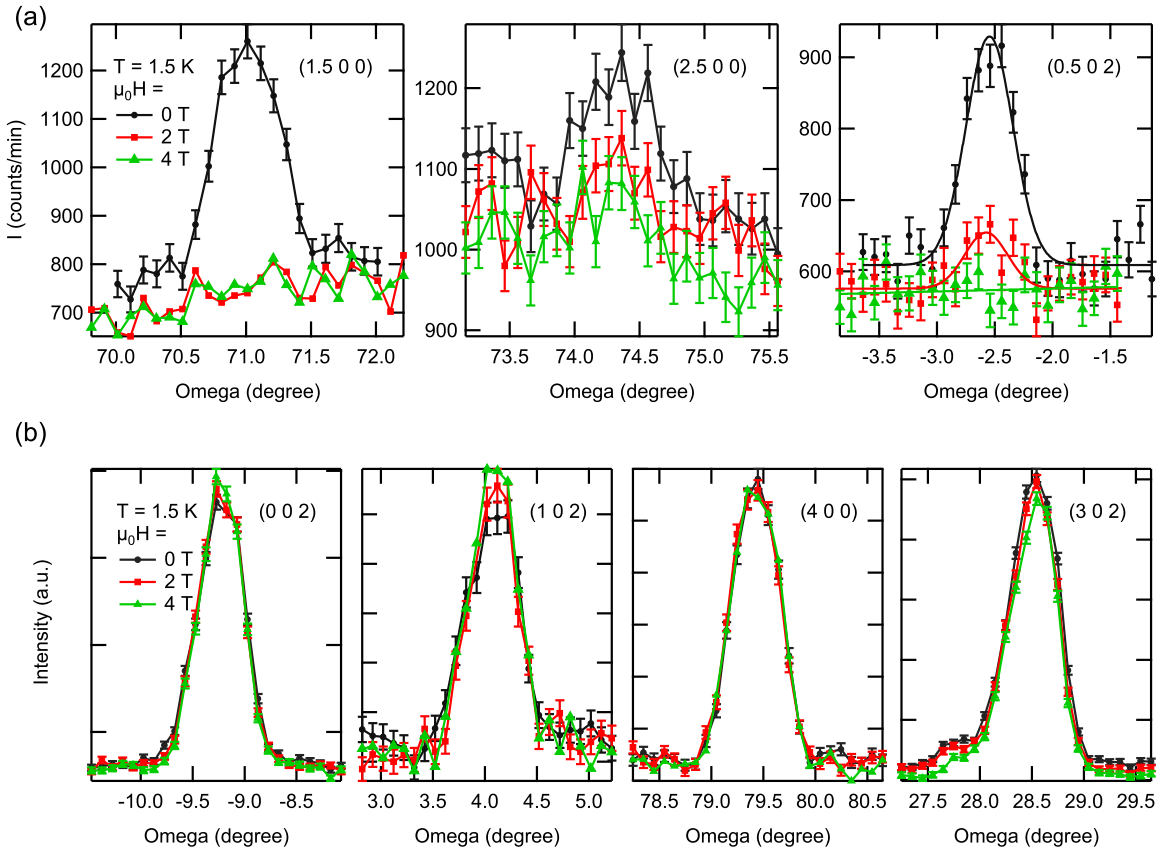


**Figure 3.24:** Neutron diffraction rocking curves of $LaCr_{1-x}Fe_xSb_3$ ($x = 0.35$) at $T = 1.5\,\mathrm{K}$ in fields $\mu_0 H = 0\,\mathrm{T}$, $2\,\mathrm{T}$ and $4\,\mathrm{T}$ of (a) antiferromagnetic peaks and (b) nuclear peaks.

field at $T = 1.5\,\mathrm{K}$ is shown in Fig. 3.20. In this $\mathrm{AFM}_b$ state, the moments primarily point along $b$ or $-b$, and the magnetic unit cell is double the crystallographic unit cell along $a$. This $\mathrm{AFM}_b$ alignment stems from a (0.5 0 0) propagation vector indicated by the (1.5 0 0) peak. As shown in Fig. 3.23(a), the (1.5 0 0) peak only appears below $T_N = 85\,\mathrm{K}$. While these zero field neutron results confirm the primary $\mathrm{AFM}_b$ alignment suggested by our anisotropic magnetization measurements, as well as the $T_N$ found from $M(T)$ and $\rho(T)$, they also reveal an additional antiferromagnetic tilt in the moments at a 22° angle towards $c$. Although $\mathrm{LaCrSb_3}$ also displays an AFM tilt towards $c$ [97], it is with a smaller 18° angle and with a different pattern. Further investigation with neutron diffraction would be necessary to determine whether the tilt towards $c$ in the $x = 0.35$ sample is as robust to field applied along $b$ as it is in $\mathrm{LaCrSb_3}$.

The field dependence of the magnetic structure is shown schematically in Fig. 3.22. At 2 T, the (1.5 0 0) peak disappears (see Fig. 3.24(a) and Fig. 3.23(b)) indicating the $b$ component of the moments are now ferromagnetically aligned. The (0.5 0 2) peak, however, persists (see rightmost panel in Fig. 3.24(a)) and denotes moments that are antiferromagnetically canted towards $a$. This alignment is shown schematically in Fig. 3.22(b) and is the cAFM state we observe to emerge in place of a quantum tricritical point.

Increasing field above 2 T causes the intensity of the nuclear (1 0 2) and (2 0 2) peaks to increase (Fig. 3.24(b) and Fig. 3.23(b), respectively), which is consistent with the observed increase in $M_b(H)$. As seen in Fig. 3.24(a), by 4 T the (0.5 0 2) peak has completely disappeared, and the system is in the polarized $\mathrm{FM}_b$ state, as shown schematically in Fig. 3.22(c).

### 3.4.3 A Study of the 1st Order FM Transition

This section details my investigation of the first order FM transition we observe in $\mathrm{LaCr_{1-x}Fe_xSb_3}$, $x = 0.15$.

For context, Jeff Harvey had grown samples $x = 0.1$ and $x = 0.2$, and through a combination of his and my magnetization measurements, we found that $x = 0.1$ has an FM ground state, while $x = 0.2$ has an AFM ground state. Following theory [126, 127, 128, 136, 129] and the experimental phase diagrams where an $\mathrm{AFM}_Q$ phase appears when the FM phase is suppressed (e.g. $\mathrm{CeAgSb_2}$ [115], $\mathrm{LaCrGe_3}$ [18],$\mathrm{CeTiGe_3}$ [87]), we expected that the FM transition would become first order at some substitution between $x = 0.1$ and $x = 0.2$. So I split the difference and grew a nominal $x = 0.15$ substitution. Not only does the $x = 0.15$ exhibit a first order FM transition (observable by the hysteresis in $M(T)$ and $\rho(T)$), it also displays hints of antiferromagnetism, which is almost too perfectly predictable given that it sits in the middle of the last FM and first AFM substitutions we observed. This result demonstrates the valuable level of tunability in the $\mathrm{La(Cr,Fe)Sb_3}$ system (as well as the benefit of being able to grow your own samples). For example, many other systems (e.g. CeRuPO [117, 122], CeFePO [121], MnP [123, 119]) have been shown to have an $\mathrm{AFM}_Q$

phase appear when $T_C$ is suppressed, but they do not study or report the first order FM transition that is expected to occur between the two magnetic orderings. This omission is most likely because of the inherent difficulty of high pressure experiments. La(Cr,Fe)$Sb_3$ on the other hand can be tuned in a surprisingly predictable way with substitution.[12]

At $x = 0.15$, we observe features in both $\rho(T)$ and $M(T)$ that are consistent with a first order FM transition. In Fig. 3.25(a) we show $M(T)$ measured using field-cooled-cooling (FCC), field-cooled-warming (FCW) and zero-field-cooled (ZFC) procedures in an $H = 200$ Oe field applied along the $b$ axis. The hysteresis between the FCC and FCW curves is evidence for a first order FM transition. The difference between the FCC/FCW and ZFC curves implies the presence of ferromagnetic domains. Therefore, while the downturn in $M$ near 100 K indicates the appearance of $AFM_b$ interactions, the ground state below 60 K is ferromagnetic. In Fig. 3.25(b) we measure $\rho(T)$ during warming ($+T$) and cooling ($-T$) in zero field. As the inset shows, there is hysteresis between $\rho(+T)$ and $\rho(-T)$. The rate of change of temperature was 0.5 K/min to minimize the difference between $\rho(+T)$ and $\rho(-T)$ due to thermal lag. In Fig. 3.25(c) we plot the differences in $M$ and $\rho$ between cooling and warming to show that both differences peak at 50 K. The hysteresis in both of these measurements indicates that the FM transition is a first order transition, which suggests that somewhere between $x = 0.1$ and $x = 0.15$ the PM-FM transition changed from second order to first order at a tricritial point.

Since a first order phase transition should theoretically appear as a divergence (experimentally, a large feature) in heat capacity ($C_p$), we also measured the heat capacity of a $x = 0.15$ sample. Despite making modifications to the default thermal-relaxation calorimetry technique used by the PPMS [164, 165], there are no clear features of a first order transition near $T_C = 50$ K nor a second order transition at $T_N = 100$ K. As deduced from our magnetization and resistivity measurements, the first order transition is potentially too broad to be observed in heat capacity. While weak itinerant ferromagnets can be known to not reveal their $T_C$ in heat capacity (e.g., $ZrZn_2$ $0.17\mu_B$/f.u. [166]), it is unusual for $LaCr_{1-x}Fe_xSb_3$ ($\sim 1.6\mu_B$/f.u.) to not show a feature in $C_p$. Still, $T_C$ in heat capacity was not initially observed in $LaCrSb_3$ [97]. It was not until a background subtraction of its nonmagnetic counterpart, $LaVSb_3$, was performed did a small feature of $T_C$ appear in $C_p$ [11]. A difficulty in observing a first order transition in heat capacity is also reported in $CeAgSb_2$ [115].

Given the flexibility of substitution in the $LaCr_{1-x}Fe_xSb_3$ system, and its relative predictability of its magnetic properties, it may be an ideal sample for studying first order FM transitions. Growing additional substitutions between $x = 0.1$ and $x = 0.2$, would enable further investigation in the vicinity of the FM-AFM transition (refer to Fig. 3.9) to study, for example, where exactly the zero field $TCP$ occurs, the

[12] Besides our discovery that the QTCP is avoided, of course.

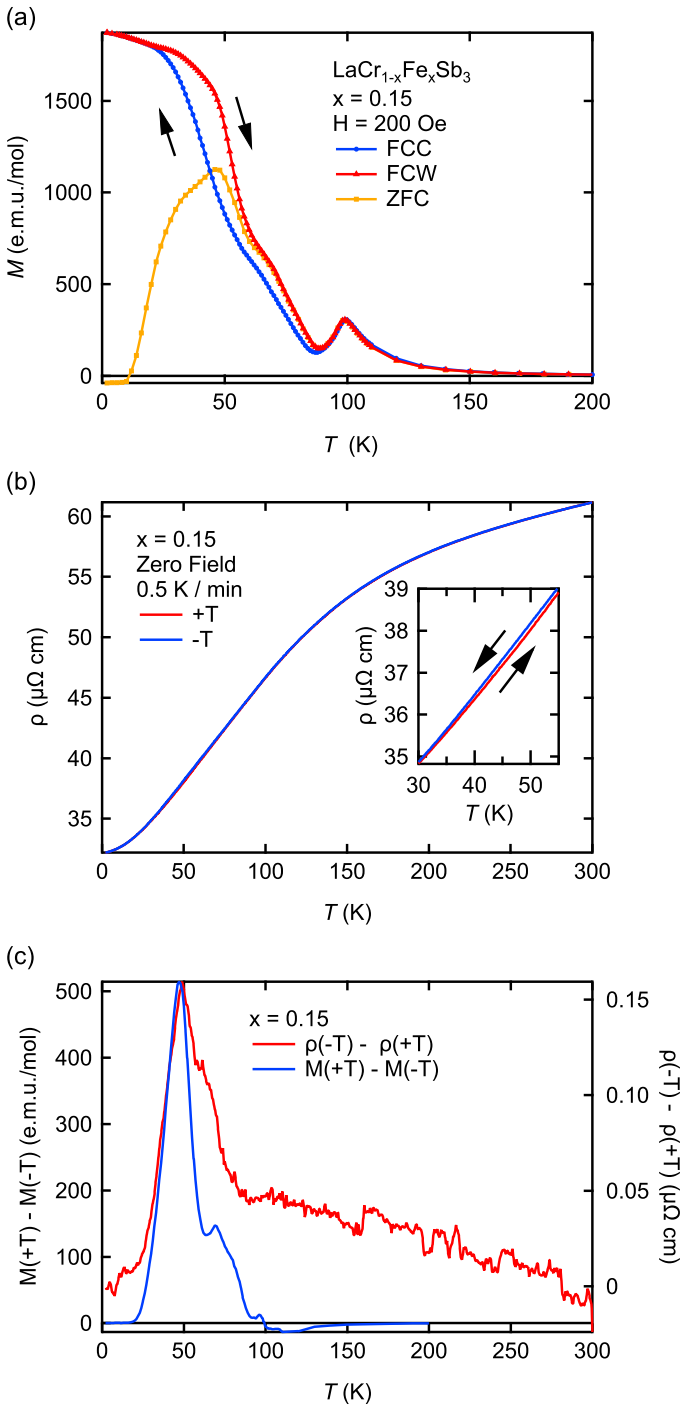


**Figure 3.25:** (a) Hysteresis is observed between the field-cooled-cooling (FCC) and field-cooled-warming (FCW) magnetization curves. The zero-field-cooled (ZFC) curve indicates the presence of ferromagnetic domains. (b) Resistivity measured in zero field upon warming (+T) and cooling (-T). The inset shows the separation of the +T and -T curves. (c) By plotting the difference between warming and cooling in magnetization and resistivity, we find that the peaks in both differences occur near 50 K.

region surrounding the Lifshitz point,[13] or in what way the first order FM transition is suppressed to zero temperature. Furthermore, without the complication of pressure as a tuning parameter, features could be determined with both anisotropic magnetization and resistivity. In conclusion, the $x = 0.15$ substitution exhibits a first order FM transition, consistent with theoretical predictions and experimental precedent, and we are hopeful that the La(Cr,Fe)$Sb_3$ system will prove to be a platform for further investigation of the transition between FM and AFM phases.

### 3.4.4 A Study of Magnetoresistance

The three dimensional temperature-chemical substitution-magnetic field phase diagram of $LaCr_{1-x}Fe_xSb_3$ was constructed from magnetization measurements. Magnetization measurements have some clear advantages over resistivity measurements. First, they are non-destructive; there is no need to affix contacts to the samples, and any grease used to mount the sample can be completely washed off with hexanes. Therefore, magnetization measurements are ideal for screening samples before resistivity, heat capacity, neutron diffraction or MOKE measurements are performed.

Additionally, since we are looking for magnetic phase transitions, the magnetic features are large and can be inferred from the signal directly. For example, a ferromagnetic transition will show a large increase in $M$, while an antiferromagnetic transition will show an abrupt decrease in $M$.[14] In our MPMS, $M(T)$ must be measured in a small applied magnetic field, however, making $T_C$ (or $T_N$) determined from features in $M(T)$ a suggestion because $T_C$ is strictly defined as the spontaneous alignment (or anti-alignment) in zero field. On the other hand, although $\rho(T)$ can be measured in zero field, the features of $T_C$ or $T_N$ in resistivity are comparatively small. This is especially true for our $LaCr_{1-x}Fe_xSb_3$ substitution series where we are intentionally adding disorder which decreases the prominence of the transition in $\rho$.

As seen in Fig. 3.26, there is a discernible feature in $\rho(T)$ for the FM samples ($x < 0.15$) that corresponds to $T_C$. When we take the temperature derivative of the resistivity, we see the resulting sharp peak and can pinpoint $T_C$. When it comes to the AFM samples at higher substitutions ($x \geq 0.2$), however, there is no clear feature in $\rho(T)$. Instead, a feature of the transition is only visible in $d\rho/dT(T)$. In Fig. 3.27, I show that features in $d\rho/dT(T)$ match the feature in $dM_b/dT$ that we used to find $T_C$ and $T_N$. Specifically, for substitutions with an FM ground state ($x < 0.2$), we observe a jump in $d\rho/dT$, which coincides with the $dM_b/dT$ minimum that signifies the steepest increase in $M_b$. For substitutions with an AFM ground state ($x \geq 0.2$) we observe a jump in $d\rho/dT$, which coincides with a $dM_b/dT$ maximum signifying the steepest

[13] The TCP and the Lifshitz point labeled in Fig. 3.11 are schematically placed, they are not true data points. Additional samples could be grown to pinpoint their location, or see if any novel features appear.

[14] As there are many magnetic features besides an AFM transition that could cause a drop in the magnetization (such as the depinning of magnetic domains [10, 9], or a spin-reorientation [96, 97]) it is important to use multiple probes to confirm magnetic transitions.

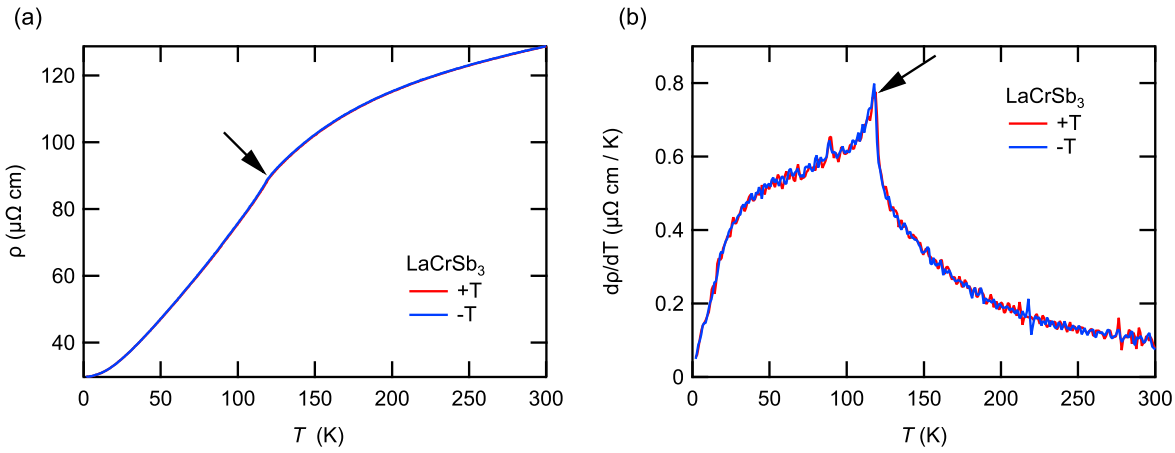


**Figure 3.26:** The temperature dependence of (a) the resistivity ($\rho$) and (b) the temperature derivative of the resistivity ($d\rho/dT$) of $LaCrSb_3$. For the purely FM samples ($x < 0.15$), features of $T_C$ are observed in both $\rho$ and $d\rho/dT$ as marked by the black arrows in both figures.

decrease in $M_b$. Without the magnetization measurements, the feature in $d\rho/dT$ tells us something occurs at that temperature, but it would be impossible to distinguish between $T_C$ and $T_N$.

Confirming that resistivity also shows features at $T_C$ and $T_N$ is good to do, but it will not make or break our core finding in $LaCr_{1-x}Fe_xSb_3$: that the field-induced transitions between the $AFM_b$ and $FM_b$ ($0.2 \leq x \leq 0.3$) phases and between the $AFM_b$ and cAFM ($x > 0.3$) phases are always first order, and a quantum tricritical point is therefore avoided. Our primary evidence for the first order nature of the $AFM_b$ to $FM_b$ or cAFM transitions is the hysteresis observed in $M(H)$.

To support our findings in $M(H)$, we also measure $\rho(H)$. Fig. 3.28 presents both $M(H)$ and $\rho(H)$ and we find agreement between the two probes. When $0.2 \leq x \leq 0.3$, there is a sharp decrease in the resistivity due to the field induced $AFM_b$ to $FM_b$ spin-flip transition. In addition, there is hysteresis in $\rho$ between the increasing and decreasing field directions consistent with the hysteresis in $M(H)$. This provides further evidence for the first order nature of the transition. When $x > 0.3$, there is still a drop in the resistivity with hysteresis during the $AFM_b$ to cAFM spin-flop transition, however, there is now also a broad bump in $\rho(H)$ due to the cAFM phase that precedes the polarized $FM_b$ state.

The $x = 0.15$ sample is interesting because it has an AFM transition $T_N = 98\,K$, but ultimately exhibits a first order FM transition ($T_C = 50\,K$,) to an FM ground state. In Fig. 3.29, I show the FM hysteresis in $M(H)$ as well as in $\rho(H)$.[15] Like hysteresis in $M$, hysteresis in $\rho$ means that two different values of resistivity can be obtained depending on the field history of the magnet. Figure 3.29(c) highlights the correspondence between the features in both measurements.

[15] $x = 0.1$ also shows FM hysteresis in $M(H)$, but $\rho(H)$ with $H||b$ was not performed.

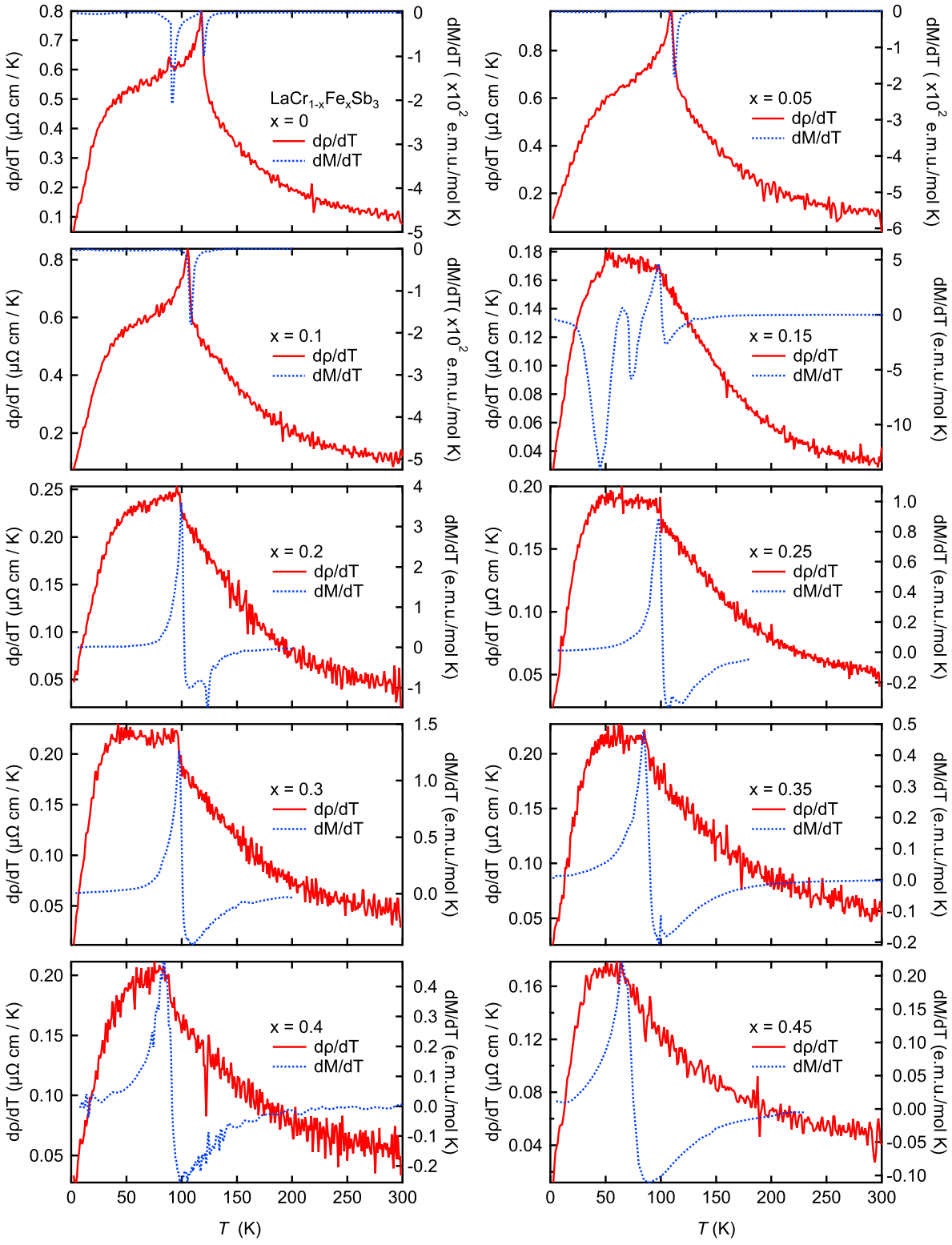


**Figure 3.27:** The minima and maxima of $dM_b/dT$ associated with $T_C$ and $T_N$, respectively, and their corresponding features in the temperature derivative of resistivity, $d\rho/dT$. $M(T)$ was measured in a small field $H = 50\,\text{Oe}$, while $\rho(T)$ was measured in zero field.

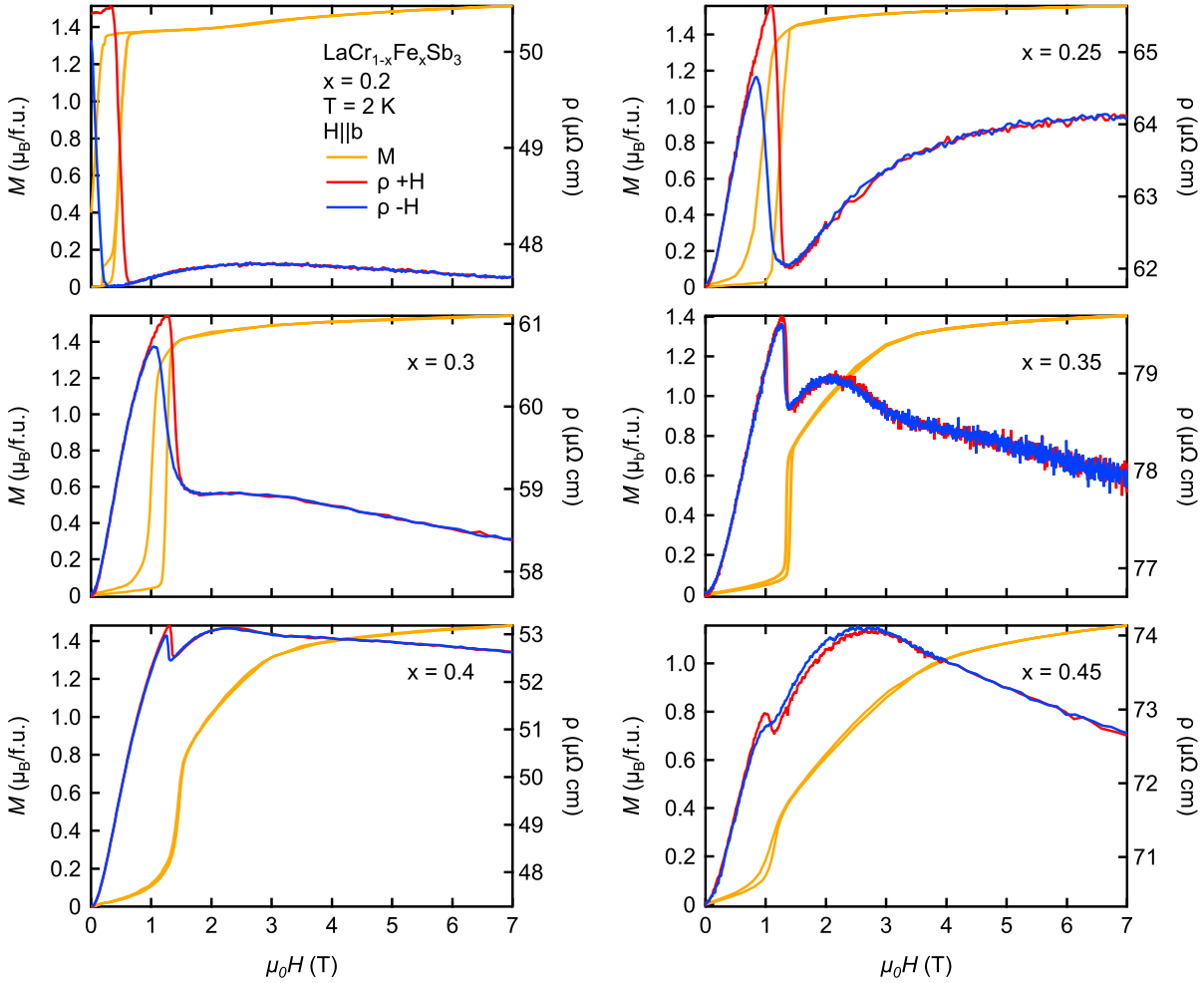


**Figure 3.28:** The field induced AFM$_b$ to polarized FM$_b$ transitions (seen in $x = 0.2$, 0.25, and 0.3) show hysteresis between increasing field (+H) and decreasing field (-H) in both magnetization and resistivity at $T = 2$ K indicating the first order nature of these transitions throughout the substitution series. The canted magnetic cAFM phase (shown here in $x = 0.35$, 0.4, and 0.45) is characterized by a linearly increasing region of $M(H)$ between the AFM$_b$ and FM$_b$ phases and appears as a broad bump in resistivity. The hysteresis in $\rho(H)$ decreases with increasing temperature and disappears at similar temperatures as the hysteresis in $M(H)$.

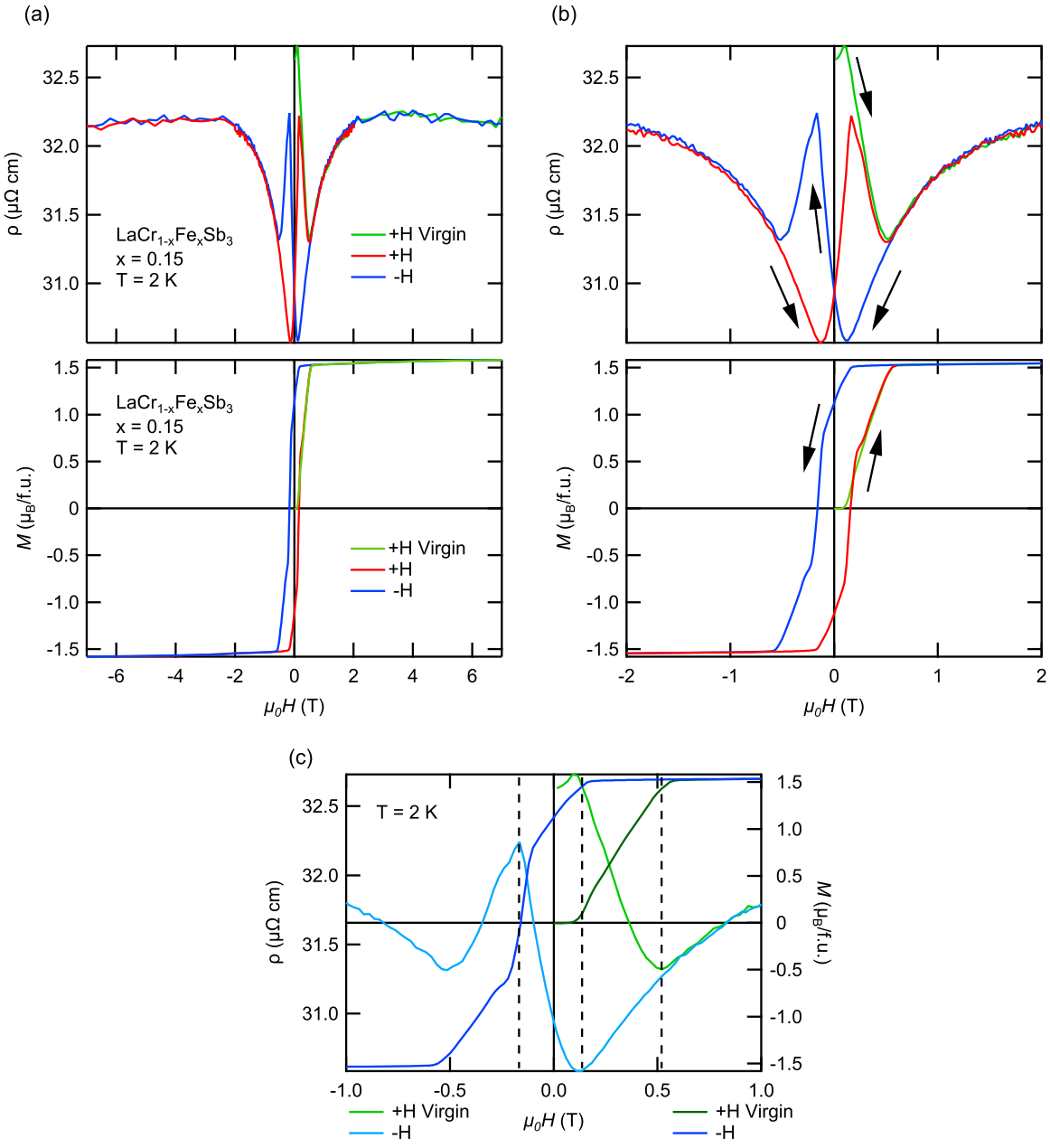


**Figure 3.29:** (a) $\rho(H)$ (top) and $M(H)$ bottom for an $x = 0.15$ sample at $T = 2\,\mathrm{K}$. (b) The same measurement as (a) but zoomed in. The black arrows emphasize how $\rho$ changes by increasing and decreasing field. (c) An overlay of the virgin curve (initial increasing field curve from a zero-field-cooled state) and the decreasing field (-H) curve of $\rho(H)$ and $M(H)$ to show the correspondence between the two measurements. The black dotted lines highlight the matching of features. From left to right: the sharp local maximum in $\rho$ occurs when $M$ crosses zero and changes sign, the rounded local minimum in $\rho$ occurs when $M$ decreases from saturation, the rounded local minimum in the virgin $\rho$ occurs when $M$ achieves saturation from the ZFC state.

**Resistivity Experimental Details**

Four terminal resistivity measurements on a selection of samples were performed in a Quantum Design Physical Property Measurement system (PPMS). Contacts with Pt wire (0.002 in diameter) were affixed using silver epoxy (EPO-TEK H20E) cured at 150°C for 1 hour. The contacts were annealed at room temperature by running up to 30 mA through each of the permutations of the four terminals. AC transport measurements were performed with a 10 mA excitation at 37 Hz with $I||c$. Measurements were performed with a fixed gain determined at 300 K (200 $\mu$V to 1 mV) to increase the data density by eliminating time spent autoranging. For magnetoresistance measurements, the crystal was oriented such that $H||b$ and affixed to the PPMS puck with Apiezon N grease or GE varnish.

### 3.4.5 A Study of Spin Flips and Flops

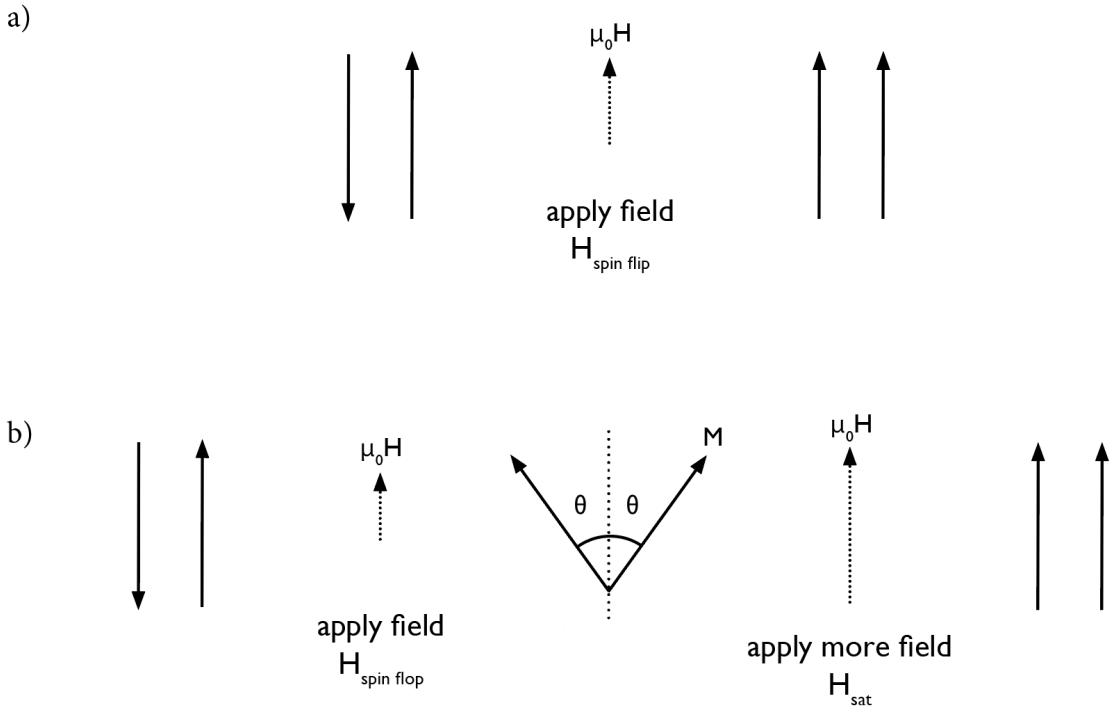


**Figure 3.30:** A schematic diagram of the alignment of magnetic moments during field induced (a) spin flip and (b) spin flop transitions. In zero field, the magnetic moments are anti-aligned. In the spin flip case, applying a critical field $H_{\text{spin flip}}$ in the direction shown causes the downward pointing moment to suddenly orient parallel to the applied field resulting in a polarized state. A spin flip occurs when the anisotropy energy is larger than the antiferromagnetic exchange energy. In the spin flop case, there is an intermediate state that occurs at $H_{\text{spin flop}}$ where both moments re-align forming an angle $\theta$ with the easy axis and the applied field direction. This canted spin state is able to occur when the antiferromagnetic exchange energy is larger than the anisotropy energy. Applying more field causes $\theta$ to decrease until the moments align at $H_{\text{saturation}}$.

It may come as a surprise that there is a scientific, rather than typographical, difference between spin flip and spin flop transitions. Both types of transitions describe the way in which an antiferromagnetic alignment ('up down') behaves when a magnetic field is applied parallel to one of the moments. A spin flip describes the sudden 180° rotation of the anti-aligned moment at $B_{\text{spin flip}}$ resulting in the immediate polarization of the magnet. On the other hand, in a spin flop transition, both moments change alignment to a canted state at $B_{\text{spin flop}}$. A schematic representation of a spin flip and a spin flop transition is presented in Fig. 3.30(a) and Fig. 3.30(b), respectively.

$LaCr_{1-x}Fe_xSb_3$ exhibits spin flips when $0.2 \leq x \leq 0.3$ and spin flops when $0.35 \leq x \leq 0.5$. Without any theoretical background, one may intuitively suspect that the spin flop state would occur at lower substitutions in closer proximity to the FM phase since the intermediate canted state contains some ferromagnetic alignment. Of course, physics is *not* intuitive, and we must first outline the theory behind what

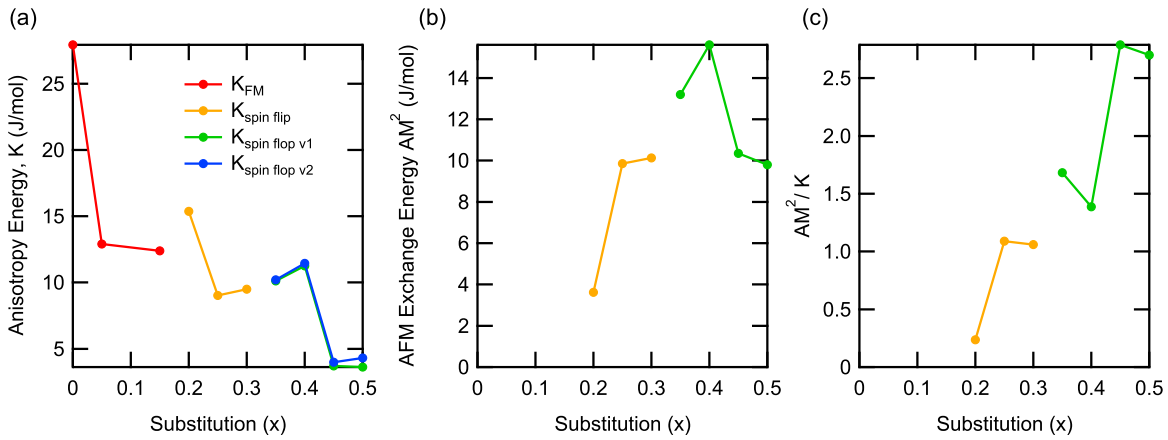


**Figure 3.31:** (a) The anisotropy energy ($K$) tends to decrease with substitution. $K_{\text{spin flop v1}}$ is calculated using Eq. 3.7 while $K_{\text{spin flop v2}}$ is calculated using Eq. 3.8. (b) The antiferromagnetic exchange energy ($AM^2$) increases with substitution, reaching a maximum at $x = 0.4$ before decreasing. (c) The ratio $AM^2/K$ increases with substitution, consistent with observing spin flips at low substitutions and spin flops at higher substitutions.

determines whether a spin flip occurs over a spin flop. This will include a simple, but intriguing, analysis of the spin flop state developed by fellow Taufour lab member Yunshu Shi.[16] Then, I will apply this theory to $LaCr_{1-x}Fe_xSb_3$. At the end of this analysis, we will be able to compare the values for the antiferromagnetic exchange constant ($A$) and the anisotropy energy ($K$) across a wide range of substitutions. This analysis will give us insight into why we observe spin flip transitions at lower substitutions, and spin flops at higher substitutions.

Whether a spin flip or a spin flop occurs depends on the relative strengths of the anisotropy energy ($K$) and the exchange energy ($AM^2$), where $A$ is the AFM exchange constant and $M$ is the magnetic moment. If the anisotropy energy is large compared to the AFM exchange energy, the canted state is energetically unfavorable and a spin flip occurs. If the anisotropy energy is small compared to the AFM exchange energy, then a spin flop occurs since the spins do not want to be aligned parallel to each other. We can analyze our $M(H)$ data across $LaCr_{1-x}Fe_xSb_3$ substitutions to see if our experimental data is compatible with this model.

The results of extracting $K$ and $AM^2$ from anisotropic $M(H)$ measurements are shown in Fig. 3.31. Figure 3.31(a) shows the anisotropy tends to decrease with substitution. This trend is consistent with the $M(H)$ measurements in Fig. 3.19 which show that overall, the magnet becomes more isotropic as substitution is increased. Fig. 3.31(b) shows that the AFM exchange energy initially increases with substitution, reaching a maximum at $x = 0.4$ before decreasing again. Naively, we can get a sense of the strength of the AFM

[16] Yunshu Shi developed an analysis of the two transitions starting with simple magnetic Hamiltonians that even experimentalists can understand. Furthermore, she was able to use this analysis to estimate the magnetic anisotropy energy for her antiferromagnetic compound $Y_2Co_3$[167], demonstrating its usefulness in analyzing the anisotropy of robust AFM compounds where magnetic saturation is not practically attainable.

exchange constant by the field at which the spin flip or spin flop occurs, and we support this notion with theory in Section 3.4.5. Whether a flip or flop occurs, however, depends on the ratio between the AFM exchange constant and the anisotropy energy. So Fig. 3.31(c) plots $AM^2/K$ which increases with substitution. This result is consistent with our observation of spin flip transitions at lower substitutions and spin flop transitions at higher substitutions.

### Anisotropy and Exchange Energy Analysis Details

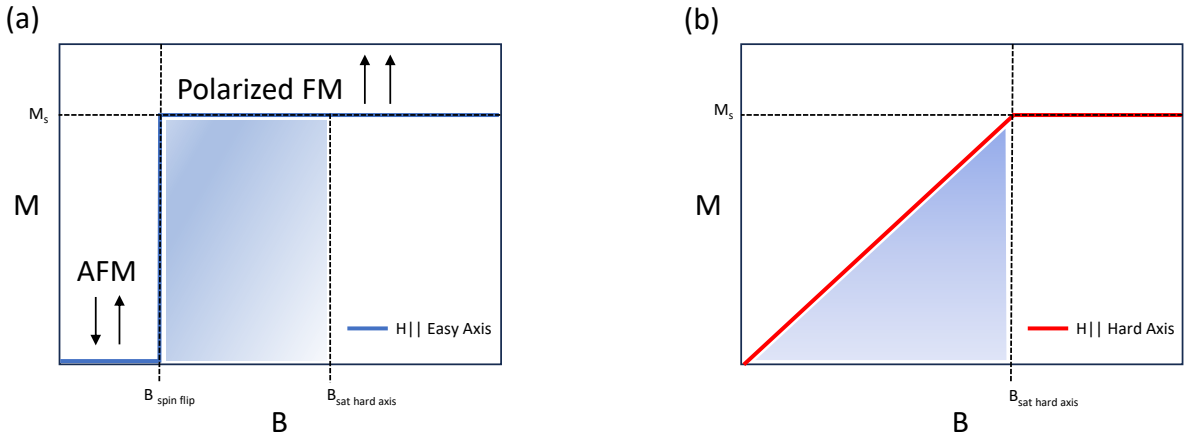


**Figure 3.32:** Schematic $M(H)$ curve for an antiferromagnet with a field-induced spin flip transition along the (a) easy axis and (b) hard axis. The shaded regions in both panels represents the energy ($M \cdot B$) required to saturate the magnetization. In this idealized approximation, this energy is $\epsilon_{\text{easy axis}} = M_s * (B_{\text{sat hard axis}} - B_{\text{spin flip}})$ and $\epsilon_{\text{hard axis}} = M_s * B_{\text{sat hard axis}}/2$. The anisotropy energy, $K$, is then difference of these two shaded regions. That is, $K = \epsilon_{\text{easy axis}} - \epsilon_{\text{hard axis}}$. $B_{\text{spin flip}}$ is the field at which the spin flip occurs, and the field at which the Hamiltonians for the AFM state and the FM state are equal.

Finding the anisotropy constants for compounds with an FM ground state was discussed in Section 2.4.3. Without demagnetization analysis, we used the Zeeman energy required to fully rotate the moment to point along the hard axis, i.e. $K = M_s B_{\text{sat hard axis}}/2$ (the area under the hard axis $M(H)$ curve) as an approximation for $K$. For substitutions with a spin flip transition, the anisotropy energy ($K$) is calculated from the area difference between the easy axis $M(H)$ curve and the hard axis $M(H)$ curve [86]. A schematic diagram of the anisotropy energy in an $M(H)$ measurement for an antiferromagnet with a spin flip transition is shown in Fig. 3.32.

Extracting the anisotropy constant from the spin flop case is handled differently. First, we write down the Hamiltonian for the local moment antiferromagnet in three potential spin alignments: the pure AFM aligned case, the canted AFM case which occurs in a spin flop transition, and the polarized FM aligned case. We will consider that the field is applied parallel to the initial alignment of the moments, and that there is anisotropy in the direction perpendicular. In addition, I acknowledge Blundell's book, Chapter 5.2.3, as a

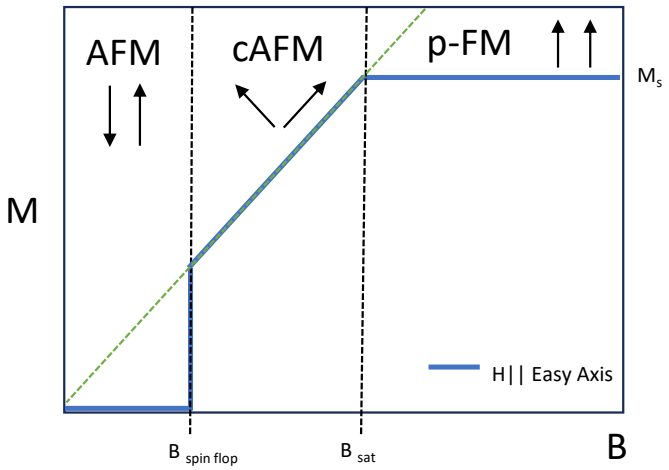


**Figure 3.33:** A schematic diagram of an $M(H)$ measurement for an antiferromagnet with a spin flop transition. The AFM, cAFM, and polarized FM (p-FM) states are bounded by the black dashed lines. $B_{\text{spin flop}}$ is the field at which the AFM-cAFM spin flop transition occurs. $B_{\text{sat}}$ is the field at which the magnetization saturates to $M_s$. The green dashed line is the slope of the magnetization in the cAFM region and can be used to find the anisotropy energy according to 3.8.

significant reference [76].

In the ground state AFM aligned case, there is the exchange energy, as well as an anisotropy energy term $K$.

$$\epsilon_{AFM} = -AM^2 - K \tag{3.1}$$

The canted AFM state (shown in the middle of Fig. 3.30(b)) occurs at an applied field, so there is an additional Zeeman term to describe the energy of a magnetic moment in a magnetic field. In the ferromagnetic case, $\epsilon_{\text{Zeeman}} = -M \cdot B$, however, in this canted AFM state, we are simultaneously considering two moments so $\epsilon_{\text{Zeeman}} = -2MB\cos\theta$, where the angle $\theta$ is the angle between the moment and the applied field. We will also modify the exchange term and the anisotropy term by some function of $\theta$ to account for the new alignment and the result is (Blundell Eq. 5.29):

$$\epsilon_{cAFM} = AM^2\cos(2\theta) - 2MB\cos\theta - K\cos^2\theta. \tag{3.2}$$

The expression for the polarized FM state is

$$\epsilon_{\text{polarized FM}} = AM^2 - 2MB - K. \tag{3.3}$$

By minimizing Eq. 3.2 (taking $\partial E/\partial\theta = 0$), we find $\cos\theta$ to be[17]

[17]Blundell ignores the anisotropy term to get $\cos\theta = \frac{MB}{2AM^2}$. While this makes the arithmetic easier, I'm not comfortable ignoring a term that we are trying to solve for. Therefore, I will demonstrate that leaving the term in yields the same result.

$$\cos\theta = \frac{MB}{2AM^2 - K}. \tag{3.4}$$

We will substitute Eq. 3.4 into Eq. 3.2 in a moment. Before we do, we recognize that the field at which the spin flop occurs ($B_{\text{flop}}$) is when the energies of the AFM state and the canted state are equal. That is,

$$\epsilon_{cAFM} = \epsilon_{AFM}$$

$$AM^2(2\cos^2\theta - 1) - 2MB_{\text{flop}}\cos\theta - K\cos^2\theta = -AM^2 - K$$

$$2AM^2\cos^2\theta - 2MB_{\text{flop}}\cos\theta - K\cos^2\theta = -K$$

$$(2AM^2 - K)\cos^2\theta - 2MB_{\text{flop}}\cos\theta = -K$$

$$(2AM^2 - K)\frac{(MB_{\text{flop}})^2}{(2AM^2 - K)^2} - 2MB_{\text{flop}}\frac{(MB_{\text{flop}})}{2AM^2 - K} = -K$$

$$\frac{(MB_{\text{flop}})^2}{(2AM^2 - K)} - 2\frac{(MB_{\text{flop}})^2}{2AM^2 - K} = -K$$

$$K = \frac{(MB_{\text{flop}})^2}{2AM^2 - K} \tag{3.5}$$

Next, we look at Eq. 3.4 under the condition that $\theta = 0$ which occurs when the magnet is saturated at $B_{\text{sat}}$.

$$1 = \frac{MB_{\text{sat}}}{2AM^2 - K}$$

$$MB_{\text{sat}} = 2AM^2 - K \tag{3.6}$$

Since both $M$ and $B_{\text{sat}}$ are measurable quantities, we can substitute Eq. 3.6 in for the denominator of Eq. 3.5 to get an expression for $K$ that can be solved with information from an $M(H)$ measurement.

$$K = \frac{M_s(B_{\text{spin flop}})^2}{B_{\text{sat}}} \tag{3.7}$$

$$K = \frac{(B_{\text{spin flop}})^2}{B_{\text{sat}}/M_s} \tag{3.8}$$

In Eq. 3.7, $M_s$, $B_{\text{spin flop}}$ and $B_{\text{sat}}$ are all quantities that can be extracted from an $M(H)$ measurement shown schematically in Fig. 3.33. Eq. 3.8 is for spin flop antiferromagnets, such as $Y_2Co_3$ [167], where $B_{\text{sat}}$ cannot be achieved with the available applied field. In these cases, the slope of the magnetization in the canted spin region after the spin flop, depicted as the green dashed line in Fig. 3.33, can be used. The inverse of this slope is $B_{\text{sat}}/M_s$, the denominator of Eq. 3.8

We can also use the expressions for $\epsilon_{pFM}$, $\epsilon_{AFM}$ and $\epsilon_{cAFM}$ to solve for the exchange energy ($AM^2$) in the spin flip and spin flop cases. For the spin flip case, the spin flip occurs when the energies of the AFM state and the polarized FM state are equal.

$$\epsilon_{AFM} = \epsilon_{pFM}$$

$$AM^2 = M_s B_{\text{spin flip}}$$

For the spin flop case, we just have to re-arrange Eq. 3.6 to get the exchange energy

$$AM^2 = \frac{MB_{\text{sat}} + K}{2} \tag{3.9}$$

### 3.4.6 A Study of Lattice Parameters

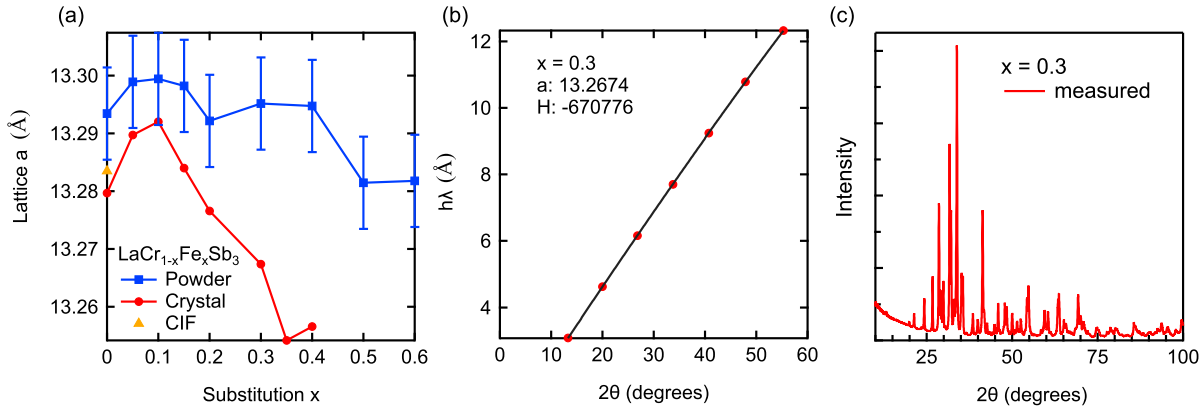


**Figure 3.34:** (a) The $a$ lattice parameter determined by powder data refinement, single crystal diffraction in the PXRD, and from the CIF file as reported by Ferguson *et al.* [91]. The error bars on the powder refinement originate from 15 measurements of Si powder made by different members of our research group. (b) By measuring a single crystal in the PXRD, only the peaks associated with the $a$ lattice parameter are measured. The location of these peaks can be fit to a line to get the lattice parameter [168]. (c) A powder x-ray pattern can be fit to a functional form using GSAS-II where the lattice parameters can be extracted.

Although we find the magnetic properties of $LaCr_{1-x}Fe_xSb_3$ to evolve with $x$ in a manner consistent with theory, one potential criticism of this project is the lack of an experimental measurement of the substitution percentage. Elemental composition can be measured with techniques such as x-ray photoelectron spectroscopy (XPS), wavelength-dispersive x-ray spectroscopy (WDS), energy dispersive x-ray spectroscopy (EDS) or electron microprobe (EMP). These methods involve bombarding the sample with an electron beam or x-rays and analyzing the energies of the emitted electrons (XPS) or x-rays (WDS, EDS). Since elements have a unique emission spectra, these methods can determine the presence of elements, as well as the proportion of elements in the sample.

There are labs that specialize in these techniques, and universities often have shared characterization facilities so labs can make use of these techniques as necessary. Practically, however, the difficulty of setting up an experiment in another lab is proportional to $e^{r/1\,m}$, where $r$ is the distance from that lab to your lab in meters. As a result, we try to do as much characterization in our lab as possible before branching out to other labs or facilities.

Besides phase confirmation, we can leverage our PXRD to check if the lattice parameters change as a function of substitution. Fe is smaller than Cr, so naively, we would expect the lattice parameters to shrink with increasing Fe substitution. Figure 3.34(a) shows the results of this analysis and is somewhat in agreement with our expectation. From the lattice parameter as a function of $x$ data, it would be possible to calculate the substitution using Vegard's Law [169, 170]. Vegard's law describes the phenomenological

observation that the lattice parameter changes linearly with substitution between the two parent compounds. Unfortunately, the fully-substituted compound, $LaFeSb_3$, does not exist.

The blue data points are derived from powder diffraction data (an example of which is shown in Fig. 3.34(c)) where the lattice parameters are calculated from 'refining,' that is, fitting a many-parameter function to the powder data, using free GSAS-II software. Using GSAS-II is an art, when to select which parameter to fit is only pseudo-formulaic, and takes some experience.

Putting a single crystal in the PXRD machine and measuring only the peaks associated with a single lattice parameter is an alternative and more tractable approach. This method is detailed by Jesche *et al.* [168] and involves fitting a line to the measured peaks as shown in Fig. 3.34(b). This method has a number of advantages compared to the powder and GSAS-II refinement method. First, it is non-destructive so its possible to check the lattice parameter before running subsequent measurements in the MPMS and the PPMS. Second, since the expected location of the diffraction peaks is known, the measurement sequence can be tailored to spend more time measuring only in those expected ranges of $\theta$, yielding sharper peaks and potentially a more accurate lattice constant. Third, fitting the data to the simple functional form can be done in any programming language. One limitation is that depending on the shape of the crystal, certain orientations, and therefore lattice parameters, are not possible to measure. Since $LaCr_{1-x}Fe_xSb_3$ grows as a rectangle where the $b$ and $c$ directions are in plane, the only lattice constant that is possible to measure using this method is $a$ (results shown in red in Fig. 3.34(a)).

# Chapter 4

# An Overview of Experimental Progress

In an effort to get to the science as quickly as possible, I have saved my discussion of instrumentation and experimental techniques for the end. Saving it for the end is in itself an indication of a crossover in mentality.

While working in the Moler Lab as an undergraduate, I was puzzled that the graduate students would rather farm out tasks like replacing failed capacitors, designing circuit boards and changing pump oil to an eager undergrad than do them themselves. At the time, I found jobs such as those more interesting than running MATLAB simulations, testing SQUIDs or measuring samples. When I asked why grad students rolled their eyes at having to machine a part or design a circuit board, Zheng Cui just sighed and said, "one day you'll understand."

Although I have gone through a slow, continuous, crossover from a focus on these experimental methods to the underlying physics, the nitty gritty of experimental physics are the parts that made me want to stay in the field, and the tasks that I still very much value to this day.

In the next sections, I will cover some advanced topics regarding the use of our two primary characterization instruments, the MPMS and the PPMS. The following sections are not a 'basics of the MPMS and PPMS', nor are they a 'how-to' guide. In his PhD thesis, Jackson Badger covered those more fundamental details. Building on his foundation, I have decided to go over more involved details. First, I will finally discuss the importance of sample alignment in the MPMS, especially when measuring ferromagnets along their hard axis. Then, I will highlight a few of the times the MPMS has broken, and how we repaired the instrument without any guidance from Quantum Design. Finally, I will detail some 'tips and tricks' that I learned while setting up resistivity measurements in the PPMS.

## 4.1 The Magnetic Property Measurement System

### 4.1.1 The Importance of Radial Alignment for Hard Axis Ferromagnets

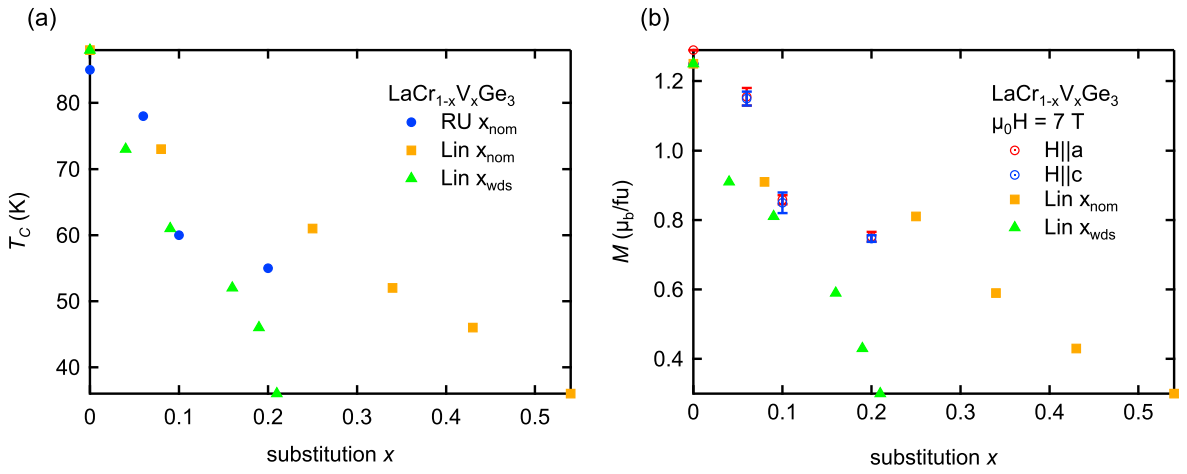


**Figure 4.1:** The reduction of (a) Curie temperature ($T_C$) and (b) magnetization at $\mu_0 H = 7$ T as increasing amounts of nonmagnetic V is substituted in for magnetic Cr is our evidence that our V-substitution is successful. In both plots, we also show the values reported by Ref. [11] (yellow squares and green triangle), and we note that our $x_{\text{nom}} = 0.1$ sample is in particularly good agreement with their $x_{\text{WDS}} = 0.09$ sample measured by wavelength-dispersive x-ray spectroscopy (WDS).

As mentioned in the short history (Section 2.1), our decision to revisit magnetization in $LaCrGe_3$ was inspired by the realization by Hafner *et al.* [3] that certain ferromagnets order along their hard magnetic axis, coupled with data presented by Lin *et al.* that such a phenomenon could be achieved in the $LaCr_{1-x}V_xGe_3$ system.

In the publication [Phys. Rev. B **88**, 094405 (2013)], Lin *et al.* present a study of the effects of V substitution for Cr in the ferromagnetic compound $LaCrGe_3$. As part of their magnetic characterization of their $LaV_xCr_{1-x}Ge_3$ samples, they present low temperature magnetization as a function of applied magnetic field measurements which depict a peculiar case where the $H||ab$ magnetization saturates to a value 10% larger than when $H||c$ (refer to Fig. 2.1(b)). Since this phenomenon does not clearly appear in $LaCrGe_3$, one may suspect V-substitution causes this so-called 'hard-axis ordering.' We regrew samples of $LaCr_{1-x}V_xGe_3$ with $x_{\text{nom}} = 0.06$, 0.1, and 0.2 and repeated the magnetization measurements and found no such feature. We were, however, able to reproduce the feature by intentionally mis-aligning the samples in our SQUID magnetometer, which emphasizes the importance of sample alignment during magnetic characterization, especially when studying anisotropic ferromagnets.

Hard axis ordering describes the case in which ferromagnetic (FM) moments order along the crystal electric field (CEF) hard axis rather than along the easy axis, as traditionally expected. This peculiar hard

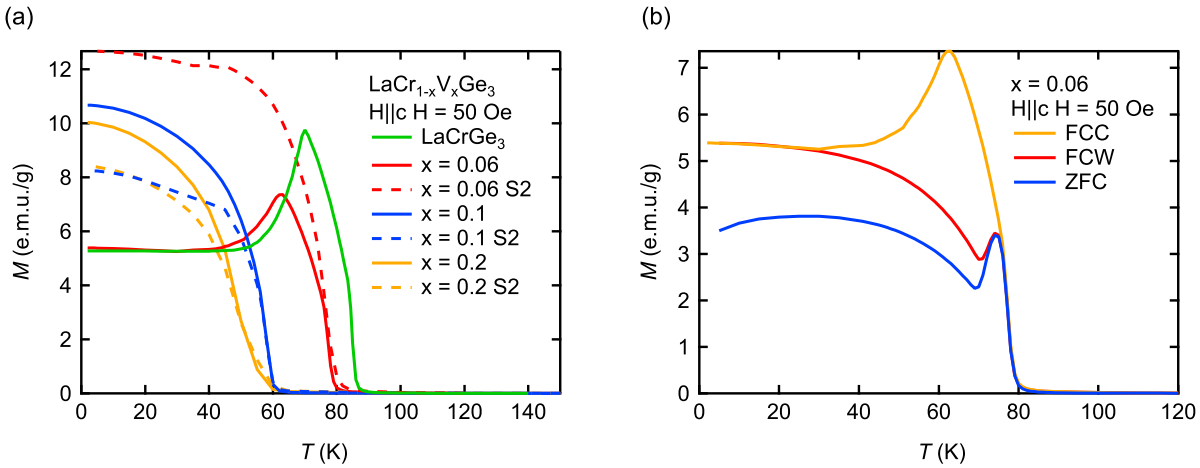


**Figure 4.2:** (a) Magnetization as a function of temperature measurements in a low applied field (50 Oe) across a variety of V substituted samples. $T_C$ is suppressed as V substitition is increased, however, clear features of high temperature domain pinning disappear above $x = 0.06$. (b) A small (0.06) nominal V substitution suppresses $T_C$, but the features of domain pinning and depinning found in the FCC, FCW, and ZFC magnetization of $LaCrGe_3$ remain.

axis ordering phenomenon has been noticed to exist in Kondo-lattice (KL) ferromagnets [3] and perhaps in metallic ferromagnets in general [171]. One consequence of hard axis ordering is clearly shown in $CeAgSb_2$, a well-studied KL ferromagnet ($T_C = 10\,K$), where the spontaneous magnetization ($M_s$) is different along the hard axis compared to the easy axis [172, 173, 174, 175](refer to Fig. 4.9(b)). Hard axis ordering shatters our textbook rotating-moment-based understanding of ferromagnetism, where $M_s$ is identical along both axes, and therefore ruins any calculation that assumes a single rotating moment picture (e.g., the anisotropy and demagnetization calculations discussed in Sections 2.4.3 and 2.4.1, respectively).

In KL systems, however, ferromagnetic ordering is achieved by Ruderman-Kittel-Kasuya-Yosida (RKKY) interactions, and this conduction electron mediated interaction between local magnetic moments is notoriously difficult to compute. As such, we were interested in exploring the phenomenon in a system without the complications of Kondo and RKKY interactions.

We found the possibility of hard axis ordering in this system exciting for a number of reasons. First, hard axis ordering in the Cr-based 3d electron ferromagnet might be easier to model, calculate, or explain compared to KL ferromagnets [176]. In addition, we wondered whether hard axis ordering could be related to the unusual magnetization as a function of temperature ($M(T)$) curves or coercivity anomaly observed in $LaCrGe_3$ [10, 37]. If our $LaV_xCr_{1-x}Ge_3$ samples exhibit hard axis ordering behavior, we could also study the phenomenon at high fields to test the limits of the hard axis and easy axis saturating to different moments.

To further explore the hard axis ordering phenomenon, we synthesized our own single crystal samples of $LaV_xCr_{1-x}Ge_3$, with $x_{nom} = 0.06, 0.1, 0.2$ with a similar procedure to Lin *et al.* [11]. In addition, we use a similar SQUID-based Quantum Design Magnetic Property Measurement System (MPMS) for our magnetic

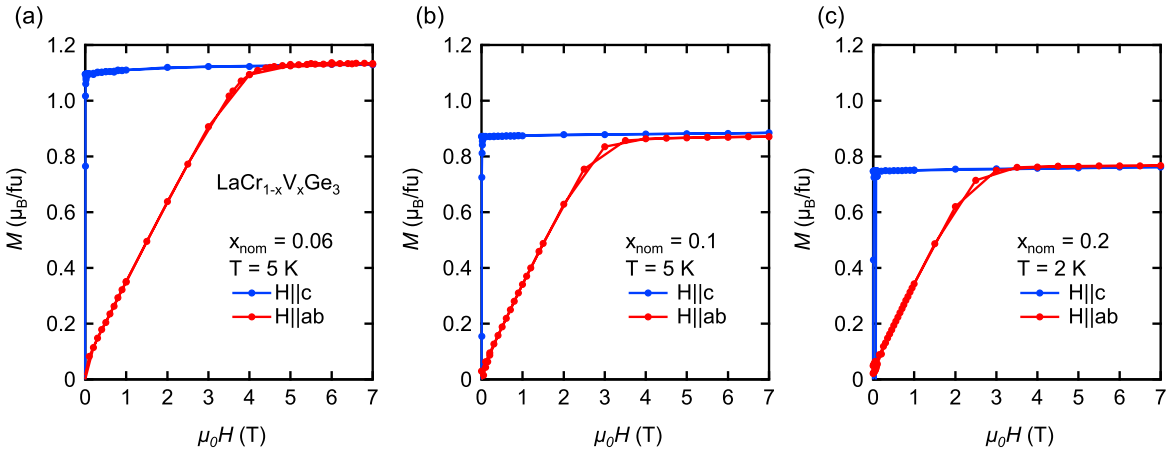


**Figure 4.3:** The results from measuring magnetization as a function of applied magnetic field ($M(H)$) along the easy axis ($H||c$) and hard plane ($H||ab$) in $LaCr_{1-x}V_xGe_3$. When care is taken to align the hard axis with the applied field, and to radially center the sample in the sample chamber, the magnetization saturates to the same value as that of the easy axis. This is the expected case in contradiction to Lin *et al.*, who published data with a significant measurement artifact that could lead to the incorrect conclusion that V-substitution induces hard axis ordering in $LaCrGe_3$ [11].

characterization. In Fig. 4.1 we show the reduction of Curie temperature ($T_C$) as well as the reduction in magnetization expected when substituting nonmagnetic V in place of magnetic Cr and consistent with Ref. [11]. $M(T)$ plots of our La(Cr,V)$Ge_3$ substitutions are shown in Fig. 4.2. Our anisotropic $M(H)$ data is shown in Fig. 4.3, and we find $M$ saturates to the same value for both $H||ab$ and $H||c$ measurements for all substitutions grown. Our results, somewhat unsatisfyingly, contradict Ref. [11] and do not show evidence for hard axis ordering.

After further investigation, we were able to determine that the discrepancy between $M_s$ along the hard axis compared to the easy axis observed in Ref. [11] is a measurement artifact attributed to poor sample alignment in the MPMS. In Fig. 4.4 we show the importance of radial centering in the MPMS sample chamber when measuring ferromagnets along a hard axis. When the sample is well-centered, the hard axis and easy axis magnetizations agree at high fields and the goodness of fit is over 99%.

We are able to reproduce the measurements in Lin *et al.* [11], by intentionally mounting the sample such that it is far from the radial center of the sample chamber. When this 'bad' alignment is used (red line in Fig. 4.4(a)), the goodness of fit shown in Fig. 4.4(b) and Fig. 4.4(c) is reduced by 5%, which results in over a 10% increase in magnetization over the 'best' alignment (green line). Such a large enhancement of the $H||ab$ magnetization from a comparatively small reduction in the goodness of fit is surprising, and unfortunately, misleading. If this discrepancy between the $H||c$ and $H||ab$ magnetization was indeed real, $LaCr_{1-x}V_xGe_3$ would be a compelling platform to study hard axis ordering. The conclusions we draw from magnetic characterization, however, rely on accurate data.

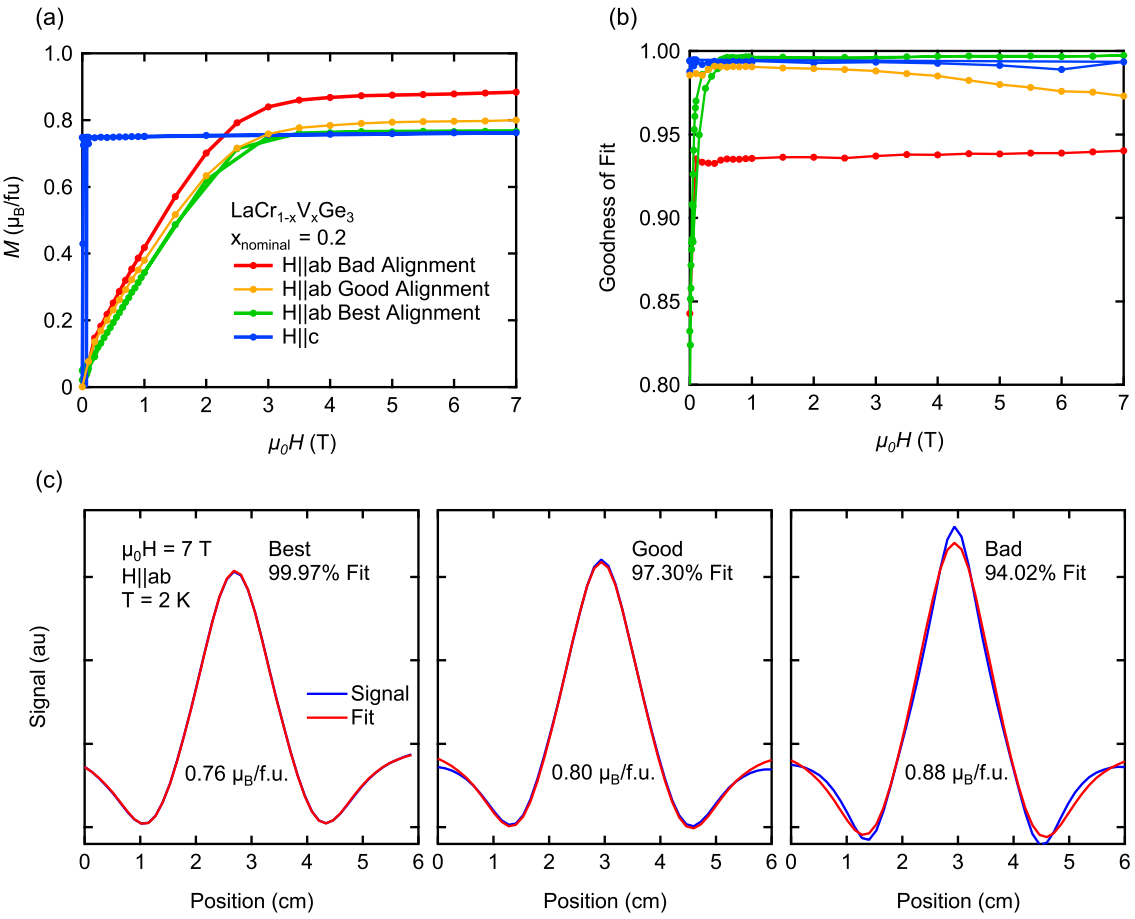


**Figure 4.4:** (a) $M(H)$ for different sample alignments of the same $LaCr_{1-x}V_xGe_3$ ($x_{\text{nominal}} = 0.2$) single crystal. We find that when measuring uniaxial ferromagnets along the hard axis, the measurement is sensitive to the radial centering of the sample in the sample chamber. When care is taken to center the sample axially in the chamber, the easy axis and the hard axis magnetizations saturate to the same value, as shown by the blue curve and the green curve, respectively. When the hard axis of the sample is mounted off-center in the sample chamber, however, significant measurement artifacts can occur. In this case, the measured magnetization exceeds the well-aligned value, as shown by the yellow and red curves. (b) A comparison of the goodness of fits across the different sample alignments. Interestingly, a 5% reduction in the goodness of fit can result in a 10% error in the resulting magnetization. (c) A comparison of the raw voltage signal and the calculated fit from the MPMS across the different hard axis alignments. Although the 'Good' and 'Bad' alignments might appear to be acceptable, they are unsatisfactory, especially when comparisons to other axes are made.

This result reinforces the care required to obtain accurate magnetization measurements in the MPMS, as there is history of sample alignment causing measurement artifacts in the MPMS. For example, thin film superconductors were found to exhibit a paramagnetic signal when mounted in certain ways due to the slight non-uniformity of the magnetic field [177]. Furthermore, a different Quantum Design application note details sample mounting techniques and specifically states that "measurement accuracy is dependent on the sample's radial position—how well it is positioned along the gradiometer centerline" [178]. With regards to hard axis ferromagnets, we detail how different hard axis ferromagnet alignment problems manifest in the data in Fig. 4.5. We believe that this is useful information for research labs who perform these measurements, as well as researchers interpreting published magnetization data.

To summarize, we regrew samples of $LaCr_{1-x}V_xGe_3$ and discovered agreement in the $M_s$ along each axis which makes hard axis ordering in this system unlikely. We also found that the anisotropic $M_s$ presented in a previous study by Lin *et al.* was a measurement artifact due to poor radial alignment, highlighting the importance of sample mounting for accurate measurements in an MPMS.

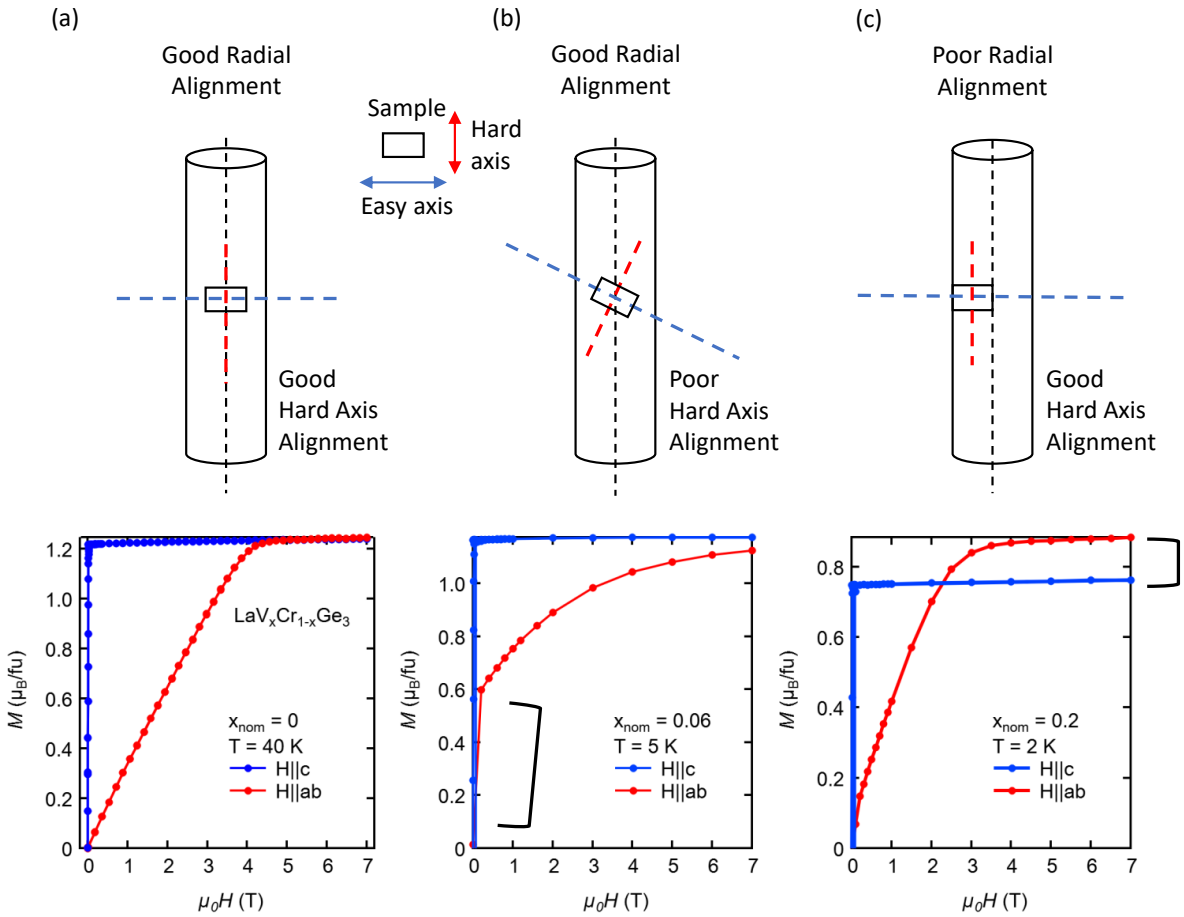


**Figure 4.5:** A schematic of different hard axis sample alignments and their effect on magnetization data. (a) When the sample is aligned in the center of the sample chamber and the hard axis is aligned with the magnetic field direction, the moment saturates to the same value and the pre-saturation magnetization forms a line that passes through the origin. (b) When the hard axis of the sample is not parallel to the field, there is an initial jump in $M$ (indicated with the black brace) which originates from the easy axis contribution which saturates with a small applied field. (c) In this case, the hard axis alignment is decent since the line formed by the pre-saturation $M$ nearly goes through the origin. The sample is not, however, well centered radially in the sample chamber which leads to measurement artifacts. In this case, the hard axis magnetization saturates to a higher value than the easy axis magnetization. One way to improve the radial alignment is to use centering caps at the end of the sample holder to help keep it straight.

**Sample mounting methods used in this experiment**

The 'Best' axial alignment (referenced in Fig. 4.4) is achieved with an acetate strip that sit in the middle of the straw. The sample is held in place on the strip with a small amount of Apiezon N grease. This mounting method is shown and diagrammed schematically in Fig. 4.6. In addition, this method is especially useful for delicate samples since there is no pressure exerted on the sample. An alternative mounting method which does not use grease, but only works for robust samples, is diagrammed in Fig. 4.7.

The 'Good' and 'Bad' alignments both used a variation of the standard 'three straw' method that (by design) pushes the sample to one side of the straw. The sample was kept on the acetate strip used in the best method, but a slit straw and a cocktail straw were used to push that strip off to the side. The difference between the 'Good' and 'Bad' alignments is simply a 180° rotation of the sample rod in the instrument, which is enough to make the raw scan data look reasonable to unacceptable. The typical 'three straw' sample mounting method is shown and diagrammed schematically in Fig. 4.8.

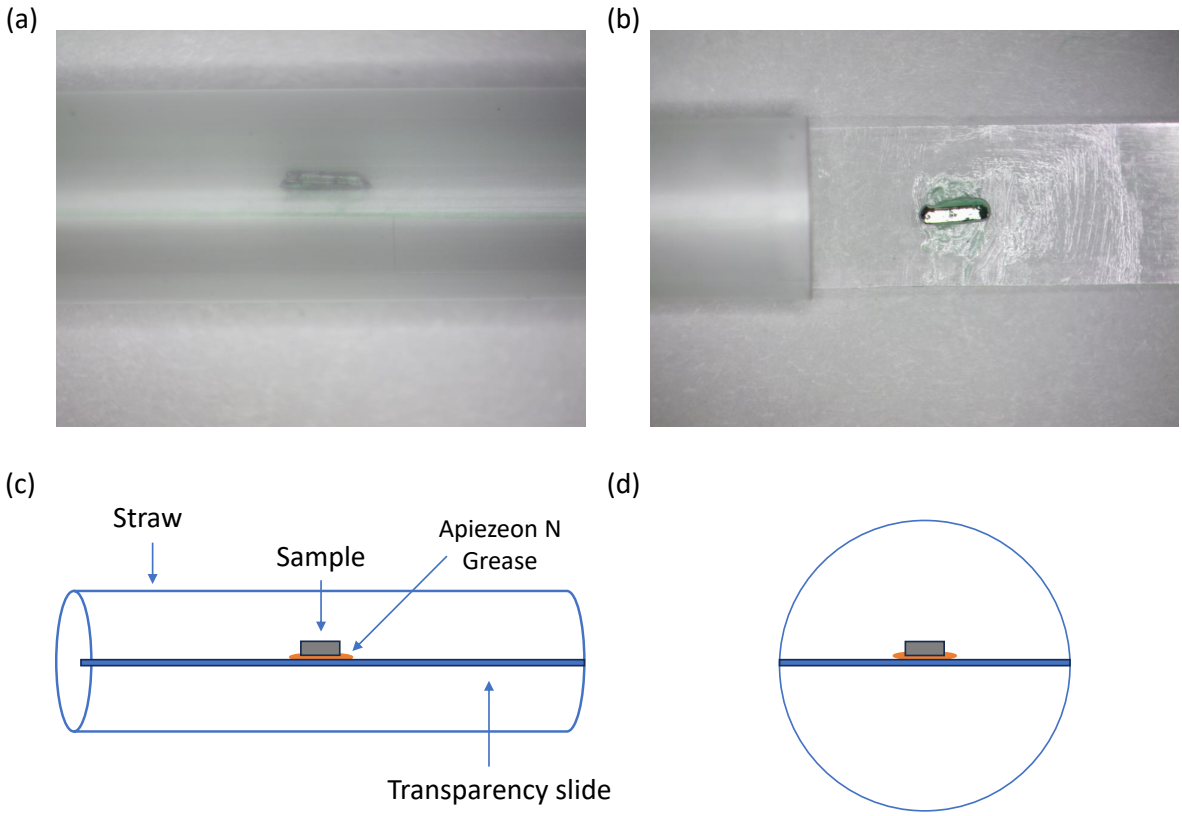


**Figure 4.6:** One mounting method that results in an axially centered sample is to cut an overhead transparency slide into a strip that can fit in the middle of a straw. These transparency slides usually have a coating on them, so they must first be cleaned with ethanol and a Kimwipe. The width of the strip is important; too wide and it will not fit, too narrow and it will not stay in place. The sample is affixed to the middle of the strip with a small amount of Apiezon N grease. (a) A photograph of what the sample looks like when it is mounting correctly. Notice how it is well aligned in the middle of the straw. (b) A photograph of the sample held in place with grease on the strip before being inserted into the straw. (c) and (d) are schematic diagrams intended to clarify how the transparency slide mounting method works.

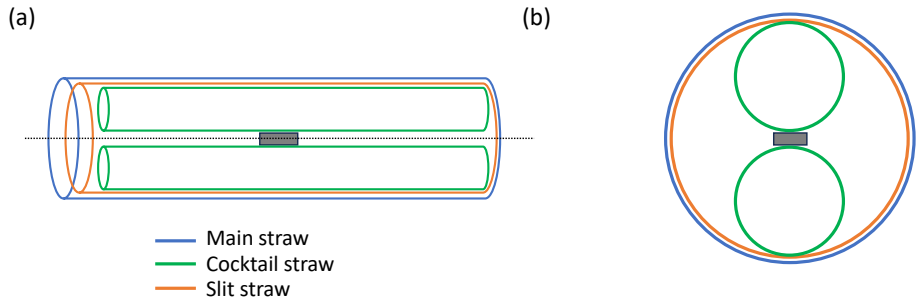


**Figure 4.7:** An alternative to the transparency slide method shown in Fig. 4.6 which still results in good axial alignment is the 'cocktail straw' method. The sample is held in between two cocktails straws (cocktail straws have a smaller diameter than regular drinking straws) which are squeezed together by a slit straw. The entire assembly is then inserted into an unmodified straw. This method does not use grease, which is preferable for samples with a small magnetic response. This method is, however, only suited to a particular shape and robustness of sample. (a) and (b) are schematic diagrams intended to clarify how the cocktail straw method of sample mounting works.

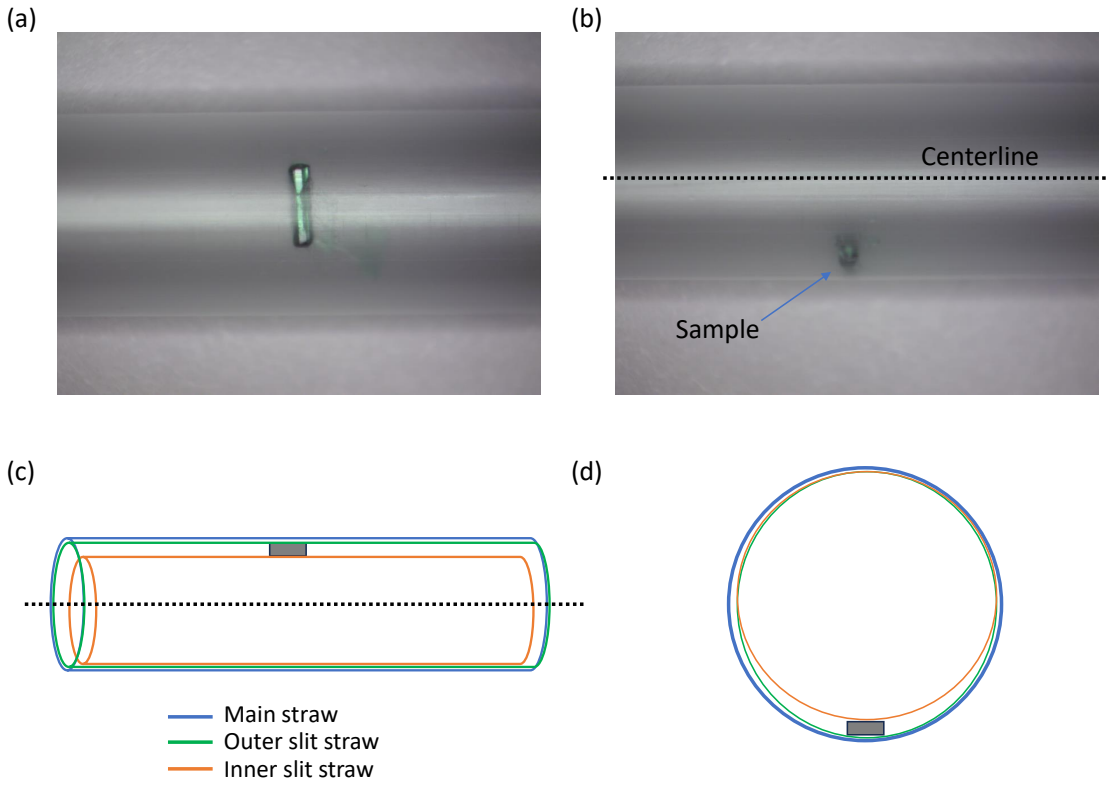


**Figure 4.8:** The three straw method involves an unmodified straw and two straws that have been shortened and slit along their length. The sample is held between these two slit straws which wrap around each other lengthwise. With the sample held in place between these two straws, the assembly is inserted into the unmodified straw. (a) Since the three straw method holds the sample in place by squeezing it between straws, it only works with robust samples. Thin and brittle samples will simply break. (b) By simply rotating the straw from the position shown in (a), it is easier to see how far away from the center the sample is held. (c) and (d) are schematic diagrams intended to clarify how the three straw method works. These also show how far off-center the sample is held using this method.

### Is Hard Axis Ordering Real?

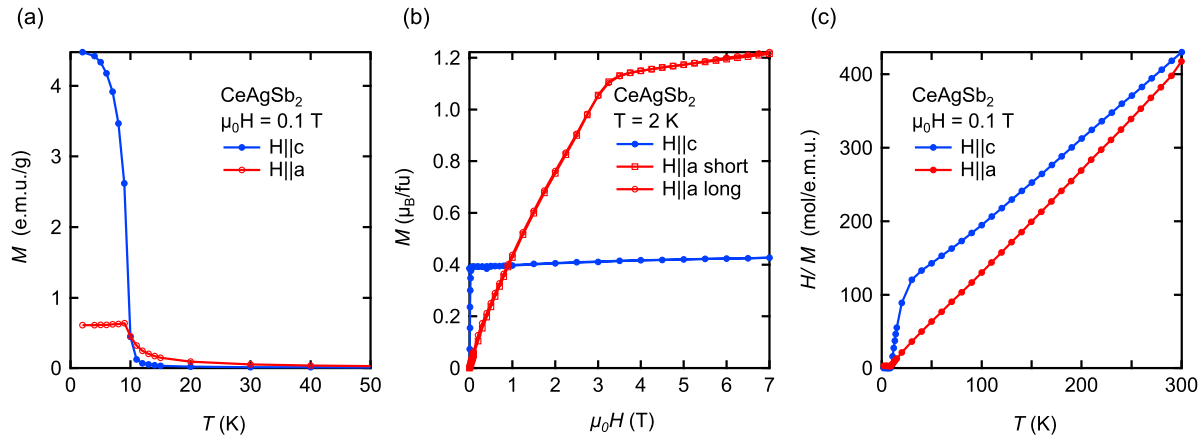


**Figure 4.9:** Magnetization measurements along each axis of $CeAgSb_2$ ($T_C = 9.6\,K$ [172, 175]). These measurements match those reported in Refs. [172, 175]. (a) In field-cooled $M(T)$, $M_c$ saturates to a higher value than $M_a$, which means that the $c$ axis is considered the "order axis." (b) $M(H)$ further shows that the $c$ axis is the order axis because $M_c$ appears to be saturated at nearly zero field. At higher fields, however, $M_a$ surpasses $M_c$ and saturates to a value nearly 3 times larger. With the larger $M_a$ in mind, the $c$ axis may be considered a hard axis. In (b), I also show how $M_a$ along each $a$ direction of the crystal is the same, confirming that a difference in demagnetization factor is not significant. (c) By plotting $H/M$ v. $T$, we find that above $T_C$, $M_c < M_a$, and $M_c$ does not follow Curie-Weiss theory.

After the realization that it is possibly, if not likely, for alignment issues to cause the hard axis magnetization to appear to saturate to a significantly larger value than the easy axis magnetization, we wondered if these issues were the cause of hard axis ordering magnetization in other compounds.

While the Kondo-lattice systems identified by Hafner *et al.* [3] were determined to order along the hard axis with AC magnetic susceptibility measurements,[1] $CeAgSb_2$ seems to reveal hard axis ordering in DC magnetization [172, 175]. Although the hard axis is shown to saturate to a value that is 300% larger than the easy axis (compared to the 10% in the erroneous La(Cr,V)$Ge_3$ measurements), we grew our own samples of $CeAgSb_2$[2] to see if the phenomenon can also be attributed to bad radial centering.

The results of my measurements on $CeAgSb_2$ are shown in Fig. 4.9. For these measurements, I used the acetate strip method to mount the sample in the radial center of the MPMS chamber. These results match the ones reported in Refs. [172, 175]. $CeAgSb_2$ has a tetragonal [179, 180] ($a = b$, $a \neq c$) crystal structure and grows in large rectangular plates. We had a suspicion that demagnetization factors might cause a discrepancy in $M(H)$, so we measured both $a$ directions (the in-plane directions) which had different dimensions on our particular sample. As seen in Fig. 4.9(b), the two $H||a$ magnetizations match exactly, so

[1] We don't currently have an easy to perform AC magnetic susceptibility. Setting one up would involve winding a coil around a sample which is possible, but not as turnkey as our DC magnetization apparatus.

[2] $CeAgSb_2$ were grown following the simple method detailed in Nikitin *et al.* [175], which is the same as in Myers *et al.* [172] except for a slightly lower maximum temperature. High purity Ce, Ag and Sb were placed in a Canfield Crucible Set in a molar ratio. The crucible set is sealed in a quartz ampoule and heated to 1180°C before cooling over 100 hours to 670°C when the excess Sb liquid flux was decanted in a centrifuge. The crystals grow as large (often crucible-limited) plates.

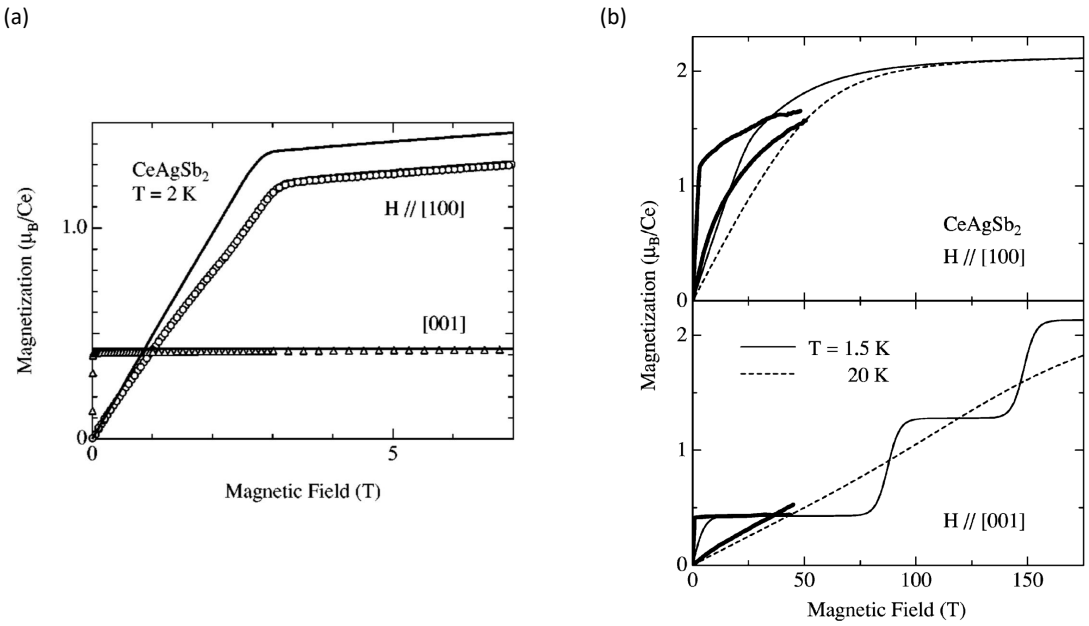


**Figure 4.10:** (a) Araki *et al.* [174] developed a theory based on crystal electric field (CEF) that reproduces the hard axis ordering magnetization curves found in $CeAgSb_2$. In this figure, the solid lines are their theory, while their data is shown as circles (H||c H//[001]) and triangles (H||a, H//[100]). (b) Takeuchi *et al.* [173] measured the anisotropic magnetization of $CeAgSb_2$ up applied fields of 50 T (shown as the thick black lines in both panels). They also developed a CEF theory that predicted that $M_c$ will increase in steps due to $4f$ level crossings (shown as the thin solid black line for $T < T_C$ and dashed line for $T = 20$ K in both panels). In order to observe the steps in the H||c magnetization, a future experiment would need to go up to at least 100 T.

demagnetization factors are not responsible for hard axis ordering in this compound.

Another avenue of exploration we considered was to see how robust to applied field the anisotropic magnetization is. That is, if we apply even higher fields, will the saturation moments along each axis eventually coincide? High field measurements were already performed up to 50 T by Takeuchi *et al.* [173], and they were shown to match the theoretical analysis of the magnetic properties due to crystal electric field (CEF) [174, 173]. Interestingly, the CEF theory shows that the $H||c$ magnetization will increase in steps due to CEF level crossings [174, 173], until $M$ along each axis finally saturates to the same value at 150 T. In conclusion, hard axis ordering in DC magnetization is possible, and $CeAgSb_2$ is a clear example.

### 4.1.2 Troubleshooting and Repair of a 20 Year Old Instrument

Theseus is the mythical founder king of Athens, and his ship needed to be repaired many times to make his yearly pilgrimage to honor the god Apollo. The question posed by philosophers is as follows, "if every part of the ship of Theseus has been replaced, is it the same ship?" The same question can be posed to our beloved Magnetic Property Measurement System, our MPMS.

The property tag on our Quantum Design reads 983011099 which means that it was purchased in 1998. The workhorse machine had lived through the graduate students of Robert Shelton, Kai Liu, Zack Fisk, and Nicholas Curro before becoming an integral member of the Taufour lab. It was 2018 when I began taking measurements with the MPMS, and as with any 20-year-old machine, there is repair and maintenance involved in keeping it working. Since I believe that repair and maintenance is core to experimental physics, and often troubleshooting broken machinery was the most enjoyable part of my day in the lab,[3] here, I recant the repairs I have made to our MPMS. Some are major, and some are minor, but they were all critical in keeping the MPMS operational and able to measure the magnetization of $LaCrGe_3$ and $LaCr_{1-x}Fe_xSb_3$ that makes up the majority of this thesis.

The first catastrophic failure took place while the Taufour lab was being built, and the MPMS sat in Professor Curro's lab. The vacuum pump used for evacuating the sample chamber and for reaching temperatures below 4.2 K, sprung an oil leak. In rotary-vane-based vacuum pumps like this Edwards RV5, oil is used to lubricate the composite vanes as they spin in a steel housing to create a negative pressure by scooping the air from a large volume and forcing it into a smaller one. In this case, the rubber shaft seals that keep the oil in the pump while allowing the shaft to rotate had failed. The fouled shaft seals caused the oil to leak out of the pump and consequently, the vanes to heat up and fail as well. Although the vanes and the shaft seals are prone to wear by design, the clean up and repair of the pump was exacerbated by the fact that the pump did not undergo regular maintenance. Since the pump was difficult to access under the MPMS cabinet, the oil was never flushed and changed, rather it was just topped off periodically when the oil level ran low.[4] As a result, instead of a clear low-viscosity liquid, the oil had become a dark sludge. By taking the pump apart, cleaning off all of the sticky oil residue, and replacing the worn parts with those from a $275 rebuild kit from Duniway.com,[5] we were able to put the pump back into service. The documentation of the process is my most-viewed Youtube video,[6] and since posting it, I received comments from quite a few

[3] Valentin is completely correct when he said that spending all of your time fixing vacuum pumps will not earn you a PhD. While not a *sufficient* condition, fixing vacuum pumps was a *necessary* part of this PhD.

[4] Given the orientation of the pump in the bottom section of the MPMS electronics cabinet, the oil sight glass was not directly visible. Quantum Design did have a semi-conveniently placed mirror in the cabinet that made the oil level possible to check, however, it is possible that the oil was only topped up when someone noticed that the oil-mist trap on the exhaust had become full. If the pump were more easily accessible, people would be more likely to give it periodic oil changes.

[5] A new Edwards RV5 costs $3000-$5000.

[6] https://www.youtube.com/watch?v=JBNMkr0HRO0

people from labs on campus, across the United States, and in other countries. While many reached out for help with their vacuum pumps, some just commented to say that my video was the inspiration they needed to repair it themselves rather than send to a service center, or buy a whole new pump altogether.

My first magnetization measurement ($M(T)$ on $LaCrGe_3$) was unusable due to an unstable SQUID signal, evident by the unpredictable spikes in the SQUID response, which led to bad data points. Disconnecting and reconnecting the yellow triaxial cables which carry the SQUID signal to the pre-amplifier seemed to help, but the flaky SQUID response would always return.[7] One way to get around this problem was to take 2 or 3 individual scans at each data point and then manually average the good points in IGOR. Although cables are often a point of failure in experimental physics, triaxial cables are difficult to come by (whereas coaxial BNC cables are abundant). Fortunately, at the time there was a spare MPMS on loan from Quantum Design in a neighboring lab. While it was an even older 5 T model, using that machine's yellow triaxial cables fixed the SQUID response like a charm, and we have not had the same problem since. Eventually, that older 5 T MPMS was sold to a group in Japan. I hope Quantum Design gave them new cables.

The next major failure occurred when I was measuring hysteresis loops for the $LaCrGe_3$. All of a sudden, the sample magnetization failed to saturate at high fields. By replacing the $LaCrGe_3$ sample with a paramagnetic Pd standard, we discovered that the measured magnetization also failed to increase with field.[8] There were two possibilities for this occurrence: either the SQUID had died, or the magnet had stopped charging. Since a SQUID failure would be truly catastrophic, we hoped it was a problem with the magnet, and opening up the MPMS electronics cabinet confirmed our suspicion. The superconducting magnet is charged with a very simple linear DC power supply made by Kepco. This type of power supply uses a transformer to step down the voltage from 120 VAC and uses diodes and capacitors to rectify and subsequently smooth out the AC voltage to a DC voltage. We found that large capacitors had lost over 50% of their rated capacitance, and that the diodes had also failed. Replacing the capacitors and diodes with parts overnight shipped from DigiKey was the first time a Weller WES51 soldering station simply did not get hot enough, and a 100W soldering gun was necessary instead. When state-of-the-art machines fail, it is often because of their common, easily replaceable parts. I met with both Quantum Design and Kepco at March Meeting 2023 in Las Vegas. While Quantum Design no longer supports our aging MPMS, they were impressed that we are able to perform "brain surgery" to keep our MPMS alive. Kepco assured me that they still make the same magnet charging power supplies if ours were to fail again.

[7] The SQUID response would curiously become unstable after transferring helium or nitrogen into the machine. This led us to believe that moisture or condensation was an issue, but in reality it was just bad cabling.

[8] We keep three paramagnetic standards to use while troubleshooting the MPMS: a Pd cylinder provided by Quantum Design, a Pt foil, and some $Gd_2O_3$ (gadolinium oxide, which is made by leaving elemental Gd out on the lab bench). As paramagnets, the $M(H)$ curve should linearly increase with field and go through the origin. Not going through the origin means that there is some remanent field, and not increasing with field might indicate a problem with the magnet.

The biggest MPMS failure and multi-day troubleshooting event took place in April 2023. While measuring, the MPMS control software, MultiVu, suddenly locked up with a GPIB[9] error for Address 6 which points to the 1822 MPMS Controller. GPIB errors can often be fixed by restarting the computer, restarting the controller, and checking the GPIB cables themselves. In this case, power cycling the electronics did not help. At first, it seemed to be a connection problem as re-seating some of the boards in the controller seemed to intermittently fix the issue. The 1822 handles all of the MPMS functions besides temperature control, which is handled by a separate 1802 controller. A failure of the 1822 electronics would be devastating given that it is no longer supported by Quantum Design. Fortunately, Peter remembered that a similar GPIB error had previously occurred with the 1802, and it was the power supply that was at fault. Sure enough, opening up the MPMS electronics cabinet to access the enclosed power supply revealed the smoking gun, or should I say, bulging capacitor.

The power supply for the MPMS provides $\pm 15\,\mathrm{V}$[10] as well as $+5\,\mathrm{V}$ to the 1822 controller. The large capacitors in a power supply smooth out and stabilize voltage, and when the capacitors fail, the voltage fluctuates too much, and the electronics they power no longer work properly. In this case, the affected capacitor was connected to the $+5\,\mathrm{V}$ supply line and sure enough, connecting an oscilloscope revealed that the voltage had a significant ripple on it. By disconnecting the faulty $+5\,\mathrm{V}$ supply and replacing it with a laboratory benchtop power supply, we were able to clear the GPIB error and learn that the 1822 controller draws at least $2.2\,\mathrm{A}$, which was surprising given it runs through a relatively thin 20 gauge wire. It is inevitable that the capacitors for the $\pm 15\,\mathrm{V}$ supply will eventually fail, and when that happens, it would make sense to get a single power supply that provides each of the requisite voltages. Until then we are using a separate laptop-style $5\,\mathrm{V}$ power brick that plugs into the wall and we have not had any issues since. It is worth mentioning that the $5\,\mathrm{V}$ supply must be plugged in before the main power switch on the front of the MPMS electronics cabinet is switched on. Otherwise, the SQUID response will be unintelligible.

The MPMS may be over 20 years old, but it was still able to give me the magnetization data that I needed to discover the novel magnetic phenomena I presented in this thesis. Here, I documented some of the more involved repairs that I had to perform so that I could continue to measure $M$. There were certainly more,[11] but this should not be a maintenance log or 'how-to.' This section is intended to show the extent

[9] GPIB stands for General Purpose Instrument Bus, it is an interface developed by HP that is still used for computers to talk to scientific instruments. Name brand (National Instruments) GPIB PCI or PCI Express interface cards are quite expensive $\sim$ \$1000. National Instruments and Keysight also make a similarly priced GPIB-USB cable which would enable the use of compact computers without expansion slots (our PPMS uses this kind of adapter). There is a \$300 GPIB-USB adapter made by Prologix, which may be useful for labs on a budget, but I do not have experience with it.

[10] Positive and negative voltages are usually used to power operational amplifiers, a.k.a. op amps

[11] August 2020. The computer that controls the MPMS failed, and I got to play the part of an IT professional for a day. There were computer crashes and erratic behavior that multiple re-installations of Windows, and hard-drive swaps could not cure. It turned out that the culprits were failed RAM modules. These failed RAM modules caused the repeated corruption of data which is why reinstalling Windows never quite worked. If you have computer problems, Quantum Design will try to sell you a Windows 7 computer for \$3000 claiming that the particular version of MultiVu only works with 32-bit versions of Windows 7.

to which labs can keep research instruments no longer supported by their manufacturer going and how the constraint of limited resources (see: unrestricted funding) makes troubleshooting, repair, and maintenance integral to experimental physics. There will be a time when the MPMS does finally break beyond repair, but until then, experimentalists will find a way to keep it going.

### MPMS Temperature Control Quirks

There is a known problem with the MPMS temperature control that can occur when the temperature is set to 2 K. Even with the best practice of slowly cooling (e.g. wait 1800 seconds at 20 K, 1800 seconds at 5 K) to minimize residual heat in the machine, the temperature can fluctuate erratically about 2 K. When this happens, the solution is to manually set the temperature to 8 K (just something out of the low-temperature range). Once the temperature has stabilized at 8 K, the temperature can then be set to 2 K again and it should stabilize properly.

A more rare occurrence is when the temperature fails to increase out of low temperature mode. When this happens, the temperature remains around 4 K. The solution in this case is to set a lower temperature set point, such as 3 K, and allow the system to stabilize. In addition, there are times when the temperature may get stuck at 4.2 K. This is due to the cooling chamber being filled with liquid helium. The helium will boil off eventually, and the temperature will rise again. Given these behaviors, I would guess that there is a feedback loop that the temperature control gets stuck in, and setting a new setpoint breaks out of the faulty loop. Both of these known temperature problems are examples of why monitoring your experiment often is important. Putting in your sample at 300 K, pressing 'Run' and expecting good data the next morning without periodically checking the status of the instrument is unwise.

### A Word of Caution: Why Our MPMS is Not a User Facility

As I hope I have demonstrated in the $LaCrGe_3$ and $LaCrSb_3$ projects, the MPMS is a versatile characterization tool. Since we are a condensed matter synthesis lab, we have the tool to measure $M$, which to us is a basic characterization. Other labs on campus may also want to measure $M$ every once in a while. As such, it is often that members of other labs will need you to run measurements.

As much as the scientists and engineers at Quantum Design have developed the MPMS so measuring $M$ can be as easy as pressing a button, there are still many factors that the user is in charge of. There is quite the variety of sample types (ferromagnet, antiferromagnet, paramagnet, diamagnet, superconductor and each with their relative strengths) and for each kind, one must think critically about sample mounting,

Replacing the RAM modules kept the computer alive for a few more months until we could get a modern replacement desktop. Contrary to what Quantum Design tells you, Windows 10 works perfectly fine as long as MultiVu is run in compatibility mode.

demagnetization factors, whether the field should be in-plane or out-of-plane and whether a background subtraction needs to be done. While there is plenty to be learned by measuring different kinds of samples, it may take more time than you think, time that you could have spent working on your own projects. It is usually a good idea to help other labs as you might need their help for one of your projects in the future. Furthermore, there is a nonzero chance that you will get on a paper. For example, I measured samples of copper-intercalated bismuth selenide ($Cu_xBi_2Se_3$) that the Vishik lab had already studied with x-ray photoelectron spectroscopy (XPS). The idea was that the samples should have been superconducting, and that we would be able to measure the $T_c$. It turned out, however, that they were not superconducting. Given the initial lack of signal measured, we had to try a few times and be careful about mounting the samples such that there would be minimal background. While this resulted in a publication (Ref. [181]), a number of side projects that required considerably more work did not. There were samples of $MgB_2$, a liquid suspension of iron-oxide nanoparticles, and samples of thin film YBCO that were measured for other groups but never amounted to much. It is not that one should not try to measure samples from other groups, just be sure to weigh the pros and cons beforehand and realize that those measurements will never be as easy or successful as they are initially proposed. I will end this discussion with another Kirtley Rule: "You can't choose your relations, but you can choose your collaborators." So choose wisely.

## 4.2 The Physical Property Measurement System

For the majority of my PhD, I had an irrational fear of the PPMS stemming from one bad experience laying contacts on a sample. I started to believe that the success of your experiment should not depend on your dexterity or the steadiness of your hands, which is why I helped make the spot welder (see Section 4.3). Although the spot welder has micromanipulators, it still has its fair share of difficulties which is why towards the end of my PhD, I developed a penchant for the hand-laid silver epoxy method. Perhaps it was the sense of urgency to finish the measurements on $LaCr_{1-x}Fe_xSb_3$ that overpowered my hesitance to take pictures of a sample, mix up silver epoxy, lay the contacts on the sample, cure the epoxy, solder the sample onto a puck, anneal the contacts and finally run the measurement in the PPMS. Perhaps it was the worry that I needed to set aside a four hour block of time, because that is how long it took me to successfully lay contacts the first time. What I failed to realize is that laying contacts is just like any other task, the more you do it, the less time it takes. In this section I will talk about the tips I learned, admittedly late in the game, that should help you be a better scientist.

We use two-part EPO-TEK H20E silver epoxy to affix 0.002 in Pt wire (or 0.001 in for samples less than 2 mm in length) to the sample. A weigh scale is used to weigh out equal masses of part A and part B onto a glass slide. Weigh paper can be attached to the glass slide with double-sided tape so the glass slide can be reused. The key tip from Peter is to keep the two parts separate until equal parts by mass are weighed out. Only then should the two parts be mixed together with a wooden splint. It helps tremendously to do the mixing under the microscope, this allows you to judge the consistency of the epoxy. The epoxy should be completely smooth and the silver sparkles evenly distributed. If there are any clumps or variations in consistency, it is worth starting over again, as there was likely a major error in the initial weighing step, and the epoxy will never lay or cure correctly. Regarding cure time, I found the specification-sheet recommended cure time and temperature—1 hour at 150°C—works best. The curing can be done in a low temperature oven. Fortunately, neither $LaCrGe_3$ nor $LaCrSb_3$ are air sensitive at least up to 150°C, so a vacuum oven was not required.

When it comes to laying the contacts, it is important to have a minimum of two, preferably three, pairs of tweezers. For manipulating the wire into the silver epoxy and onto the sample, excellent, not just good, tweezers are paramount. The \$35[12] Swiss-made TDI-5-SA qualify as excellent and are well worth the additional \$10 over the Italian-made ones. Be meticulously careful with them, replace the tip-protector when they are not in use, and never let anyone else use your tweezers. Once the tips are bent, they are never the same. The second pair of tweezers should be reserved for 'dirtier' work such as handing samples, holding

[12]Valentin made it seem like they were prohibitively expensive, but I would recommend purchasing some extras if you can.

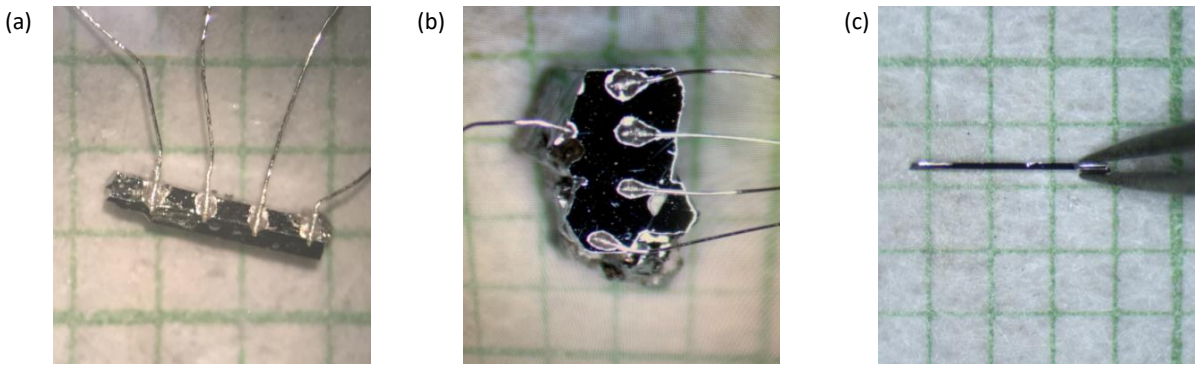


**Figure 4.11:** How the sample grows often dictates the easiest way to lay contacts for resistivity measurements. Since $LaCrGe_3$ grows as a hexagonal rod along the $c$ axis, it is natural to lay contacts such that the current flows along the $c$ direction as shown in panel (a). For certain measurements, such as studies of the anomalous Hall effect (AHE), the easy magnetization direction matters. Panel (b) shows an $ab$ face of a relatively large $LaCrGe_3$ sample. This face was polished flat with 0.1$\mu$m polishing paper so contacts could be made such that the current runs perpendicular to the easy magnetization direction. A fifth lead (leftmost contact) was also attached to measure a Hall voltage, however, further optimizations (such as reducing the thickness of the sample) needed to be made for a successful AHE measurement. Some resistivity measurements with a particular current direction are prohibitively impractical. (c) For example, the pictured $LaCrSb_3$ $x = 0.45$ sample is incredibly thin along the $a$ axis, so even if two current leads were placed on the large rectangular $bc$ faces of the sample, there would be no way to place voltage sensing leads along the narrow $a$ dimension.

the Pt wire as it is annealed with the flame of a lighter,[13] and for sticking the Pt wire into the molten ball of solder on the PPMS puck. The TDI-3-SA tweezers are good for these purposes.

Once the epoxy is mixed properly, the tip of a 2-3 cm section of annealed Pt wire is dipped into the silver epoxy and then carefully laid onto the sample. This work must be done under a microscope and a total of four contacts must be affixed. The shape of the sample often dictates the easiest way four contacts can be laid onto the sample, with other orientations being significantly more difficult. Although they have different crystal structures, both $LaCrSb_3$ and $LaCrGe_3$ grow long in their $c$ axis direction, so it is most practical to lay contacts with $I||c$ as shown in Fig. 4.11(a). With the right sample, and some additional sample preparation, it is possible to lay contacts such that the current flows in a different direction. For example, in Fig. 4.11(b) a large $ab$ face of $LaCrGe_3$ has been polished so that $I||ab$. With the contacts laid onto the sample, the epoxy is cured by placing the sample in a low temperature oven at 1 hour at 150°C as previously mentioned.

Unlike benchtop resistance measurements of resistors which only require two probes, four probes are necessary for accurate measurements of the resistivity of metals at low temperatures.[14] In a two terminal

[13]Pt wire comes on a spool from the factory, so it has a natural curve and spring to it. The spring can be eliminated so that the wire holds whatever shape it is bent into by simply heating it up with the flame from a generic Bic-style lighter. It is preferable to use a not-so-good pair of tweezers to hold the wire while the flame is run over it so your good pair of tweezers are not ruined by black soot and a loss of temper.

[14]I have Aaron Rosenberg to thank for taking the time to teach me the basics behind four-terminal measurements during undergrad. I also have Professor Inna Vishik to thank for asking me the "why are four terminals needed?" to get me back on track during my qualifying exam amidst my struggle to answer difficult questions about crystal structure and the underlying theory of magnetoresistance (as it turns out, like magnetism, there is no unifying theory of magnetoresistance.)

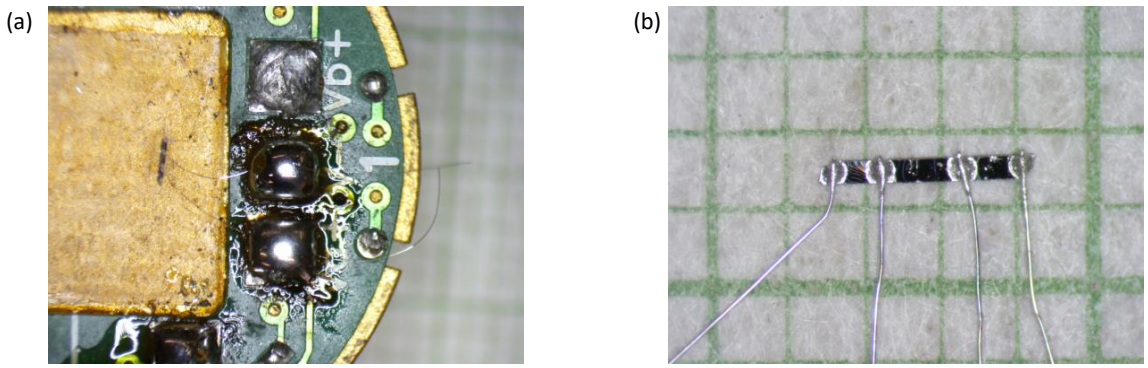


**Figure 4.12:** (a) This photograph highlights the difference between fresh solder joints reflowed with flux (the bottom two silvery domes in the middle) and an old solder joint (top, dull grey labelled Vb+). These silvery joints lead to the two voltage sensing contacts better observed in panel (b). (b) An example of hand-laid silver epoxy contacts on a bar shaped sample of $LaCr_{1-x}Fe_xSb_3$. The two outer contacts are connected to a current source, while the two inner contacts are connected to a voltmeter.

measurement, reading the voltage difference between the two terminals includes the resistance of the probe wires, also known as the lead resistance. In general-purpose electronics, the lead resistance of copper wires is usually negligible since the resistances measured are typically greater than 1Ω. The metallic ferromagnets I study, however, can have sample resistances in the mΩ range. Given the sample size, this translates to a resistivity of around $40\mu\Omega$cm where the resistivity of the wires that go through the cryostat is no longer negligible. Furthermore, different sections of wiring in the PPMS may be made of different materials[15] depending on where minimizing the heat load is important. The possibility of calculating the lead resistance to subtract it out becomes even more difficult given that the wire is at a range of temperatures so the resistivity is not constant. A four-terminal or four-probe measurement eliminates the need to consider lead resistance. With an ideal current source[16] connected to the two outer contacts, and an ideal voltmeter[17] connected to the two inner contacts only the sample resistance is measured.

After the wires are affixed to the sample, they must be soldered[18] to the PPMS puck. I recommend re-flowing solder joints after they have been thermally cycled in the PPMS. In practice, running a low-temperature measurement seems to age the solder so that it hesitates to flow. To renew the existing solder

[15]Instead of copper, phosphor bronze or manganin might be used for lower thermal conductivity at the expense of a higher electrical resistivity.

[16]An ideal current source provides the set amount of current regardless of what circuit it is connected to.

[17]an ideal voltmeter has infinite impedance such that absolutely no current flows through the voltmeter, and therefore no current flows through the leads of the voltmeter either.

[18]We, along with other physics departments, seem to be the only labs on university campuses that still use regular 60/40 Pb/Sn rosin core solder. Electrical engineering labs, for example, have a strict rule against leaded solder and instead use a lead-free alloy of Sn-Ag-Cu. Although one might suspect the phasing out of lead solder in labs is due to the health concerns of breathing the fumes expelled during soldering (which theoretically should just be the rosin flux since the boiling point of lead is 1749 °C and soldering irons are usually set to 700 °C), or from potential cross-contamination with students' lunch, the banning of lead solder originated from the environmental and health concerns related to their disposal [182]. While our small scale research lab generates a negligible amount of leaded solder waste when compared to industrial applications, it is likely that our familiar leaded solder will be banned. Fortunately, industry has done extensive testing on the strength of the contact, aging and thermal cycling of these lead-free solders [183] so it is good to know that there are viable alternatives, even if it does require setting our soldering irons to different temperatures or buying different solder fluxes.

on the puck, brush the solder with a cotton-tipped applicator (Q-tip) dipped in liquid rosin solder flux. In electronics, solder flux is a rosin made primarily of abietic acid that cleans oxidation and helps the solder flow. Heating the flux-coated solder with a soldering iron, should re-flow the solder such that it becomes shiny and glassy. Fig. 4.12(a) shows the difference between an old, cryogenically-cycled solder joint and a re-flowed joint. Flux may be conductive, so excess flux should be cleaned from the circuit board using a Q-tip soaked in ethanol or isopropyl alcohol. Using acetone is an expensive mistake as it will melt the puck's circuit board and cause un-fixable shorts. Flux can also be applied to existing solder joints if you suspect the solder did not make the best contact with the Pt wire. In the event that the solder is too old or there simply too much solder on the puck's gold solder pads, I recommend removing all of the solder and starting over with new solder. There are a few methods for removing solder, but I have had the most luck with desoldering wick. Desoldering wick is a copper braid that is coated in flux so when heated with a decent soldering iron, the solder wicks up off the solder pad onto the copper braid.

Once the sample is soldered to the PPMS puck, the puck is placed in a breakout box to measure the room temperature resistances. At first, the resistances between contacts will vary widely from 50Ω to 50kΩ, or in some cases they may even register as an open circuit. To fix these high resistances, the contacts are annealed by running current through each of the permutations of the contacts with a current source (we use a Lakeshore Model 120 Current Source). For my samples, 10mA was often sufficient to anneal the contacts to the desired resistance of less than 5Ω. While my samples were large and robust enough to withstand annealing currents of up to 100mA, for smaller needle-like samples, however, Peter Klavins warns against using too much current as it is possible for them to burn up like a fuse. With the mechanics of preparing the sample for measurement out of the way, I will highlight a couple of my findings with regards to writing measurement sequences.

Figure 4.13 demonstrates the effect of the rate of heating and cooling, as well as the excitation current, on $\rho(T)$ measurements. In short, the best resistivity data comes from slow temperature changes and large excitation currents. Fig. 4.13(a) shows the exact $LaCr_{1-x}Fe_xSb_3$ $x = 0.15$ sample used in the following measurements. The $x = 0.15$ sample exhibits a first order ferromagnetic transition which is expected to present as hysteresis in $\rho$ between warming and cooling. Therefore, it was important to find measurement settings such that any hysteresis was due to the phase transition rather than an instrumental artifact such as thermal lag.[19] Fig. 4.13(b) reveals what happens when the temperature is swept too quickly. There is a clear difference between resistivity upon warming ($\rho(+T)$) and upon cooling ($\rho(-T)$), however, that difference (hysteresis) does not correspond to a feature of the first order FM transition, as seen in the blue line in

[19]Thermal lag describes the phenomenon where the PPMS thermometer and the sample temperature do not agree. Usually, the sample temperature lags behind the thermometer temperature. Slowing down the rate of change gives more time for the sample to reach thermal equilibrium.

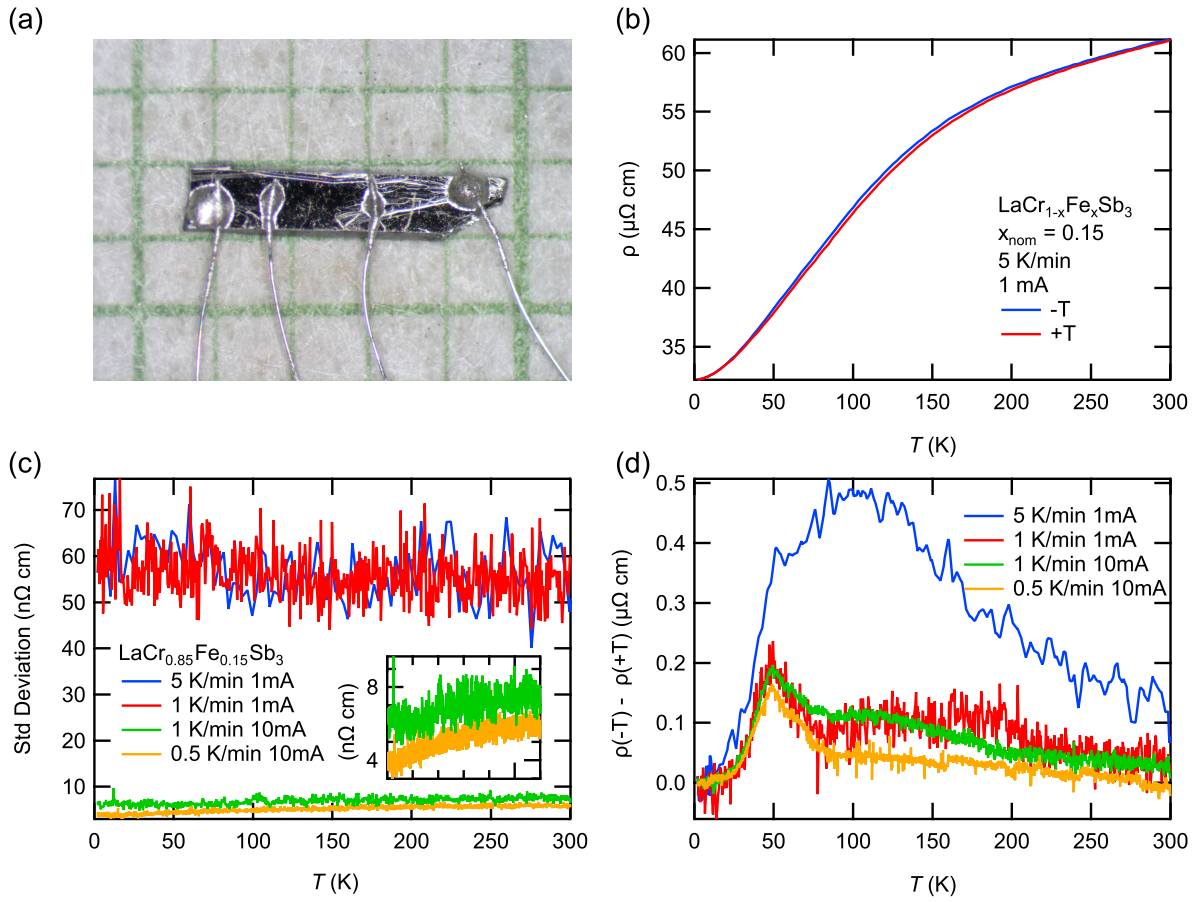


**Figure 4.13:** (a) The $LaCr_{0.85}Fe_{0.15}Sb_3$ sample the following resistivity data was measured on photographed on mm-grid paper. (b) The temperature dependence of resistivity upon cooling (-T) and warming (+T) at a rate of 5 K/min. The too fast rate of cooling/warming results in thermal lag evident by a visible and misleading hysteresis. (c) A comparison of the standard deviation (a measure of the goodness of fit of the AC transport measurement) across different cooling rates and excitation currents. While there is little difference between the 5K/min and 1K/min measurements performed with a 1mA excitation current, increasing the current to 10mA improves the standard deviation by an order of magnitude. The inset highlights the improvement from reducing the rate to 0.5K/min. (d) Plotting the difference between $\rho(-T)$ and $\rho(+T)$ only shows a hysteresis consistent with a first order ferromagnetic transition (and consistent with magnetization measurements) when the warming/cooling rate is sufficiently small and the excitation current is sufficiently large.

Fig. 4.13(d). The hysteresis associated with the transition (to be consistent with the magnetization measurement) only appears when the temperature sweep rate is lowered to 0.5 K/min (any faster than 1 K/min tends to lead to thermal lag) and the excitation current is increased to 10 mA. While these parameters work well for this compound, some experimentation might be necessary for your particular sample.[20] In Fig. 4.13(c) we see how the standard deviation, a measure of the error for resistivity measurements, is affected by the temperature sweep rate, as well as the excitation current used.

I have anecdotal evidence that slowing down the rate of change is not always beneficial, however. In an attempt to get more data points near the field-induced transition in $LaCr_{1-x}Fe_xSb_3$ (examples can be seen in Fig. 3.28), I lowered the field-sweep rate from 10 Oe/sec to 5 Oe/sec. I have preliminary measurements that show that a 5 Oe/sec magnet charging rate makes the measurement worse and leads to data-breaking noise. Further investigation is required to better determine the effect of field sweep rate on $\rho(H)$ measurements.

Besides the rate of change, there are two other factors that can help increase the data density if needed. The first is to measure one sample at a time, since the PPMS measuring electronics take time to switch between two samples. The other is to turn off the autoranging feature and instead use a fixed gain. For my samples, the resistivity did not change appreciably throughout a temperature or field sweep, so fixing the gain at room temperature was appropriate.

The next step after the PPMS measurement is done is the data analysis. Going from resistance (extrinsic) to resistivity (intrinsic) is a simple formula based on the dimensions of the sample.

$$\rho = \frac{RA}{L} \tag{4.1}$$

Where $R$ is the resistance measured, $A$ is the cross-sectional area of the sample measured, and $L$ is the distance between the two voltage sensing leads. While $R$ is the value measured by the PPMS, $A$ and $L$ must also be measured to get $\rho$. To obtain $A$ and $L$, photographs are taken of the sample on mm-grid paper. With the millimeter grid as a reference, the sample dimensions and the lead spacing can be found using software. Different members of the lab have used different programs for this step. Jeff Harvey used Photoshop (slow, expensive), while Jackson Badger had luck with ImageJ (free, very steep learning curve) coupled with an additional plugin.[21] Hanshang Jin discovered the website eleif.net/photomeasure, that is quick and easy to use. It is what I used for all of the resistivity measurements presented in this thesis.

[20] For example, I found that using an excitation current of 10 mA gives good results. 10 mA may be too much for a thinner, smaller sample, using perhaps thinner Pt wire. In addition, the increased Joule heating from using a larger current might need to be taken into consideration.

[21] https://forum.image.sc/t/imagej-macro-to-measure-distance-between-two-lines-edges/42019

## 4.3 Development of a Spot Welder

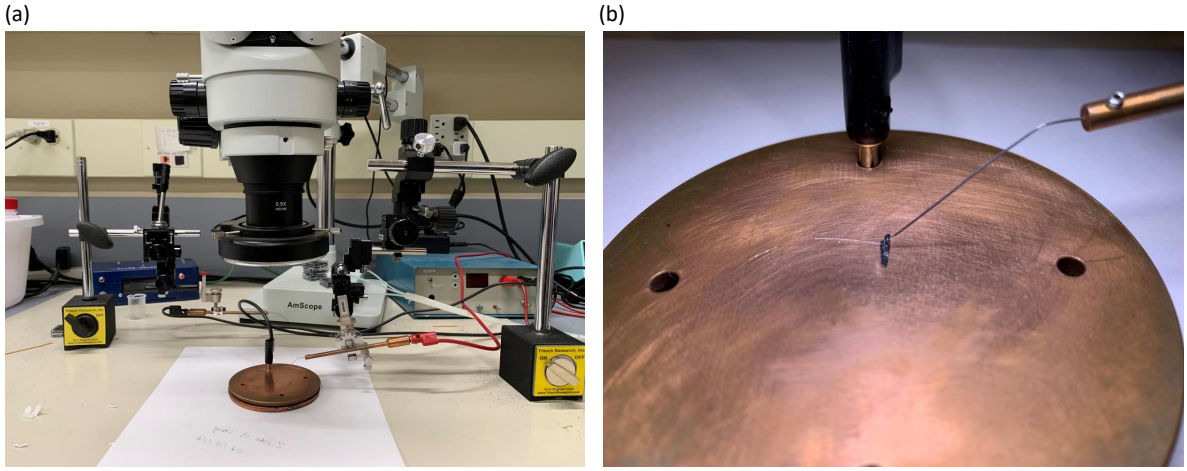


**Figure 4.14:** (a) Our spot welding station. The process is done under a microscope. Micromanipulators (a Narishige MMO-4 oil controlled micromanipulator in conjunction with a Narishige UMM-3C manipulator) are used to position the welding leads onto the sample. The micromanipulators are held securely to the table with GJ-1 or GJ-8 magnetic bases from Tritech Research. The blue box on the left holds the Arduino-based electronics that are the subject of this section. (b) A close up of the spot welding setup. The conductive copper plate is grounded with the black banana cable. The sample sits on the copper plate and a thin gold wire is place on top of the sample. The tungsten needle presses the gold wire onto the sample and is electrically connected to the positive terminal of the spot welder. When the weld current is applied, the gold wire is fused to the surface of the sample.

A spot welder, in the traditional sense, is a tool designed to attached two pieces of sheet metal together. It does so by flowing a large current through two electrodes that pinch the two pieces of metal in contact. The current quickly heats up the two pieces of metal at a single spot until they melt and weld together, forming a near permanent bond. In a condensed matter physics lab, the idea of a permanent bond between two metals is ideal for affixing wires onto small samples for resistivity measurements.

As demonstrated in Section 3.4.4, resistivity measurements are another tool in our toolbox to probe phase transitions. They can reveal $T_C$ or $T_N$ at zero field, and they can also indicate field-induced transitions such as the AFM-FM spin flip transitions in the La(Cr,Fe)$Sb_3$ system (see Fig. 3.28). While most of the resistivity data presented in this thesis used silver epoxy to affix wires to the samples, the silver epoxy method may not be appropriate in some situations. First, since they are laid by hand, samples shorter than 1 mm are extremely difficult to work with. Second, obtaining a suitable bond with silver epoxy generally requires a relatively large contact area. While this constraint also limits how small a sample can be measured, it also increases the uncertainty in the distance measurement between the two voltage contacts. With a spot welding setup designed for working with small metallic samples, however, these limitations can be overcome. Since the welding electrodes can be attached to micromanipulators, the effective dexterity of the user is increased and smaller samples can be handled. Furthermore, since a spot welder fuses the wire to the sample

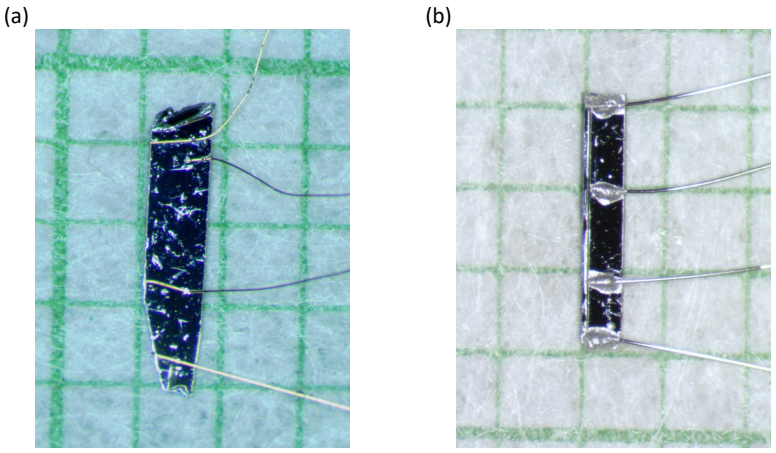


**Figure 4.15:** Four contacts laid on $LaCr_{0.65}Fe_{0.35}Sb_3$ samples using the (a) spot welding method and (b) silver epoxy method. The size of the spot welded contacts is significantly smaller than the silver epoxy contacts.

at a single point, it is easier to discern where the contact is made and from where the distances between the leads should be measured (compare Fig. 4.15(a) to Fig. 4.15(b)).

While the wide range of commercial applications for spot welders has resulted in a variety of spot welding machines (*e.g.* there are large robotic spot welders for manufacturing cars and smaller hand held ones for making custom lithium ion battery packs), research scientists need to build their own spot welders for their niche purposes. In 1959, Hill [184] developed a spot welder specifically for the purpose of affixing thin wires onto samples. His design, in which the current is sourced from a charged bank of capacitors, was an improvement over Hart and Elkin's (1945 [185]) method for welding thin thermocouple wires based on shorting a 120 V battery. Given the DC voltage source, the amount of current available for welding was changed by adding or removing capacitors. Radcliffe and White (1961 [186]) demonstrated that using an adjustable voltage source would work as well, and this would become the technique that is used in modern spot welders. Babic *et al.* (1971 [187]) improved upon the design by replacing the mechanical switch used to trigger the capacitor discharge with a solid state switch known as a thyristor. Further improvements to the design of the spot welder circuit, such as circuitry to de-bounce the mechanical switch that triggers the thyristor in the first place, were made by Walker and Moss (1998 [188, 189]), who also describe considerations for spot welding in detail.

In the aforementioned designs, the duration the welding current is applied for is controlled directly by a manually controlled switch. The resulting variation of the time the current is applied leads to inconsistency between contacts, and the inability to get less than the full discharge of the capacitors during welding is potentially damaging to the samples. Therefore, Hiraoka (1998 [190]) added an integrated circuit to provide

precise timing and used a MOSFET[22] instead of a thyristor to make it easier to turn the welding current off. As additional features and improvements have been added over the years, the spot welding circuit has become increasingly complicated. Since the circuits are based on analog electronics, each feature added, whether for performance, repeatability, or safety, brings with it additional passive (resistors, capacitors, diodes, switches, etc.) and active (transistors, integrated circuits, etc.) components. The complexity of the circuit can be a significant barrier to entry for experimental physics labs in universities. The greater the number of components, the greater the chance of making a mistake, especially for a physics grad student whose primary goal is to obtain data, not to build better electronics. In fact, it was a single mistake in the schematic and printed circuit board designed by our departmental electronics shop that highlighted the need for a simpler solution.

Initially, the goal for my redesign of the spot welder was to salvage what the electronics shop had made just to get it working so we could start measuring samples. By replacing the analog electronics responsible for the triggering and timing of the welding current with an Arduino microcontroller, I was able to dramatically simplify the design. This version is easier and less costly to construct than previous designs due to the reduced number of components. In addition, since the microcontroller is programmable, it is more versatile and easier to use. Depending on the needs of a particular lab, features can be modified or added by writing code rather than changing or adding physical components. On one hand, if your lab needs a spot welder to affix contacts to small metallic samples, this would be the one to build. On the other hand, this project also demonstrates how programmable digital electronics can replace many of the analog electronics that condensed matter physicists have held onto for decades.

**Failure analysis of version 1**

According to the current CEO of Seagate,[23] Dave Mosley,[24] a job in 'failure analysis' is the natural position for an experimental physicist pivoting to industry. With this in mind, the first step to developing our version of the spot welder was to figure out why the one we were given did not work. Upon testing, we found that we could not get a pulse of current[25] out of the machine. After a good deal of troubleshooting and looking through the datasheets for each integrated circuit (IC) in the circuit, I found the mistake. The first IC in the circuit[26] was wired incorrectly, causing the circuit to be in a permanently triggered ('high') state. As shown in Fig. 4.16, pins 14 and 15 had been erroneously swapped. While this is an error anyone

[22] metal-oxide-semiconductor field-effect transistor

[23] Seagate has a majority share of the spinning platter hard drive market.

[24] Dave Mosley finished his Ph.D. at Davis in 1994 in Robert Shelton's lab.

[25] It is the large pulse of current that causes the welding of metals, but in the lab, the best way to measure current is often to measure the voltage across a known resistor. In any case, technically I was probing around looking for pulses of voltage, not current.

[26] The 74HC123, a 'dual retriggerable monostable multivibrator with reset.'

(a)

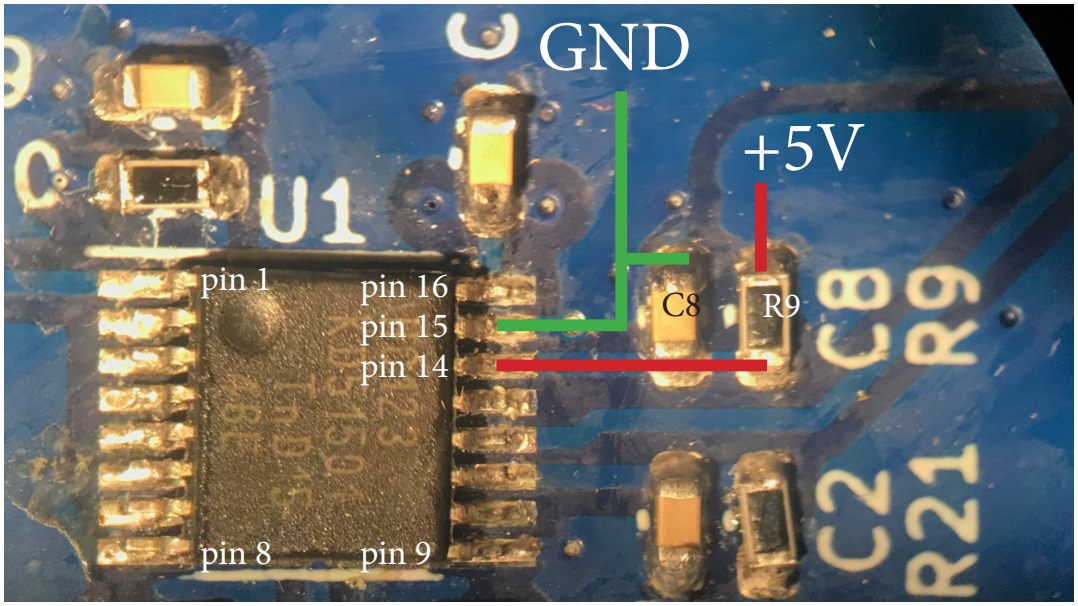


(b)

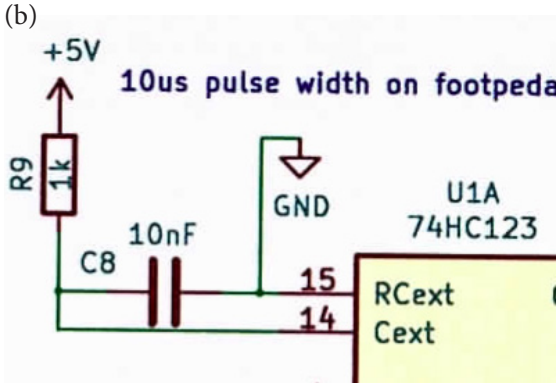


(c)

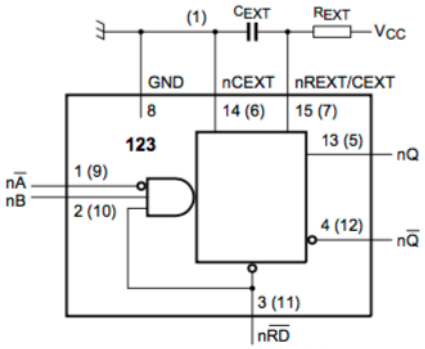


**Figure 4.16:** (a) A photograph of the printed circuit board (PCB) focused on the improperly wired 74HC123 integrated circuit (IC) which was intended to determine if the switch was pressed and send an adjustable width of pulse to the MOSFET driver. For scale, the size of the footprint of this IC is about 5x5 mm. The green and red lines are used to highlight the conductive paths. (b) The schematic designed by our departmental electronics shop (full schematic shown in Fig. 4.17) is consistent with the PCB, but does not match the (c) datasheet provided by the manufacturer (Nexperia). It was the small mistake of swapping pins 14 and 15 that led to our redesign. If the through-hole version of the 74HC123 was used instead of the surface-mount package, it would have been possible to swap the electrical connections to pins 14 and 15 and the spot welder would have worked as intended.

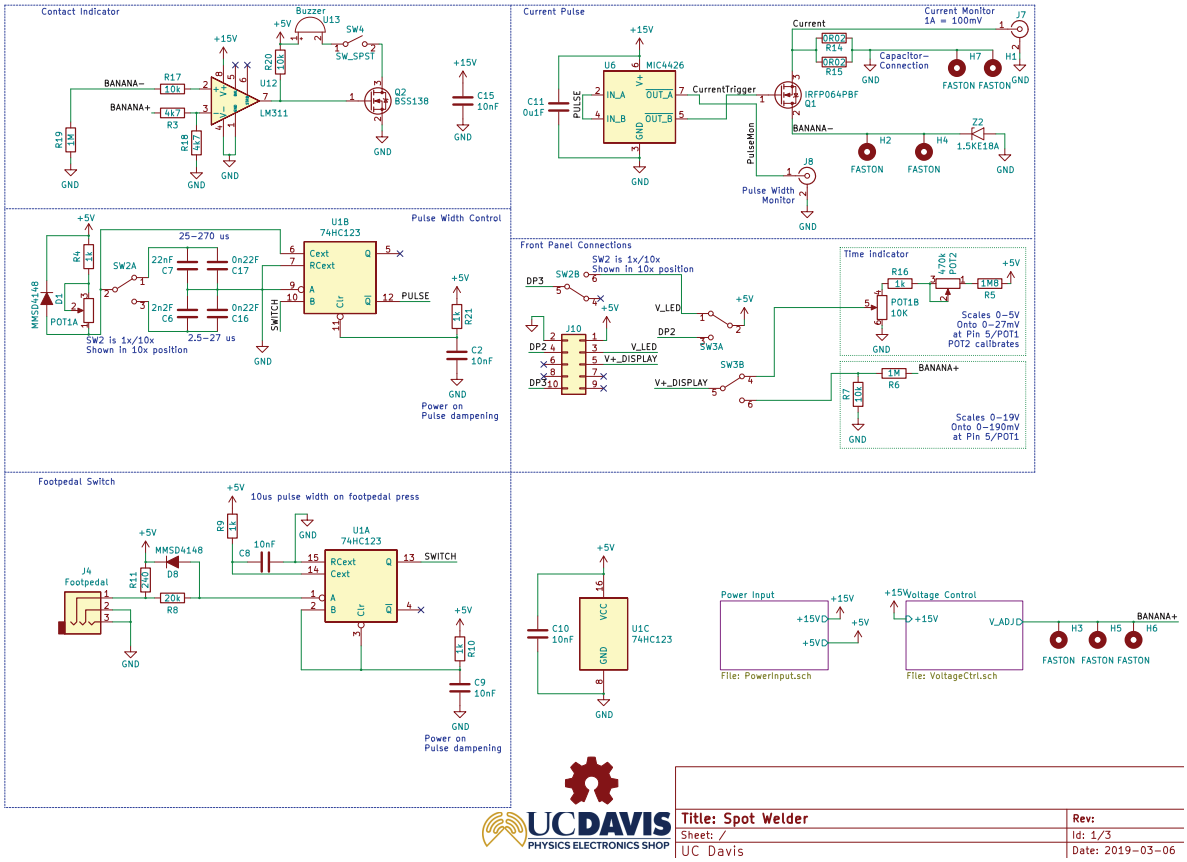


**Figure 4.17:** The original electrical schematic of the spot welder. While it is possible to accomplish all of the tasks with analog components, there are certain ones where using a programmable digital microcontroller is more efficient, cost effective, and versatile. In my implementation, the 'Pulse Width Control,' 'Footpedal Switch,' and 'Front Panel Connections' sections of this circuit diagram were replaced with an Arduino, a few buttons, and an LCD screen (Fig.4.19). The contact indicator was replaced by a digital multimeter set to test for continuity. We kept the current pulse section of the schematic, since controlling large currents is a job suited for a MOSFET driver and MOSFET.

who has had to design a mildly complicated circuit has made, it was a catastrophic error given the use of small surface mount components and a non-modular printed circuit board design. Although this could be viewed as a human error and seen as a testament to the importance of prototyping, I argue that the problem lies in the design of the spot welder circuit itself.

As I mentioned in this section's introduction, the spot welding circuit had gotten increasingly complicated as improvements and features were added over the years. Since the spot welding circuit exclusively used analog electronics, each additional feature required a slew of additional components, and therefore, more chances for a mistake to be made. Given the complexity of the original circuit shown in Fig. 4.17, it is a miracle more errors were not made.

**Replacing analog components with digital components**

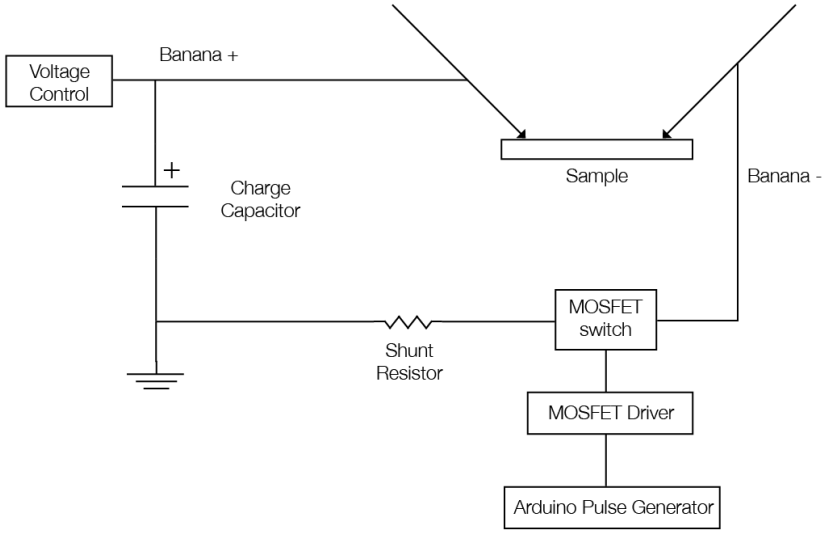


**Figure 4.18:** A block diagram for the spot welding circuit. The Arduino Pulse Generator is the new component we developed. When the user flips a switch, the Arduino Pulse Generator sends pulse of variable duration (see Fig. 4.21) to the MOSFET driver. The MOSFET driver is designed to optimally trigger the MOSFET which, in this implementation, open or closes the path to ground of the charged capacitor. The capacitor is charged to a variable voltage by the Voltage Control. The charged capacitor is connected to the tungsten welding leads (depicted as arrows) with 18 AWG wire. The thin gold wire to be affixed to the sample is placed in between the tungsten welding lead and the sample. When the capacitor is discharged through the circuit, the wire is welded to the sample.

The block diagram for the spot welder is shown in Fig. 4.18 and our benchtop setup is shown in Fig. 4.14. The 'Arduino Pulse Generator' in the block diagram is the part that I developed and replaces the footpedal switch, pulse width control, and front panel connections sections of the schematic shown in Fig. 4.17. The circuit for the Arduino Pulse Generator is shown in Fig. 4.19, which also shows that the contact indicator section of Fig. 4.17 has been replaced by an inexpensive digital multimeter. By making these changes, we were able to make a spot welder with fewer parts that is easier and less expensive to construct. In addition, with a programmable microcontroller, new features can be added by writing lines of code, rather than adding new components and designing new circuit boards.

Figure 4.19 shows the circuit diagram for the Arduino Pulse Generator and Fig 4.20 shows the box that it is housed in. I will now go over each section of the original schematic and discuss how it was replaced by a programmable microcontroller.

The 'footpedal switch section' is intended to detect when the switch goes from off to on, and trigger a single pulse from the 'pulse width control section.' Without this circuitry, known as an 'edge-trigger,' it would be difficult for the user not to inadvertently trigger multiple pulses. With programmable digital electronics, however, this circuitry's behavior can be accomplished with a simple 'if' statement in code.

The 'pulse width control section' is intended to provide a variable length of pulse. In electronics, a pulse

is a length of time where the voltage is held 'high' (+5 V in this case) when the normal state of the voltage is 'low' (0 V in this case). An example of a pulse is shown as the yellow line in Fig. 4.21. In the original schematic, this variable timing is accomplished with a variable resistor and switching between two different values of capacitors. Not only is there a limitation in the range of pulse times available, there is a significant number of parts involved as well. Furthermore, it may be difficult to achieve repeatable pulse times with this design. With an Arduino, however, the pulse time is simply controlled by code and can be changed precisely and repeatably with buttons on the front panel.

The 'contact indicator' is intended to tell the user that the tungsten welding probe, wire to be affixed, and sample are in suitable electrical contact for welding. Even under the microscope, it is difficult to see whether these three things are touching each other. In practice, when these three things are in good electrical contact, the resistance measured is under $\sim 5\,\Omega$. Instead of the contact indicator circuitry in the original schematic, this function could be replaced by an inexpensive digital multimeter set to test for resistance or continuity. The multimeter is connected to the red (Banana + in Fig. 4.18) and black (Banana − in Fig. 4.18) banana plugs shown in Fig. 4.23. A multimeter's continuity function gives an audible buzz when electrical continuity is measured.

The 'front panel connections' never worked properly, but were intended to selectively display the voltage of the capacitor and the pulse time. It is hard for me to imagine driving a display without a programmable microcontroller as the original schematic shows. In any case, with a serial-enabled LCD,[27] it is possible to display both the capacitor voltage and the pulse time simultaneously. I also programmed it to tell the user if the pulse was delivered.

One of the only sections of the original schematic that is still in use is the 'current pulse' section. This section, reproduced in Fig. 4.22 is the only part that an Arduino or other digital microcontroller can not replace. Switching large currents on and off is better left to the MOSFET driver and MOSFET in this circuit. Fortunately, this section worked, and we were able to connect the Arduino Pulse Generator directly to it.

[27]For example: https://www.sparkfun.com/products/10097 or https://www.sparkfun.com/products/16397

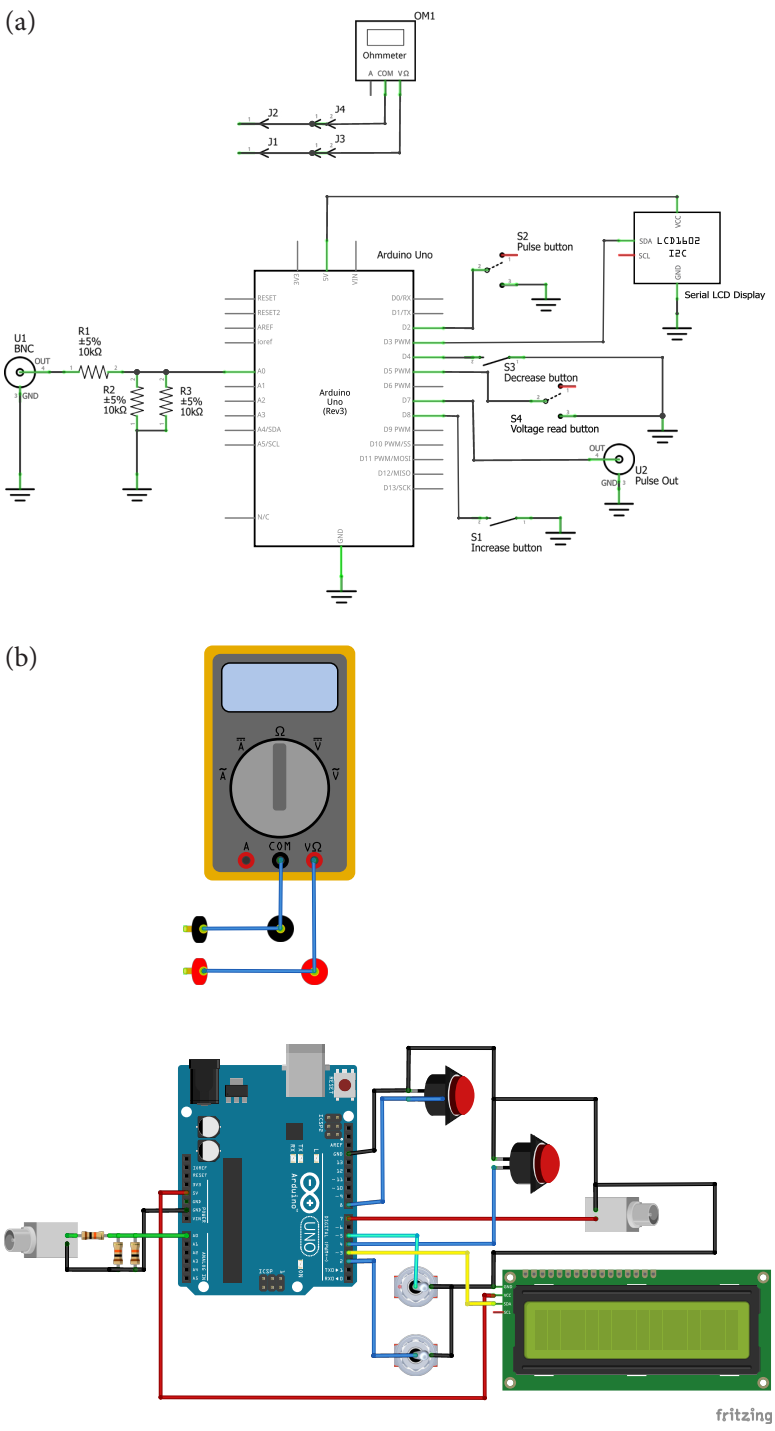


**Figure 4.19:** (a) Electrical schematic diagram of the digital front end of the spot welder. (b) Real parts diagram of the digital front end of the spot welder. This simple design replaces much of the schematic shown in Fig. 4.17.

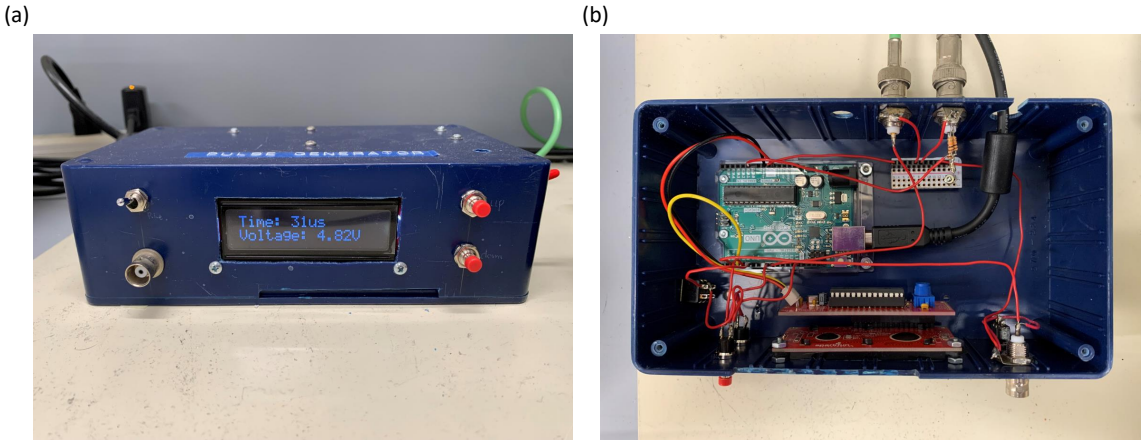


**Figure 4.20:** The (a) outside and (b) inside of the box housing the digital front end for the spot welder circuit. (a) The toggle switch on the left is used to trigger and reset the pulse. The BNC connector below the toggle switch allows for an external footswitch to be connected so that both hands can be free to use the micromanipulators for controlling the welding probes. The LCD display shows important information such as the pulse time, voltage, and whether the pulse was initiated. The red pushbuttons on the right are for adjusting the pulse duration. On the right side of the box is a red switch which toggles between the standard 'pulse mode' and the 'voltage read mode.' In pulse mode, the box delivers a pulse of a programmable duration when the toggle switch on the front is switched. In voltage read mode, the Arduino reads the voltage of the capacitor (pictured in Fig. 4.23) and displays the voltage on the LCD. (b) Inside the box, we can see the components of the new design. The the teal PCB is the Arduino microcontroller, the brains of the operation. The red PCBs are the LCD display and a LCD driver board. There are a handful of switches and BNC connectors (one for sending the pulse, one for reading voltage) that are are connected to the Arduino with standard wire. The whole unit is powered over USB (+5 V).

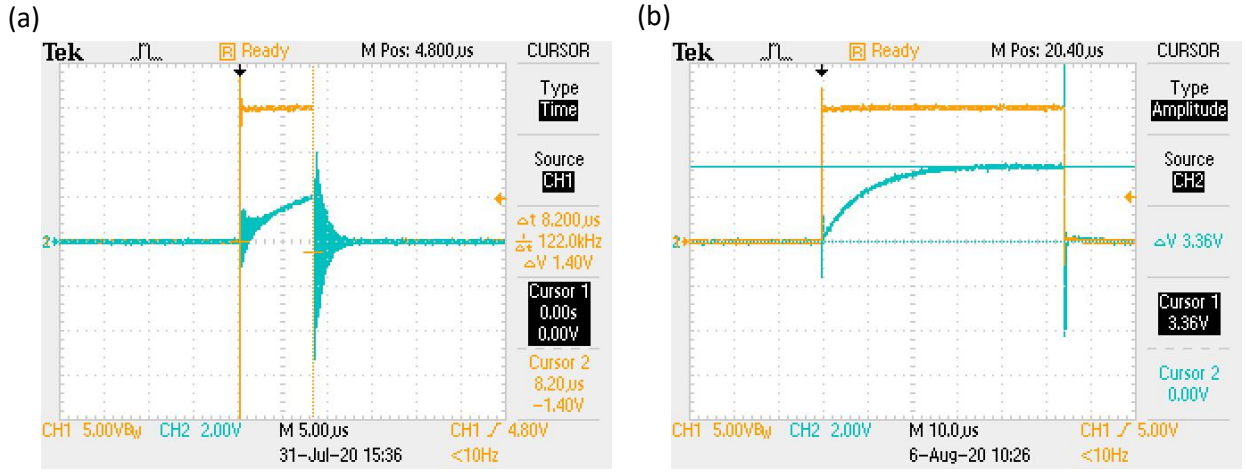


**Figure 4.21:** Oscilloscope traces of the voltage pulse from the Arduino (yellow line) and the current (blue line) from the capacitor during testing. In place of a sample, a 16 gauge wire was used. (a) The minimum pulse time of 8 $\mu$s that the Arduino can output due to its clock speed. With 2 V per division and a conversion of 1 A = 100 mV in the schematic (Fig. 4.17, current monitor) we see that the current only reaches 20 A. However, there are sources that debate the validity of measuring short pulses of current by the voltage across a shunt resistor due to parasitic inductance (Ref. [188]). (b) With longer pulse time of $\approx 27\,\mu$s, we see that the current reaches a saturated value of nearly 40 A. The amperage can be increased or decreased by increasing or decreasing the voltage used to charge the capacitor.

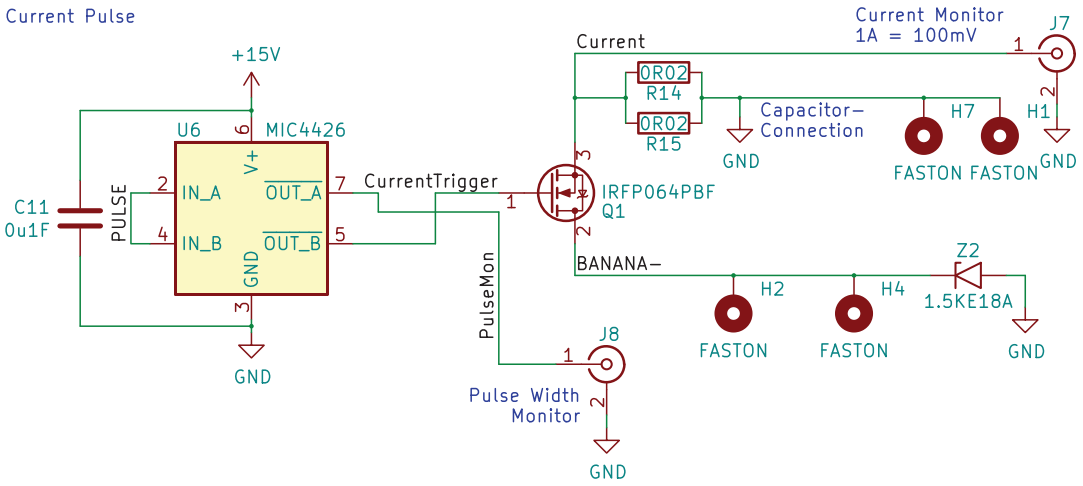


**Figure 4.22:** The 'Current Pulse' section of the original schematic in Fig. 4.17 is the only section that is still in use. The output of the Arduino Pulse Generator is connected to 'PULSE' of the MIC4426 which is an IC designed to drive MOSFETs. In this case, the IRFP064PBF MOSFET is responsible for switching the path for the capacitor to discharge through on and off. This part of the schematic is housed in the box pictured in Fig. 4.23.

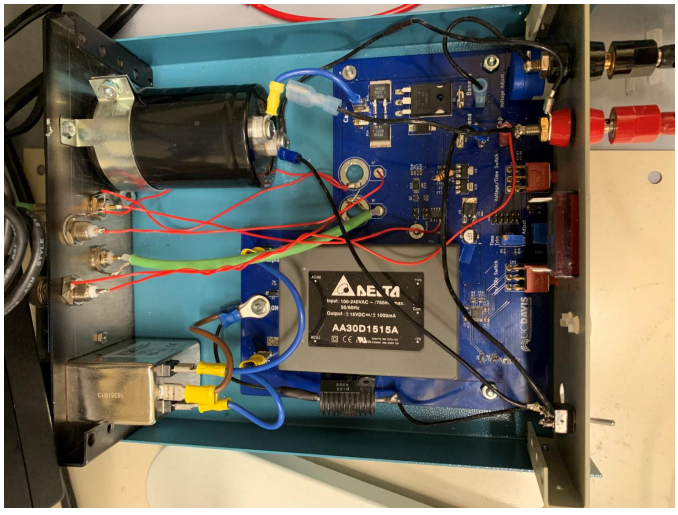


**Figure 4.23:** An inside look into the original spot welding box. While some of the circuity (specifically the schematic shown in Fig. 4.22) is still used in our implementation, most of the circuit board shown is bypassed and not in use. This means that a version 2 could have a much smaller and simpler printed circuit board. The main 22000 $\mu$F charge capacitor is the black cylinder in the top left and is rated for 63 V. There is also a switch that is not shown in the schematic which can be used to disconnect and safely discharge the capacitor. This allows for an instantaneous reading of the voltage setting rather than having to wait for the capacitor to charge up to the set voltage.

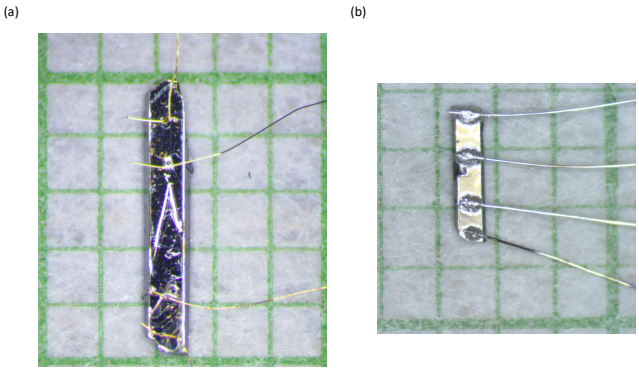


**Figure 4.24:** A $LaCr_{0.75}Fe_{0.25}Sb_3$ sample wired for resistivity measurements using (a) spot welding and (b) silver epoxy methods. (a) Damage to the surface of the sample caused by the spot welder can be seen on the second contact from the top. This is most likely due to using too high a voltage. (b) Although this is a smaller sample than the one shown in (a), it is still possible to use silver epoxy to lay contacts.

### 4.3.1 Conclusion

In this section, I focused on the development of the spot welding box rather than the spot welding process. While it was designed to put contacts on samples that would not otherwise be measurable due to their small size, the spot welding process has quite a steep learning curve. Finding the voltage and pulse time suitable for your particular samples takes some experimentation, as does getting accustomed to the micromanipulators and the finding the right amount of pressure the welding needle needs to apply to the wire and sample. Many of the practical considerations needed for successful spot welding are discussed by Walker and Moss in Refs. [188, 189]. While I had some success in laying contacts with the spot welder, as evident in Fig. 4.15 and Fig. 4.24, I found that if the samples are large enough, it is easier and faster to use silver epoxy. Of course, I did not have to do any pressure work where samples must be polished down to be small enough to fit into a pressure cell. Using the spot welder would be a necessity in those cases.

As for the spot welding electronics, I think it is important to be aware of the simplicity, cost-effectiveness and versatility of programmable digital electronics. Comparable spot welders for sale are based on the original analog schematic and cost thousands of dollars, which can be prohibitively expensive for university labs. In addition, not every physics department has an electronics shop that can develop a schematic and design a custom printed circuit board, nor are these the kinds of tasks an advisor would want their Ph.D. student to spend time on. The incorporation of digital electronics into this new design of the spot welder circuit makes spot welding more accessible. Expanding upon this idea, we were able to use an Arduino ($30) and a serial LCD display ($21) to make a readout for a second-hand Pfeiffer vacuum gauge that otherwise would have cost upwards of $2000. In addition to being a useful tool that helps us measure resistivity, the spot welder can also be viewed as a case study in the utility of digital electronics in the laboratory.

## 4.4 Synthesis Logbook

This section summarizes all of the syntheses I completed while in the Taufour lab. I detailed the single crystal synthesis of $LaCrGe_3$ in Section 2.2 and $La(Cr,Fe)Sb_3$ in Section 3.2. Since the recipes for the single crystal synthesis of these two compounds were well established, I was fortunate not to have to spend too much time experimenting with growth parameters (e.g., temperature profile, stoichiometric ratio, crucible material, element purity, etc.) to obtain measurable samples for my two main projects. In addition to $LaCrGe_3$ and $La(Cr,Fe)Sb_3$, there were a few other compounds that I grew single crystals of for potential collaborations or to satisfy a particular curiosity.

### 4.4.1 $LaCrGe_3$

| **Batch** | **Date** | **Elements** | **Furnace** | **Results** |
|---|---|---|---|---|
| RU | MM/YY | La:Cr:Ge | Name | Notes |
| RU120 | 04/18 | 4N:3N plates:5N powder, 6N | Snowy | Further from door, needles. |
| RU121 | 04/18 | 4N:3N plates:6N | Snowy | Close to door, large crystals |
| RU128 | 05/18 | 4N:3N plates:5N | Unknown | Small needles |
| RU129 | 05/18 | 4N:3N plates:6N | Unknown | Big single crystals |
| RU176 | 09/18 | Ames:4N:6N | Haddock | Small needles |
| RU177 | 09/18 | Ames:4N:6N | Haddock | Close to door, large crystals |
| RU186 | 09/18 | Ames:4N:6N | Haddock | Deep in furnace |
| RU187 | 09/18 | Ames:4N:6N | Haddock | Close to door, large crystals |
| RU192 | 11/18 | Ames:4N:6N | Haddock | Furnace malfunction, fast cooling. |
| RU213 | 03/19 | Ames:4N:6N | Haddock | Medium-sized crystals |
| RU218 | 04/19 | Ames:4N:6N | Haddock | Large clean crystals |
| RU219 | 04/19 | Ames:4N:6N | Haddock | Large clean crystals |

**Table 4.1:** A table of $LaCrGe_3$ batches. Initially, I used 4N 'REacton' La, but switched to using La from Ames Lab once I had access to it. The Ames Lab La is more pure. In practice, it is easier to cut than the 4N REacton La. The 3N Cr plates are easy to cut, but are a dull gray. In contrast, the 4N crystallites are shiny, but nearly impossible to cut. Therefore, when I switched to using the higher purity Cr, I started with the mass of one or two Cr crystallites and calculated the masses of the other elements from there. Once I used up the small amount of 5N Ge powder we had on hand, I exclusively used the 6N Ge pieces. In my experience, the larger pieces stay in place better during arc melting. After the RU186 and RU187 batches, we realized that the reaction run closer to the door consistently yielded large single crystals, while the reaction run deeper into the furnace resulted in small needle-like clusters. RU218 and RU219 were run as close to the door as possible, and both batches resulted in large single crystals.

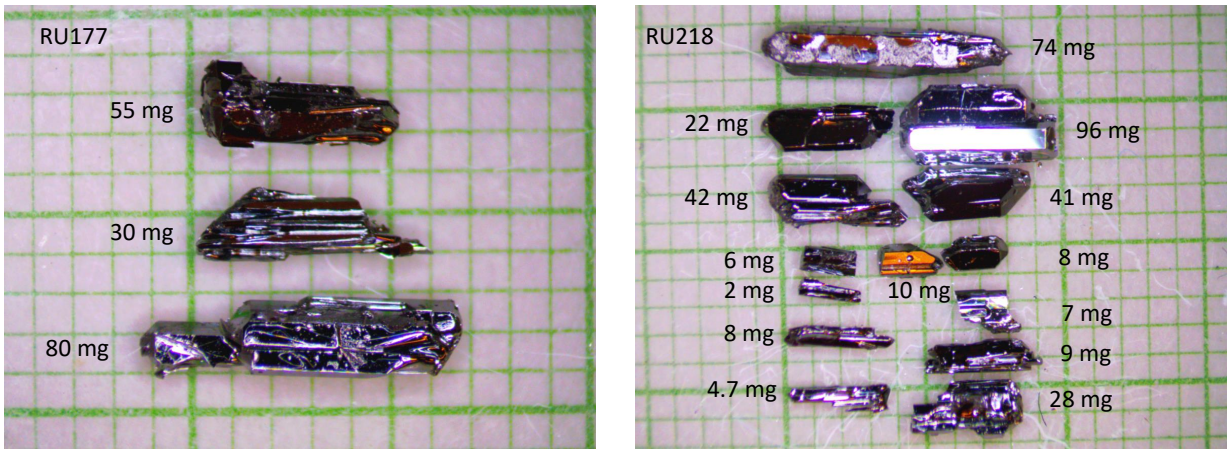


**Figure 4.25:** Pictured are examples of the largest $LaCrGe_3$ crystals that I grew. These samples were photographed on mm-grid paper and the masses are listed next to each sample. These samples were given to Kelly Neubauer of Pengcheng Dai's Lab at Rice University for inelastic neutron scattering measurements. Despite some of these samples being over ten times more massive than the ones I measured in the MPMS, they needed to make a mosaic out of all of the samples pictured for their measurements.

### 4.4.2 La(Cr,V)$Ge_3$ and La(Cr,Mo)$Ge_3$

| **Batch** | **Date** | **Elements** | **Furnace** | **Results** |
|---|---|---|---|---|
| RU | MM/YY | La:Cr:V/Mo:Ge | Name | Notes |
| RU302 | 03/20 | Ames:4N:Mo, arc melted powder:6N | Haddock | x = 0.073 |
| RU303 | 04/20 | La:Cr:V:Ge | N/A | Abandoned b/c COVID lockdown |
| RU308 | 06/20 | 4N:4N:V, etched:6N | Haddock | x = 0.06, large crystals |
| RU314 | 07/20 | 4N:4N:V, etched:6N | Snowy | x = 0.1, many big crystals |
| RU486 | 05/22 | 4N:4N:V, etched:6N | Snowy | x = 0.2, flux covered, try 865 spin |
| RU495 | 06/22 | La:Cr:V:Ge | N/A | Abandoned. V sub ≠ HAO |

**Table 4.2:** A table of $LaCrGe_3$ batches with V or Mo substitutions.

Unless noted otherwise, the $LaCr_{1-x}V_xGe_3$ ($x = 0.06$, 0.10 and 0.20) and $LaCr_{1-x}Mo_xGe_3$ substitutions were grown following the steps (see Section 2.2) and furnace profile (see Fig. 2.2) of my $LaCrGe_3$ syntheses.

$LaCr_{1-x}V_xGe_3$ was grown in an attempt to reproduce the peculiar hard axis ordering magnetization curves in Ref. [5]. The $x = 0.06$, and $x = 0.10$ samples were grown with the same $12.75 : 12.75 - 12.75x : 12.75x : 74.5$ stoichiometric ratio as I used in my $LaCrGe_3$ synthesis. The $x = 0.20$ sample used the $(13 + 2x) : (13 - 13x) : 10x : 74 + x$ ratio detailed in Ref. [5] in a final attempt to reproduce the hard axis ordering (HAO) curves. In the end, it was the sample alignment in the MPMS, not the synthesis method, that caused the HAO curves to appear (this is detailed in Section 4.1.1). The vanadium I used for these samples was etched in nitric acid ($HNO_3$) by a former student. Non-etched vanadium is green,[28] and it turns a dull gray after being etched in nitric acid.

[28]This is apparently due to its oxidation state. For more information, ask a chemist.

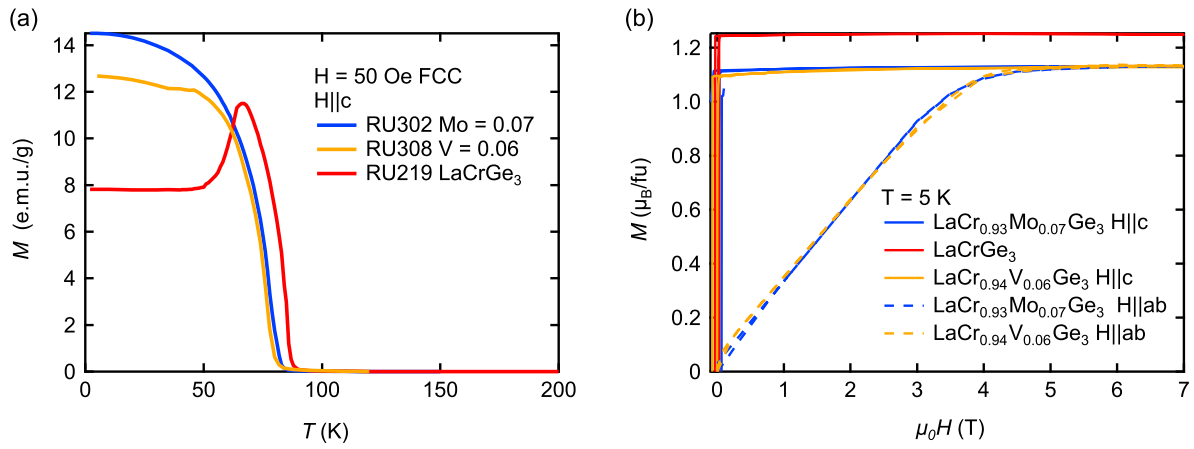


**Figure 4.26:** (a) From the $M(T)$ curves along the easy axis, we find that both V and Mo substitutions lower $T_C$. (b) In the $M(H)$ we see that both V and Mo substitutions lower the spontaneous magnetization ($M_s$). With well-aligned samples, the hard axis saturates to the same magnetization that the easy axis does for both substituted samples.

I decided to try a molybdenum (Mo) substitution out of curiosity. I figured that a Mo substitution would work since Cr-V and Cr-Mo steel alloys are both used for making tools (wrenches, socket sets, etc.). In addition, Ge is a good flux for Mo and lowers its melting temperature from over 2600°C to below the 1200°C maximum that our quartz ampoules allow. The resulting crystals were small, however, and seemed malformed.

Preliminary magnetization data of the V and Mo substitutions is shown in Fig. 4.26 and Table. 4.2 shows the relevant batch numbers.

### 4.4.3 La(Cr,Fe)$Sb_3$

| Batch | Date | Elements | Furnace | Results |
|---|---|---|---|---|
| RU | MM/YY | La:Cr:Fe:Sb | Name | Notes |
| RU280 | 01/20 | Ames:4N:4N powder:5N pieces | Snowy | x = 0.35 |
| RU301 | 03/20 | Ames:4N:4N powder:5N pieces | Snowy | x= 0.15 |
| RU306 | 06/20 | Ames:4N:4N powder:5N pieces | Haddock | x = 0.45 Excellent crystals |
| RU307 | 06/20 | Ames:4N:4N powder:5N pieces | Haddock | x = 0.55 Ratio adjusted, not magnetic |
| RU315 | 07/20 | Ames:4N:4N Powder:5N pieces | Snowy | x = 0.55 |
| RU338 | 10/20 | 4N:4N:4N powder:5N pieces | Snowy | x = 0.25 |

**Table 4.3:** A table of $LaCr_{1-x}Fe_xSb_3$ batches.

I described the synthesis details of $LaCr_{1-x}Fe_xSb_3$ in Section 3.2. I summarize the batches I grew in Table 4.3. All of the successful batches were grown with a $8 : 8-8x : 8x : 84$ stoichiometric ratio. For RU307, the stoichiometric ratio was changed to $7 : 7-7x : 7x : 86$ in an attempt to improve the yield of La(Cr,Fe)$Sb_3$ over the large plates[29] that accompany the target phase at higher Fe-substitutions. The change in ratio turned out to be a step in the wrong direction; none of the samples in the RU307 were magnetic. Photographs of most of the $LaCr_{1-x}Fe_xSb_3$ samples I grew are shown in Fig. 3.4 and Fig. 4.27 shows additional photographs comparing the effect of Fe substitution on sample mass and thickness.

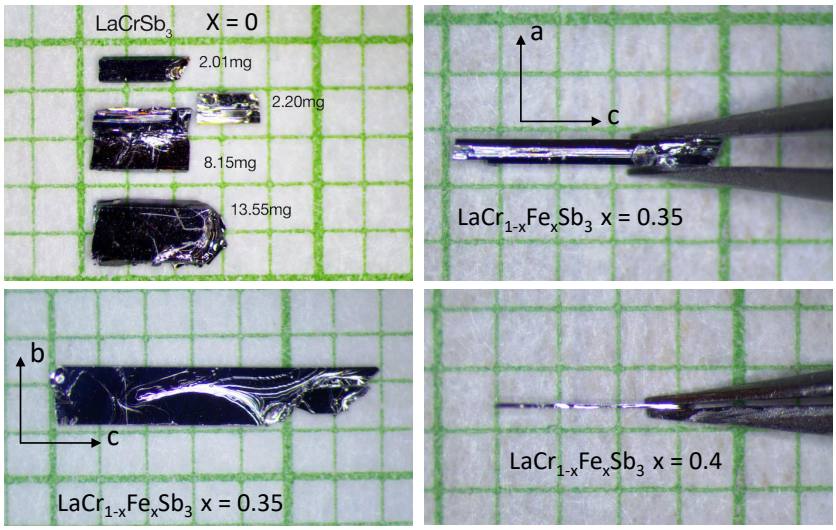


**Figure 4.27:** Additional examples of $LaCr_{1-x}Fe_xSb_3$ single crystals. A grid size of 1 mm is used throughout. The two photographs on the right highlight how substitution affects the sample thickness ($a$ dimension). Up to $x = 0.35$, the crystals were fairly robust. At $x = 0.4$ and beyond, the crystals still have significant $bc$ dimension, but they are typically thin and brittle.

[29] The La(Cr,Fe)$Sb_3$ single crystals are accompanied by large plates of a secondary phase. This secondary phase is potentially $LaSb_2$, which is non-magnetic. XRD would be able to confirm the phase. I ignored it once I discovered it was non-magnetic.

### 4.4.4 MnBi

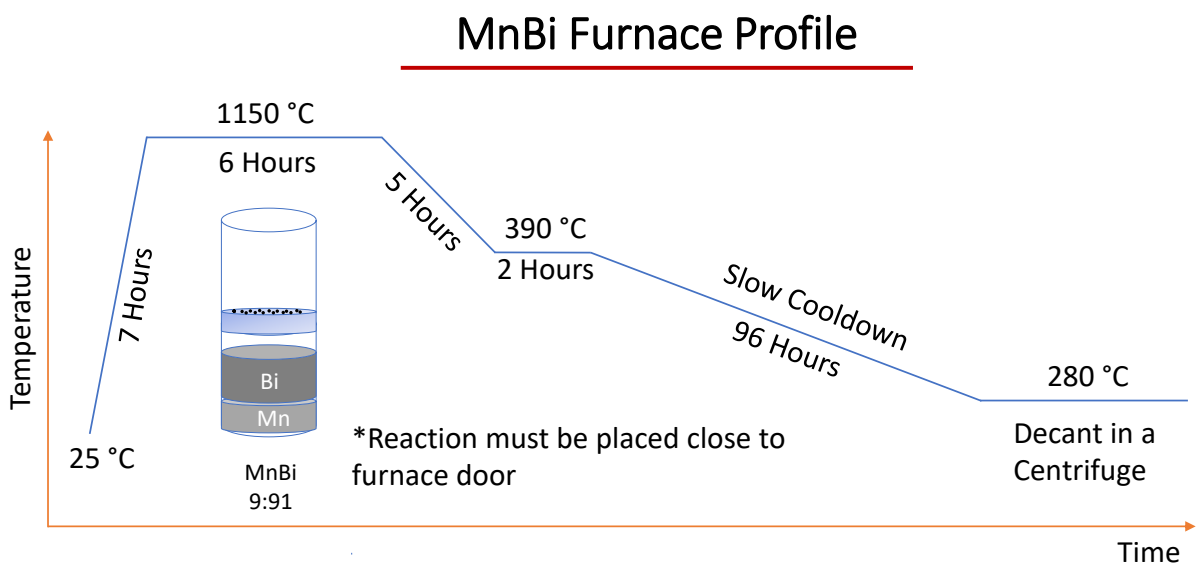


**Figure 4.28:** The temperature profile for the synthesis of MnBi single crystals. Mn and 6N Bi shot are put into a crucible in a 9 : 91 stoichiometric ratio. As a note, it is important to place the sealed ampoule near the door of the furnace for single crystals to form. In addition, there is anecdotal evidence that shaking the ampoule intermittently throughout the synthesis results in larger crystals.

MnBi ($T_C = 630\,K$ due to peritectic decomposition [191]) was grown for a potential collaboration with Professor Shanti Deemyad (University of Utah). The goal of the collaboration was to compare and contrast the pressure dependence of the structural properties of high $T_C$ and low $T_C$ ferromagnets with high pressure (up to 60 GPa) single crystal X-ray diffraction. MnBi was the first ferromagnet that I grew that is magnetic at room temperature, and it made me realize the importance of having a pair of non-magnetic tweezers. MnBi is also often used as a teaching tool; a first synthesis for new members of the lab since the constituent elements are relatively affordable and easy to work with. In fact, the furnace profile shown in Fig. 4.28 was developed by a former undergraduate researcher in our lab. The downside of this synthesis is that the resulting crystals are often not that large.

I found that for MnBi, much like for $LaCrGe_3$, it is important to have the reaction close to the furnace door for successful crystal growth. On 04/19, I ran two batches at the same time, RU222 and RU223. While they each had the same 9 : 91 stoichiometric ratio, RU222 was placed near the door, whereas RU223 was placed deep into the furnace. The reaction near the door yielded crystals, while the reaction placed deeper into the furnace did not. Our theory is that placing the reaction close to the door induces a temperature gradient which encourages mixing via convection currents within the ampoule. Valentin mentioned the following additional evidence that mixing is important for this synthesis. Specifically, some of the biggest MnBi crystals that he has seen were made by a colleague, Dr. Brian Sales. In conversation, as well as in

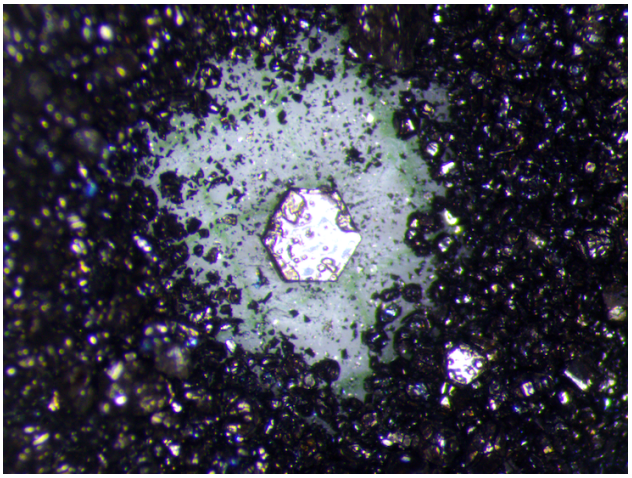

**Figure 4.29:** An example of a single crystal of MnBi. As you can guess from this photograph of the *ab* plane, MnBi has a hexagonal crystal structure.

writing,[30] Dr. Sales notes that the key to cm-sized single crystals is to vigorously shakes the crucible while at high temperature ($\approx 1000°$C) to mix the molten liquid inside.[31]

[30] Dr. Brian Sales wrote an informative overview of single crystal synthesis in Chapter 1 of the book *Fundamentals of Quantum Materials: A Practical Guide to Synthesis and Exploration* [192]. In it, he describes how he was unsuccessful in reproducing the large MnBi single crystals he had grown only a few months prior. After no luck experimenting with growth parameters, he turned to his lab notebook entry and rediscovered the key step: shaking the crucible near 1000°C. He emphasizes the importance of taking good notes. In hindsight, this textbook should be required reading for any student starting out in a synthesis lab.

[31] The idea being that with the Bi melted (270°C), the Mn (1244°C) pieces float to the top and may not fully participate in the reaction.

### 4.4.5 $Fe_5B_2P$

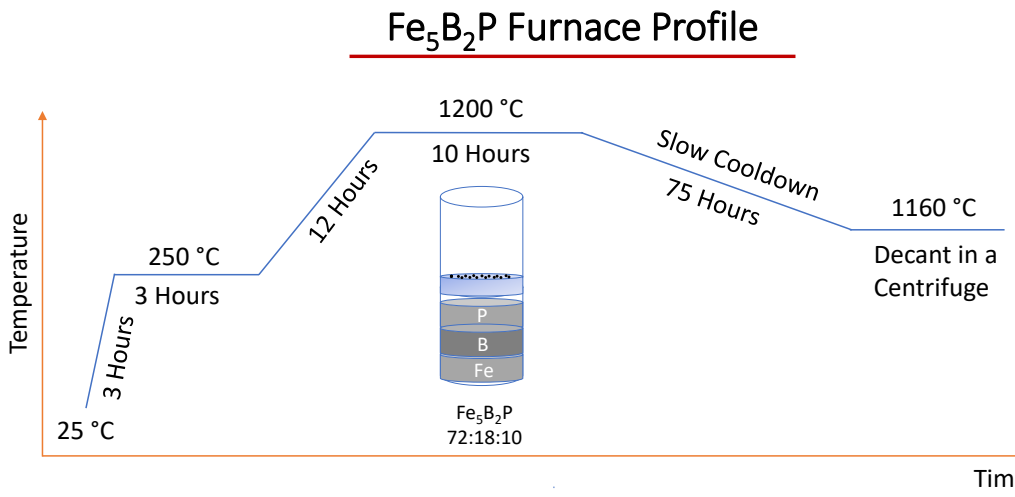


**Figure 4.30:** The temperature profile for the synthesis of $Fe_5B_2P$ single crystals following the procedure in Ref. [82].

$Fe_5B_2P$ ($T_C \approx 655\,K$ [82]) is another high temperature ferromagnet I grew (5/19 RU228) for the collaboration with Professor Shanti Deemyad. I used 4N iron powder, 6N boron pieces, and 6N phosphorus in a $72:18:10$ stoichiometric ratio following the synthesis procedure in Ref. [82]. The procedure is diagrammed in Fig. 4.30 and the resulting crystals are pictured in Fig. 4.31.

Notice that the spin temperature for this synthesis is a relatively high 1160°C. At this high temperature, there are two reasons for why you have to be swift when taking the reaction out of the furnace and putting it into the centrifuge to spin. First, the flux will solidify rapidly since the difference in temperature between the furnace and the room is so large. Second, the heat-resistant gloves that we use when reaching into the furnace will begin to smoulder if you are too slow. Since there are a number of things that can go wrong during this step of the synthesis, we always have a spotter to manage the furnace door, catch a dropped ampoule or put out any fires. My $Fe_5B_2P$ synthesis was my first and only spin with Valentin as my spotter. It could not have gone better.

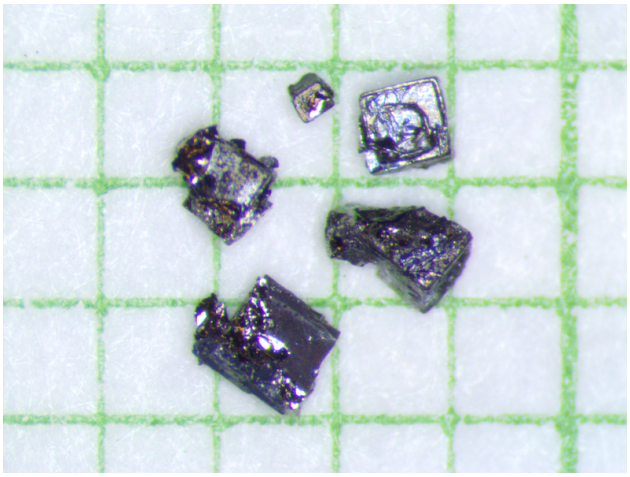

**Figure 4.31:** $Fe_5B_2P$ single crystals.

### 4.4.6 $CeAgSb_2$

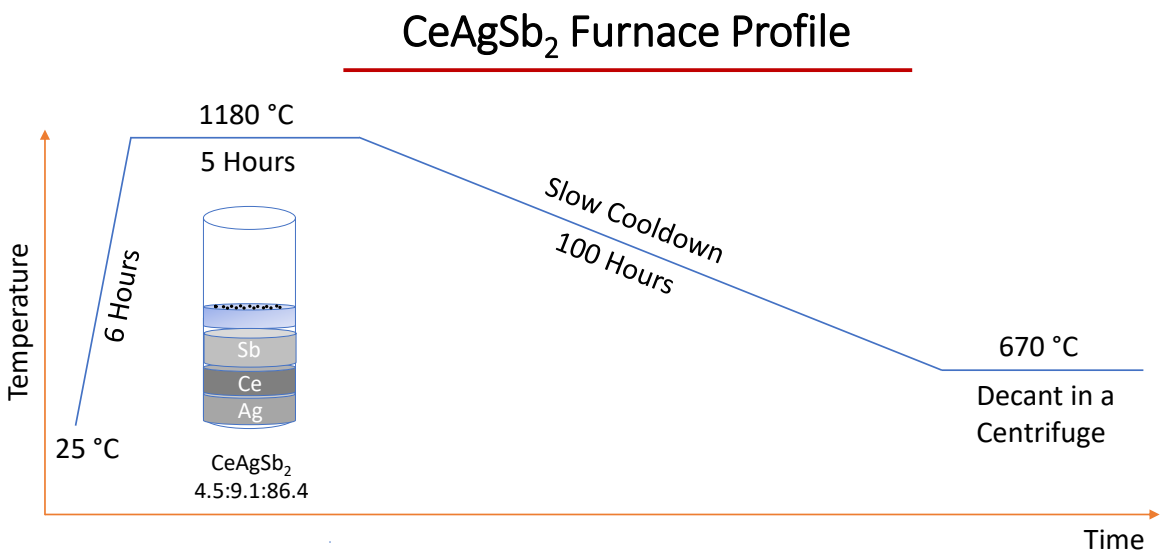


**Figure 4.32:** The temperature profile for the synthesis of $CeAgSb_2$ single crystals following the procedure in Ref. [175].

$CeAgSb_2$ was grown (RU511 8/22) to verify the hard axis ordering reported by Refs. [172, 175]. I used Ames Lab Ce, 5N Ag shot, and 5N Sb shot in a 4.5 : 9.1 : 86.4 stoichiometric ratio. From top to bottom, the elements were stacked in the order Sb, Ce, and Ag. I ran this in the relatively new box furnace called Tobbi according to the temperature profile diagrammed in Fig. 4.32 which came from Ref. [175].

# Bibliography


[1] Journey K. Byland, Yunshu Shi, David S. Parker, Jingtai Zhao, Shaoqing Ding, Rogelio Mata, Haley E. Magliari, Andriy Palasyuk, Sergey L. Bud'ko, Paul C. Canfield, Peter Klavins, and Valentin Taufour. Statistics on magnetic properties of Co compounds: A database-driven method for discovering Co-based ferromagnets. *Physical Review Materials*, 6(6):063803, June 2022.

[2] T. Jungwirth, X. Marti, P. Wadley, and J. Wunderlich. Antiferromagnetic spintronics. *Nature Nanotechnology*, 11(3):231–241, March 2016.

[3] D. Hafner, Binod K. Rai, J. Banda, K. Kliemt, C. Krellner, J. Sichelschmidt, E. Morosan, C. Geibel, and M. Brando. Kondo-lattice ferromagnets and their peculiar order along the magnetically hard axis determined by the crystalline electric field. *Physical Review B*, 99(20), May 2019.

[4] Valentin Taufour, Udhara S. Kaluarachchi, Sergey L. Bud'ko, and Paul C. Canfield. Ferromagnetic quantum criticality: New aspects from the phase diagram of $LaCrGe_3$. *Physica B: Condensed Matter*, 536:483–487, May 2018.

[5] Xiao Lin, Valentin Taufour, Sergey L. Bud'ko, and Paul C. Canfield. Suppression of ferromagnetism in the $LaV_xCr_{1-x}Ge_3$ system. *Physical Review B*, 88(9), September 2013.

[6] Brubaker Zachary E. *High Pressure Studies of Quantum Materials*. PhD thesis, University of California Davis, Sept 2019.

[7] Elena Gati, John M. Wilde, Rustem Khasanov, Li Xiang, Sachith Dissanayake, Ritu Gupta, Masaaki Matsuda, Feng Ye, Bianca Haberl, Udhara Kaluarachchi, Robert J. McQueeney, Andreas Kreyssig, Sergey L. Bud'ko, and Paul C. Canfield. Formation of short-range magnetic order and avoided ferromagnetic quantum criticality in pressurized LaCrGe3. *Physical Review B*, 103(7):075111, February 2021.

[8] Haiying Bie, Oksana Ya. Zelinska, Andriy V. Tkachuk, and Arthur Mar. Structures and physical properties of rare-earth chromium germanides $RECrGe_3$ (Re = La-Nd, Sm). *Chemistry of Materials*, 19(18):4613–4620, June 2007.

[9] Zihao Shen, X D Zhu, Rahim R Ullah, Peter Klavins, and Valentin Taufour. Anomalous depinning of magnetic domain walls within the ferromagnetic phase of the Weyl semimetal $Co_3Sn_2S_2$. *Journal of Physics: Condensed Matter*, 35(4):045802, December 2022.

[10] R. R. Ullah, P. Klavins, X. D. Zhu, and V. Taufour. Magnetic domain depinning as possible evidence for two ferromagnetic phases in $LaCrGe_3$. *Physical Review B*, 107(18):184431, May 2023.

[11] Xiao Lin, Valentin Taufour, Sergey L. Bud'ko, and Paul C. Canfield. Suppression of ferromagnetism in the $LaV_xCr_{1-x}Sb_3$ system. *Philosophical Magazine*, 94(12):1277–1300, March 2013.

[12] Jackson Badger. *Structural Characterization and Physical Properties of Superconducting $LaNiGa_2$ and Antiferromagnetic $CeIn_3$*. PhD thesis, University of California, Davis, California, 2021.

[13] Mei Li, Cuiping Guo, Changrong Li, and Zhenmin Du. A thermodynamic description of the Cr-Ge system. *Journal of Alloys and Compounds*, 481(1-2):283–290, July 2009.

[14] M. Venkatraman and J. P. Neumann. The Cr-Sb (chromium-antimony) system. *Journal of Phase Equilibria via Binary Alloy Phase Diagrams, Second Edition, Ed. T.B. Massalaski, ASM International*, 11(5), October 1990.

[15] Paul C. Canfield, Tai Kong, Udhara S. Kaluarachchi, and Na Hyun Jo. Use of frit-disc crucibles for routine and exploratory solution growth of single crystalline samples. *Philosophical Magazine*, 96(1):84–92, January 2016.

[16] K. Rana, H. Kotegawa, R. R. Ullah, J. S. Harvey, S. L. Bud'ko, P. C. Canfield, H. Tou, V. Taufour, and Y. Furukawa. Magnetic fluctuations in the itinerant ferromagnet $LaCrGe_3$ studied by La139 NMR. *Physical Review B*, 99(21), June 2019.

[17] K. Rana, H. Kotegawa, R. R. Ullah, E. Gati, S. L. Bud'ko, P. C. Canfield, H. Tou, V. Taufour, and Y. Furukawa. Magnetic properties of the itinerant ferromagnet $LaCrGe_3$ under pressure studied by La139 NMR. *Physical Review B*, 103(17):174426, May 2021.

[18] Valentin Taufour, Udhara S. Kaluarachchi, Rustem Khasanov, Manh Cuong Nguyen, Zurab Guguchia, Pabitra Kumar Biswas, Pietro Bonfà, Roberto De Renzi, Xiao Lin, Stella K. Kim, Eun Deok Mun, Hyunsoo Kim, Yuji Furukawa, Cai-Zhuang Wang, Kai-Ming Ho, Sergey L. Bud'ko, and Paul C. Canfield. Ferromagnetic quantum critical point avoided by the appearance of another magnetic phase in $LaCrGe_3$ under pressure. *Physical Review Letters*, 117(3), July 2016.

[19] Udhara S. Kaluarachchi, Sergey L. Bud'ko, Paul C. Canfield, and Valentin Taufour. Tricritical wings and modulated magnetic phases in $LaCrGe_3$ under pressure. *Nature Communications*, 8(1), September 2017.

[20] Dietrich Belitz, T. R. Kirkpatrick, and T. Vojta. Nonanalytic behavior of the spin susceptibility in clean Fermi systems. *Phys. Rev. B*, 55(15):9452–9462, April 1997.

[21] A. V. Chubukov, C. Pepin, and J. Rech. Instability of the quantum-critical point of itinerant ferromagnets. *Phys. Rev. Lett.*, 92(14):147003, April 2004.

[22] G. J. Conduit, A. G. Green, and B. D. Simons. Inhomogeneous Phase Formation on the Border of Itinerant Ferromagnetism. *Phys. Rev. Lett.*, 103(20):207201, Nov. 13 2009.

[23] Una Karahasanovic, Frank Krüger, and Andrew G. Green. Quantum order-by-disorder driven phase reconstruction in the vicinity of ferromagnetic quantum critical points. *Phys. Rev. B*, 85(16):165111, April 2012.

[24] S. J. Thomson, F. Krüger, and A. G. Green. Helical glasses near ferromagnetic quantum criticality. *Phys. Rev. B*, 87(22):224203, June 2013.

[25] C. J. Pedder, F. Krüger, and A. G. Green. Resummation of fluctuations near ferromagnetic quantum critical points. *Phys. Rev. B*, 88:165109, October 2013.

[26] D. Belitz and T. R. Kirkpatrick. Quantum triple point and quantum critical end points in metallic magnets. *Phys. Rev. Lett.*, 119:267202, December 2017.

[27] Marcin M. Wysokinski. Mechanism for transitions between ferromagnetic and antiferromagnetic orders in d-electron metallic magnets. *Scientific Reports*, 9(1):19461, December 2019.

[28] Udhara S. Kaluarachchi, Sergey L. Bud'ko, Paul C. Canfield, and Valentin Taufour. Tricritical wings and modulated magnetic phases in $LaCrGe_3$ under pressure. *Nature Communications*, 8(1):546, 2017.

[29] V. Taufour, Dai Aoki, G. Knebel, and Jacques Flouquet. Tricritical Point and Wing Structure in the Itinerant Ferromagnet $UGe_2$. *Phys. Rev. Lett.*, 105(21):217201, November 2010.

[30] N Tateiwa, K Hanazono, T. C. Kobayashi, K Amaya, T Inoue, K Kindo, Y Koike, N Metoki, Y Haga, R Settai, and Y Onuki. Magnetic properties of a pressure-induced superconductor $UGe_2$. *J. Phys. Soc. Jpn.*, 70(10):2876–2879, October 2001.

[31] C. Pfleiderer and A. D. Huxley. Pressure dependence of the magnetization in the ferromagnetic superconductor $UGe_2$. *Physical Review Letters*, 89(14):147005, September 2002.

[32] F. Hardy, C. Meingast, V. Taufour, Jacques Flouquet, H. v. Loehneysen, R. A. Fisher, N. E. Phillips, Andrew D. Huxley, and J. C. Lashley. Two magnetic Gruneisen parameters in the ferromagnetic superconductor $UGe_2$. *Phys. Rev. B*, 80(17):174521, November 2009.

[33] V. Taufour, D. Aoki, G. Knebel, and J. Flouquet. Tricritical point and wing structure in the itinerant ferromagnet $UGe_2$. *Physical Review Letters*, 105(21), November 2010.

[34] Debarchan Das, T Gruner, H Pfau, U B Paramanik, U Burkhardt, C Geibel, and Z Hossain. Heavy fermion and Kondo lattice behavior in the itinerant ferromagnet $CeCrGe_3$. *Journal of Physics: Condensed Matter*, 26(10):106001, February 2014.

[35] Haiying Bie. *New ternary rare-earth antimonides and germanides: bonding, structures, and physical properties*. PhD thesis, University of Alberta, Edmonton, Canada, 2009.

[36] B. Bosch-Santos, G. A. Cabrera-Pasca, E. L. Correa, B. S. Correa, T. N. S. Sales, K-W. Moon, C. L. Dennis, Q. Huang, J. B. Leao, J. W. Lynn, and A. W. Carbonari. Magnetic and structural properties of the intermetallic $Ce_{1-x}La_xCrGe_3$ series of compounds. *Physical Review Materials*, 5(11):114406, November 2021.

[37] M. Xu, S. L. Bud'ko, R. Prozorov, and P. C. Canfield. Unusual coercivity and zero-field stabilization of fully saturated magnetization in single crystals of $LaCrGe_3$. *Phys. Rev. B*, 107:134437, April 2023.

[38] N. Kimura, N. Kabeya, H. Aoki, K. Ohyama, M. Maeda, H. Fujii, M. Kogure, T. Asai, T. Komatsubara, T. Yamamura, and I. Satoh. Quantum critical point and unusual phase diagram in the itinerant-electron metamagnet UCoAl. *Physical Review B*, 92(3):035106, July 2015.

[39] W. Wu, A. McCollam, S. A. Grigera, R. S. Perry, A. P. Mackenzie, and S. R. Julian. Quantum critical metamagnetism of $Sr_3Ru_2O_7$ under hydrostatic pressure. *Phys. Rev. B*, 83:045106, January 2011.

[40] A. Palacio Morales, A. Pourret, G. Knebel, G. Bastien, V. Taufour, D. Aoki, H. Yamagami, and J. Flouquet. Thermoelectric power quantum oscillations in the ferromagnet $UGe_2$. *Physical Review B*, 93(15):155120, April 2016.

[41] Jörg Sichelschmidt, Thomas Gruner, Debarchan Das, and Zakir Hossain. Electron spin resonance of the itinerant ferromagnets $LaCrGe_3$, $CeCrGe_3$ and $PrCrGe_3$. *Journal of Physics: Condensed Matter*, 33(49):495605, October 2021.

[42] G. T. Tan, S. Dai, P. Duan, Y. L. Zhou, H. B. Lu, and Z. H. Chen. Colossal magnetoresistance behavior and esr studies of $La_{1-x}Te_xMnO_3$ ($0.04 < x < 0.2$). *Phys. Rev. B*, 68:014426, July 2003.

[43] X. D. Zhu, E. K. Ko, G. Kimbell, and J. Robinson. An optimized scheme for detecting magneto-optic effects in ultrathin films with sagnac interferometry. *Review of Scientific Instruments*, 93(9):093101, September 2022.

[44] X. D. Zhu. Symmetry consideration in zero loop-area sagnac interferometry at oblique incidence for detecting magneto-optic kerr effects. *Review of Scientific Instruments*, 88(8):083112, August 2017.

[45] X. D. Zhu. Magnetic domains and unusual hysteresis loops of yttrium iron garnet crystals revealed by magneto-optic effects. *AIP Advances*, 11(8):085214, August 2021.

[46] X. D. Zhu, R. Ullah, and V. Taufour. Oblique-incidence sagnac interferometric scanning microscope for studying magneto-optic effects of materials at low temperatures. *Review of Scientific Instruments*, 92(4):043706, April 2021.

[47] Mohamed A. Kassem, Yoshikazu Tabata, Takeshi Waki, and Hiroyuki Nakamura. Low-field anomalous magnetic phase in the kagome-lattice shandite $Co_3Sn_2S_2$. *Phys. Rev. B*, 96:014429, July 2017.

[48] Mohamed A Kassem, Yoshikazu Tabata, Takeshi Waki, and Hiroyuki Nakamura. Unconventional critical behaviors at the magnetic phase transition of $Co_3Sn_2S_2$ kagomé ferromagnet. *Journal of Physics: Condensed Matter*, 33(1):015801, October 2020.

[49] Qiang Zhang, Satoshi Okamoto, German D. Samolyuk, Matthew B. Stone, Alexander I. Kolesnikov, Rui Xue, Jiaqiang Yan, Michael A. McGuire, David Mandrus, and D. Alan Tennant. Unusual exchange couplings and intermediate temperature weyl state in $Co_3Sn_2S_2$. *Phys. Rev. Lett.*, 127:117201, September 2021.

[50] Jian-Rui Soh, ChangJiang Yi, Ivica Zivkovic, Navid Qureshi, Anne Stunault, Bachir Ouladdiaf, J. Alberto Rodríguez-Velamazán, YouGuo Shi, Henrik M. Rønnow, and Andrew T. Boothroyd. Magnetic structure of the topological semimetal $Co_3Sn_2S_2$. *Phys. Rev. B*, 105:094435, March 2022.

[51] Jiyu Hu, Xucai Kan, Zheng Chen, Ganhong Zheng, and Yongqing Ma. The magnetic, thermal transport properties, magnetothermal effect and critical behavior of $Co_3Sn_2S_2$ single crystal. *Journal of the American Ceramic Society*, 105(7):4827–4839, 2022.

[52] Jianlei Shen, Qingqi Zeng, Shen Zhang, Wei Tong, Langsheng Ling, Chuanying Xi, Zhaosheng Wang, Enke Liu, Wenhong Wang, Guangheng Wu, and Baogen Shen. On the anisotropies of magnetization and electronic transport of magnetic weyl semimetal $Co_3Sn_2S_2$. *Applied Physics Letters*, 115(21):212403, 2019.

[53] H.C. Wu, P.J. Sun, D.J. Hsieh, H.J. Chen, D. Chandrasekhar Kakarla, L.Z. Deng, C.W. Chu, and H.D. Yang. Observation of skyrmion-like magnetism in magnetic weyl semimetal $Co_3Sn_2S_2$. *Materials Today Physics*, 12:100189, 2020.

[54] Ella Lachman, Ryan A. Murphy, Nikola Maksimovic, Robert Kealhofer, Shannon Haley, Ross D. McDonald, Jeffrey R. Long, and James G. Analytis. Exchange biased anomalous Hall effect driven by frustration in a magnetic kagome lattice. *Nature Communications*, 11(1), January 2020.

[55] Qiang Zhang, Yuanpeng Zhang, Masaaki Matsuda, Vasile Ovidiu Garlea, Jiaqiang Yan, Michael A. McGuire, D. Alan Tennant, and Satoshi Okamoto. Hidden local symmetry breaking in a kagome-lattice magnetic Weyl semimetal. *Journal of the American Chemical Society*, 144(31):14339–14350, July 2022.

[56] Changmin Lee, Praveen Vir, Kaustuv Manna, Chandra Shekhar, J. E. Moore, M. A. Kastner, Claudia Felser, and Joseph Orenstein. Observation of a phase transition within the domain walls of ferromagnetic $Co_3Sn_2S_2$. *Nature Communications*, 13(1), May 2022.

[57] Sandeep Howlader, Ranjani Ramachandran, Shama, Yogesh Singh, and Goutam Sheet. Domain structure evolution in the ferromagnetic kagome-lattice weyl semimetal $Co_3Sn_2S_2$. *Journal of Physics: Condensed Matter*, 33(7):075801, November 2020.

[58] Gong Chen, Arantzazu Mascaraque, Hongying Jia, Bernd Zimmermann, MacCallum Robertson, Roberto Lo Conte, Markus Hoffmann, Miguel Angel González Barrio, Haifeng Ding, Roland Wiesendanger, Enrique G. Michel, Stefan Blügel, Andreas K. Schmid, and Kai Liu. Large Dzyaloshinskii-Moriya interaction induced by chemisorbed oxygen on a ferromagnet surface. *Science Advances*, 6(33), August 2020.

[59] Giorgio Bertotti. *Hysteresis in magnetism.* Academic Press, 1998.

[60] Etienne du Tremolet de Lacheisserie, Damien Gignoux, and Michel Schlenker, editors. *Magnetism.* Springer, 2004.

[61] K.P. Belov, R.Z. Levitin, S.A. Nikitin, and A.V. Ped'ko. Magnetic and magnetoelastic properties of dyprisoum and gadolinium. *Soviet Physics JETP*, 13(6), December 1961.

[62] C. D. Graham. Some magnetic properties of Gd single crystals. *Journal of Applied Physics*, 34(4):1341–1342, April 1963.

[63] L.F. Bates and A.J. Pacey. Magnetothermal measurements on gadolinium. *Proceedings of the Physical Society*, 78(878):878–882, 1961.

[64] W D Corner, W C Roe, and K N R Taylor. The magnetocrystalline anisotropy of gadolinium. *Proceedings of the Physical Society*, 80(4):927–933, October 1962.

[65] YaWei Li, Hu Zhang, Tim Yan, KeWen Long, HuaSheng Wang, YanJun Xue, Chen Cheng, and HouBo Zhou. Successive magnetic transitions and magnetocaloric effect in $Dy_3$ $Al_2$ compound. *Journal of Alloys and Compounds*, 651:278–282, December 2015.

[66] B. Barbara, C. Becle, R. Lemaire, and D. Paccard. High-performance magnets of rare-earth intermetallics due to an unusual magnetization process. *IEEE Transactions on Magnetics*, 7(3):654–656, September 1971.

[67] H. R. Hilzinger and H. Kronmüller. Spin configuration and intrinsic coercive field of narrow domain walls in $Co_5$R-compounds. *Physica Status Solidi (b)*, 54(2):593–604, December 1972.

[68] Bernard Barbara. Magnetization processes in high anisotropy systems. *Journal of Magnetism and Magnetic Materials*, 129(1):79–86, January 1994.

[69] B. Barbara. Propriétés des parois étroites dans les substances ferromagnétiques à forte anisotropie. *Journal de Physique*, 34(11-12):1039–1046, 1973.

[70] Lin Zu, Boyao Lyu, Jin Tang, Jianhua Gao, Fengguang Liu, Yinchang Du, Peng Wu, Yaodong Wu, Yutao Chen, Jialiang Jiang, Wensen Wei, Haifeng Du, and Weisheng Zhao. Magnetic domains in a uniaxial magnet $Dy_3Al_2$. *Applied Physics Letters*, 119(3):032404, July 2021.

[71] M. D. Kuz'min. Shape of temperature dependence of spontaneous magnetization of ferromagnets: Quantitative analysis. *Physical Review Letters*, 94(10):107204, March 2005.

[72] J.M. Cadogan, Pierric Lemoine, Brianna R. Slater, Arthur Mar, and Maxim Avdeev. Neutron diffraction study of the hexagonal perovskite-type compound $LaCrGe_3$. *Solid State Phenomena*, 194:71–74, November 2012.

[73] Amikam Aharoni. Demagnetizing factors for rectangular ferromagnetic prisms. *Journal of Applied Physics*, 83(6):3432–3434, March 1998.

[74] S. J. Blundell. *Magnetism in Condensed-Matter*. Oxford, 2001.

[75] Steven H. Simon. *The Oxford Solid State Basics*. Oxford University Press, June 2013.

[76] Stephen Blundell. *Magnetism in Condensed Matter*. Oxford University Press, October 2001.

[77] N. Kimura, M. Endo, T. Isshiki, S. Minagawa, A. Ochiai, H. Aoki, T. Terashima, S. Uji, T. Matsumoto, and G. G. Lonzarich. de Haas–van Alphen effect in $ZrZn_2$ under pressure: Crossover between two magnetic states. *Physical Review Letters*, 92(19):197002, May 2004.

[78] Tineke Van Peski-Tinbergen and A.J. Dekker. Spin-dependent scattering and resistivity of magnetic metals and alloys. *Physica*, 29(9):917–937, September 1963.

[79] Tadao Kasuya. Electrical resistance of ferromagnetic metals. *Progress of Theoretical Physics*, 16(1):58–63, July 1956.

[80] P.G. De Gennes and J. Friedel. Anomalies de résistivité dans certains métaux magníques. *Journal of Physics and Chemistry of Solids*, 4(1-2):71–77, January 1958.

[81] Ganping Ju, Yingguo Peng, Eric K. C. Chang, Yinfeng Ding, Alexander Q. Wu, Xiaobin Zhu, Yukiko Kubota, Timothy J. Klemmer, Hassib Amini, Li Gao, Zhaohui Fan, Tim Rausch, Pradeep Subedi, Minjie Ma, Sangita Kalarickal, Chris J. Rea, Dimitar V. Dimitrov, Pin-Wei Huang, Kangkang Wang, Xi Chen, Chubing Peng, Weibin Chen, John W. Dykes, Mike A. Seigler, Edward C. Gage, Roy

Chantrell, and Jan-Ulrich Thiele. High density heat-assisted magnetic recording media and advanced characterization—progress and challenges. *IEEE Transactions on Magnetics*, 51(11):1–9, November 2015.

[82] Tej N. Lamichhane, Valentin Taufour, Srinivasa Thimmaiah, David S. Parker, Sergey L. Bud'ko, and Paul C. Canfield. A study of the physical properties of single crystalline $Fe_5B_2P$. *Journal of Magnetism and Magnetic Materials*, 401:525–531, March 2016.

[83] F.R.S W. Sucksmith and J.E. Thompson. The magnetic anisotropy of cobalt. *Proceedings of the Royal Society of London. Series A. Mathematical and Physical Sciences*, 225(1162):362–375, September 1954.

[84] Tej Nath Lamichhane, Olena Palasyuk, Vladimir P. Antropov, Ivan A. Zhuravlev, Kirill D. Belashchenko, Ikenna C. Nlebedim, Kevin W. Dennis, Anton Jesche, Matthew J. Kramer, Sergey L. Bud'ko, R. William McCallum, Paul C. Canfield, and Valentin Taufour. Reinvestigation of the intrinsic magnetic properties of $(Fe_{1-x}Co_x)_2B$ alloys and crystallization behavior of ribbons. *Journal of Magnetism and Magnetic Materials*, 513:167214, November 2020.

[85] E.R. Callen and H.B. Callen. Anisotropic magnetization. *Journal of Physics and Chemistry of Solids*, 16(3-4):310–328, November 1960.

[86] R. M. Bozorth. Directional ferromagnetic properties of metals. *Journal of Applied Physics*, 8(9):575–588, September 1937.

[87] Udhara S. Kaluarachchi, Valentin Taufour, Sergey L. Bud'ko, and Paul C. Canfield. Quantum tricritical point in the temperature-pressure-magnetic field phase diagram of $CeTiGe_3$. *Physical Review B*, 97(4), January 2018.

[88] Sven Friedemann, Will J. Duncan, Max Hirschberger, Thomas W. Bauer, Robert Küchler, Andreas Neubauer, Manuel Brando, Christian Pfleiderer, and F. Malte Grosche. Quantum tricritical points in $NbFe_2$. *Nature Physics*, 14(1):62–67, September 2017.

[89] Markus Brylak and Wolfgang Jeitschko. Ternary antimonides $LnTSb_3$ with Ln = La-Nd, Sm and T = V, Cr. *Zeitschrift für Naturforschung B*, 50(6):899–904, June 1995.

[90] Klaus Hartjes, Wolfgang Jeitschko, and Markus Brylak. Magnetic properties of the rare-earth transition metal antimonides $LnVSb_3$ and $LnCrSb_3$ (Ln - La-Nd, Sm). *Journal of Magnetism and Magnetic Materials*, 173(1-2):109–116, September 1997.

[91] Michael J. Ferguson, Ryan W. Hushagen, and Arthur Mar. Crystal structures of $La_3ZrSb_5$, $La_3HfSb_5$, and $LaCrSb_3$. Structural relationships in ternary rare-earth antimonides. *Journal of Alloys and Compounds*, 249(1-2):191–198, March 1997.

[92] N. P. Raju, John E. Greedan, Michael J. Ferguson, and Arthur Mar. $LaCrSb_3$: a new itinerant electron ferromagnet with a layered structure. *Chemistry of Materials*, 10(11):3630–3635, November 1998.

[93] M.L Leonard, I.S Dubenko, and N Ali. Investigation of the ferromagnetism in $RCrSb_3$ (R=La, Ce, Pr, Nd). *Journal of Alloys and Compounds*, 303-304:265–269, May 2000.

[94] I. S. Dubenko, P. Hill, and N. Ali. Magnetic properties of $LaCr_{1-x}M_xSb_3$ (M=V, Mn, Fe, Cu, and Al). *Journal of Applied Physics*, 89(11):7326–7328, June 2001.

[95] W.A. MacFarlane, K.H. Chow, Z. Salman, A.V. Tkachuk, and A. Mar. A $\mu$SR study of the unusual magnetism of $LaCrSb_3$. *Physica B: Condensed Matter*, 374-375:71–74, March 2006.

[96] D. D. Jackson, M. Torelli, and Z. Fisk. Anisotropy in magnetic and transport properties of $LaTSb_3$ (T = Cr,V). *Physical Review B*, 65(1):014421, December 2001.

[97] E. Granado, H. Martinho, M. S. Sercheli, P. G. Pagliuso, D. D. Jackson, M. Torelli, J. W. Lynn, C. Rettori, Z. Fisk, and S. B. Oseroff. Unconventional metallic magnetism in $LaCrSb_3$. *Physical Review Letters*, 89(10), August 2002.

[98] Z. E. Brubaker, J. S. Harvey, J. R. Badger, R. R. Ullah, D. J. Campbell, Y. Xiao, P. Chow, C. Kenney-Benson, J. S. Smith, C. Reynolds, J. Paglione, R. J. Zieve, J. R. Jeffries, and V. Taufour. Pressure-induced suppression of ferromagnetism in the itinerant ferromagnet $LaCrSb_3$. *Physical Review B*, 101(21), June 2020.

[99] D. D. Jackson and Z. Fisk. Effect of rare-earth doping in $RCrSb_3$ (R=La, Pr, Sm, and Gd). *Physical Review B*, 73(2), January 2006.

[100] Haijie Chen, Awadhesh Narayan, Lei Fang, Nicholas P. Calta, Fengyuan Shi, Duck Young Chung, Lucas K. Wagner, Wai-Kwong Kwok, and Mercouri G. Kanatzidis. From complex magnetism ordering to simple ferromagnetism in two-dimensional $LaCrSb_3$ by hole doping. *Physical Review B*, 94(13), October 2016.

[101] P. Monthoux, D. Pines, and G. G. Lonzarich. Superconductivity without phonons. *Nature*, 450(7173):1177–1183, December 2007.

[102] Johnpierre Paglione and Richard L. Greene. High-temperature superconductivity in iron-based materials. *Nat. Phys.*, 6(9):645–658, September 2010.

[103] Philipp Gegenwart, Qimiao Si, and Frank Steglich. Quantum criticality in heavy-fermion metals. *Nat. Phys.*, 4(3):186–197, March 2008.

[104] G. R. Stewart. Unconventional superconductivity. *Advances in Physics*, 66(2):75–196, April 2017.

[105] S. S. Saxena, P. Agarwal, K. Ahilan, F. M. Grosche, R. K. W. Haselwimmer, M. J. Steiner, E. Pugh, I. R. Walker, S. R. Julian, P. Monthoux, G. G. Lonzarich, A. Huxley, I. Sheikin, D. Braithwaite, and J. Flouquet. Superconductivity on the border of itinerant-electron ferromagnetism in $UGe_2$. *Nature*, 406(6796):587–592, August 2000.

[106] Dai Aoki, Andrew D. Huxley, Eric Ressouche, Daniel Braithwaite, Jacques Flouquet, JP Brison, E Lhotel, and C Paulsen. Coexistence of superconductivity and ferromagnetism in URhGe. *Nature (London)*, 413(6856):613–616, October 2001.

[107] N. T. Huy, A. Gasparini, D. E. de Nijs, Y. Huang, J. C. P. Klaasse, T. Gortenmulder, A. de Visser, A. Hamann, T. Görlach, and H. v. Löhneysen. Superconductivity on the border of weak itinerant ferromagnetism in UCoGe. *Physical Review Letters*, 99(6):067006, August 2007.

[108] E. Slooten, T. Naka, A. Gasparini, Y. K. Huang, and Anne de Visser. Enhancement of Superconductivity near the Ferromagnetic Quantum Critical Point in UCoGe. *Phys. Rev. Lett.*, 103(9):097003, August 2009.

[109] M. Uhlarz, C. Pfleiderer, and S. M. Hayden. Quantum phase transitions in the itinerant ferromagnet $ZrZn_2$. *Physical Review Letters*, 93(25):256404, December 2004.

[110] T. Goto, Y. Shindo, H. Takahashi, and S. Ogawa. Magnetic properties of the itinerant metamagnetic system $Co(S_{1-x}Se_x)_2$ under high magnetic fields and high pressure. *Physical Review B*, 56(21):14019–14028, December 1997.

[111] M. Brando, D. Belitz, F. M. Grosche, and T. R. Kirkpatrick. Metallic quantum ferromagnets. *Reviews of Modern Physics*, 88(2):025006, May 2016.

[112] Noriyuki Kabeya, Hirotaka Maekawa, Kazuhiko Deguchi, Noriaki Kimura, Haruyoshi Aoki, and Noriaki K. Sato. Non-fermi liquid state bounded by a possible electronic topological transition in $ZrZn_2$. *Journal of the Physical Society of Japan*, 81(7):073706, July 2012.

[113] Youhei Yamaji, Takahiro Misawa, and Masatoshi Imada. Quantum and topological criticalities of Lifshitz transition in two-dimensional correlated electron systems. *J. Phys. Soc. Jpn.*, 75(9):094719, September 2006.

[114] Youhei Yamaji, Takahiro Misawa, and Masatoshi Imada. Quantum metamagnetic transitions induced by changes in fermi-surface topology: Applications to a weak itinerant-electron ferromagnet $ZrZn_2$. *Journal of the Physical Society of Japan*, 76(6):063702, June 2007.

[115] V. A. Sidorov, E. D. Bauer, N. A. Frederick, J. R. Jeffries, S. Nakatsuji, N. O. Moreno, J. D. Thompson, M. B. Maple, and Z. Fisk. Magnetic phase diagram of the ferromagnetic Kondo-lattice compound $CeAgSb_2$ up to 80 kbar. *Physical Review B*, 67(22):224419, June 2003.

[116] S. Lausberg, J. Spehling, A. Steppke, A. Jesche, H. Luetkens, A. Amato, C. Baines, C. Krellner, M. Brando, C. Geibel, H.-H. Klauss, and F. Steglich. Avoided ferromagnetic quantum critical point: Unusual short-range ordered state in CeFePO. *Physical Review Letters*, 109(21):216402, November 2012.

[117] Hisashi Kotegawa, Toshihiro Toyama, Shunsaku Kitagawa, Hideki Tou, Ryota Yamauchi, Eiichi Matsuoka, and Hitoshi Sugawara. Pressure–temperature–magnetic field phase diagram of ferromagnetic Kondo lattice CeRuPO. *Journal of the Physical Society of Japan*, 82(12):123711, December 2013.

[118] Christopher D. O'Neill, Gino Abdul-Jabbar, Didier Wermeille, Philippe Bourges, Frank Krüger, and Andrew D. Huxley. Field-induced modulated state in the ferromagnet prptal. *Phys. Rev. Lett.*, 126:197203, May 2021.

[119] J.-G. Cheng, K. Matsubayashi, W. Wu, J.P. Sun, F.K. Lin, J.L. Luo, and Y. Uwatoko. Pressure induced superconductivity on the border of magnetic order in MnP. *Physical Review Letters*, 114(11):117001, March 2015.

[120] Hisashi Kotegawa, Toshiaki Uga, Hideki Tou, Eiichi Matsuoka, and Hitoshi Sugawara. Avoided ferromagnetic quantum critical point in CeZn. *Physical Review B*, 106(18):l180405, November 2022.

[121] A. Jesche, T. Ballé, K. Kliemt, C. Geibel, M. Brando, and C. Krellner. Avoided ferromagnetic quantum critical point: Antiferromagnetic ground state in substituted CeFePO. *physica status solidi (b)*, 254(1), July 2016.

[122] E. Lengyel, M. E. Macovei, A. Jesche, C. Krellner, C. Geibel, and M. Nicklas. Avoided ferromagnetic quantum critical point in CeRuPO. *Physical Review B*, 91(3):035130, January 2015.

[123] M. Matsuda, F. Ye, S. E. Dissanayake, J.-G. Cheng, S. Chi, J. Ma, H. D. Zhou, J.-Q. Yan, S. Kasamatsu, O. Sugino, T. Kato, K. Matsubayashi, T. Okada, and Y. Uwatoko. Pressure dependence of the magnetic ground states in MnP. *Physical Review B*, 93(10):100405, March 2016.

[124] Li Xiang, Elena Gati, Sergey L. Bud'ko, Scott M. Saunders, and Paul C. Canfield. Avoided ferromagnetic quantum critical point in pressurized $La_5Ce_2Ge_3$. *Physical Review B*, 103(5):054419, February 2021.

[125] Honghong Wang, Tae Beom Park, Soohyeon Shin, Jihyun Kim, Hanoh Lee, and Tuson Park. Temperature-pressure phase diagram of the ferromagnetic Kondo lattice compound $CePtAl_4Si_2$. *Physical Review Materials*, 7(7):075003, July 2023.

[126] D. Belitz, T. R. Kirkpatrick, and Thomas Vojta. First order transitions and multicritical points in weak itinerant ferromagnets. *Physical Review Letters*, 82(23):4707–4710, June 1999.

[127] D. Belitz, T. R. Kirkpatrick, and Jörg Rollbühler. Tricritical behavior in itinerant quantum ferromagnets. *Physical Review Letters*, 94(24):247205, June 2005.

[128] T. R. Kirkpatrick and D. Belitz. Universal low-temperature tricritical point in metallic ferromagnets and ferrimagnets. *Physical Review B*, 85(13):134451, April 2012.

[129] Dmitry Miserev, Daniel Loss, and Jelena Klinovaja. Instability of the ferromagnetic quantum critical point and symmetry of the ferromagnetic ground state in two-dimensional and three-dimensional electron gases with arbitrary spin-orbit splitting. *Phys. Rev. B*, 106:134417, October 2022.

[130] T. R. Kirkpatrick and D. Belitz. Ferromagnetic quantum critical point in noncentrosymmetric systems. *Physical Review Letters*, 124(14), April 2020.

[131] Hisashi Kotegawa, Eiichi Matsuoka, Toshiaki Uga, Masaki Takemura, Masahiro Manago, Noriyasu Chikuchi, Hitoshi Sugawara, Hideki Tou, and Hisatomo Harima. Indication of Ferromagnetic Quantum Critical Point in Kondo Lattice $CeRh_6Ge_4$. *Journal of the Physical Society of Japan*, 88(9):093702, 2019.

[132] Bin Shen, Yongjun Zhang, Yashar Komijani, Michael Nicklas, Robert Borth, An Wang, Ye Chen, Zhiyong Nie, Rui Li, Xin Lu, Hanoh Lee, Michael Smidman, Frank Steglich, Piers Coleman, and Huiqiu Yuan. Strange-metal behaviour in a pure ferromagnetic Kondo lattice. *Nature*, 579(7797):51–55, March 2020.

[133] An Wang, Feng Du, Yongjun Zhang, David Graf, Bin Shen, Ye Chen, Yang Liu, Michael Smidman, Chao Cao, Frank Steglich, and Huiqiu Yuan. Localized 4f-electrons in the quantum critical heavy fermion ferromagnet $CeRh_6ge_4$. *Science Bulletin*, 66(14):1389–1394, July 2021.

[134] Y. Sang, D. Belitz, and T. R. Kirkpatrick. Disorder Dependence of the Ferromagnetic Quantum Phase Transition. *Phys. Rev. Lett.*, 113(20):207201, November 2014.

[135] Tatsuo Goko, Carlos J. Arguello, Andreas Hamann, Thomas Wolf, Minhyea Lee, Dmitry Reznik, Alexander Maisuradze, Rustem Khasanov, Elvezio Morenzoni, and Yasutomo J. Uemura. Restoration of quantum critical behavior by disorder in pressure-tuned (Mn,Fe)Si. *npj Quantum Materials*, 2(1):44, August 2017.

[136] D. Belitz and T. R. Kirkpatrick. Quantum triple point and quantum critical end points in metallic magnets. *Physical Review Letters*, 119(26):267202, December 2017.

[137] Takahiro Misawa, Youhei Yamaji, and Masatoshi Imada. $YbRh_2Si_2$: Quantum tricritical behavior in itinerant electron systems. *Journal of the Physical Society of Japan*, 77(9):093712, September 2008.

[138] Takahiro Misawa, Youhei Yamaji, and Masatoshi Imada. Spin Fluctuation Theory for Quantum Tricritical Point Arising in Proximity to First-Order Phase Transitions: Applications to Heavy-Fermion Systems, $YbRh_2Si_2$, $CeRu_2Si_2$, and $\beta$-$YbAlB_4$. *J. Phys. Soc. Jpn.*, 78(8):084707, August 2009.

[139] S. Hamann, J. Zhang, D. Jang, A. Hannaske, L. Steinke, S. Lausberg, L. Pedrero, C. Klingner, M. Baenitz, F. Steglich, C. Krellner, C. Geibel, and M. Brando. Evolution from Ferromagnetism to Antiferromagnetism in $Yb(Rh_{1-x}Co_x)_2Si_2$. *Phys. Rev. Lett.*, 122:077202, February 2019.

[140] T. Moriya and K. Usami. Coexistence of Ferro- and Antiferromagnetism and Phase-Transitions in Itinerant Electron-Systems. *Solid State Commun.*, 23(12):935–938, 1977.

[141] K. Hartjes, W. Jeitschko, and M. Brylak. Magnetic properties of the rare-earth transition metal antimonides $LnVSb_3$ and $LnCrSb_3$ (Ln=La-Nd, Sm). *J. Magn. Magn. Mater.*, 173(1-2):109–116, September 1997.

[142] Manuel Richter, Jan Rusz, Helge Rosner, Klaus Koepernik, Ingo Opahle, Ulrike Nitzsche, and Helmut Eschrig. Unconventional metallic magnetism in $LaCrSb_3$. *Journal of Magnetism and Magnetic Materials*, 272-276:E251–E252, May 2004.

[143] Nitesh Kumar, Neetu Lamba, Jacob Gayles, Congcong Le, Praveen Vir, Satya N. Guin, Yan Sun, Claudia Felser, and Chandra Shekhar. Giant Anomalous Hall Conductivity in the Itinerant Ferromagnet $LaCrSb_3$ and the Effect of f-Electrons. *Adv. Quantum Technol.*, 4(6):2100023, 2021.

[144] Wei Jiang, Duarte J. P. de Sousa, Jian-Ping Wang, and Tony Low. Giant Anomalous Hall Effect due to Double-Degenerate Quasiflat Bands. *Phys. Rev. Lett.*, 126:106601, March 2021.

[145] J. Custers, P. Gegenwart, H. Wilhelm, K. Neumaier, Y. Tokiwa, O. Trovarelli, C. Geibel, F. Steglich, C. Pepin, and P. Coleman. The break-up of heavy electrons at a quantum critical point. *Nature*, 424(6948):524–527, 2003.

[146] P. Gegenwart, J. Custers, C. Geibel, K. Neumaier, T. Tayama, K. Tenya, O. Trovarelli, and F. Steglich. Magnetic-Field Induced Quantum Critical Point in $YbRh_2Si_2$. *Phys. Rev. Lett.*, 89:056402, July 2002.

[147] Erwin Schuberth, Marc Tippmann, Lucia Steinke, Stefan Lausberg, Alexander Steppke, Manuel Brando, Cornelius Krellner, Christoph Geibel, Rong Yu, Qimiao Si, and Frank Steglich. Emergence of superconductivity in the canonical heavy-electron metal $YbRh_2Si_2$. *Science*, 351(6272):485–488, January 2016.

[148] D. H. Nguyen, A. Sidorenko, M. Taupin, G. Knebel, G. Lapertot, E. Schuberth, and S. Paschen. Superconductivity in an extreme strange metal. *Nat. Commun.*, 12(1):4341, 2021.

[149] T. F. Smith, J. A. Mydosh, and Wohlfart E. P. Destruction of ferromagnetism in $ZrZn_2$ at high pressure. *Phys. Rev. Lett.*, 27(25):1732, 1971.

[150] Shinya Takashima, Minoru Nohara, Hiroaki Ueda, Nao Takeshita, Chieko Terakura, Fumiko Sakai, and Hidenori Takagi. Robustness of non-fermi-liquid behavior near the ferromagnetic critical point in clean $ZrZn_2$. *Journal of the Physical Society of Japan*, 76(4):043704, April 2007.

[151] N. Kabeya, H. Maekawa, K. Deguchi, N. Kimura, H. Aoki, and N. K. Sato. Phase diagram of the itinerant-electron ferromagnet $ZrZn_2$. *Physica Status Solidi B*, 250(3):654–656, March 2013.

[152] K. G. Sandeman, G. G. Lonzarich, and A. J. Schofield. Ferromagnetic superconductivity driven by changing Fermi surface topology. *Phys. Rev. Lett.*, 90(16):167005, Apr 25 2003.

[153] F Honda, N Metoki, T D Matsuda, Y Haga, and Y Onuki. Long-period, longitudinal spin density modulation in an itinerant 5f magnetic compound $UCu_2Si_2$. *J. Phys.-Condes. Matter*, 18(2):479, 2006.

[154] Jiaqi Cai, Dmitry Ovchinnikov, Zaiyao Fei, Minhao He, Tiancheng Song, Zhong Lin, Chong Wang, David Cobden, Jiun-Haw Chu, Yong-Tao Cui, Cui-Zu Chang, Di Xiao, Jiaqiang Yan, and Xiaodong Xu. Electric control of a canted-antiferromagnetic chern insulator. *Nature Communications*, 13(1), March 2022.

[155] S.-K. Bac, K. Koller, F. Lux, J. Wang, L. Riney, K. Borisiak, W. Powers, M. Zhukovskyi, T. Orlova, M. Dobrowolska, J. K. Furdyna, N. R. Dilley, L. P. Rokhinson, Y. Mokrousov, R. J. McQueeney, O. Heinonen, X. Liu, and B. A. Assaf. Topological response of the anomalous Hall effect in $MnBi_2Te_4$ due to magnetic canting. *npj Quantum Materials*, 7(1), April 2022.

[156] Naoto Nagaosa, Jairo Sinova, Shigeki Onoda, A. H. MacDonald, and N. P. Ong. Anomalous Hall effect. *Rev. Mod. Phys.*, 82:1539–1592, May 2010.

[157] Jonathan Kipp, Kartik Samanta, Fabian R. Lux, Maximilian Merte, Dongwook Go, Jan-Philipp Hanke, Matthias Redies, Frank Freimuth, Stefan Blugel, Marjana Lezaic, and Yuriy Mokrousov. The chiral Hall effect in canted ferromagnets and antiferromagnets. *Communications Physics*, 4(1):99, 2021.

[158] Hua Chen, Qian Niu, and A. H. MacDonald. Anomalous Hall Effect Arising from Noncollinear Antiferromagnetism. *Phys. Rev. Lett.*, 112:017205, January 2014.

[159] Satoru Nakatsuji, Naoki Kiyohara, and Tomoya Higo. Large anomalous Hall effect in a non-collinear antiferromagnet at room temperature. *Nature*, 527(7577):212–215, November 2015.

[160] Weiwei Lin, Jiaming He, Bowen Ma, Matthew Matzelle, Jinsong Xu, John Freeland, Yongseong Choi, Daniel Haskel, Bernardo Barbiellini, Arun Bansil, Gregory A. Fiete, Jianshi Zhou, and C. L. Chien. Evidence for spin swapping in an antiferromagnet. *Nat. Phys.*, 18(7):800–805, 2022.

[161] Bryan C. Chakoumakos, Huibo Cao, Feng Ye, Alexandru D. Stoica, Mihai Popovici, Madhan Sundaram, Wenduo Zhou, J. Steve Hicks, Gary W. Lynn, and Richard A. Riedel. Four-circle single-crystal neutron diffractometer at the high flux isotope reactor. *Journal of Applied Crystallography*, 44(3):655–658, May 2011.

[162] J.M. Perez-Mato, S.V. Gallego, E.S. Tasci, L. Elcoro, G. de la Flor, and M.I. Aroyo. Symmetry-based computational tools for magnetic crystallography. *Annual Review of Materials Research*, 45(1):217–248, July 2015.

[163] Juan Rodríguez-Carvajal. Recent advances in magnetic structure determination by neutron powder diffraction. *Physica B: Condensed Matter*, 192(1-2):55–69, October 1993.

[164] J.C. Lashley, M.F. Hundley, A. Migliori, J.L. Sarrao, P.G. Pagliuso, T.W. Darling, M. Jaime, J.C. Cooley, W.L. Hults, L. Morales, D.J. Thoma, J.L. Smith, J. Boerio-Goates, B.F. Woodfield, G.R. Stewart, R.A. Fisher, and N.E. Phillips. Critical examination of heat capacity measurements made on a quantum design physical property measurement system. *Cryogenics*, 43(6):369–378, June 2003.

[165] Vincent Hardy, Yohann Bréard, and Christine Martin. Derivation of the heat capacity anomaly at a first-order transition by using a semi-adiabatic relaxation technique. *Journal of Physics: Condensed Matter*, 21(7):075403, January 2009.

[166] E. A. Yelland, S. J. C. Yates, O. Taylor, A. Griffiths, S. M. Hayden, and A. Carrington. Ferromagnetic properties of $ZrZn_2$. *Phys. Rev. B*, 72:184436, November 2005.

[167] Yunshu Shi, David S. Parker, Eun Sang Choi, Kasey P. Devlin, Li Yin, Jingtai Zhao, Peter Klavins, Susan M. Kauzlarich, and Valentin Taufour. Robust antiferromagnetism in $Y_2Co_3$. *Physical Review B*, 104(18):184407, November 2021.

[168] A. Jesche, M. Fix, A. Kreyssig, W. R. Meier, and P. C. Canfield. X-ray diffraction on large single crystals using a powder diffractometer. *Philosophical Magazine*, 96(20):2115–2124, June 2016.

[169] L. Vegard. Die konstitution der mischkristalle und die raumfullung der atome. *Zeitschrift fur Physik*, 5(1):17–26, January 1921.

[170] A. R. Denton and N. W. Ashcroft. Vegard's law. *Phys. Rev. A*, 43:3161–3164, March 1991.

[171] F. Krüger, C. J. Pedder, and A. G. Green. Fluctuation-driven magnetic hard-axis ordering in metallic ferromagnets. *Physical Review Letters*, 113(14), October 2014.

[172] K.D Myers, S.L Bud'ko, I.R Fisher, Z Islam, H Kleinke, A.H Lacerda, and P.C Canfield. Systematic study of anisotropic transport and magnetic properties of $RAgSb_2$ (R=Y, La–Nd, Sm, Gd–Tm). *Journal of Magnetism and Magnetic Materials*, 205(1):27–52, October 1999.

[173] Tetsuya Takeuchi, Arumugam Thamizhavel, Tomoyuki Okubo, Mineko Yamada, Noriko Nakamura, Takeshi Yamamoto, Yoshihiko Inada, Kiyohiro Sugiyama, Andrei Galatanu, Etsuji Yamamoto, Koichi Kindo, Takao Ebihara, and Yoshichika Ōnuki. Anisotropic, thermal, and magnetic properties of $CeAgSb_2$ explanation via a crystalline electric field scheme. *Physical Review B*, 67(6):064403, February 2003.

[174] Shingo Araki, Naoto Metoki, Andrei Galatanu, Etsuji Yamamoto, Arumugam Thamizhavel, and Yoshichika Ōnuki. Crystal structure, magnetic ordering, and magnetic excitation in the $4f$-localized ferromagnet $CeAgSb_2$. *Phys. Rev. B*, 68:024408, July 2003.

[175] S. E. Nikitin, A. Podlesnyak, J. Xu, D. Voneshen, Manh Duc Le, S. L. Bud'ko, P. C. Canfield, and D. A. Sokolov. Magnetic field induced softening of spin waves and hard-axis order in the Kondo-lattice ferromagnet $CeAgSb_2$. *Physical Review B*, 104(11):115169, September 2021.

[176] Manh Cuong Nguyen, Valentin Taufour, Sergey L. Bud'ko, Paul C. Canfield, Vladimir P. Antropov, Cai-Zhuang Wang, and Kai-Ming Ho. Using first-principles calculations to screen for fragile magnetism: Case study of $LaCrGe_3$ and $LaCrSb_3$. *Physical Review B*, 97(18), May 2018.

[177] M McElfresh, S Li, and R Sager. Effects of magnetic field uniformity on the measurement of superconducting samples. Technical Report 1104, Quantum Design, Quantum Design, 1996.

[178] QD Applications Scientists. Mpms application note 1014-201: Sample mounting considerations. Technical report, Quantum Design, 2000.

[179] H Flandorfer, O Sologub, C Godart, K Hiebl, A Leithe-Jasper, P Rogl, and H Noël. On the cerium valence in ternary compounds $CeMSb_2$ and $CeM'Bi_2$; M=Mn,Fe,Co,Ni,Cu,Zn,Pd,Ag,Au and M'=Ni,Cu,Zn,Ag. *Solid State Communications*, 97(7):561–565, February 1996.

[180] Yuji Muro, Naoya Takeda, and Masayasu Ishikawa. Magnetic and transport properties of dense Kondo systems, $CeTSb_2$ (T=Ni, Cu, Pd and Ag). *Journal of Alloys and Compounds*, 257(1–2):23–29, July 1997.

[181] Adam L Gross, Lorenz Falling, Matthew C Staab, Metzli I Montero, Rahim R Ullah, David M Nisson, Peter Klavins, Kristie J Koski, Nicholas J Curro, Valentin Taufour, Slavomir Nemsak, and Inna M Vishik. Copper migration and surface oxidation of $Cu_xBi_2Se_3$ in ambient pressure environments. *Journal of Physics: Materials*, 5(4):044005, October 2022.

[182] Dongkai Shangguan. *Lead-free solder interconnect reliability*. ASM International, 2005.

[183] Nan Jiang, Liang Zhang, Zhi-Quan Liu, Lei Sun, Wei-Min Long, Peng He, Ming-Yue Xiong, and Meng Zhao. Reliability issues of lead-free solder joints in electronic devices. *Science and Technology of Advanced Materials*, 20(1):876–901, September 2019.

[184] J D Hill. Power unit for welding fine wires. *Journal of Scientific Instruments*, 36(8):369, August 1959.

[185] E D Hart and W H Elkin. Welding fine thermocouple wires. *Journal of Scientific Instruments*, 23(1):17, January 1946.

[186] S V Radcliffe and J S White. Two simple methods for spot welding wires. *Journal of Scientific Instruments*, 38(9):363, September 1961.

[187] E Babic, B Leontic, and M Vukelic. A thyristor device for pulse spot-welding of thin wires and foils. *Journal of Physics E: Scientific Instruments*, 4(5):382–383, May 1971.

[188] I. R. Walker and C. J. Moss. Spot welder for making small electrical contacts. *Review of Scientific Instruments*, 69(7):2747–2756, July 1998.

[189] I. R. Walker and C. J. Moss. Further considerations on the preparation of small electrical contacts by spot welding. *Review of Scientific Instruments*, 71(5):2228–2232, May 2000.

[190] Takeshi Hiraoka. The simple spot-welding apparatus. *Review of Scientific Instruments*, 69(7):2808–2809, July 1998.

[191] Michael A. McGuire, Huibo Cao, Bryan C. Chakoumakos, and Brian C. Sales. Symmetry-lowering lattice distortion at the spin reorientation in MnBi single crystals. *Physical Review B*, 90(17), November 2014.

[192] J Paglione, N P Butch, and E E Rodriguez. *Fundamentals of Quantum Materials: A Practical Guide to Synthesis and Exploration*. World Scientific, January 2021.